CRANFIELD UNIVERSITY

Usani Unoh Ofem

Laser Assisted Arc Welding Process for Dry Hyperbaric Deep water Application

School of Applied Sciences

Welding Engineering

PhD Thesis

Academic Year: 2010 - 2013

Supervisor: Supriyo Ganguly and Stewart Williams

November 2013

CRANFIELD UNIVERSITY

School of Applied Sciences

Welding Engineering

PhD Thesis

Academic Year 2010 - 2013

Usani Unoh Ofem

Laser Assisted Arc Welding Process for Dry Hyperbaric Deep water Application

Supervisor: Supriyo Ganguly and Stewart Williams

November 2013

This thesis is submitted in partial fulfilment of the requirements for the degree of
Doctorate of Philosophy

Dedication

To my mother

Eugenia Ofem

1947 - 2005

“Real knowledge, like everything else of the highest value, is not to be obtained easily. It must be worked for, studied for, thought for, and more than all, it must be prayed for”

Thomas Arnold

ABSTRACT

Hyperbaric Gas Metal Arc Welding (GMAW) is an important technology for repair welding of deep sea pipelines and linking of existing pipeline networks to newer ones through tie-ins and hot-tap welding. With increasing water depth the process becomes susceptible to hydrogen assisted cracking due to the very fast cooling rate of the weld caused by higher habitat gas density and resulting higher thermal diffusivity. Maintaining sufficient heat in the welding zone is vital to avoid a potential cracking tendency especially as moisture pick-up may be difficult to avoid during hyperbaric welding operations. In addition to this, hyperbaric GMAW has a limitation of low heat input because it is operated at a short arc length or dip transfer mode to avoid process instability at high pressure. Also, the short arc length generates weld spatter that may affect weld quality.

The research presented in this thesis, investigated the use of an industrial laser in conduction mode for the purpose of providing significant additional heat input to control the weld thermal cycles of GMAW. Advanced GMAW power sources such as the Fronius Cold Metal Transfer (CMT) and EWM ColdArc have also been investigated for reduced weld spatter generation.

Studies were conducted to investigate the weld pool thermal cycles and resulting metallurgical phase formation in hyperbaric GMAW at different pressures ranging from 1 bar to 200 bar. This was followed by welding trials at one atmosphere to compare the process characteristics of traditional dip transfer GMAW with some advanced GMAW power sources such as CMT and ColdArc. The main experimental trials to investigate a laser assisted GMAW (CMT) process were performed at one atmosphere condition. A thermal model was developed using Abaqus software to predict the weld metal and heat affected zone thermal cycle in a laser assisted GMAW (CMT) process at one atmosphere and under high ambient pressures. Finally, investigation was carried out to evaluate the benefit of the laser assisted process in lowering diffusible hydrogen content from the weld metal.

The hyperbaric GMAW experimental results showed that the weld pool cooling rate increases with pressure due to higher chamber gas density and resulting thermal diffusivity. But this effect is not prominent for thicker plates. Therefore, it was concluded that heat conduction through the steel thickness dominates convective losses to the chamber gas environment. It was also shown that the welding arc shrinks as pressure

increases in order to minimise energy loss to the environment. This defined the weld bead profile; although it was found that beyond 100 bar pressure the weld penetration depth remained effectively unchanged. Apart from the hardness of the weld made at 1 bar, there was little difference between those at 18, 100 and 200 bar. However, all of the welds show hardness peaks greater than 350 HV_{10} recommended for offshore structures.

It was observed that CMT produced the lowest weld spatter compared to the traditional GMAW and ColdArc. However, this advantage is constrained to low wire feed speed (3 to 5 m/min) beyond which it becomes relatively unstable. For the laser assisted GMAW (CMT) trials, it was shown that the laser serves as a spatially resolved heat source, reheating the weld bead and reducing the cooling rate. For the laser parameters investigated, over 200% reduction of cooling rate could be achieved when compared with GMAW alone. It was also demonstrated that the additional laser thermal input will extend the weld residence time at high temperature (over 300 °C). This will prolong the weld cooling time such that dissolved hydrogen can diffuse out before it comes to room temperature. The laser was shown to significantly reduce the weld peak hardness from about 420 $HV_{0.5}$ to values below 350 $HV_{0.5}$, which will be beneficial for hyperbaric welding. The model prediction of the weld thermal cycles was in good agreement with the experimental results. Therefore, it could be used to predict the weld metal and HAZ cooling rate of a laser assisted GMAW (CMT) process although the model would need to be calibrated for higher pressure data. It was also demonstrated that additional laser heat can reduce the weld hydrogen content to acceptable limits of 5 ml/100 g of weld metal even for high moisture content in the welding environment.

In conclusion, the addition of laser heating to GMAW will reduce the weld cooling rate, extend the weld pool cooling time, and expel diffusible weld hydrogen. All of these would be immensely beneficial in terms of improving the quality and reliability of structures fabricated through hyperbaric GMAW.

ACKNOWLEDGEMENTS

My utmost gratitude is to Almighty God for the gift of life and knowledge out of His infinite and absolute store of knowledge.

This doctoral thesis is the culmination of a research programme sponsored by the Petroleum Technology Development Fund (PTDF) of Nigeria. I therefore wish to express my gratitude to the government of Nigeria through the PTDF for sponsoring my studies at Cranfield University, U.K, and the Raw Materials Research and Development Council for granting me study leave.

I am profoundly indebted to Prof Stewart Williams and Dr Supriyo Ganguly who were my academic supervisors. Their knowledge, guidance, contributions and patience were invaluable throughout the period of this research work. There was little I could have done without Dr Neil Woodward. His wealth of experience in hyperbaric welding was as vital as the support I received from him through the provision of relevant research papers, design of experimental procedures and operating the hyperbaric chamber. My appreciation also goes to Dr Paul Colegrove who was my subject adviser. I gained valuable experience from him when he supervised my MSc thesis, and this paved the way for a successful PhD research.

All members of staff of the Welding Engineering and Laser Processing Centre especially the technical staff deserve mention for their different contributions and support to my research work. I want to thank Mr Flemming Nielson and Mr Brian Brooks for their help and support during the experimental work. To my friends and colleagues: Daniel, Eurico, Sonia, Gonzalo, Ibrahim, Stephan, Filomeno, Anthony, Wojciech, Mathew, Tamas, Matyas, Pedro, Jialuo, Fude, Jibrin, Ayoola, I say thanks for your friendship, support and encouragement.

I wish to specially thank my mum, Eugenia Ofem posthumously and my dad, Lawrence Ofem for their prayers and modest upbringing. The same appreciation goes to all my siblings for their love and support.

Finally, how can I thank my beloved wife, Immaculata Ofem enough for her unending prayers, love, patience and support as we weathered several storms together during the period of this research work? And off course our beloved children, Precious, Jesse and Michael; I love you all and you are a blessing to me.

LIST OF PUBLICATIONS

Some of the chapters of this thesis have been, or are intended to be published elsewhere. For each of the published work, the author made principal contributions. A list of these is given below:

- U.U. Ofem, S. Ganguly, S. Williams. Evaluation of Laser Assisted Gas Metal Arc Welding for Deep Water Hyperbaric Application. International Journal of Offshore and Polar Engineering (2013) Accepted, in press.

- U.U. Ofem, S. Ganguly, S. Williams, N. Woodward. Investigation of Thermal Cycles and Metallurgical Characteristics of Hyperbaric Gas Metal Arc Welding. Submitted to International Journal of Offshore and Polar Engineering.

- U.U. Ofem, S. Ganguly, S. Williams. Control of Cooling Behaviour in Hyperbaric Gas Metal Arc Welding by Laser Assistance, The Laser User, Issue 69, Spring 2013

- U.U. Ofem, S. Ganguly, S. Williams. Laser Assisted Arc Welding Process for Dry Hyperbaric Deep Water Application. Proceedings of the 17TH Offshore West Africa Conference, Accra, Ghana, Accepted, in press

TABLE OF CONTENTS

LIST OF FIGURES

LIST OF TABLES

LIST OF NOMENCLATURE

Δ_t and d_t	Variation of time
P_{inst}	Instantaneous arc power
Ar	Argon
CO_2	Carbon dioxide
O_2	Oxygen
Ni	Nickel
M_O	Molybdenum
H_2	Hydrogen
Cr	Chromium
Ti	Titanium
HV	Vickers hardness
δ_{max}	Maximum tensile stress
F_m	Maximum cohesive resistive force
HD	Hydrogen concentration
E_B	Binding energy
K	Boltzmann's constant
Ms	Martensite start
Q_{weld}	Weld heat input
Q_{CMT}	CMT heat input
Q_{Laser}	Laser heat input
η	Process efficiency
V	Arc voltage
I	Welding current
v	Welding speed

SE_X	Standard error of mean
E_P	Specific point energy
t_i	Interaction time
H_{DM}	Hydrogen in deposit metal

LIST OF ABBREVIATIONS

3-D	Three Dimensions
AC	Alternating Current
AF	Acicular Ferrite
AWS	American Welding Society
BCC	Body Centred Cubic
BCT	Body Centred Tetragonal
BM	Base Metal
BS	British Standard
CC	Cold Cracking
CCT	Continuous Cooling Transformation
CE	Carbon Equivalent
CGHAZ	Coarse Grained Heat Affected Zone
CMT	Cold Metal Transfer
CTWD	Contact Tip to Work Distance
EPRS	Emergency Pipeline Repair System
FCAW	Flux Cored Arc Welding
FCC	Face Centred Cubic
FGHAZ	Fine Grained Heat Affected Zone
FPSO	Floating, Production, Storage and Offloading
FZ	Fusion Zone
GBF	Grain Boundary Ferrite
GMAW	Gas Metal Arc Welding
GoM	Gulf of Mexico
GTAW	Gas Tungsten Arc Welding

HAC	Hydrogen Assisted Cracking
HACC	Hydrogen Assisted Cold Cracking
HAZ	Heat Affected Zone
HC	Hydrogen Cracking
HCP	Hexagonal Close Packed
HEAC	Hydrogen Environment Assisted Cracking
HIC	Hydrogen Induced Cracking
HISC	Hydrogen Induced Stress Cracking
HSLA	High Strength Low Alloy Steel
IHAC	Internal Hydrogen Assisted Cracking
IIW	International Institute of Welding
M	Martensite
MAG	Metal Active Gas
MIG	Metal Inert Gas
MMAW	Manual Metal Arc Welding
OD	Outside Diameter
OP	Oxidation Potential
PF	Polygonal Ferrite
PRS	Pipeline Repair System
RCU	Remote Control Unit
RMS	Root Mean Square
ROV	Remotely Operated Vehicle
RPRS	Remote Pipeline Repair System
SCT	Short Circuit Transfer
SMAW	Shielded Metal Arc Welding

SMYS	Specified Minimum Yield Stress
STT	Surface Tension Transfer
TIG	Tungsten Inert Gas
TS	Travel Speed
VME	Virtual Machine Environment
WCS	Weld Control System
WF	Widmanstatten Ferrite
WFS	Wire Feed Speed
WM	Weld Met

1 Introduction

Scope

This chapter presents an overview of the industrial background and developments of dry hyperbaric welding of deep water pipelines. The aim and objectives of the research and thesis outline are also presented.

1.1 **Industrial Background**

Underwater welding in an environment of inert gas at elevated pressure is referred to as dry hyperbaric welding. It is a technique that is used for the high quality installation and repair of offshore steel structures [120]. The term dry hyperbaric welding is to stress that the welding arc is not making close contact with the surrounding water as is the case with wet welding [120]. Less critical weld repair of offshore structures can be undertaken by wet welding, which involves divers employing manual metal arc welding (MMAW) techniques at relatively shallow water depths.

To date mechanised hyperbaric welding projects executed by petroleum companies or their contractors are diver-assisted and are implemented at relatively shallow water depths using semi-automated Gas Tungsten Arc Welding (GTAW), which has been shown to become increasingly unstable beyond 300 m [20; 120]. Also, there is legislation in Norway that stipulates a maximum diver's depth of 180 m. This and the need for cost effective solutions for equipment installation and repair in increasingly remote offshore environments whilst ensuring safety of operating personnel and the environment has driven research efforts towards the development and implementation of diver-less or remotely operated hyperbaric welding.

The ever increasing global demand for oil and natural gas against the background of dwindling onshore production during the last two decades has driven petroleum companies to explore remote offshore locations [126]. Offshore oil and gas production from shallow water (≤ 400 metres), deep water (>400 to ≤1,500 metres), and ultra-deep water (>1,500 metres) has been remarkable in the last fifteen years, with deep water production making steady continuous growth (Figure 1-1) [127]. Since reservoirs in shallow waters have been extensively explored, drilling activities and pipeline installation are being shifted into increasingly deep waters.

Production from deep water started in the 1990s, and rapidly reached 1.5 million barrels per day (mb/d) by 2000. This has since tripled to about 4 mb/d in

2010 (Figure 1-1), and both deep water and ultra-deep water productions are predicted to make significant contributions to global supply in years to come [127].

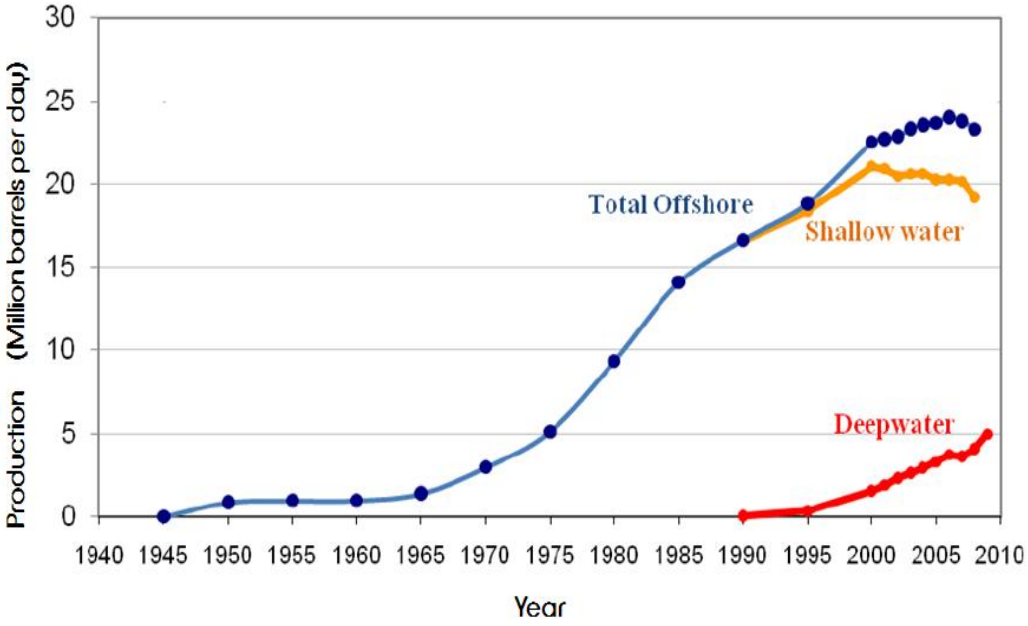

Figure 1-1: World offshore crude oil production [127]

In the last decade, offshore contributed about 70% to the major petroleum discoveries worldwide, with the US Gulf of Mexico (GoM) being the most significant deep water region in terms of investment and production [127]. About one-third of global deep water spending of about $21 billion was invested in this region in 2009, contributing almost one third of US crude oil output of 5.3 mb/d in the same year [127]. Other notable deep water producers are: Brazil, Angola and Nigeria, which together with the US account for three-quarters of world deep water production in 2010 [127]. The remainder comes from thirteen other countries as shown in Figure 1-2. Although not included in Figure 1-2, Ghana is an emerging deep water producer on account of recent discoveries and investments.

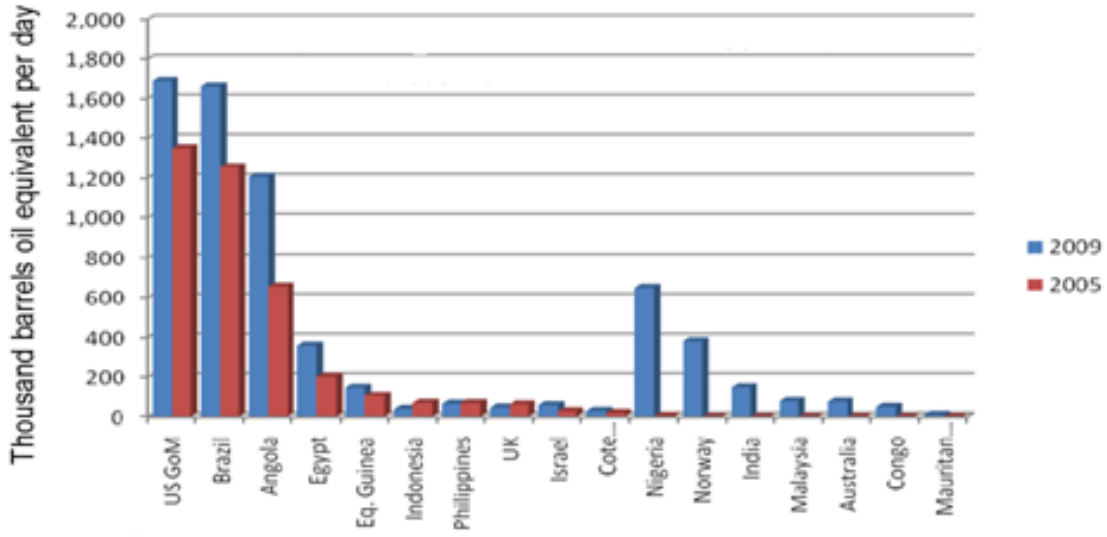

Figure 1-2: Deep water oil and gas producing countries [127]

Currently many deep water fields are being exploited by Floating, Production, Storage and Offloading vessels (FPSOs), which are shuttle tankers with high operating cost [94]. The exploitation of deep water fields by laying a large network of subsea pipelines for transporting the crude oil from the fields to shore without the need for production platforms would considerably reduce operating costs. Such pipeline facilities are presently not widely available, although there have been significant developments in Europe. There are indications that globally, North West Europe is currently the main region where significant subsea pipeline installation and repair have been carried out using hyperbaric welding operations [20].

There is considerable experience in the oil and gas industry for repair of pipelines in shallow waters. The repair and maintenance is done by diver-assisted hyperbaric welding operations. Statoil and Subsea 7 are notable companies that have developed reliable hyperbaric systems that have been used to weld a range of pipe diameters under different water depths. Statoil and Norsk Hydro developed the Pipeline Repair System (PRS), which is a comprehensive suite of tools for the tie-in and contingency repair welding of subsea pipelines. It is managed by Statoil on behalf of 40 companies that share costs in order to have access to the equipment [14]. Subsea 7 utilizes a similar

system called the Emergency Pipeline Repair System (EPRS) for the same applications. These systems have been successfully deployed in the North Sea and different parts of the world with excellent results [81]. For example, in 2011, Technip performed 4 ties-ins of 48” (1219 mm) diameter pipeline in the Baltic Sea for Nord Stream pipeline using the PRS [43].

In the North Sea or the near reaches of the GoM where oil exploration has been relatively intensive, there is an existing comprehensive network of pipelines for conveying petroleum products from the offshore field to land [94]. The cost of developing neighbouring fields may be considerably reduced by linking new production facilities to the existing infrastructures through hot tap welding onto a nearby pipeline [94]. Similarly, some production platforms which were installed in the North Sea in the 1970s/80s and are coming to end of production life are being decommissioned. These will require hyperbaric welding intervention to install by-pass pipeline arrangements in order to retain the use of existing pipeline infrastructure [20].

The construction and repair welding of deep water pipelines will require the use of robust techniques that can meet the challenges of working in such extreme environments.

1.2 **Developments in Deep Water Pipeline Welding**

It is crucial to ensure the structural integrity of a deep water pipeline welded joint, and this requires welding procedures that will produce welds with acceptable mechanical properties under such a remote and demanding service environment. Hyperbaric welding is an important underwater welding technique and offers huge prospects for deep water pipeline welding. Welding is performed inside a subsea habitat which prevents the physical contact between the welding arc and surrounding water. This has made it possible to produce welds with better mechanical and metallurgical properties than those made with a wet-welding technique, and in most cases as good as those made at one atmosphere [75]. It has been used for high quality installations and repairs around the world, particularly in the North Sea region for many years.

Research in this area over the past decade has focused primarily on the development of remotely controlled hyperbaric welding for deep water applications. Cranfield University has been involved in research and development on hyperbaric welding for over three decades. The University has a unique hyperbaric welding chamber that has been designed to simulate pressure conditions down to 250 bar, which is equivalent to 2,500 m water depth. The capability of this facility is more than twice that of any other chamber of comparable size in the world [81]. The Engineering and Physical Science Research Centre (EPSRC) as well as companies such as Statoil, Subsea 7, BP, Chevron, Texaco, Isotek, and Esab funded a series of research programmes in the late 1990s. Statoil has since further invested in hyperbaric welding procedure qualification for deep water pipeline repair and hot tap welding applications.

These programmes have led to the development of a fully automated hyperbaric Gas Metal Arc Welding (GMAW) process with potential operational capability of welding up to 2,500 m of sea depth for pipeline repair and hot tap welding operations. The process has been selected as the initial technology for sleeve repair of large diameter pipeline (i.e. greater than 30”), for operations down to 1,000 m water depth [81]. Field trials in 2011 in a Norwegian Fjord performed at sea depths of 370 m and 940 m for hot tap and sleeve repair applications respectively demonstrated the robustness of the process (Figure 1-3) [105]. This was followed in 2012 by the first ever completely remotely operated hot tap installation on a live gas pipeline, without stopping the pipeline production. This feat was achieved by Statoil when a tie-in point was welded on to the Asgard B production flow line at a water depth of 265 m (the remote hot tap cutting machine is shown in Figure 1-4) [139].

Figure 1-3: Picture of Trial vessel, Submersible Remote Pipeline Repair and Hot Tap welding equipment [8]

Figure 1-4: Remote Hot Tap Cutting machine as used for the Asgard B Gas Compression Project [139]

Ensuring quality is paramount in these applications requiring the most reliable processes possible. Issues in hyperbaric welding are that as water depth increases, there is a corresponding increase of gas density and thermal diffusivity in the welding habitat due to elevated pressures. In addition, the surrounding sea water at a temperature of about 4 °C acts as heat sink. There is also the difficulty of effective preheating for thick sections of subsea pipelines, which requires a significant amount of energy to be transported to great water depths. These factors combined result in a high weld metal cooling rate and possible formation of microstructures susceptible to Hydrogen Assisted Cracking (HAC). Maintaining sufficient heat in the welding zone is vital to avoid a potential cracking tendency, especially as moisture pick-up may be difficult to avoid during hyperbaric welding operations. Improved weld zone heating would reduce the weld metal cooling rate, and allow enough time for the absorbed

hydrogen to diffuse out before solidification, reducing the risk of Hydrogen Assisted Cracking.

The GMAW process performs significantly better than other arc processes at higher pressure because it is less sensitive to variations in pressure [43; 120], making it a viable preference for deep water hyperbaric welding applications. Nevertheless, in order to achieve a stable welding process, it is operated with a very short arc length of the order of 1 mm – 2 mm [42; 53; 163]. This is to counteract the formation of opposing electromagnetic plasma jets which cause instabilities due to the high rate of heat extraction from the welding arc [54; 120]. The arc length can be controlled either by adopting a short circuit or dip molten metal transfer condition, or by operating a self-adjusting arc [120].

Dip transfer GMAW is characterised by low heat input due to low welding current and voltage [50; 103; 166]. During short circuiting, the welding wire touches the molten weld pool, momentarily extinguishing the arc. At the initiation of short circuit, the arc voltage drops rapidly due to the low electrical resistance of the arc caused by the liquid bridge [50; 103]. Simultaneously, the welding current rises quickly to the short circuit current (Figure 1-5). The combined effects of electromagnetic pinch force and surface tension helps in molten metal droplet detachment thereby breaking the short circuit. When the liquid bridge breaks, the voltage rises quickly in order to re-establish the arc (Figure 1-5). According to Goecke [50], the arc re-ignition takes place at a fairly high electrical power because of induction in the welding circuit giving rise to significant spatter level that can affect weld quality.

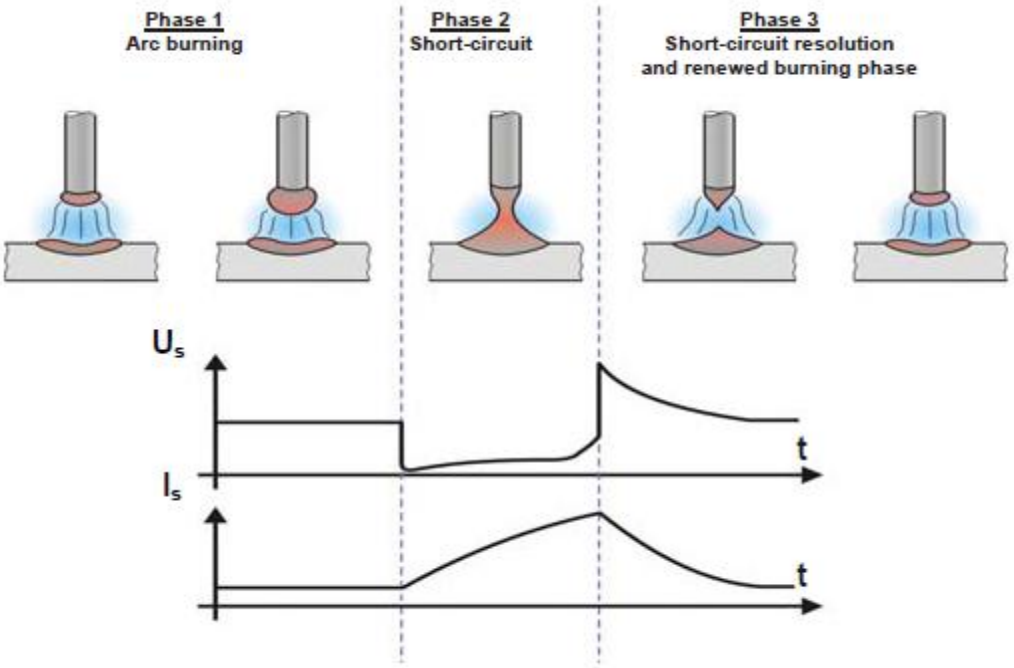

Figure 1-5: Schematic illustration of current and voltage outlines in short circuit welding [50]

For the research presented in this thesis, an industrial laser has been investigated in conduction mode for the purpose of providing significant additional heat input to control weld thermal cycles of hyperbaric GMAW. Advanced GMAW power sources such as the Fronius Cold Metal Transfer (CMT) and EWM ColdArc have also been investigated for reduced weld spatter generation. For subsea applications, the laser beam may be delivered through an optical fibre from a surface vessel to the welding habitat. The approach involves using a defocused laser beam at a lower power density (~10^3 Wmm^{-2}), which does not cause material vaporisation in combination with the GMAW process. The laser will thermally assist the arc welding process by providing significant additional heating to the welding zone to reduce the cooling rate; hence the term laser assisted arc welding.

1.3 **Motivation for the Research Project**

The Remote Pipeline Repair System (RPRS) is new equipment being developed by Statoil to be deployed and operated remotely for fillet welded sleeve repair applications. Field trials have been successful but with significant levels of weld spatter. Induction heating has not yet been found to be an effective means of pre-heating. This is further exacerbated by the high degree of cooling from the sea water, which acts as a heat sink surrounding the welding habitat at a temperature of about 4 °C. The heat extraction is more extreme for the remote hot tap welding application when the pipeline is conveying live gas product as this further increases the weld pool cooling rate. There is also the potential presence of water vapour inside the welding habitat. When these factors are combined with the relatively low heat input of the hyperbaric GMAW process used to date, there is a risk that welds are produced with hardened metallurgical phases which increase the risk of hydrogen assisted cracking.

The main motivation for this research is therefore to investigate improving the quality and reliability of remote hyperbaric welding by applying laser heating as an additional heat source to GMAW in order to reduce the risk of hydrogen assisted cracking and improve the resultant mechanical properties. In addition, controlled dip transfer GMAW processes have been studied in conjunction with the laser heating to minimise weld spatter.

The primary research questions to be addressed here are: can the remote hyperbaric GMAW process be significantly improved by the use of laser heating to reduce sensitivity to HAC and controlled dip transfer to reduce weld spatter levels?

The technical approach to the research work was developed with the following points, as illustrated in Figure 1-6:

- Investigation of thermal cycle and metallurgical characteristics of hyperbaric GMAW by analysing current and voltage waveforms, determination of heat input and cooling rate, weld bead shape and hardness mapping. This is to fully understand the effect of pressure on weld cooling rate and resultant mechanical properties
- Characterisation of traditional and controlled dip transfer GMAW by comparing current and voltage waveforms, heat input and cooling rate, and weld bead profiles of standard short circuit GMAW with CMT and ColdArc for a potential improvement of weld quality by reducing spattering
- Characterisation of laser assisted GMAW at atmospheric conditions through determination of optimised laser and GMAW parameters, thermal cycles and cooling rates, effect of beam shape on cooling rate, microstructural evaluation and hardness measurement. This is to investigate applying a laser in combination with GMAW for additional weld zone heating.
- Development of a thermal model to simulate the thermal cycle and resulting cooling rate of the weld metal and HAZ. This is to characterise the weld thermal profile of laser assisted GMAW, and potentially predict weld cooling rates under different conditions.
- Evaluate moisture pick-up and hydrogen analysis of the weld metal for GMAW and laser assisted GMAW to demonstrate the potential influence of a laser in removal of weld metal diffusible hydrogen content.

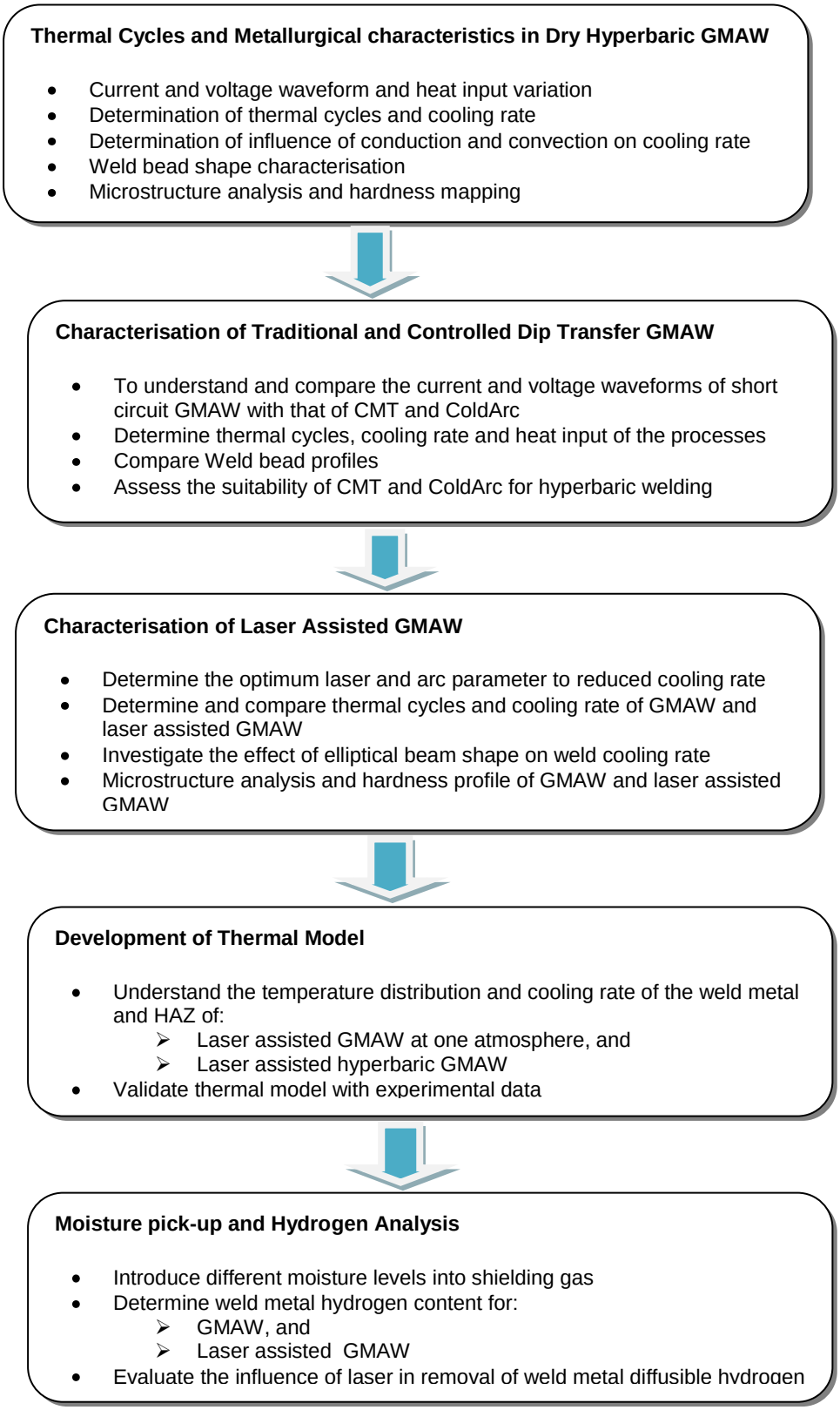

Figure 1-6: Structure of research scope in this thesis

1.4 **Aim and Objectives**

The primary aim of this thesis is to investigate a laser assisted GMAW process to provide additional significant heat input to reduce the hydrogen assisted cracking tendency and lower weld spatter in hyperbaric welding operations. A laser in conduction mode has been investigated for the purpose of providing additional heat input to control weld thermal cycles, and an advanced GMAW power source such as Cold Metal Transfer (CMT) and ColdArc have been used to minimise spatter levels.

The main project objectives are as follows:

(i) Investigate and characterise the cooling rates associated with the current remote hyperbaric GMAW process at different pressure levels;

(ii) Investigate the use of a laser in conduction mode to control weld thermal cycles in GMAW, and to assess the potential improvements offered; and

(iii) Evaluate the influence of a laser operated in the same mode as (ii) in the removal of weld metal hydrogen levels, and to demonstrate the significance of the findings.

1.5 Structure of the Thesis

This thesis is organised in 8 chapters and appendices.

Chapter 1 presents an overview of the industrial background and development of dry hyperbaric welding of deep water pipeline, the main aim and objectives of the research and the structure and organisation of the thesis.

Chapter 2 presents a literature review, which is focused on the main areas of this research: hyperbaric welding, hydrogen assisted cracking, and laser welding in a hyperbaric environment.

Chapters 3, 4, 5, 6, and 7 comprise the main experimental works covered by this research. This includes: the equipment and materials, experimental methods, results and their analysis, discussion and conclusion.

Chapter 3 reports on the investigation of the weld pool thermal cycles and metallurgical characteristics in dry hyperbaric GMAW at different pressures varying from 1 bar to 200 bar.

In Chapter 4, the process characteristics of traditional dip molten metal transfer or short circuit GMAW is compared with some advanced GMAW power sources such as Cold Metal Transfer (CMT) and ColdArc. The heat input, current and voltage waveforms, thermal cycles and weld bead profiles are compared.

Chapter 5 is the central focus of this research. It presents studies on laser assisted controlled dip transfer GMAW (CMT) trials at one atmosphere. The control of the thermal cycle of CMT welding by the use of a laser in conduction mode in terms of extended weld pool cooling time and longer resident time at high temperature was presented.

Chapter 6 presents the numerical study of temperature distribution in laser assisted GMAW (CMT). This covers the development and application of a predictive model which was then calibrated by experimental data. The model may be used under different pressures.

Chapter 7 reports the final experimental work. This covers a study on the simulation of moisture pick-up and hydrogen analysis of the weld metal at one atmosphere for laser assisted GMAW (CMT).

Finally, in chapter 8 the practical implications and main conclusions of the work developed as well as recommendations for further work are presented.

2 Literature Review

Scope

This chapter reviews the three main areas of this research focus: dry hyperbaric welding, hydrogen assisted cracking in hyperbaric welding and laser assisted welding in hyperbaric environment. Underwater welding in general is briefly discussed before focusing on the main areas.

2.1 Underwater Welding

Welding is vital for structural applications in nearly all manufacturing industries including the oil and gas industry. Although mechanical connectors may be used, welding remains the most reliable and efficient method for installation and repair of large diameter subsea pipelines [75], and it has enhanced the development of offshore construction over the years.

Underwater welding came into existence in 1917 and was further developed in the 1990s [63]. It is largely used for repair and maintenance of offshore structures and for localised repair of barges and ships. The American Welding Society (AWS) D 3.6, *Specification for Underwater Welding* classifies underwater welding currently in use into five categories [23].

- Dry Welding at One Atmosphere – Welding is carried out in a pressure vessel at approximately one atmosphere pressure and it is independent of depth.
- Dry Welding in a Habitat – Welding is carried out at ambient pressure in a habitat from which water is displaced with gas such that the welder/diver works without diving equipment.
- Dry Chamber Welding – Welding is performed at ambient pressure in a dry habitat with an open bottom that allows only the head and shoulders of the welder/diver in full diving equipment
- Dry Spot Welding – Welding in a small transparent enclosure that is filled with gas at ambient pressure and the welder/diver is outside in the water
- Wet Welding – Welding at ambient pressure with the diver/welder in the water without any barrier between the welding arc and water.

Labanowski et al [75] presented a detailed review of underwater welding processes and gave a schematic classification of the different categories as shown in Figure 2-1, while Figure 2-2 represents underwater welding in a dry condition. In Figure 2-1 the five techniques described above are grouped into three categories. Some authors simply classified welding as wet or dry under

water welding while in addition, others included coffer dam welding, which is welding in a dry chamber that is open to the atmosphere. Other techniques of underwater welding considered in the literature were solid state welding processes such as explosive and friction welding [75].

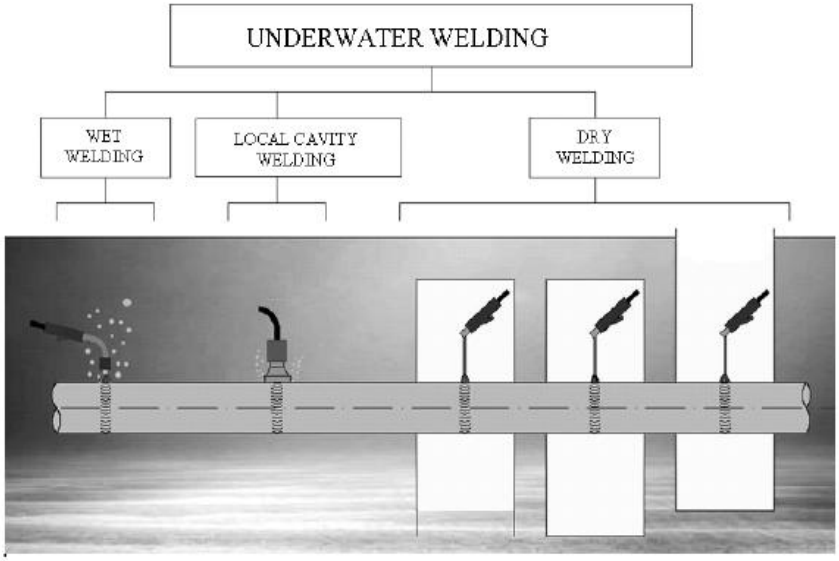

Figure 2-1: Schematic classification of underwater welding [75]

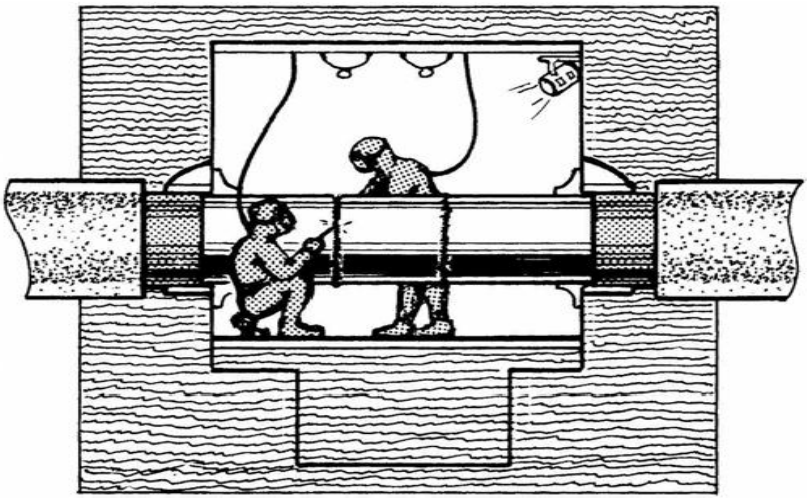

Figure 2-2: Schematic of underwater welding in a dry condition [75]

2.2 Dry Hyperbaric Welding

2.2.1 Overview

Dry hyperbaric welding or simply hyperbaric welding, which is the second category shown in the AWS classification was first used in the Gulf of Mexico (GoM) in September 1967 by Ocean Systems Limited for hot tap and tie-ins. Afterwards, it has become a common underwater joining method for steel components in the North Sea but less frequently used in the GoM [92]. This may be because hyperbaric welding operations were mostly carried out at shallow water depths in the North Sea. Also, offshore operators and petroleum companies appear to be less confident about repairing damaged pipelines in deep sea [94].

Hyperbaric welding has often been described in the literature as welding under high pressure in a chamber underwater. Richardson et al [120] described the process as welding in a gaseous environment at elevated pressure, referring to the word *dry* as often used to stress that the welding arc is not making direct contact with the surrounding water as is the case with wet welding. Nixon [92] described hyperbaric welding as an engineering compromise between wet and one atmosphere welding since it eliminates the attendant difficulties of both techniques which are the wet environment and high pressure differential across the chamber respectively.

The joints to be welded or repaired are enclosed within a working habitat which is made of relatively lightweight materials, since it only needs to resist low pressure differences. Water is displaced from the habitat by filling it with gas (usually inert). Simple hydrostatics indicates that the maximum pressure differential is at the top of the chamber while the gas and water will exist at the same pressure at the bottom of the chamber. Therefore, the internal pressure in the chamber will exceed the external pressure by an amount equivalent to the height of the chamber and is normally a few tenths of a bar. According to Nosal [5] the habitat is made water and gas tight, but does not need to support any pressure difference larger than a small fraction of 1 bar. This pressure

differential is easily resisted by the weight of a light steel structure making deployment and sealing of the habitat operationally feasible [63; 92]. Essentially, the environment inside the habitat is at the same hydrostatic pressure as exerted by the surrounding sea water [94]. Figure 2-2 is an illustration of diver-assisted dry hyperbaric welding in a habitat.

Welds made under hyperbaric conditions are generally of significantly better quality than those obtained in wet conditions. In most cases, these welds have mechanical properties that meet the specification requirement of an equivalent surface atmospheric weld [75]. However, the large amount of support equipment required and the costs involved are higher than for wet welding [25; 144]. The cost and time for hyperbaric weld repairs are estimated to be twice that of wet weld repairs [75].

Although there are several applications of hyperbaric welding such as pipeline repairs, tie-ins, hot taps, expansion loops, structural repairs etc., which involve the use of various items of specialised equipment and complexity, more pipeline tie-ins seem to have been completed and at deeper depths than other types of weld repairs. Akselsen et al [1] reported that a total number of 71 tie-ins have been made with the Pipeline Repair System (PRS) since its commissioning in 1987. Since tie-ins are used to connect subsea pipelines to a water platform or a riser, and for a by-pass when decommissioning a platform [2], their claim seems to suggest that more operations have been performed using hyperbaric welding.

Research in hyperbaric welding is mainly concerned with ensuring that at any specified environmental condition and composition, welding parameters are developed to ensure that welds are produced with properties that meet specifications and standards [92]. The Cranfield University research programme on hyperbaric welding, which spans over three decades has strongly established the application of the process using GMAW for deep water operations at pressure of up to 250 bar, which is equivalent to a water depth of approximately 2,500 m (8,200 ft.). This was achieved using the University's hyperbaric centre equipped with the world's highest pressure welding chamber.

This facility is being used for a research and development programme on the procedures and technology for the Remote Pipeline Repair System (RPRS) [102].

SINTEF Research Institute, Norway has also been involved in R&D on hyperbaric welding since the early 1970's and has a dedicated laboratory for mechanised hyperbaric welding. It has been involved in the development of equipment and qualification of all the welding procedures used by Statoil and Hydro with the PRS [1]. The research and development of GKSS, Germany focused upon the investigation and development of welding processes, procedures and equipment for production and repair purposes in dry hyperbaric and wet welding since 1980 [143]. There are also other hyperbaric welding facilities in various institutions around the world that also perform research on hyperbaric welding.

The technology for hyperbaric welding is well-known and a well-researched area. Research in the field over the past decade has focused primarily on development of remotely operated welding, with a view to implementing the technology at depths beyond a divers reach, currently set at 180 m sea water depth for planned dives [120]. An example of this is the development of the RPRS by Statoil. Therefore, the challenge is to develop a minimum intervention and long term welding process operation with optimised welding and process control parameters capable of producing welds that meet the relevant quality specifications and standards.

2.2.2 Challenges for Hyperbaric Welding

Welding in a hyperbaric environment comes with different challenges. The welding habitat tends to be moist, which is inevitable since there must be an opening in the habitat to allow the divers/welders, ROVs and equipment in, and as such, water vapour may be present [92]. The increased density of gas in the chamber due to elevated pressure also leads to faster cooling of the molten pool than at one atmosphere. Senvers [130] reported that the thermal conductivity of a gas increases with density.

Amin [5] and Le Bail et al [76] have shown in Figure 2-3 and Figure 2-4 the dependency of the thermal conductivity of argon and helium, commonly used chamber gases in hyperbaric welding on pressure and temperature. Amin [5] reported that the thermal conductivity of argon increases with both ambient temperature and pressure. He also reported that helium is less pressure dependent than argon. But, its temperature dependency is stronger than argon as shown in Figure 2-3. Le Bail et al [76] have shown in Figure 2-4 how the thermal conductivity of argon varies at higher temperatures and pressures. It increases with pressure, but the variation with temperature is stronger at a very high pressure of 1550 bar.

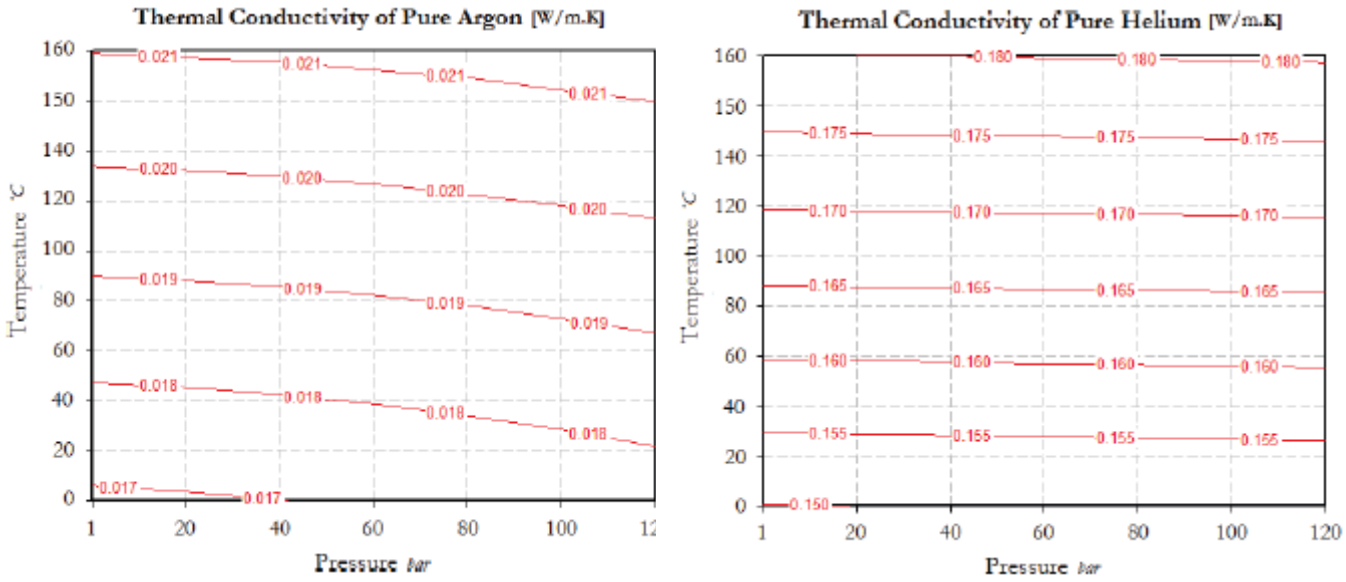

Figure 2-3: Thermal conductivity of argon (left) and helium (right) as a function of pressure and temperature [5]

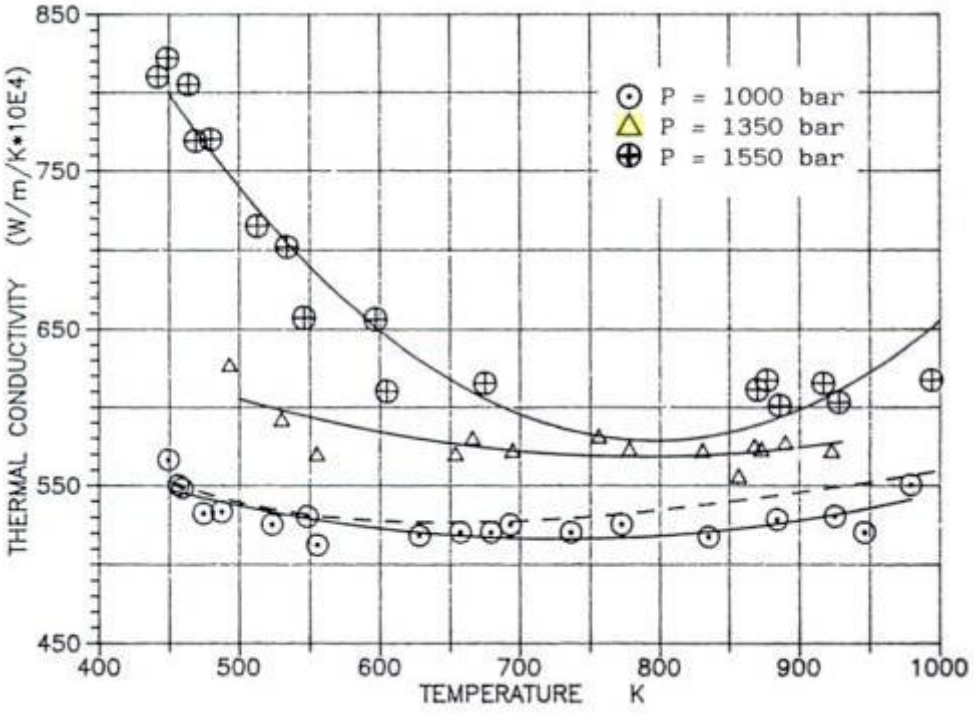

Figure 2-4: Experimental data points of the thermal conductivity of argon: Isobaric variation against temperature [76]

More significantly, the higher pressures will have a profound influence on the physical and chemical processes occurring in the welding arc. As a result, the weld pool chemistry and the arc structure are significantly different from welding at one atmosphere [92]. These effects are expected to increase with depth as the ambient pressure will be greater.

Richardson et al [120] reported that high water vapour content in the welding environment can exert considerable influence on chemical reactions and gas absorption at the weld pool surface, and hence on the mechanical properties of the resultant welds. In addition, the hyperbaric environment gives rise to a modified energy transport behaviour, which affects welding process stability as well as the structure and properties of the welds. The overall effect of pressure on the process is governed to a large extent by changes in arc properties. Labanowski et al [75] observed that pressure increases cause the welding arc to become unstable, and the presence of diffusible hydrogen and hardened microstructures in the weld may cause cracking. The influence of pressure on

welding arc, weld metal formation and microstructure, cooling rate, joint strength and spattering ratio has also been studied by Enjo et al [35].

2.2.3 Hyperbaric Welding Techniques

Almost all standard arc welding processes can be used in hyperbaric welding with Shielded Metal Arc Welding (SMAW), GMAW, Flux Cored Arc Welding (FCAW), and Gas Tungsten Arc Welding (GTAW) being the commonly used processes [75]. Based on economic and technical selection criteria, Milhailescu et al [88] suggested that GMAW, GTAW and SMAW are the most advantageous processes. SMAW is the least preferred among the three due to its low productivity and poor weld quality. GTAW is recommended for the root layer welding because of its high quality welds, while GMAW is recommended for both the root and fill passes [88].

The influence of pressure on the welding process must be well understood for the process to be effectively deployed in hyperbaric welding, and procedures must be developed to compensate for these effects [92]. The typical operating pressure range for different arc welding processes is shown in Figure 2-5.

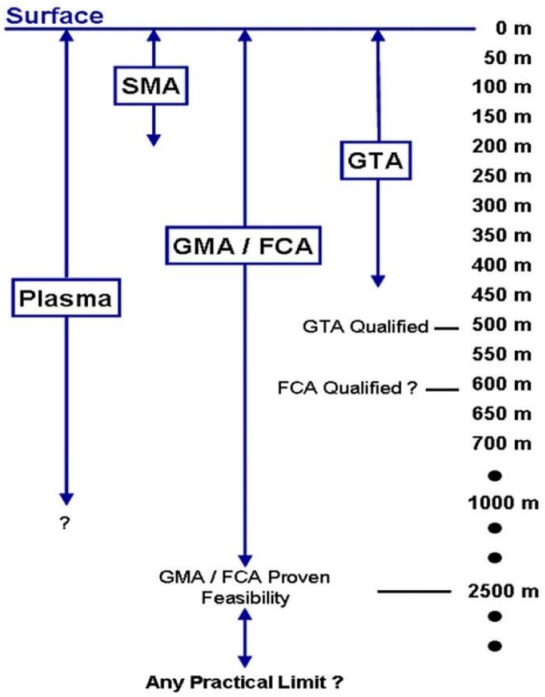

Figure 2-5: Illustration of approximate depth limits for arc welding processes [120]

The depth range for the SMAW process is restricted to the tolerable human diving range since the process is essentially manual. The depth limit for the GTAW process is reliant on the acceptable stability level for a given process, which should not exceed 500 m to 700 m for general applications. Plasma arc welding is reported to offer additional stability at high pressure when operating in the melt-in (no keyhole) mode as a result of radial constriction of the arc close to the electrode tip [52; 53; 119]. This is because a successful operation depends on relatively large diameter constrictions (of the order 6 mm) and a short set-back, usually less than 2 mm. These significantly reduce lateral movement of the arc on the work piece surface when compared with GTAW; leading to more stable weld penetration [52]. Nevertheless, process stability limits are related to turbulence at the arc boundary and energy transport to the constricting nozzle, which results in nozzle melting at high pressures [1]. Experimental welding trials have shown that the process can be stable at depths exceeding 1000 m [119]; but it remains sensitive to electrode positioning and welding torch design. As a result, the process has not been used for any offshore repair or installation application to date. The GMAW and FCAW processes have been shown not to have any pressure dependent process limitation. As a result, they have received considerable attention over the past few years and have been demonstrated to be stable down to 2,500 m [120].

2.2.3.1 Gas Tungsten Arc Welding

GTAW also known as Tungsten Inert Gas welding (TIG) in the UK is a comparatively well-developed hyperbaric welding technique that has been frequently used for automated and semi-automated applications[120]. Hyperbaric manual GTAW systems are normally identical to surface based equipment, the main modification being the removal of the operators control switch on the torch and power supply is controlled by the surface support crew [92]. The high level of control that the surface operator exerts over the process makes it very successful for critical welding situations such as the root and hot pass welds on pipe joints, and for capping passes and temper beads where the shape and

hardness of materials at the toe of the weld must be controlled for fatigue resistance [92].

All the tie-ins reported by Akselsen et al [1] used weld procedures developed with remotely controlled GTAW in a dry pressure chamber which simulates sea water depth. The process has been used for a water depth range of 16 m – 600 m, but has only been qualified to 360 m [1]. Figure 2-6 and 2-6 show the groove configuration and macrostructure of a typical hyperbaric GTAW weld respectively.

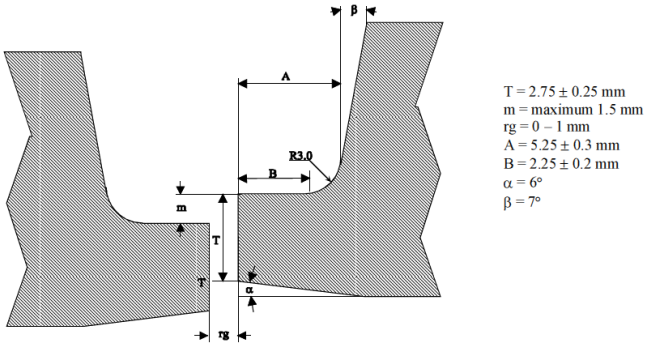

Figure 2-6: Groove configuration for dry hyperbaric GTAW [1]

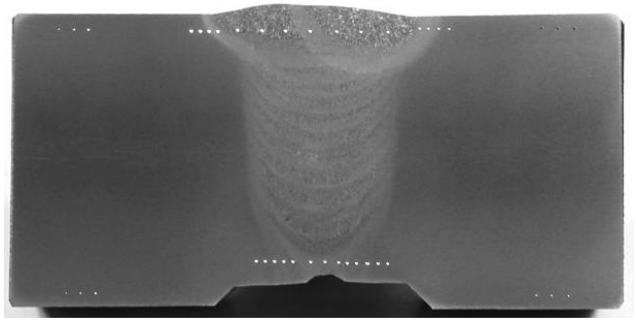

Figure 2-7: A typical hyperbaric GTAW pipe weld in the 6 o` clock position of a 35.2 mm thick X70 steel Pipe welded under pressure equal to 200 m sea depth[1]

Some of the process advantages are that: it is a well understood process; produces fine grained weld metal with high toughness, produces little or no fumes and spatter [120]. Also, it is a versatile process in application and well established for root pass completion. However, the drawback of the process is that changes in water depth and consequently changes in pressure make it necessary for adjustments to be made to the welding parameters. This is

illustrated in Figure 2-8 where the arc voltage used in the root pass was plotted against habitat pressure [1]. Although effective at depths to at least 400 m, the process arc stability gradually deteriorates as pressure increases[120]. The results of studies conducted by Wang [153] show that arc voltage, current density and arc brightness all increase with ambient pressure.

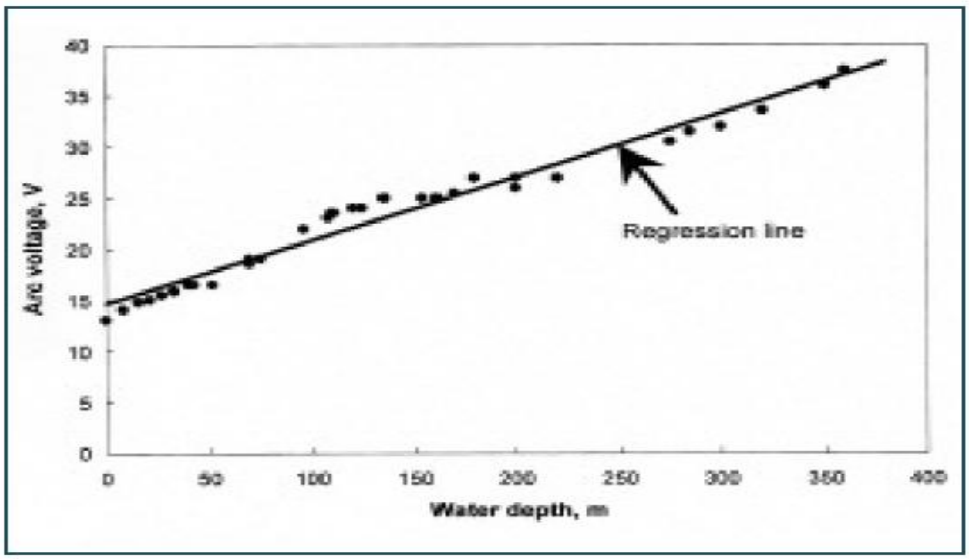

Figure 2-8: Effect of seawater depth (pressure) on arc voltage used in dry mechanised hyperbaric GTAW of root pass [1]

The increase in operating voltage is believed to be caused by the enhanced heat extraction due to the hyperbaric environment, as a result, the arc can minimise heat losses by reducing its diameter. This then requires that the arc current be carried by a smaller arc cross sectional area, which increases the current density and ionization level. The additional energy required increases the arc voltage [92]. As reported by Richardson [119], the physical properties of the plasma changes and particle densities increase in proportion to the absolute pressure when the ambient pressure is raised above one atmosphere.

Ozden and Gursel [101] showed that the stability of the GTAW arc and of the process at elevated pressure is controlled largely by the conditions of the tungsten electrode. Erosion rates of the electrode, defined in terms of electrode

tip shortening are lower for 2% La_2O_3 (Lanthanated) doped electrode than for those doped with 1% ThO_2 (Thoriated).

Due to the depth limitations of the GTAW process, Nixon [92] predicted that it will most likely be supplanted by either plasma welding or some form of GMAW for future diver-less hyperbaric welding systems. This is actually the case with fully automated GMAW presently being qualified for the proposed Remote Pipeline Repair System.

2.2.3.2 Gas Metal Arc Welding

GMAW is also known as Metal Inert Gas welding (MIG) in the UK. Strictly speaking, the term MIG should only be used when the shielding gas is inert. When active gas such as carbon dioxide or oxygen is used, it is referred to as Metal Active Gas (MAG) welding [92]. The main changes to the standard surface GMAW are due to the need to keep the power supply and process controls on the surface separated from the consumable feed system by service umbilical. The wire feed motor and electrode reel are put in a water tight container into which the service umbilical that supplies the welding current, power and control signals and shielding gas are connected [92].

Nixon [92] further reported that the high electric field strength observed with the hyperbaric GTAW process was also an issue with GMAW, resulting in an increased arc voltage variation due to changes in the electrode to work piece distance. Therefore, the process stability is reduced due to the characteristic of the welding power supply that causes changes in the arc current.

Richardson et al [120] described GMAW and FCAW as promising processes for hyperbaric operation, especially for deep water application. However, at depths greater than 120 m, the welding arc becomes completely turbulent with the arc root contracting due to rapid heat extraction. The difference in current density between the arc roots and arc column promotes the formation of opposing electromagnetically driven plasma jets as pressure increases [163]. The opposing plasma jets becomes more or less equal forces as the ambient pressure

increases as shown in Figure 2-9 [116]. The plasma velocity falls and the arc root moves rapidly over the molten metal surface with considerable changes in radiation emission and arc position at frequencies exceeding 10 Hz [54; 114; 120].

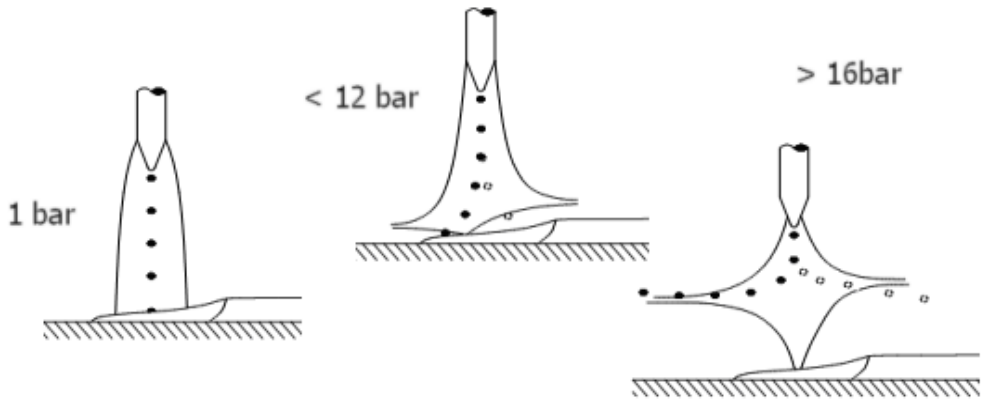

Figure 2-9: Schematic of GMAW arc behaviour at different pressures [118]

Despite the random movement of the arc, the time averaged behaviour of the process remains relatively constant over a typical time period related to weld pool movement and solidification[120]. Consequently, a stable process may be maintained, provided control measures are adopted by means of power manipulation in response to conditions within the immediate arc. Figure 2-10 shows the typical transient behaviour of the current and voltage with that of the 0.25 s time averaged response, which largely demonstrates process stability [117]. Richardson et al [117] further suggested that process stability is not necessarily synonymous with electrical stability. They illustrated this with current and voltage data which although depicting a stable electrical performance, with well-defined waveform structure, showed unacceptable process stability and vice versa. This informed their proposal that overall process stability is difficult to quantify and has to be based on visual assessment of arc stability, spatter levels and resultant weld bead appearance.

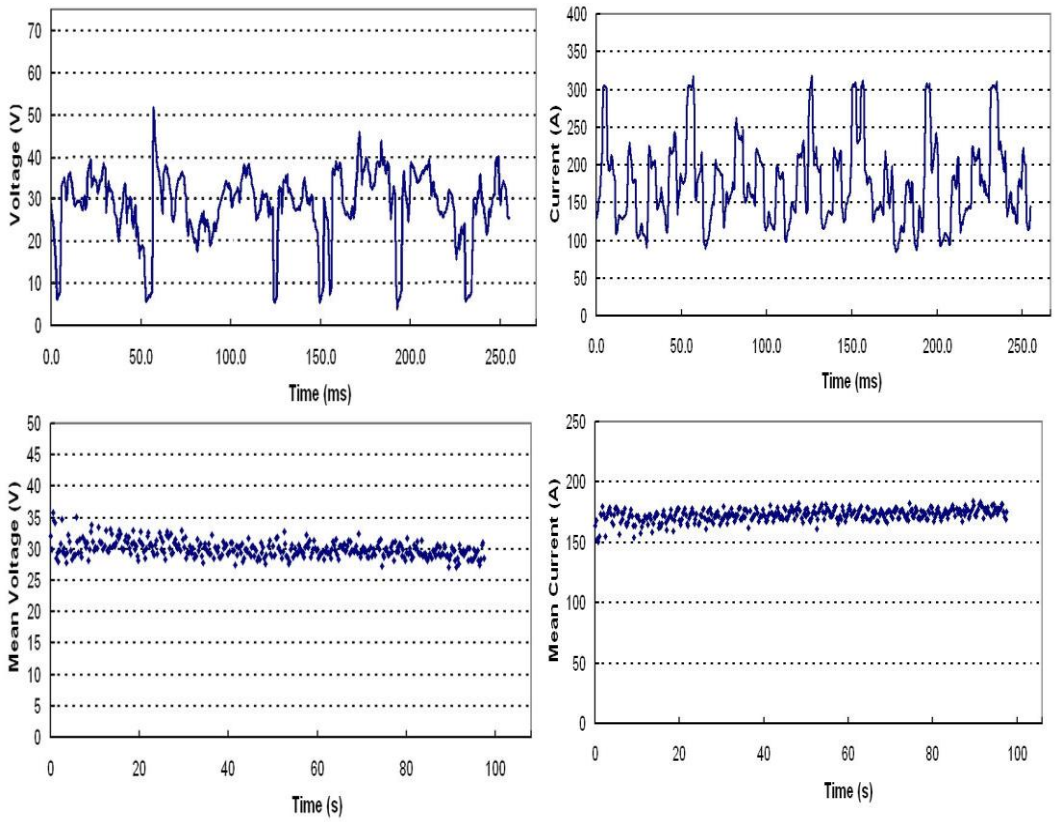

Figure 2-10: Transient and time averaged voltage and current signals from a GMA weld made at 2,500 m in an argon atmosphere [93]

At elevated pressures, welding with comparatively short arc lengths, of the order of 1 mm or less may reduce the electromagnetic plasma jets. This reduces the difference between the current density at the arc root and in the arc column thereby diminishing the net forces [53; 163].

The arc length can be controlled by applying a relatively high wire feed rate thereby forcing the process to adopt a dip-transfer condition or by operating a self-adjusting arc [120]. Typical transient signals of current and voltage depicting dip transfer and self-adjusting arc process are shown in Figure 2-11. The degree of self-adjustment must be chosen such that it provides the optimum level of current variation per unit change in arc length, independent of the operating pressure [163]. According to Richardson et al [120], the current and voltage waveform shown in Figure 2-11(a) is similar to that obtained for a stable condition at one bar although there is greater time interval between successive dips.

Since the voltage is pressure dependent, the static slope characteristic of the power source must also vary with pressure to operating depths of at least a few hundred metres. At greater depths, the metal vapour dominated arc plasma is only weakly affected by pressure, and under these conditions, the optimum self-adjusting characteristic is effectively independent of depth[120]. Details of process operation have been reported elsewhere [1; 113; 116].

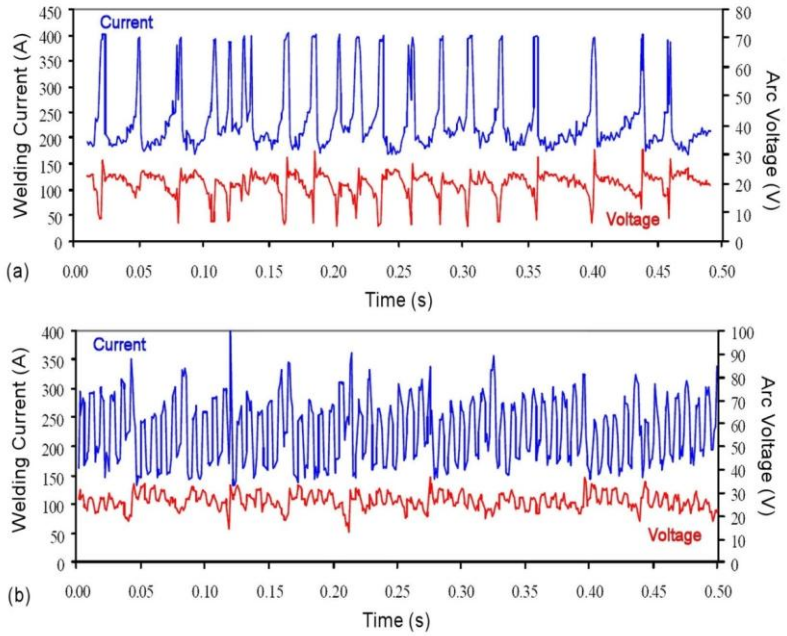

Figure 2-11: Transient voltage and current waveforms for (a) a dip transfer root pass and (b) a self-adjusting pulsed fill pass made at a depth of 350 m [163]

The established current delivery control procedures of the GMAW process has made it suitable for welding operations over a wide range of pressures. Significant progress in both process control and process application at high ambient pressures has been recorded in recent years [163]. The viability of the process for butt welding of X65 pipeline material has been successfully demonstrated for pressures ranging from 20 bar to 250 bar equivalent to water depths of 200 m to 2,500 m without any sign of pressure dependent limitation [163]. The positional capability of the process has also been demonstrated by making orbital (5G) welds on X65 pipeline materials that gave acceptable mechanical properties [163].

The main area of concern in hyperbaric GMAW which this research work intends to explore is the low heat input of the process. The heat input is given by the product of welding current and arc voltage and an arc efficiency value divided by the welding speed [103]. In addition, the high cooling rate associated with hyperbaric welding, the potential moisture presence inside the welding habitat, and the high restraint conditions on the solidifying weld increases susceptibility to hydrogen assisted cracking (HAC). Also, traditional dip transfer GMAW produces considerable spatter levels. These form the basis of the investigation of laser assisted controlled dip transfer GMAW, in which the laser will provide additional heat input to the process. In this thesis, the Cold Metal Transfer (CMT) and ColdArc process will be investigated for minimisation in weld spatter generation.

2.2.3.3 Flux Cored Arc Welding

The Flux Cored Arc Welding operation is very similar to GMAW. The main difference is that the former uses an electrode wire with flux inside the wire core while the latter uses a solid wire. The development of FCAW has closely followed that of solid wire GMAW with much of the equipment and process technology being identical [92]. When the limitations of solid wire GMAW were identified, the use of tubular or metal cored wire were suggested to improve the process characteristics and mechanical properties of the resultant weld metal, especially the toughness and strength.

It is important to note that apart from welding power source technology, the other driving force for fully automated hyperbaric GMAW is optimised metal cored wire composition. Woodward et al [163] reported that Charpy impact tests carried out on a specimen extracted from the root area of X65 pipeline steel made using solid wire GMAW allowed room for improvement. Over the past two and half decades, tubular wires have been specially formulated for hyperbaric welding [162; 163]. Metal cored wire (1 mm diameter) developed by ESAB has been specially formulated to deal with two specific aspects of hyperbaric GMAW conditions: a fully inert argon atmosphere and high weld cooling rate due to increased gas density with operating pressure [162].

Commercially available metal cored wires mostly contain higher oxygen contents than solid wires. In addition to promoting acicular ferrite formation, oxygen also promotes fine molten metal transfer across the arc due to oxidation of the droplet surface which lowers its surface tension[120]. Experimental metal cored wires studied for resultant mechanical properties have adopted elemental compositions of 0.05 – 0.95% Ni, 0.01 – 0.04% Ti and 216 – 485 ppm oxygen[120; 160; 163].

Nosal [94] observed that weld metal oxygen content reported in the literature were in the range of 300 - 800 ppm. However, his studies with solid wire GMAW under hyperbaric conditions showed low oxygen contents in the range of 180 – 250 ppm. He attributed this to the inert shielding and inert environment used in his work and suggested that consumable design for high pressure use may not be applicable to inert environments. Richardson et al [120] reported that the poor toughness of orbital GMAW welds on X70 pipeline steel at a depth of 1,630 m (Figure 2-12) were associated with low weld metal oxygen contents, which was linked with low volume fraction of acicular ferrite. Oxide inclusions, particularly those containing titanium and nickel act as nucleation sites for acicular ferrite formation [89; 120; 162]. Weld metal oxygen content in the range of 250 – 350 ppm is associated with enhanced toughness [81]. Higher content of oxygen in the weld metal could still produce acicular ferrite. Although, Marino et al [82] indicated that it could lead to rapid deterioration of toughness when the optimum value is exceeded. Further work on metallurgical development with metal cored wire was reported by Woodward [160]

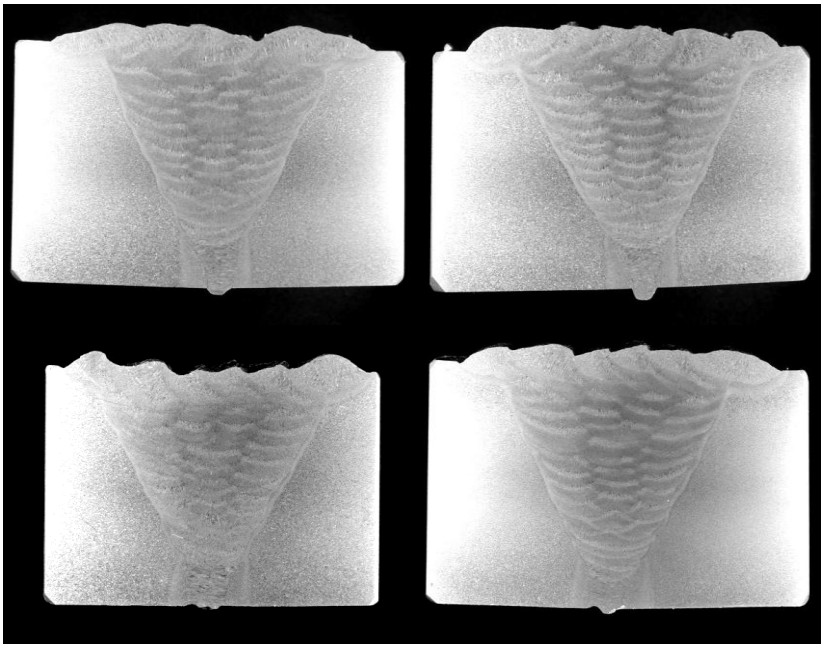

Figure 2-12: Photo-macrographs of solid wire orbital GMA welds (flat position) made on 29 mm wall thickness X70 pipeline steel at a depth of 1,630 m [117]

2.2.4 Factors Affecting the Mechanical Properties of Hyperbaric Welds

According to Richardson et al [120], the microstructure and mechanical properties of hyperbaric welds are influenced by cooling rate, consumable and parent metal composition and the thermodynamic history of the parent metal. These together with the weld thermal cycle, determine the structure and properties of the weld metal (WM) and Heat Affected Zone (HAZ). The production of high quality welds depends considerably on the right choice of consumables and welding condition. For a large number of applications, welds should have matching or over-matching strength compared with the parent metal, while displaying acceptable fracture toughness, corrosion resistance and resistance to cracking[120]. These factors will be examined in detail.

2.2.4.1 Base metal and consumable

Akselsen et al [1] showed that sulphur levels in the consumable can affect penetration during GTAW root welding with relatively higher levels (0.013 wt%) offering higher penetration than lower levels (0.006 wt%) for X70 pipeline steel at a depth of 75 m. Similar welds made at 75 m – 200 m showed that whilst

over-matching welds of similar strengths were made using consumables with slightly different compositions, toughness deteriorated with increasing pressure for welds made with low alloy wire containing 1Ni 0.5Mo. Results were independent of pressure for welds made with a similar consumable containing 2Ni 0.5Mo. Variation of measured fracture toughness at -30 °C was closely linked to microstructure. Richardson et al [120] suggested that the formation of high carbon martensite-austenite islands around prior austenite grain boundaries may have caused the reduction of toughness. Partial transformation due to re-heating by subsequent weld passes may have been responsible for these changes [1].

Hardness profiles measured for hyperbaric GMA welds have been extensively reported in the literature[2; 120; 161; 163]. It was reported that the maximum hardness recorded for orbital GMA welds on X70 pipeline steel at a depth of 1,630 m (Figure 2-12) was 264 HV_{10} in the weld metal, which was well within the maximum of 325 HV_{10} specified in AWS D3.6. It also met the BS 4515 standard for non-sour service, even though it exceeded the 250 HV_{10} specified for sour service conditions [117; 138]. The weld metal strength shown in Table A-1 of Appendix A indicates under matching strength of the weld metal relative to the parent metal whilst ductility exceeds that of the parent metal [117]. However, results of positional linear welds made on X65 pipeline steel at the same pressure were in contrast, having consistent over matching strengths of the weld metal relative to parent metal (Table A-2 in Appendix A) [117]. Since the same solid wire consumable (triple deoxidised Thyssen K-Nova) was used for both grades of steel, Richardson et al [117] suggested that while the consumable has adequate strength for the X65 steel, it under matches the X70. Therefore, they concluded that an alternative wire of higher strength will be required for the X70 steel. This is because the weld metal should have a higher strength than the parent metal so that deformation should occur on the tougher parent metal.

Impact toughness tests carried out on the X70 specimen over a temperature range of 0 °C to -80 °C indicate reduction of toughness with increasing number of passes as shown in Figure 2-13 [117; 120]. Across the temperature range, low

impact energies were obtained for the 41 pass weld, while between 0 °C to -20 °C improved toughness was shown for the 28 pass weld. This behaviour may be connected with weld heat input and resultant microstructure. As reported by Richardson et al [117], the mean current for the 41 pass weld was relatively low (110 A to 115 A). Therefore, despite the more weld beads deposited, the fraction of reheated materials is smaller than for the 28 pass weld, which has a mean current range of 175 A to 180 A [117]. They also suggested that the wide scatter shown in Figure 2-13 may be indicative of a range of microstructures being sampled at the Charpy notches. In contrast, the toughness of super martensitic joint welded with 13Cr 6Mo consumable was acceptable across the temperature range (Figure 2-14) [117; 120]. This may be due to the high nickel content (3.5 % to 6.0 %) in super martensitic steel, which enhances the austenitic structure leading to improved impact toughness [128].

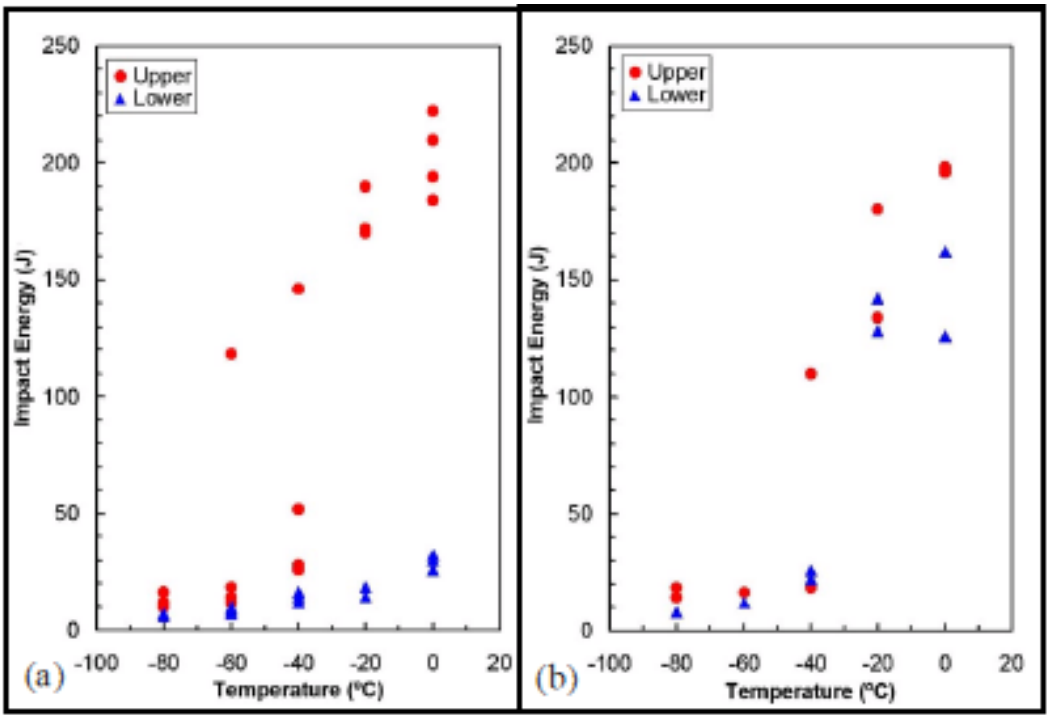

Figure 2-13: Notch toughness of orbital GMAW welds made on 29 mm wall thickness X70 steel at 1,630 m depth (a) 41 pass weld , (b) 28 pass weld [117]

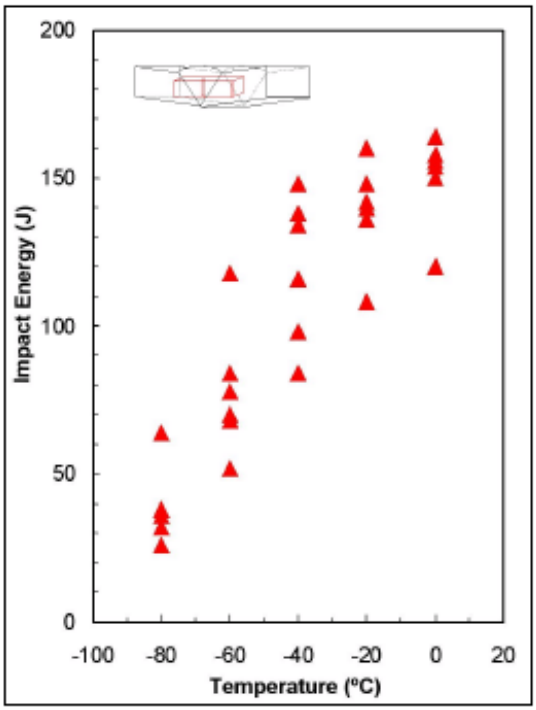

Figure 2-14: Notch toughness of an orbital GMA weld made on a super-martensitic pipe at 1,630 m [117]

2.2.4.2 Hyperbaric chamber gas

During diver-assisted hyperbaric arc welding, additional gas from the welding torch is employed to shield the molten pool in the gas filled welding habitat. In the proposed diver-less operation, welding can be performed with or without additional shielding gas. Amin [5] reported that it is possible to separate the chamber and shielding gas when more expensive gas mixtures are required to protect the weld pool. Welding trials carried out in the Norwegian Fjord in 2011 were performed without additional shielding [105].

The commonly used chamber gases are argon and helium. The choice of these inert gases is important because the chamber may contain water vapour, which can exert considerable influence on chemical reactions and gas absorption at the weld pool surface under high pressure. Consequently, mechanical properties of the resultant welds could be undermined [2; 3; 9; 66; 1632; 3; 10; 65]. As a result, the use of active gases such as carbon dioxide, oxygen, hydrogen or nitrogen may worsen these problems. According to Amin [5], the oxidation potential (OP) of carbon dioxide and oxygen will not only change the arc

physics but will also cause losses of valuable alloying elements in the weld metal. Manganese and silicon were reported to be the most prone constituents, whose losses are proportional to the percentage of active gases in the chamber gas [5]. Equation (2-1) was used to define the oxidation potential [84].

$$OP = \%O_2 + C.\sqrt{\%CO_2} \quad (2\text{-}1)$$

where *C* is a constant. This relationship is optimised for welding at atmospheric pressure. For a hyperbaric process, the partial pressure of the gases plays a prominent role. For example, the oxidation potential will be higher at 10 bar compared to 1 bar for a welding chamber pressurised with a mixture of (Ar, 5% CO_2, 2% O_2) due to higher partial pressure [5].

Ambient pressure influences the thermal behaviour of chamber gases during hyperbaric welding. Swetan [142] conducted studies on hyperbaric SMA welding at 1–19 bar pressure and reported that welds made in a helium environment showed higher cooling rate than those in argon environment due to the higher thermal conductivity of helium. He further reported that the total cooling time from peak temperature to 100 °C decreases with pressure and was shorter in a helium environment than in argon. Consequently, welds made with helium at high pressure may exhibit higher hardness and lower toughness than those made with argon.

The thermal conductivity of helium (~0.142 W/m-k) at 1 bar and room temperature is about eight times that of argon (~0.016 W/m-k) under the same condition. It has been reported by Sengers [130] that thermal conductivity of gases increase with density and pressure. This would account for the higher cooling rate of welds made in the helium environment.

It is worth mentioning that at high pressures, argon can have a narcotic effect on divers/welders, so it is considered hazardous for manned hyperbaric welding operations. However, it is the preferred chamber gas for remotely controlled hyperbaric welding operations. The main benefit of using a helium and oxygen habitat or chamber gas is that it is similar to the gas mixtures breathed by divers

when in saturation at depths greater than 50 m, but the high cost of helium is also an issue of concern [92].

2.2.4.3 Shielding gas

Different studies on hyperbaric SMAW and GMAW as reported by Nosal [94] have shown that the oxygen and carbon contents of hyperbaric welds tend to increase with pressure when the shielding gas contains active gases such as oxygen and carbon dioxide. This was attributed to the increase of partial pressure of the gases at elevated pressure.

As the partial pressure increases, the number of gas molecules per unit volume increases, resulting in higher gas concentration. This may lead to increased gas pick up by the welds. To avoid the problem of using active gases, Richardson [112] worked with completely inert gas for pressures above 20 bar, and ensured process stability by controlling electrical characteristics.

Dos Santos et al [33] attributed the high cooling rate of hyperbaric welds to changes made to the flow of shielding gas. He explained that in order to obtain effective shielding at high pressure, a greater mass flow of shielding gas must be supplied to the weld bead and weld pool to counteract the ambient pressure. This will have a cooling effect, which increases with pressure as greater mass of gas will impinge on the surface, for constant volume flow rate.

This claim requires further scrutiny because among the factors that affect convective cooling coefficient such as type of fluid and flow, geometric shape, surface condition, viscosity, etc., velocity has the greatest influence. But the increase of gas density at elevated pressure will result in higher viscosity [130], and consequent reduction of fluid velocity. Therefore the convective cooling effect is expected to decrease with pressure.

2.2.4.4 Heat Input

High heat input will generally tend to favour a slower cooling rate. This will cause a relatively large volume of weld pool to be formed since more parent

metal and filler wire will be melted, thus allowing ample time for hydrogen that may be present to be expelled before the weld pool solidifies. Consequently, reducing the tendency to hydrogen assisted cracking.

The time it takes the molten metal to cool from peak temperature to ambient temperature is crucial in determining the microstructure and mechanical properties of the weld metal. Nosal [94] stated that at the high temperatures (T> 1000°C) of the weld bead, the cooling rate is much higher than at lower temperatures. For example, the time it will take to cool from 2000 °C to 1000 °C ($\Delta t_{2000/1000}$) will be much shorter than that between 1000 °C to 100 °C ($\Delta t_{1000/100}$). He attributed this to the high thermal gradient present with greater heat flux. But at temperatures close to ambient, the thermal gradient will be smaller. In this low temperature regime, changes in thermal gradient will have a large effect on total cooling time. Therefore, cooling at low temperature will control the total cooling time [94].

Richardson et al [120] reported that weld metal cooling time for hyperbaric GMA/FCA welding from 800 °C to 500 °C ($\Delta t_{8/5}$) are comparatively short (of the order 2 s to 3 s for joints preheated to 25 °C and 100 °C). It was further reported by the authors that cooling rates are almost independent of pressure in the depth range 180 m to 370 m. Such high cooling rates in the presence of high restraint conditions can give rise to hydrogen induced cracking especially inside a moist hyperbaric chamber. This justifies the need for additional heat input to the process.

2.2.5 Applications

Three main applications of hyperbaric welding have been identified to be particularly useful. They are: structural repair, pipeline tie-in and hot tap. The necessities of structural repair of offshore structures including pipelines are relatively frequent, especially in areas where the seabed is prone to erosion and where there are fishing activities. Other reasons may be due to poor design and fabrication, corrosion and impact from dropped load or marine equipment.

Structural repairs are mostly carried out on offshore platforms, tubular lattice work, legs or risers, etc. This includes installation of replacement parts of pipe work or repair to compromised weld sections, pup pieces or whole braces [20]. Pipeline repair may be undertaken by either cutting out the failed section or replacing it with a short length of new pipe joined by butt welding or by fillet welding a two part sleeve onto the damaged area.

The connection of a subsea pipeline to a platform or other offshore structure is called a 'tie-in'. This may involve connections between a pipeline end and riser end using a spool piece at the base of a platform [20]. Tie-ins are also used as a by-pass when a platform is to be decommissioned whilst retaining use of the existing pipeline facility.

A 'Hot tap' involves fillet welding a specialist sealed 'Tee' component which is connected to an isolation valve onto an existing pipe. Remote cutting tools are then activated to pierce the parent pipe. There is no opportunity for penetration of sea water or egress of petroleum product since the new component is welded to the pipe. The pipe continues to carry petroleum products during the procedure and there is no need to stop production. It is a cost effective means of gaining product flow access by another pipeline, and has been adapted as a standard method for tying new oil and gas fields to existing ones [94]. Schematic illustrations of butt and fillet weld pipeline repair techniques, and hot tap welding are shown in Figure 2-15 to 2-16 respectively.

An alternative called cold tap involves stopping the flow of oil or gas in the existing pipe, emptying it of products using plugs or stoppers and then welding a 'T' section at the appropriate location. To stop pumping is expensive as it involves loss of many days or weeks of production for the companies that use the pipe; hence hot tapping is commonly used.

Over the last decade the majority of research and development efforts on hyperbaric welding have been geared towards diver-less installation and repair applications [14; 52-54; 81; 93; 113-115; 117; 156; 162-164]. Studies carried out by these authors have also shown that the application of hyperbaric welding, especially

for diver-less deep water operations is not limited by welding process or material considerations but by the pace of development and practicability of employing remotely operated technologies.

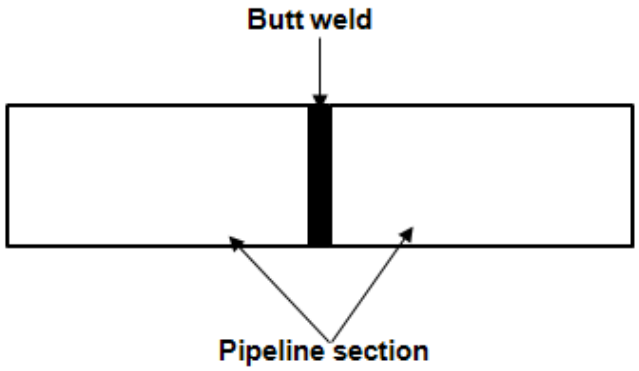

Figure 2-15: Schematic illustration of butt weld pipeline repair

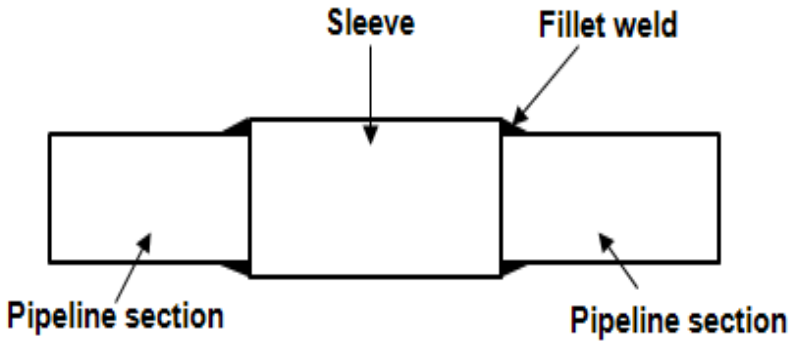

Figure 2-16: Schematic illustration of pipeline sleeve repair with fillet welds

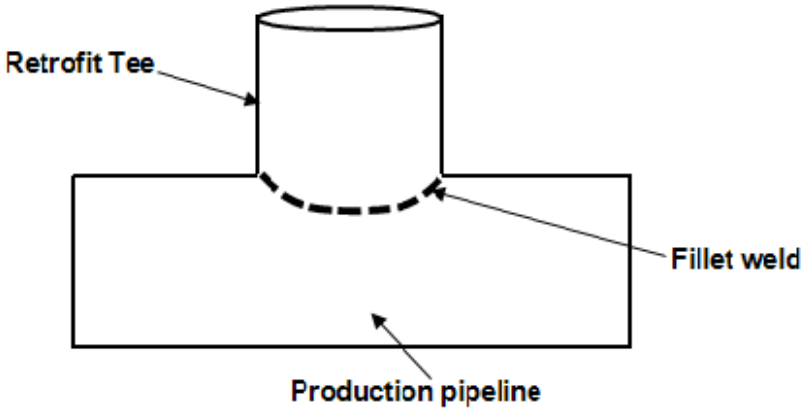

Figure 2-17: Schematic illustration of hot tap welding

2.2.5.1 Pipeline Repair System (PRS)

The PRS is a broad set of tools and equipment for subsea pipeline repair and construction, ranging from isolation plugs and cleaning tools to welding habitat chambers and large manipulation and installation frames as represented in Figure 2-18 and 2-18. It is managed by Statoil on behalf of a consortium of about 40 pipeline operators that share costs in order to have access to the equipment [14]. The PRS currently utilises the mechanised cold wire GTAW process, controlled from a surface diving vessel and has been deployed for many diver assisted alignment and welding installations in the North Sea [120; 156]. It was recently employed in the Baltic Sea for the Nord Stream project [43].

Richardson et al [120] described a typical subsea pipeline repair operation as involving the use of two large PRS 'H' frames, each weighing 70 tonnes and capable of lifting 120 tonnes for pipeline manipulation. The frames have capacity to move pipelines in the lateral, vertical and axial directions. The pipe is prepared for welding by combined tools using a high pressure water jet for cutting and removal of both concrete and anti-corrosion coatings. The replacement part called the spool piece is lowered into position and roughly aligned to the pipeline with the hydraulic 'H' frames before lowering the habitat over the pipe ends. The remotely operated pipe doors with flexible sealing skirts are closed around each pipe, allowing injection of pressurised gas to displace

water in the habitat. All these operations can be performed without divers inside the habitat.

However, welding head installation and fine alignment and abutment of the pipeline joints are still performed manually. Since these factors are key to successful butt welding, and also considering the depth limitations of GTAW process, and safety issues associated with deep sea diving, attention is moving to fully automated or diver-less operations called the Remote Pipeline Repair System (RPRS) for operations deeper than 180 m [14; 120; 156].

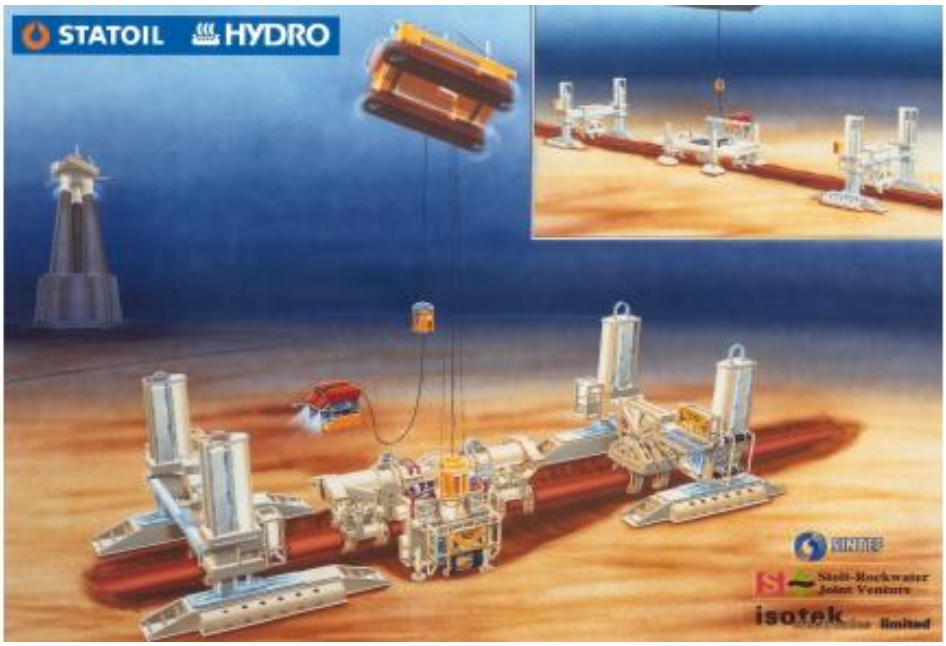

Figure 2-18: Illustration of the Pipeline Repair System spread at the seabed [156]

Figure 2-19: PRS welding habitat during installation for welding at Langeled pipeline [43]

2.2.5.2 Remote Pipeline Repair System (RPRS)

Statoil is currently developing new equipment that will employ hyperbaric GMAW for fillet welded contingencies, which can be deployed and operated remotely without diver assistance. This is known as the Remote Pipeline Repair System (RPRS) [14].

The use of a sleeve repair provides better operational flexibility when compared with butt welding used in the PRS. This is both in terms of required tolerances to pipe ovality and radial offset and angular alignment of the pipe ends since the sleeve design includes a root gap. The sleeve design will also include environmental seals to prevent water ingress during welding [120]. Studies by Huismann et al [66] and Woodward [156] have shown that a complete sleeve construction involves placing a section of pipeline (spool piece) between the two pipe ends before sliding an oversized sleeve over either end. The sleeves are then secured with four fillet welds.

Woodward [156] reported on a finite element analysis which showed that high stresses on the fillet weld occur at the weld toe and root regions. The model revealed that the leg length of the fillet weld must be long enough to prevent high stresses at the weld toe, which may cause yielding of the pipe material. This is used for a more evenly distributed load on the pipe. For example, the Asgard Transport Pipeline with a system pressure of 242 bar required a leg length of 120 mm with a weld height of over 30 mm [120].

Woodward et al [163] have extensively studied process performance for sleeve repair applications (see Figure 2-20), and welding conditions have been developed to bridge any root gap using optimised welding parameters that did not change with welding position. The work has been qualified for production wires on X60 and X70 pipelines using remote repair sleeve of X65 grade. It was reported that the procedure is suitable for application on the Asgard Transport, Langeled, Troll P10/P11, Zeepipe 2A and 2B and Europipe 2 pipelines in the North Sea [163].

According to Richardson et al [120] a diver-less remote hot tap cutting operation on a pressurised pipeline in the Ormen Lange Field of the Norwegian Sea was performed in August 2009 using a pre-installed tee. Field trials using a fully automated hyperbaric GMAW process in a Norwegian Fjord, which was sponsored by Statoil, demonstrated the feasibility of sleeve repair welding at 370 m and 940 m sea water depth [105]. Fully remote hot tap and sleeve repair test welds are shown in Figure 2-21.

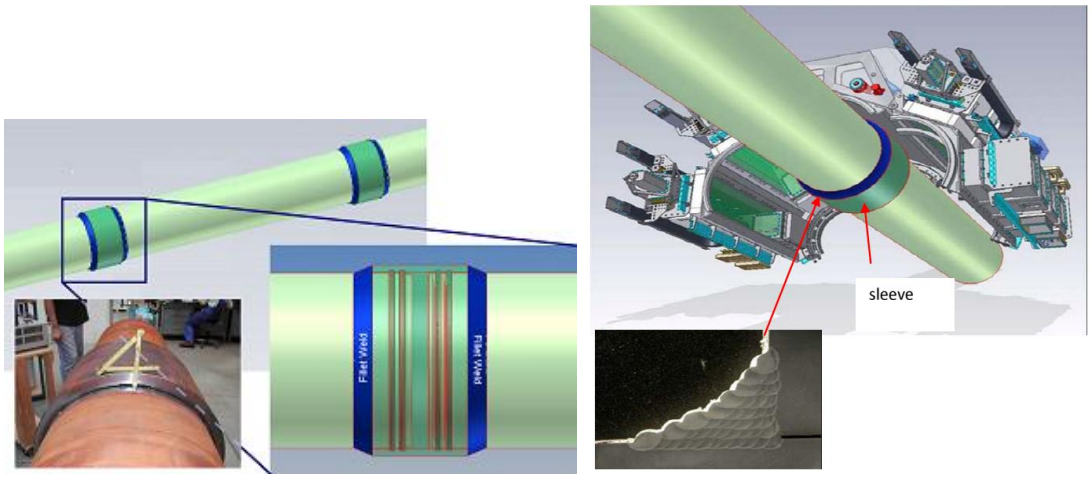

Figure 2-20: (left) Sleeve concept for pipeline connections and repairs. Inset photograph shows a laboratory mock-up of a sleeve joint, (right) sketch of the welded concept [43; 156]

Figure 2-21: 3-Pass retrofit Tee fillet weld for remote hot tapping and 59-pass sleeve repair weld [105]

As a future focus, Fostervoll et al [43] reported on the challenge of replacing the GMAW fillet welds with conventional butt welds, which was described to be more advantageous both in terms of robustness and reduced welding time.

They further reported that the arc on time for a typical pipeline joint can be reduced to about 1/10 by changing to a butt weld. Also, the authors observed that due to its process characteristics, one-sided full penetration root pass welding, as used in the PRS diver assisted GTAW, was found to be too challenging with GMAW. These have elicited interest in developing technology for GMAW butt welding of pipelines, which may replace sleeve repair in the future. Interestingly, work has started in that direction as part of a 5 year (2009-2013) research programme sponsored by The Research Council in Norway, Statoil, Gassco, Technip and EFD Induction, and managed by SINTEF [43].

2.2.6 Summary

Considerable research effort on hyperbaric welding is focused on the development and application of arc welding processes in relation to the offshore construction and repair industry. Most of these works investigated the effect of environmental conditions on welding process behaviour or on the properties of the weld metal. In the past decade, research efforts have shifted towards implementing dry hyperbaric GMA welding for deep water diver-less or remote application. The driving force for these developments is the need to achieve cost effective solutions to equipment installation and repair in increasingly remote and hostile offshore environments, whilst ensuring safety of operating personnel and the environment. This has been aided by improvements in welding power source technology as well as optimised welding consumables.

2.3 Hydrogen Assisted Cracking in Hyperbaric Welding

2.3.1 Overview

The application of dry hyperbaric welding for deep sea repair of pipelines and pipeline tie-in operations is fraught with some challenges such as low heat input, high weld cooling rate and potential moisture presence in the welding chamber. These conditions increase susceptibility to hydrogen assisted cracking (HAC), which undermines the structural integrity of hyperbaric welds. HAC is a major concern in hyperbaric welding because the three main factors that control it are hydrogen content, hardened microstructure and tensile stress, and are all likely to be present during hyperbaric welding.

There is potential presence of water vapour inside the hyperbaric welding chamber as divers/welders or remotely operated vehicles (ROVs) will need to have access to the welding chamber. The moisture dissociates inside the intense heat of the welding arc to form hydrogen and oxygen. This increases the chances of hydrogen pick-up during welding especially at high pressure. The fast cooling rate of the weld metal during hyperbaric welding may result in the formation of martensite, which reduces weld toughness, especially for pipeline steels that have carbon equivalent (CE_{IIW}) greater than 0.40. The surrounding pipe immersed in the sea just outside the comparatively small hyperbaric chamber acts as a massive heat sink, which also exacerbates the high cooling rate. There is high restraint to the solidifying weld metal, which introduces tensile stresses. Huismann et al [65] reported that every weld experiences shrinkage from cooling, and under restraint conditions the shrinkage results in plastic deformation of the weld zone. As the restraint increases the plastic deformation becomes higher. All of these conditions may lead to the production of hyperbaric welds that are susceptible to HAC.

Adequate preheating could reduce HAC susceptibility, but in the hyperbaric environment, the effect of preheat may be limited considering that the surrounding heat sink and degree of cooling is relatively high. Olden and Akselsen [95] reported that the narrow operational window under hyperbaric

conditions constrained the selection of welding parameters and preheating for GTAW. These challenges become even more crucial for diver-less or remotely operated hyperbaric welding operations because of the need for stringent control of welding parameters and other processes.

2.3.2 The Hydrogen Cracking Phenomenon

Hydrogen assisted cracking shown in Figure 2-22 typically occurs at stress concentration points such as the root or toe of the weld and can propagate through the weld metal to the heat affected zone (HAZ). The detrimental effects of hydrogen on steel is well established and one of the main issues affecting the structural integrity of offshore installations [17; 41; 49; 86; 91; 146; 167]. Different terminologies have been used in the literature to describe the HAC phenomenon: hydrogen cracking, cold cracking, hydrogen induced cracking, hydrogen induced stress cracking, hydrogen assisted stress corrosion cracking, hydrogen assisted cold cracking, delayed cracking and under bead cracking [47; 57; 151; 152].

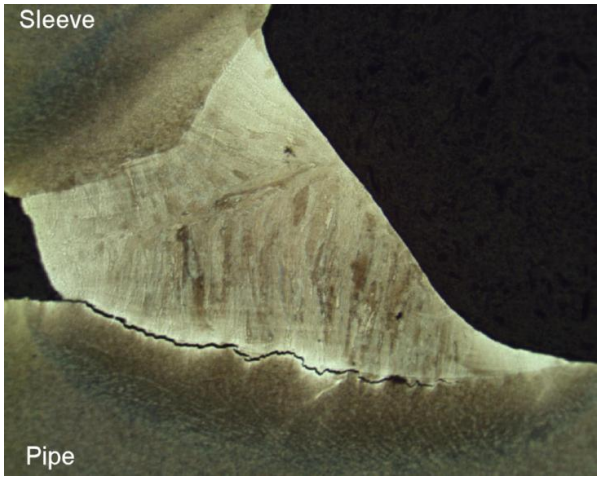

Figure 2-22: Hydrogen assisted crack in a sleeve repair fillet weld [42]

Despite the use of different terminologies, there seem to be convergent opinions on the fundamental characteristic of the HAC phenomenon. That is presence of hydrogen in the lattice structure of steel may reduce the ductility of steel, thereby increasing cracking susceptibility. Hauge [57] described hydrogen embrittlement as a wider term consisting of several failure mechanisms of which

HAC is one. This cracking occurs as the metal suffers embrittlement by the atomic hydrogen present in its microstructure.

Gangloff [47] related the HAC phenomenon to reduction of the resistance of high strength alloys to crack propagation due to the presence of hydrogen, and termed this as either internal hydrogen assisted cracking (IHAC) or hydrogen environment assisted cracking (HEAC). The effect of hydrogen in these alloys are localised around the crack tip, and the source of the supplied hydrogen can be used to distinguish IHAC from HEAC. Apart from this, they share common characteristics [47]. Different manufacturing operations such as welding, casting, heat treatment, electro-chemical machining, surface chemical cleaning; etc. can introduce atomic hydrogen into the metal microstructure. It can also be by exposure to the environment e.g. gaseous hydrogen exposure at high temperature and by electrochemical reactions at low temperature [47].

In IHAC, as the hydrogen "charged" metal is stressed this initiates subcritical crack growth. The absorbed hydrogen from the adjacent microstructure is redistributed to the crack tip due to loading, which promotes crack growth. On the other hand, HEAC combines mechanical loading and chemical reaction. The atomic hydrogen produced is subsequently taken up into the crack tip [47]. It was further reported that IHAC and HEAC exhibit the same features for high strength metals: both are initiated at stress intensity levels lower than the fracture toughness $K_{IC.}$ An extensive study on HAC of high strength alloys was undertaken by Gangloff [47].

2.3.3 Mechanism of Hydrogen Assisted Cracking

The subject of hydrogen assisted damage mechanisms has been extensively investigated in the literature [15; 62; 85; 90; 97-99; 149; 150]. Until recently, numerous contrary suggestions have been offered as the mechanism of HAC based on the interaction between local hydrogen concentration and local mechanical load for cracking to occur on the atomic scale at the crack tip. However, these theories are not easily verified [47; 57; 152]. Nevertheless, Viyanit [152] reported that researchers are unanimous that the HAC phenomenon cannot be described by a single mechanism. He therefore suggested that a basic understanding of the

general mechanisms of HAC, as well as the hydrogen uptake and diffusion processes, and a basic determination of mechanical loads may provide sufficient explanations of the phenomenon. Viyanit [152] and Gangloff [47] reported the details of these processes in their studies. However, a general description of the different HAC mechanisms covered in the literature is given.

2.3.3.1 Pressure Theory

According to Viyanit [152] this is the oldest proposed HAC mechanism. The theory specifies that blisters and internal cracking are formed when unstressed specimens are charged with hydrogen, which precipitates and recombines to molecules at internal defects such as voids, non-metallic inclusions and flakes, and then generates internal pressure within the defects. Zapffe and Sims [165] proposed that the main portion of absorbed hydrogen in iron consists of partially ionised molecules occluded in micro-voids, non-metallic inclusions, etc.

As more hydrogen atoms are absorbed and consequent precipitation of molecular hydrogen becomes sufficiently pronounced or if the lattice reinforcement is weak, nucleation and growth of micro-cracks may occur even without external stress [152]. As depicted in Figure 2-23, micro-cracks eventually coalesce to form macroscopic cracks that play a significant role in rupture of the material. Since stresses in steel structures are of tri-axial type, it implies that the imposed stress may result in rupture of the material [77].

With regard to welding, it has to be considered that hydrogen molecules are often formed at elevated temperatures, and the resultant pressure occurs during cooling [152].

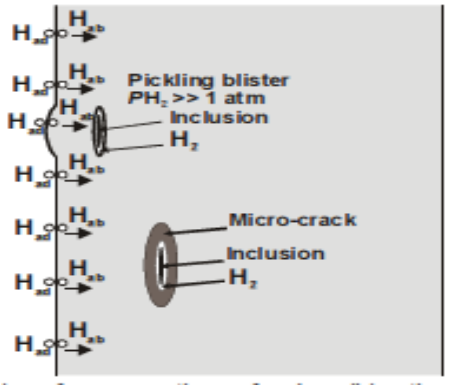

Figure 2-23: Schematic illustration of HAC using the pressure theory [152]

2.3.3.2 Hydrogen Enhanced De-cohesion (HEDE)

The HEDE model is based on the effect of hydrogen on the cohesive strength of the iron lattice. Studies have often made references to Troiano [149] as the proponent of this theory [47; 57; 152]. It was further proposed by Oriani [97; 100] that the average cohesion forces between iron atoms can be reduced by dissolved hydrogen as shown in Figure 2-24. This assumption may be strengthened by the fact that steel fractures in a brittle manner in a hydrogen environment, which implies that it is easier for the metal to respond to applied stress by the cleavage of the iron-iron atomic bonds instead of plastic deformation [57; 152]. The high local hydrogen concentration may be found in the lattice in front of the crack tip [57]. This is because the local concentration of hydrogen is increased by the positive component of elastic stress, since hydrogen must first diffuse into severe elastically stressed region where it accumulates in front of the crack tip [97].

The fundamental principle of this model infers that: crack propagation can occur if the local maximum tensile stress $\sigma_{\max}$ at a point in front of the crack tip and normal to the crack plane equals the maximum cohesive resistive force of the metal nF_m per unit area of the cracking plane [97].

$$\sigma_{\max} = n.F_m.\ HD\ , \qquad (2\text{-}2)$$

where n represents the number of metal atoms per unit area of the cracking plane, F_m is the maximum cohesive resistive force of iron atoms and HD is the total hydrogen concentration in the considered system

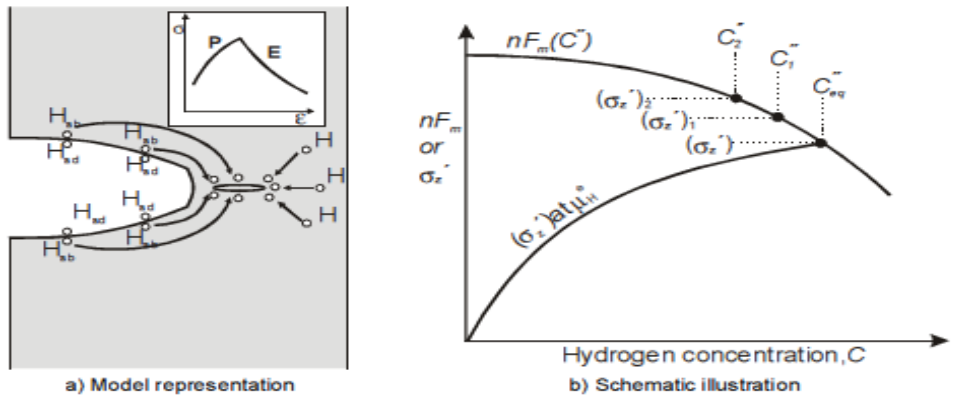

Figure 2-24: Decohesion theory describing HAC phenomenon (a) Model representation (b) schematic illustration of the equilibrium hydrogen concentration [97]

This theory explains the delayed cracking of HAC on the assumption that hydrogen diffusion is required to transport hydrogen atoms into the critical strain region in front of the crack tip, and this is time dependent.

2.3.3.3 Dislocation Interaction Theory

This theory assumes that the presence of hydrogen around a dislocation can change the movement of the dislocation, which can influence the fracture behaviour of materials through changes in the extent and character of plasticity [152]. It was suggested by Nelson [90] that the influence of hydrogen on a dislocation produces either a hardening or softening effect depending on the material and on alloying composition.

Regarding the hardening effect, Cottrel [26] assumed that hydrogen will interact with the high tensile stress field close to the dislocation to form a hydrogen cloud (Cotrell-atmosphere) that can strongly obstruct dislocation movement such that more dragging force will need to be applied for a dislocation to move. Consequently, the change in slip character makes deformation at the crack tip

more difficult, hence crack propagation will take place at low levels of external load.

Conversely, the softening effect is based on the assumption that hydrogen may reduce the fracture toughness of the material. Beacham [13] observed that dissolved hydrogen on the crack tip surface assists the movement of dislocation instead of restricting it. Failure of the metal matrix will occur when the critical strain is reached within the specific crack zone ahead of the crack tip as shown schematically in Figure 2-25 [152] .

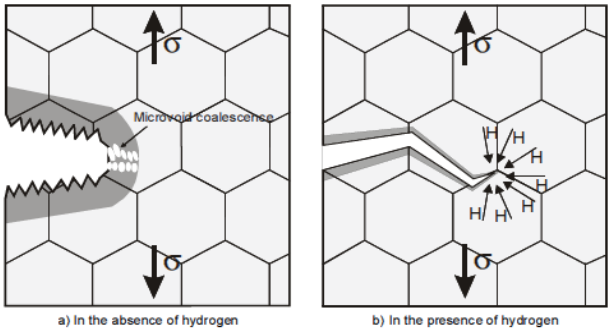

Figure 2-25: Schematic demonstration of crack propagation in high strength steels based on Beacham's assumption [13; 90]

2.3.3.4 Hydrogen Enhanced Local Plasticity (HELP)

Comprehensive studies dealing with the softening effect of dislocation interaction theory have been conducted by Birnbaum and Sofronis [17; 137] who developed the hydrogen enhanced localised plasticity mechanism. The basis of their assumption is that high capabilities of local deformation are produced due to hydrogen presence in solid solution, which reduces the obstacles to dislocation movement. Therefore, the highly localised plastic failure decreases the strength of the material rather than embrittlement because the localised zone is softened by the presence of hydrogen. The significance of this mechanism is that the crack propagation characteristic of relatively pure metals and metal alloys can be different: fracture tends to be along slip planes for pure metals, and along the plane of maximum normal stress due to the action of multiple slip systems [152].

Tien et al [147] described the effect of hydrogen concentration on dislocation by the Boltzmann equation as follows:

$$HD_{dis} = HD_{\infty} exp\ -\frac{E_B}{KT} \quad (2\text{-}3)$$

where E_B is the binding energy of hydrogen to dislocation (0.1 – 0.5 eV), K is Boltzmann's constant, T is the absolute temperature, HD_{dis} is the hydrogen concentration on the dislocation, and HD_{∞} is the equilibrium hydrogen concentration at the pick-up site.

2.3.3.5 Adsorption Theory

The binding energy of metal atoms has been thought to be reduced by atomic hydrogen, particularly at the location of the extreme root of notch, below a critical level of shear stress which is required to create new fracture surfaces. This implies that crack initiation and propagation occur without the dissolution of the metal as shown in Figure 2-26 [19] .

Since crack initiation and propagation have been assumed to take place by rupture of material as explained by Boellinghaus [19] the application of this theory to HAC remains contentious [152]. It was also reported by Lynch [77] that the energy required for fracture in materials almost entirely involves plastic deformation, and as such surface energy should not be significant. Therefore, the adsorption theory does not seem to give an accurate account of the dynamic stages of crack propagation [47; 152].

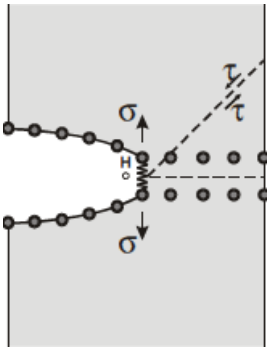

Figure 2-26: Schematic illustration of the adsorption theory [154]

2.3.3.6 Hydride Theory

Viyanit [152] reported that the embrittlement of metallic materials by the formation of a second phase known as metal hydride has also been categorised as HAC. Hauge [57] referred to hydrogen embrittlement as a wider term for several hydrogen failure mechanisms. But, Gangloff [47] disagrees with such generalisation on the ground that the atomistic mechanism of hydrogen embrittlement does not clearly define the precise nature of hydrogen damage mechanisms.

Hydride formation in materials can be grouped into four categories depending on metal-hydrogen bond formed, which could be: Ionic hydrides, transition hydrides, intermediate hydrides and covalent hydrides [90]. It was further explained that the transition hydrides are quite important, particularly for structural alloys. However, not all transition metals, e.g. Fe, Ni, Cu, Cr and Mo can form metal hydrides. Transition metals in Group-V, including Nb, V, Ta, Zr, Ti and Mg can possibly react with hydrogen to form metal hydrides with the involvement of other mechanisms as described by Birnbaum [16].

An extensive study on hydride formation especially for Group-V metals has been reported by Nelson [90]. The metal hydrides simply assist in decreasing the material strength and ductility. As a result, the brittle fracture mode can be observed on the crack surface at very low strain rates and temperatures at which hydrogen can still be transported to the crack tip [152]. The mechanism of hydride embrittlement is represented in Figure 2-27.

There is no doubt that the formation of metal hydride in the matrix lattice can cause embrittlement in alloys. According to Viyanit [152], this mechanism cannot describe embrittlement of iron based alloys because iron does not form a metal hydride.

Since most high strength steels are alloyed with elements such as Nb, Ti, V, etc. that can form metal hydrides, Viyanit [152] claim that metal hydride cannot describe embrittlement in steels may not necessarily hold.

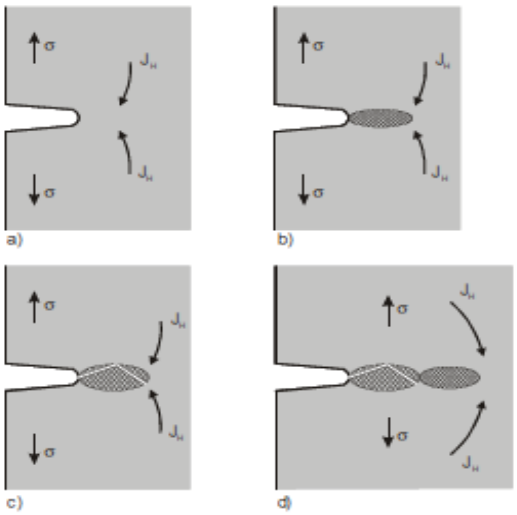

a) Flux of hydrogen to the crack tip due to reduction of the hydrogen chemical potential in the tensile stress field.

b) Formation of the hydride due to reduction of the hydride chemical potential by the applied stress.

c) Cleavage of the hydride along its cleavage plane resulting in crack advance.

d) A repeat of the crack propagation process.

Figure 2-27: Schematic illustration of hydride theory showing crack propagation in the metallic hydride region ahead of the crack tip by stress induced hydride formation [16]

2.3.4 Hydrogen Transport Mechanism in Steel

Hydrogen is transported through the iron lattice by diffusion and the main mechanism is by interstitial jumps [57]. Hydrogen diffusion requires generally chemical gradients of hydrogen concentration, and such gradients are generated by different hydrogen sources [152]. The transportation of atomic hydrogen through steel and metallic materials generally is significantly influenced by the material crystal structure. A closer look at the steel lattice shows that it is built up from different microstructures, each having their own properties regarding hydrogen diffusion. The α-ferritic body-centred cubic (BCC) crystal has an open lattice structure, which allows a high hydrogen diffusion rate and low solubility. The more close-packed face-centred cubic (FCC) lattice structure of γ-austenite makes it more difficult for hydrogen to diffuse through the lattice resulting in high solubility of hydrogen atoms. Smailowski [135] reported that the solubility of hydrogen in the matrix structure of steel is directly proportional to the amount of the (austenite) FCC-crystal structure. The martensitic structure can be both body-centred tetragonal (BCT) and hexagonal close packed (HCP). Both these structures are closer packed than BCC, resulting in a martensite diffusion rate in between that of ferrite and austenite.

Table 2-1 represents the hydrogen diffusion rate and solubility of these microstructures [96], and Figure 2-28 represents hydrogen diffusion coefficients in two types of steel.

Table 2-1: Comparison of the hydrogen diffusion rate and solubility of common steel microstructures

Microstructure	Lattice structure	Diffusion rate	Solubility
Austenite	FCC	LOW	HIGH
Ferrite	BCC	HIGH	LOW
Martensite	BCT and HCP	MEDIUM	MEDIUM

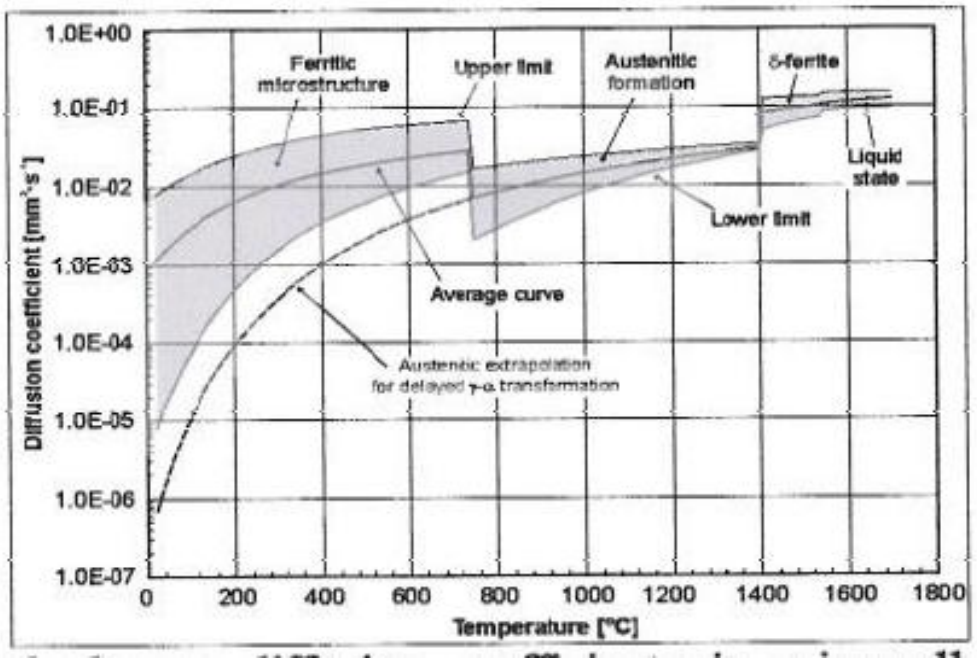

Figure 2-28: Scatter band of hydrogen diffusion coefficients in micro-alloyed and low carbon steel [18]

The lattice sites of steel can be both octahedral and tetrahedral as shown in Figure 2-29. The tetrahedral interstice is a stable absorption site for hydrogen in the FCC crystal structure, and is more stable for atomic hydrogen than the octahedral site in the BCC crystal structure [152].

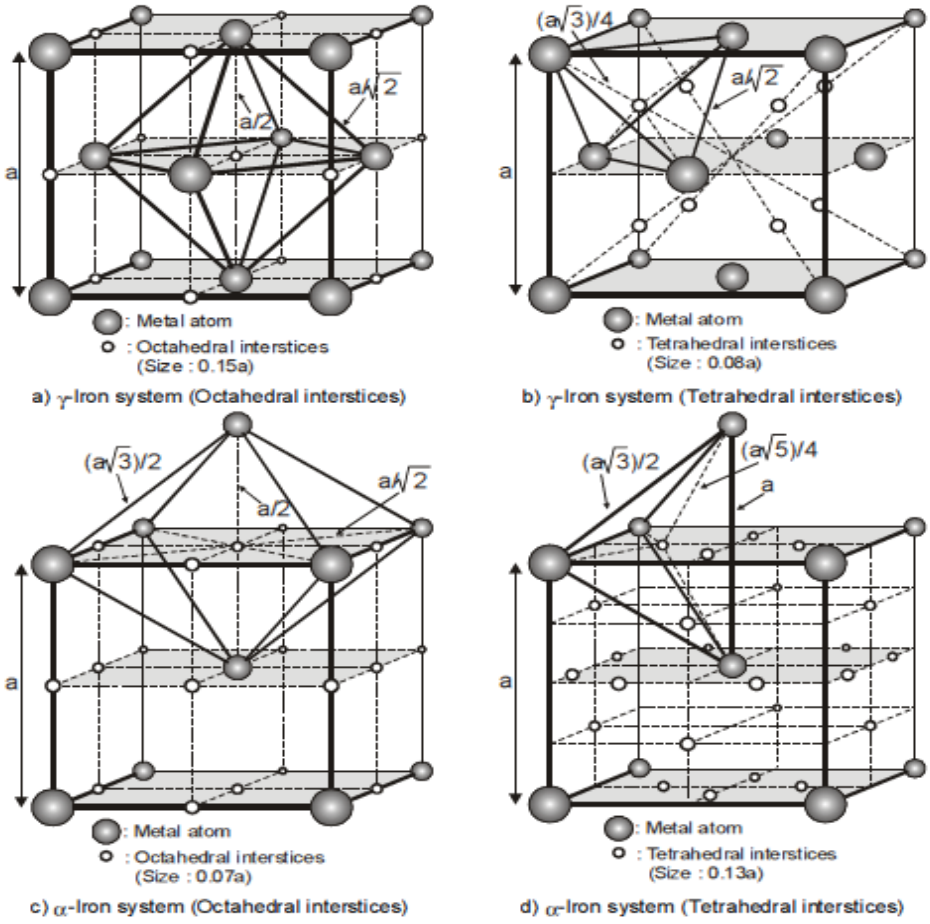

Figure 2-29: Schematic illustration of octahedral and tetrahedral lattice sites in (a) FCC structure and (b) BCC structure [135]

2.3.5 Factors that Influence Hydrogen Assisted Cracking in Hyperbaric Welding

The factors that influence HAC in hyperbaric welding are the same as welding at one atmosphere, except that it is usually more difficult to control the former due to potential presence of moisture in the welding environment. HAC results from three independent conditions occurring simultaneously: hydrogen in the weld metal, susceptible microstructure and tensile stresses. We shall now examine these factors more closely.

2.3.5.1 Hydrogen

It has been extensively reported that hydrogen reduces the fracture strain of metals. Huismann et al [65] demonstrated that hydrogen content as low as 1 to 3

ml /100 g Fe caused dramatic reduction of fracture strain as shown in Figure 2-30. During hyperbaric welding 2-10 ml /100 g Fe hydrogen are readily achievable [65]. The International Institute of Welding (IIW) stipulates that to avoid HAC the hydrogen content of the weld metal should not exceed 5 ml H_2/100 g Fe.

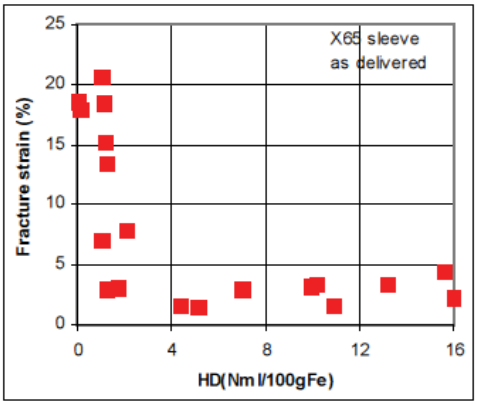

Figure 2-30: Influence of hydrogen content on fracture strain [65]

Although the hydrogen content of high strength pipeline steels is low, hydrogen may diffuse from the weld metal into the base metal. Huismann et al [65] simulated the presence of significant hydrogen content near the melt line as represented in Figure 2-31. They also demonstrated that further hydrogen diffuses from the weld metal into the HAZ after cooling. Therefore, reducing the hydrogen level where critical conditions are present will reduce the risk of HAC

Figure 2-31: Hydrogen distribution after welding, HAZ gets significant hydrogen only near the melt line [65]

2.3.5.2 Microstructure

The weld thermal cycle determines its microstructure, which also depends on the material. The X65 pipeline steel used for deep sea applications could have carbon equivalent (CE_{IIW}) higher than 0.4, which makes it susceptible to martensite formation especially during the fast cooling that is associated with hyperbaric welding. This microstructure has high hardness and low fracture toughness. Huismann et al [65] reported that for sleeve repair, the combined thickness of the pipe is very high (35 mm and 50 mm) compared with the relatively low heat input, and that will exacerbate the cooling condition. In the same study, it was shown that using 0.6 kJ/mm heat input led to a cooling time in the range of 800 °C to 500 °C ($\Delta t_{8/5}$) of 2 s to 3 s. As shown in Figure 2-32, such high cooling rates will evolve a martensitic and bainitic microstructure for the X65 steel used.

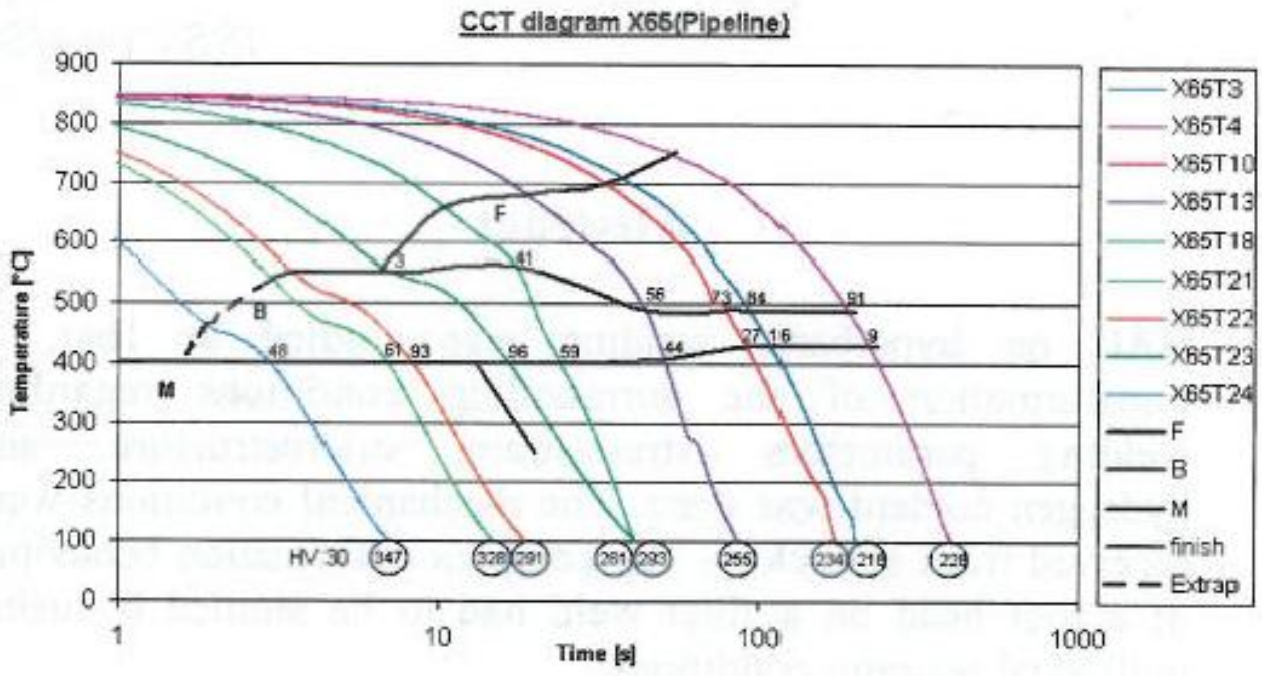

Figure 2-32: CCT diagram (1350 °C peak temperature) for X65 steel [65]

2.3.5.3 Mechanical Behaviour

The restraint conditions on the solidifying weld metal determine the stress/strain field. The weld metal is subjected to high restraint during hyperbaric welding of pipelines. Huismann et al [65] reported that the root bead gets high restraint, which makes it prone to HAC and that fillet welds showed greater risk to HAC than butt welds due to higher intensity of restraint. This implies that the shrinkage stress on the weld metal will be low if the restraint of the plate is low. High restraint conditions cause high shrinkage stresses, which result in plastic deformation of the weld zone [65].

2.3.6 Preventing Hydrogen Assisted Cracking of Hyperbaric Welds

If one or more of the conditions listed above are removed or controlled below a threshold values hydrogen cracking will not occur. Most importantly, limiting hydrogen in the weld reduces cracking susceptibility since it is the main cause. But these conditions are difficult to control in hyperbaric welding as some level of hydrogen pick-up may be inevitable. Huismann et al [65] reported that the expected hydrogen content of the weld metal is between 5 and 10 ml/100 g Fe, which is picked-up from water vapour in the hyperbaric welding habitat. Viyanit [152] reported that the susceptibility of welded components to HAC can be reduced if the local hydrogen concentration in sensitive regions is constrained below the critical value, because it is impractical to avoid a build-up of stress-strain distribution in fabrication welding, particularly in offshore construction.

If a weld remains at high temperature after welding due to preheat, inter pass temperature control or post heating, hydrogen that was picked up by the weld has the ability to diffuse away. This is because the average hydrogen diffusion in steel depends on temperature among other factors. For example, at 100 °C it is typically 1000 times faster than at 20 °C or room temperature [31]. In addition to preheat, the wall thickness of the joint and number of weld passes has an effect on the diffusion of hydrogen from the weld. Huismann et al [65] used a combination of preheating and post weld heating to avoid HAC.

Given the high cooling rate of deep water hyperbaric arc welding, the author is proposing the provision of additional heat input to the welding arc in order to extend the weld cooling time. This will allow more time for dissolved hydrogen to escape from the weld metal and HAZ region, thus eliminating the main cause of HAC. Hence, the investigation of laser assisted arc welding process whereby the laser will provide post weld heating to the weld zone.

2.3.7 Summary

There is vast resource in the literature on hydrogen assisted cracking (HAC) that focused on hydrogen damage and transport mechanisms in steels. Although, different mechanisms were proposed as possible causes of HAC, most authors were of the opinion that a single mechanism cannot be used to explain all observed behaviours. There were therefore suggestions that in addition to the mechanisms, a basic understanding of hydrogen uptake and diffusion process, as well as determination of local loads may provide sufficient explanations of the phenomenon.

Only a few references were found on HAC of hyperbaric welds. However, the factors that cause HAC are essentially the same for welds made in one atmosphere condition except that the former is more difficult to control because of the potential presence of moisture in a hyperbaric chamber. Hydrogen, hardened microstructure and tensile stresses caused by restraint to the solidifying weld metal were identified as factors responsible for HAC. The proposed preventive measures were appropriate pre- and post- weld heating as these will enhance the diffusion of dissolved hydrogen away from the weld metal and HAZ, thereby eliminating the primary cause of the problem.

The fast cooling associated with deep water hyperbaric arc welding may limit the effect of pre-heat; therefore, the author is proposing a laser assisted arc welding process whereby the laser will provide additional heat to help keep the weld metal at a higher temperature for a longer time. This will extend the cooling time of the weld metal so that dissolved hydrogen will have enough time to escape before diffusing to stress concentration points.

2.4 Laser Welding in Hyperbaric Environment

2.4.1 Overview

Laser welding is an established process that has found many industrial applications especially in the automotive sector. The application of laser welding for underwater repair of structural steel has also received some attention particularly in the nuclear industry. Szelagowski et al [145] reported that underwater laser beam welding is not a new technology even though it has not received wide acceptability. In addition to fillet weld trials and qualification, underwater laser beam cladding was developed by Toshiba [129]. Laser beam welding has also been developed as a viable underwater repair technology by WEC Welding and Machining for use in the nuclear power industry [23].

The technology and experience from underwater laser welding in the nuclear industry can be transferred to the oil and gas industry as a viable technology for repair of offshore structures [129]. However, the limitations of wet welding such as: risk of hydrogen cracking in hardenable steels, porosity, lack of fusion and potential for poor mechanical properties of welded joints have been identified as potential issues of the process.

As the exploitation of oil and gas reserves moves into deeper waters, these limitations become even more critical, necessitating the development of advanced welding techniques for repair and installation of offshore structures. Laser welding in a hyperbaric gas environment will potentially give improved weld quality compared to laser underwater (wet) welding since it will be performed in a dry environment. However, there is a dearth of information in the literature on laser welding in a hyperbaric environment. The author can only report on studies by Shannon et al [133] and Hilton et al [61] in this area.

In most applications laser welding involves operating the laser in a keyhole regime. That is when the power density of the focused laser beam is high enough to cause melting and vapourisation of the material [133]. Although this

allows for high welding speed, low distortion and deep weld penetration, it is intolerant to tight joint fit-up and the keyhole instability can limit weld quality.

There are also inherent drawbacks with this process for repair and installation of offshore structures. Firstly, keyhole laser welding is a low heat input per unit length process, and considering the high cooling rate at elevated pressure, the tendency for HAC will be high. Secondly, the efficiency and performance of laser welding in a hyperbaric environment is hampered by high pressure conditions. As reported by Shannon et al [133], the formation of large a plume during laser welding in hyperbaric condition causes the laser energy to be attenuated and results in collapse of the keyhole. This limits welding to conduction mode. It must be mentioned that this study was based on a CO_2 laser, which could potentially be absorbed by the plume because of its relatively long wavelength (10.64 microns). A solid state laser such as fibre laser is transparent to the plasma generated because of its much shorter wavelength (1.07 microns) and could have given a different result.

In this work, the laser is operated in the conduction-welding regime. The laser beam is defocused or at a low power density, which will not cause material vapourisation. It is a more stable process and reduces fit-up problems since the beam is larger. However, it is relatively slow and the high heat input per unit length can cause higher distortion.

Laser welding and arc welding processes can be combined in a common melt pool as a hybrid process to achieve a synergy. Laser hybrid processes have been extensively reported in the literature [4; 29; 71; 83; 89; 104; 107; 107; 108; 110; 111; 124; 125; 131; 132]. These have mostly involved operating the laser in the keyhole mode in combination with a GMAW process. This approach has been shown to overcome fit-up problems associated with laser keyhole welding but the additional process benefits of deep weld penetration have not been significant [134]. Also weld pores can be a problem due to keyhole instability.

The approach of this research work is to operate the laser in the conduction-welding mode, combining with a GMAW process. The arc will lead the laser to

enhance optical absorption. However, both heat sources are not in a common melt pool. The laser is merely assisting the arc by providing additional heating; hence the term laser assisted arc welding.

A brief overview of hybrid laser keyhole and conduction welding will be given in the following section. This will be followed by induction assisted laser welding process, which has potential benefit of reducing the weld cooling rate.

2.4.2 Laser Keyhole and Conduction Welding

One of the benefits of laser GMAW hybrid welding is to improve penetration depth, and this is achieved by keyhole welding, which is shown in Figure 2-33 (a). Ion [68] and Reutzel et al [124] described the keyhole as fundamentally a cylindrical cavity with molten metal walls, which are kept from collapsing by equilibrium forces created by vapour pressure and those exerted by the molten material inside the keyhole. A schematic of keyhole welding is depicted in Figure 2-34.

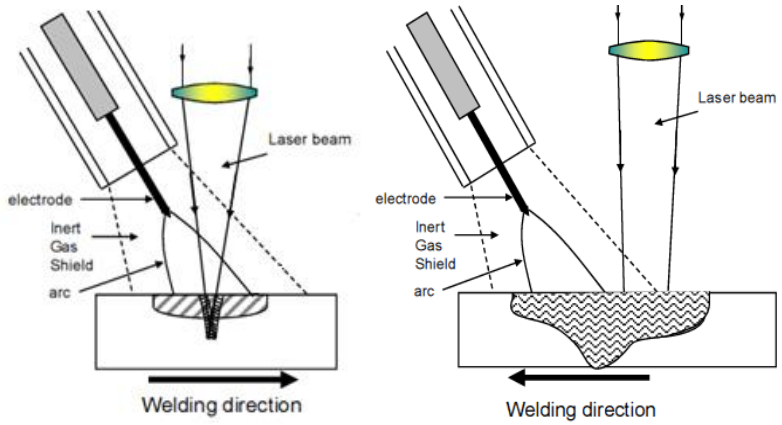

Figure 2-33: (a) Schematic of hybrid keyhole (b) conduction welding [155]

A keyhole is formed if the power density of the focused laser beam is high enough (~ 10^{10} W m^{-2}) to cause melting and vapourisation of the material before heat is removed from the processing zone by thermal conduction [124]. When the metal is molten, absorption of the laser beam is remarkably improved [72; 108]. Energy absorption by the material and overall energy transfer efficiency is determined by two mechanisms: Inverse Bremsstrahlung absorption (energy

transfer from photons to electrons) and Fresnel absorption (multiple reflections at the wall of the keyhole) [68; 72; 124]. The vapour inside the keyhole may be ionised and could form plasma, which improves the laser absorption. However, to achieve deep penetration, it is necessary to weld at low travel speed, in which case the process can be severely affected by the plasma and plume escaping from the keyhole and forming above it [124]. These defocus the laser beam and reduce its power density [68; 80; 108; 124; 133].

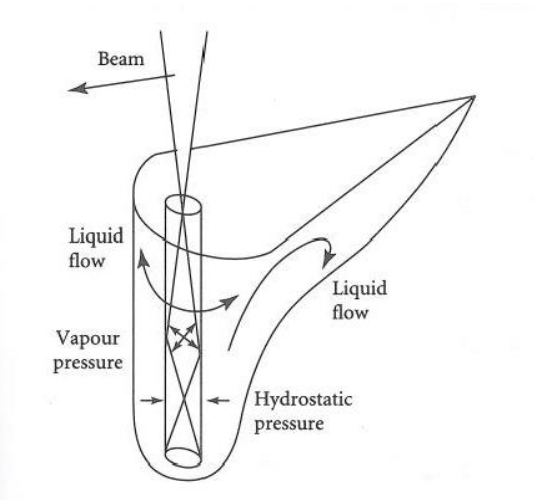

Figure 2-34: Principles of laser keyhole welding [68]

When the laser beam is defocused or at a lower power, it is in the conduction-welding mode, as shown in Figure 2-33 (b). In this case the laser power density is in the order of 10^9 Wm^{-2}, which is used to join materials without significant vapourisation [68]. Conduction-like welds give a hemispherical weld bead with low depth-width ratio, similar to that of the GMAW [68]. The principal mode of conduction welding is by direct heating, which involves absorption and conduction of the laser energy into the surrounding material.

Studies by Thong et al [148] showed that increase in laser spot diameter during hybrid conduction welding led to increased wettability of the weld deposit. In addition, since the laser radiation did not penetrate inside the material, less disturbance of the weld pool was observed, thereby making the process less susceptible to gas entrapment. This is in contrast to keyhole welding which can cause porosity due to intermittent closures of the keyhole [34]. Findings reported

by Rasmussen and Dubourg [108] showed that with decreased power density, smoother weld bead was achieved, but at decreased travel speed. This makes the process suitable for welding thin plates unlike keyhole welding that is suitable for welding thick plates of up to 20 mm. Figure 2-35 shows the macrographs of a typical laser hybrid keyhole and conduction mode welds.

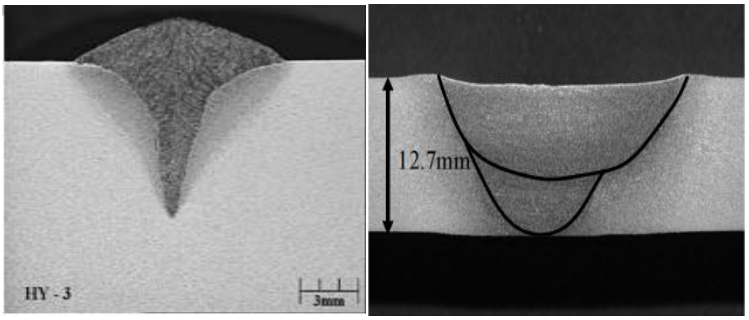

Figure 2-35: Macrographs of hybrid keyhole (left) and conduction (right) welds [155]

It is important to mention that while several works on laser GMAW hybrid keyhole welding have been reported in the literature, there is limited information on the hybrid welding in conduction mode. This may be because the former is reported to have several industrial applications or because there is little understanding of the applicability of the latter. Interestingly, laser hybrid conduction welding is a more stable process and easier to control than hybrid keyhole welding, which may be characterised by instabilities that can limit weld quality. Also, laser hybrid conduction welding has been found to be thermally very efficient, leading to additive effects in terms of weld penetration.

It must be stressed that the aim of this research work is not a classical laser GMAW hybrid process because both heat sources are not in a common processing zone as is the case with laser arc hybrid welding. In this case, the laser is used for post-weld heating. Hence it is used in conduction mode to provide additional heat input to the GMAW process to increase the cooling time and reduce susceptibility to hydrogen assisted cracking.

2.4.3 Induction Assisted Laser Welding

The concept of induction assisted laser welding depicted in Figure 2-36 is based fundamentally on the need to control the high cooling rate related to laser welding. The process involves the use of an integrated induction head to provide heat that is confined to the welding location thereby establishing favourable conditions for crack free welding of components that are ordinarily difficult to weld. Mach et al [78] described the application of induction technology in welding processes as a suitable way to circumvent the undesirable effects and expand the potential range of modern welding methods such as laser, GMAW and hybrid. In order to prevent loss of toughness and high hardness in the weld seam, Jahn et al [70] used a welding procedure involving a CO_2 laser in combination with inductive pre-heating to prevent the formation of martensite. Lowering of cooling rate can be easily and favourably achieved by incorporating induction heating with a laser process.

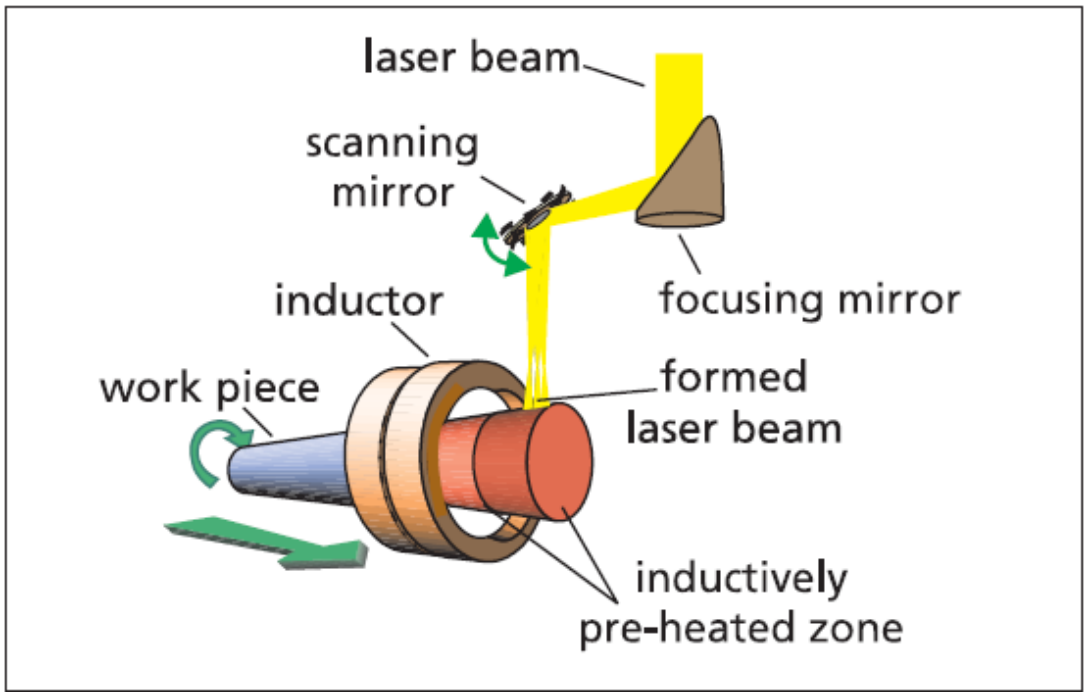

Figure 2-36: Schematic diagram of induction assisted laser processing [60]

2.4.3.1 Induction Heating

There are different forms of induction heating that are widely used for industrial hardening, brazing, tempering, soldering and pre-heating. They offer the advantage of a good combination of speed, control and consistency. The fundamental principle of the process involves using a large coil with high frequency alternating current to induce heating in any adjoining metal surface by electromagnetic induction. The magnetic flux induces eddy current which resistively heat up the material without any direct contact between the metal and coil. This generates precise and localised heating. The opposing eddy currents also create “the skin effect” which causes the impedance below the metal surface to increase as frequency increases [39].

Since the effect of induction heating is highly localised, intense heat is generated in adjacent metal to the coil with only a short range effect. An induction heating system is shown in Figure 2-37.

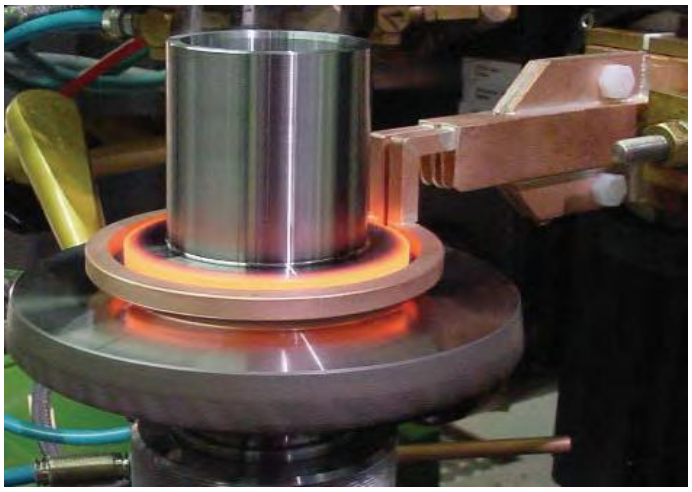

Figure 2-37: Induction heating [46]

2.4.3.2 Process Characteristics

The time-temperature cycle or the cooling curve shown in Figure 2-38 during laser welding can be influenced by integrated inductive heat input to the process. This enhances the weld properties of components made from heat treatable as well as advanced high strength multi-phase steels. Similarly,

improvement of mechanical properties by induction assisted laser welding of high strength low alloy (HSLA) steel can also be expected [70].

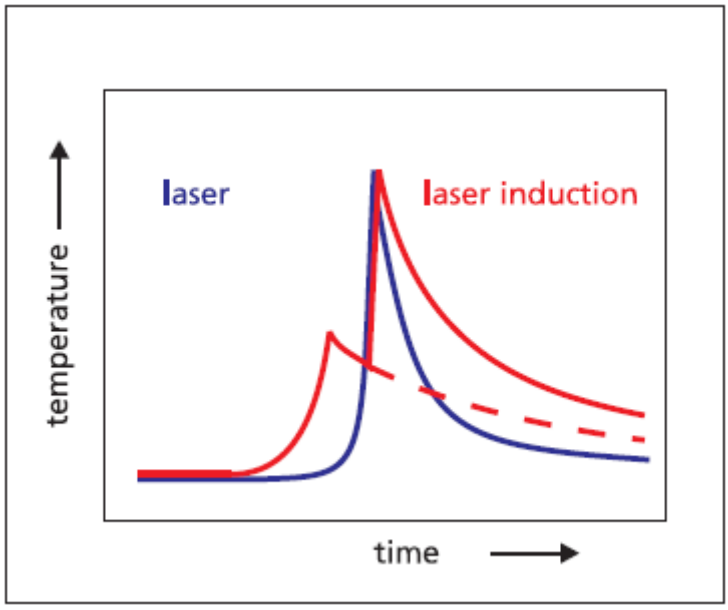

Figure 2-38: Effect of induction heating on the thermal cycle during laser processing [45]

As shown in Figure 2-38, the blue curve representing pure laser welding has a shorter cooling time than the red one, which represents induction assisted laser welding. This shows that induction heating provides additional heat that leads to longer cooling time and consequently a slower cooling rate. This will be beneficial to the mechanical properties of the resultant hybrid weld. Different studies have investigated the metallurgical effects that the combination of induction heating and laser welding has on several materials and sheet thicknesses [44; 48; 70; 78; 123].

Jahn et al [70] showed in Figure 2-39 that induction assisted laser beam welding offers two fundamental opportunities. The red continuous curve depicts the fast cooling rate of pure laser welding, while inductive pre-heating, post-weld heating or both gave an increase in the effective cooling time, which will reduce or prevent the formation of martensite.

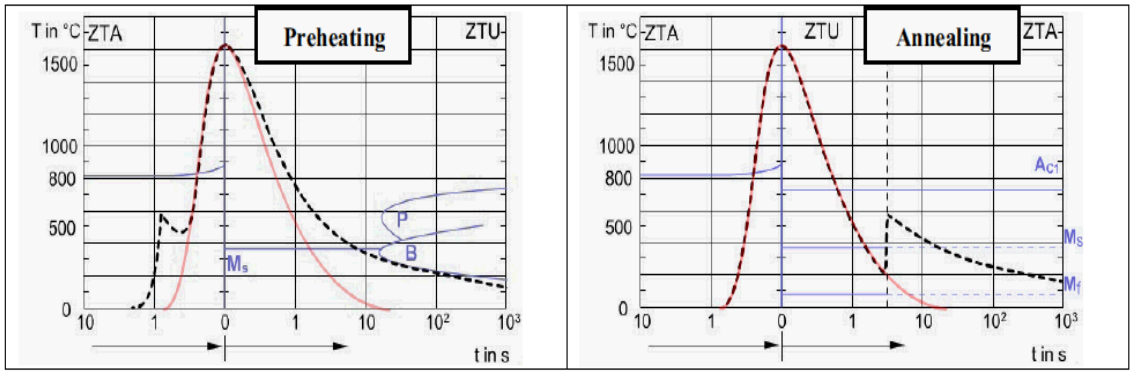

Figure 2-39: Schematic of time- temperature curve: LBW + preheating (left), LBW + annealing (right) [70]

The strategy adopted by Jahn et al [70] for crack free cooling of the weld seam during solidification in laser beam welding and inductive annealing processes shown in Figure 2-39 (right) was to establish the martensite start temperature M_S and thereafter start the short time inductive heating of the weld seam. The maximum induction heating temperature should be restricted to values below the austenite formation temperature A_{C1} in order to prevent additional microstructure transformation during inductive heating, and reduce the global heat input [70]. Figure 2-40 shows the weld microstructures of the welded joints with and without induction heating.

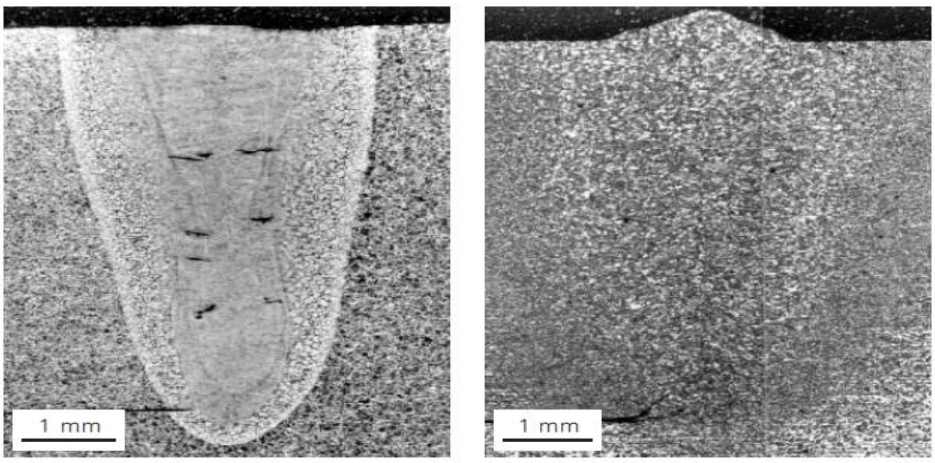

Figure 2-40: Laser weld joint without induction (left) and with induction (right) [45]

2.4.3.3 Application of Induction Heating

The induction heating system developed by EFD Induction AS, Norway was used for pre-heating in the Statoil Tampen Link project that connected the Statfjord field gas export line with the Shell UK export pipeline. This underlines the amazing versatility of induction heating when it was successfully used for the manual hot tap welding of a branch pipe on to a pressure gas pipe which is below 145 m depth in the North Sea. Induction heating was employed because it was the only feasible method to provide direct heating to the pipe without significantly heating the surrounding area. This technology was principally appropriate for subsea operations because of its compliance with safety regulations, and it was its first ever application in subsea operation [39]. The rapid cooling effect of the flowing gas in the pipe was balanced by the high heat input from the induction heating system thereby bringing the temperature to the required range before welding. Figure 2-41 shows induction coils connected to a test pipe before welding the connecting pipe.

Figure 2-41: Three induction coils on a test pipe (left) and welding the branch (right) [39]

Laser beam welding of a wide spectrum of steels is enhanced by induction heating. These steels include: case hardened, high carbon, cold worked tool steels as well as some select grades of cast iron. In combination with other techniques, induction assisted laser welding provides a new approach for the design and production of components [45].

Fraunhofer [44] reported a breakthrough in induction assisted laser welding of differential gear sets, which only some years back were mechanically assembled. Figure 2-42 shows the welded and bolted gear sets. The technology also finds application in induction assisted laser beam cladding, transformation hardening and surface re-melting. It offers advantages to these processes, which include among others: low dilution and crack free cladding of high carbon and alloyed steels, quick and economical case hardening of intricate parts and improved resistance against abrasive lubrication.

Induction assisted laser beam welding systems have also been used to weld high strength pipes with different success rates, depending on the pipe thickness and the steel grade [48].

Figure 2-42: Welded (right) and bolted (left) differential gear sets

The longitudinal welding by laser and/or plasma process of high grade pipeline steel up to 16 mm thick for energy transportation, otherwise known as the LAWPIPET programme is an initiative of the EU comprising companies, which include: steel manufacturers, pipe producers, pipe laying contractors, and universities. The overall objective of the programme was to produce high grade steel pipeline with high toughness and resistance to hydrogen cracking using an induction assisted laser welding process [73].

According to Gerardin et al [48], the programme was designed to use a high power laser source of up to 45 kW in association with a 600 kW induction heating source to weld heavy sections of different pipe grades such as X65HIC,

X70HIC, X70 and X80. Results from their study underscore the importance of defining the pre-heating temperature limits in induction assisted laser welding in order to enhance energy efficiency of the process and avoid introducing undesirable microstructural phases.

2.4.4 Summary

There have been few reported works regarding the application of lasers in underwater welding, which have been mostly in the nuclear power industry, while only two authors reported its application in a hyperbaric environment.

Several researchers have reported their work on laser arc hybrid welding processes, which involve the combination of a laser (primary heat source) and a secondary heat source in a common processing zone. These were mostly laser keyhole hybrid welding. There has been little mention of laser conduction hybrid welding in the literature. Induction assisted laser welding has been described as a laser hybrid welding process, which can be used to control the high cooling rate associated with laser welding

Induction heating power can be delivered for deep water application, but would require modifications to the current systems. In this study, the laser beam is mainly intended to assist the GMAW process by providing additional heat input to reduce the cooling rate of the weld metal. The laser beam is defocused to facilitate welding in conduction mode; hence the term laser assisted arc welding. This is a novel work and as a result information has not been found in the literature.

3 Thermal Cycle and Metallurgical Investigation in Dry Hyperbaric GMAW

Scope

The effect of ambient pressure on the arc, weld pool characteristics and resultant mechanical properties during hyperbaric welding has been reported. However, there are no reported works concerning the empirical determination of the influence of the hyperbaric chamber gas pressure on the weld pool cooling rate. Understanding the weld pool cooling rate is a critically important factor governing the resultant weld microstructure and mechanical properties.

This chapter investigates the weld pool thermal cycles and resulting metallurgical characteristics in hyperbaric GMAW at different pressures. The pressures vary from 1 bar to 200 bar, which represents 1 atmosphere to 2,000 metres of sea water depth. Single instrumented bead-on-pipe welds were performed on two different material thicknesses to evaluate the effect of conduction by the pipe material and convection by the chamber gas on weld metal cooling time. A cooling block calibration test was also performed in order to isolate the effect of the chamber gas on cooling time i.e. without the effect of the welding process. The weld pool thermal cycles and resulting cooling times were determined by embedding thermocouples in the steel sections. Microstructure analysis and micro hardness mapping were performed to understand the metallurgical phase formation. Possible experimental errors are discussed, followed by the presentation and discussion of results.

3.1 Aim and Objectives

The main focus of the research presented in this chapter is to understand the influence of the habitat or chamber gas pressure on the thermal cycle of the hyperbaric GMAW process. To achieve this, welding trials were performed at different pressures using the 250 bar hyperbaric chamber facilities at Cranfield University. The main objectives were as follows:

- To determine weld pool thermal cycles and cooling times at different argon gas pressures;
- To establish whether there is a relationship between the ambient chamber pressure and weld pool cooling time for the material thicknesses tested; and
- To use a cooling block calibration experiment to evaluate the influence of ambient argon gas pressure on convective heat loss; i.e. without the effect of the welding process.

3.2 Materials and Equipment

The materials used for this study are presented in this section. These include: pipeline steel, mild steel and welding consumables. The equipment used for the welding trials, weld instrumentation, cooling block calibration, and metallurgical characterisation (Macrostructure, microstructure and hardness tests) are also presented.

3.2.1 Materials

3.2.1.1 Steels

Two different grades of steel were used for this experiment. They are 25 mm thick sections of seamless X65 pipeline steel with specified minimum yield strength (SMYS) of 450 MPa and 5 mm thick sections of mild steel. The chemical compositions are given in Table 3-1.

3.2.1.2 Welding Wire

The welding wire used was metal-cored ESAB CoreWeld HBQ with a nominal diameter of 1.0 mm. This wire has been used in the recent hyperbaric research work performed at Cranfield. The as-deposited chemical composition is given in Table 3-2.

3.2.1.3 Chamber Gas

The chamber was filled with 99.99 % pure argon. No additional shielding gas was used.

Table 3-1: Chemical composition of steel grades

Material	OD/WT (mm)	Chemical analysis in wt. %														Carbon equivalent	
		C	Mn	Cr	Ni	Cu	V	Al	Mo	Si	S	P	B	Nb	Ti	CE_{IIW} [a]	P_{cm} [b]
X65	324/25.4	0.08	1.65	0.11	0.16	0.17	<0.004	0.03	0.08	0.22	<0.03	0.014	<0.0005	0.02	<0.01	0.45	0.18
Mild steel	-	0.08-0.13	0.03-0.50	-	-	-	-	-	-	trace	0.04	0.04	-	-	-	-	-

(a) $CE_{IIW} = C+(Mn+Si)/6+(Cr+Mo+V)/5+(Ni+Cu)/15$
(b) $P_{cm} = C+Si/30+Mn/20+Cu/20+Ni/60+Cr/20+Mo/15+V/10+5B$
(c) OD is outside diameter, and WT is wall thickness

Table 3-2: As-Deposited Welding Chemical Composition

Material	Chemical analysis in wt. %														
	C	Mn	Cr	Ni	Cu	V	Al	Mo	Si	S	P	B	Ti	O	N
ESAB CoreWeld HBQ (Ø1.0 mm)	0.07	1.32	0.03	0.50	<0.01	0.01	<0.01	0.02	0.42	0.01	0.01	<0.0005	0.01	0.036	0.004

3.2.2 Equipment

The equipment used for the hyperbaric welding trials is presented in this section.

3.2.2.1 Hyperbaric Chamber

The hyperbaric welding chamber is a 250 bar pressure chamber of 1.2 m^3 internal volume. It contains a three axis Cartesian manipulator for linear welds in all positions, or a four axis orbital head for welding in the 5 G position [117; 159]. It is equipped with pressurised water cooling system, fume extraction and clean gas re-circulation, shielding gas and all necessary electrical supplies [117]. A photograph of the chamber is shown in Figure 3-1.

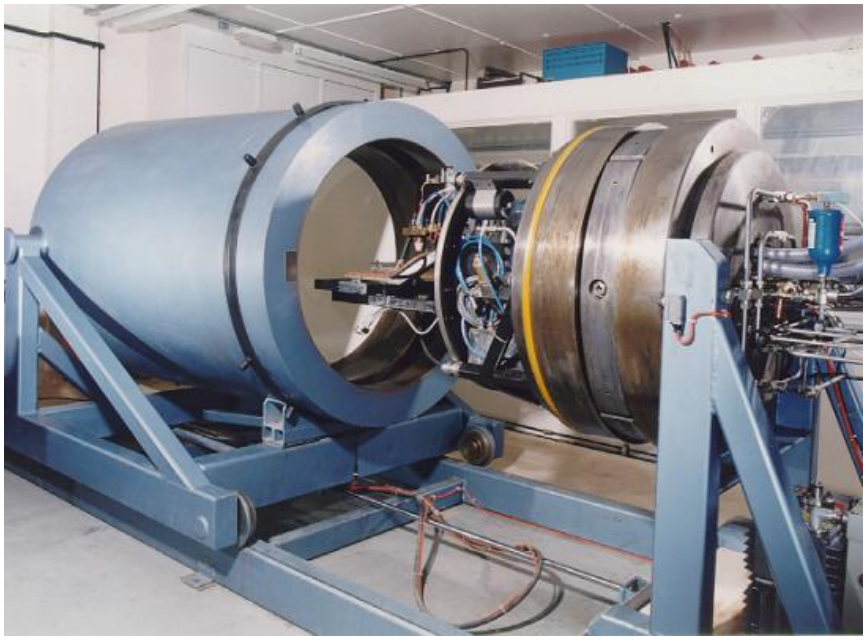

Figure 3-1: 250 bar hyperbaric chamber

3.2.2.2 Welding Power Source

The welding power source is a modified inverter power source comprising three units of Fronius Trans Pocket TP 450 connected in series to deliver up to 450 A and 200 V (Figure 3-2) [117]. To achieve optimum power source control, a

combined digital and analogue computer was used. The analogue system generates the output characteristic while the digital control provides the user interface and pulse generation capabilities. The output values were updated at a fixed frequency of 10 kHz [117]. Operation of the power source control is reported by Richardson et al [115] .

Figure 3-2: Fronius Trans Pocket TP 450 power sources in series

3.2.2.3 Welding Control System

The Weld Control System (WCS) was developed by Isotek, employing hardware and software similar to those used offshore for the THOR and PRS systems. It comprises a top station user interface and bottom station real time (VME based) computer. The system controls all the sequencing and welding parameters [117]. Figure 3-3 is a photograph of the control station showing the pressure and welding monitoring units.

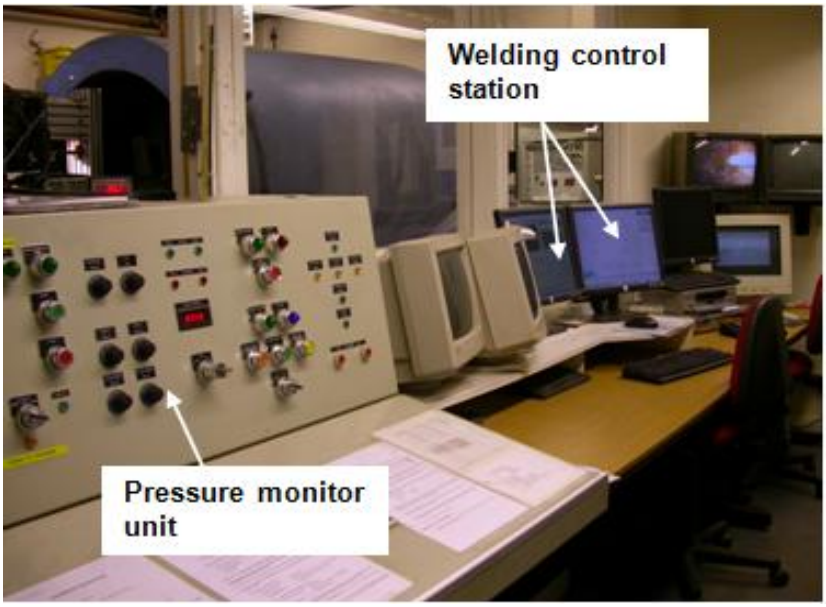

Figure 3-3: Control station

3.2.2.4 Weld Instrumentation

The instruments used for monitoring welding current, arc voltage and wire feed speed behaviour, and generating weld thermal cycles are presented in this section

3.2.2.4.1 Measurement of Welding Parameters and Thermal Cycle

A DL 750 Scopecorder, as shown in Figure 3-4, was used for the real time acquisition of transient welding current and arc voltage data, and wire feed speed. The instrument gives the flexibility of capturing data at a very high sampling rate of up to 50,000 samples per second. It consists of twelve channels that can be used to simultaneously measure the welding current, arc voltage, wire feed speed, and temperature using K and R-type thermocouples.

Probes were used for the welding current and arc voltage measurements. One end of the current probe was connected to the instrument and the other end clamped to the earth wire to measure the current. Similarly, a voltage probe was connected to the instrument and clamped around the welding plate to measure the voltage between the power source and the plate.

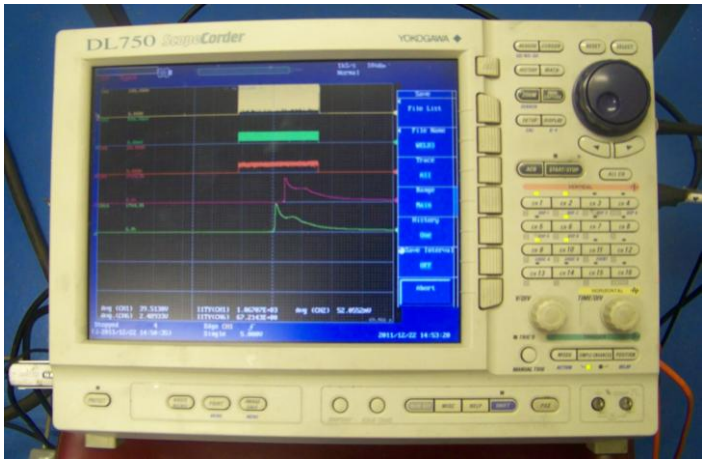

Figure 3-4: DL750 Scopecorder

R-type (Pt-13%Rh) and K-type (NiCr-Ni) thermocouples were used in this research to measure the temperature of the weld metal and the Heat Affected Zone (HAZ) respectively. The R-type can capture temperature up to 1600 °C while the K-type can measure up to 1370 °C [64]. One end of the R-type thermocouple was embedded inside the test piece to make contact with the melt pool, while the K-type was attached on the surface of the test piece. The other ends were connected to the Scopecorder, which logs the temperature and time during welding.

3.2.2.4.2 Capacitance Discharge Welder

A capacitance discharge welder SR-48 shown in Figure 3-5 was used to join the thermocouple tips. It was also used to attach the thermocouple to the test pieces.

Figure 3-5: Capacitance discharge welder

3.2.2.5 Characterisation

The instruments used for the metallurgical and mechanical characterisations are presented here.

3.2.2.5.1 Metallographic Examination

The welded samples were prepared for metallography using the Buehler Metaserv 2000 and Motopol automatic grinding machines. 120, 240, 1200 and 2500 grit papers were used for grinding, while 6 µm diamond paste and 0.05 µm colloidal silica were used for polishing. The etchants used were as follows:

- 10% nital (10% nitric acid in ethyl alcohol) for macrographs
- 2% nital (2% nitric acid in ethyl alcohol) for micrographs.

The samples were examined using an optical microscope.

3.2.2.5.2 Micro Hardness Measurement

The hardness testing machine used in this work is shown in Figure 3-6. It is an automatic hardness tester that uses a diamond indenter, and has two lenses of 10 and 40 times magnifications. It is equipped with a table that moves in the x, y and z directions.

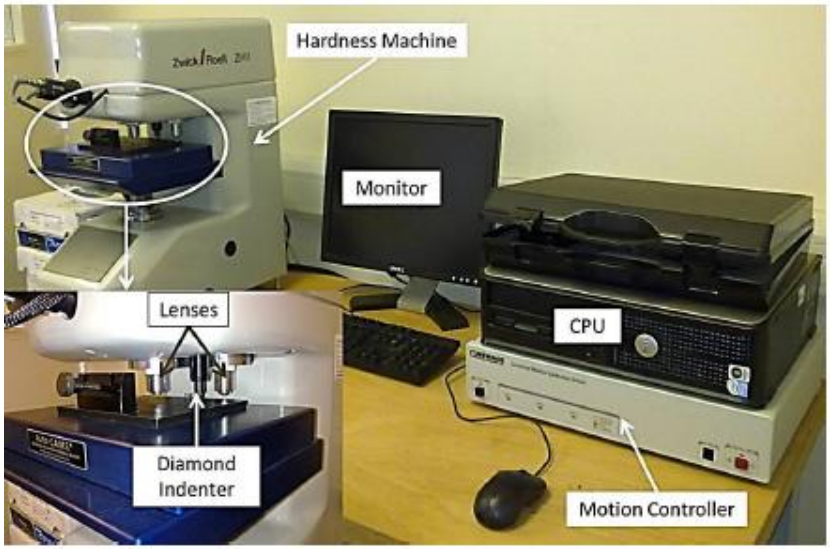

Figure 3-6: Zwick Roell micro hardness testing machine

The same set-up was used for weld instrumentation and metallurgical characterisation for all the experiments described in this thesis. Therefore, references will be made to them in subsequent chapters.

3.3 Experimental Methods

3.3.1 Welding Trials at Different Pressures

Woodward [157] conducted comprehensive studies on welding parameters at different pressure levels for both single pass and multi-pass welds using the 250 bar hyperbaric chamber. Pulsed and short circuit settings were reported in his work. This experiment employs the optimised parameters used in his report, and the values are given in Table B-1 of Appendix B.

Instrumented bead-on-pipe welding was performed on (240×60×25) mm section of X65 pipeline steel at different pressures inside the 250 bar pressure chamber. After evacuation, the chamber was pressurised with 100 % argon gas with no additional shielding gas. The thermal cycles at different locations of the pipe were determined with embedded R-type and attached K-type thermocouples. Four pressure levels of 1, 18, 100, and 200 bar were chosen to represent one atmosphere, shallow water, deep water and ultra-deep water conditions respectively. For 18 and 100 bar pressure, three welds were made at 5 mm/s, 6 mm/s and 7 mm/s welding speed with a constant wire feed speed (WFS) of 8 m/min. At 1 bar and 200 bar pressure, only one weld was made at 7 mm/s welding speed as this provided sufficient data to compare the thermal cycles at different levels of chamber pressure. A constant contact tip to work distance (CTWD) of 11 mm was used.

Welding trials were also performed under identical conditions using the same parameters on thinner material to further investigate the effect of gas pressure upon weld metal cooling rate. These were instrumented bead-on-plate welding on a thinner section (240×60×5) mm of mild steel.

Pipeline steels selected for deep water applications are comparatively high wall thickness X65 steel because of the need for high collapse strength especially when not pressurised. This informed the choice of this material for the welding trials. Welding trials on thin plate were performed to investigate the influence of material thickness on weld metal cooling rate behaviour with respect to ambient

pressure. Figure 3-7 and Figure 3-8 show the completed welds on both materials.

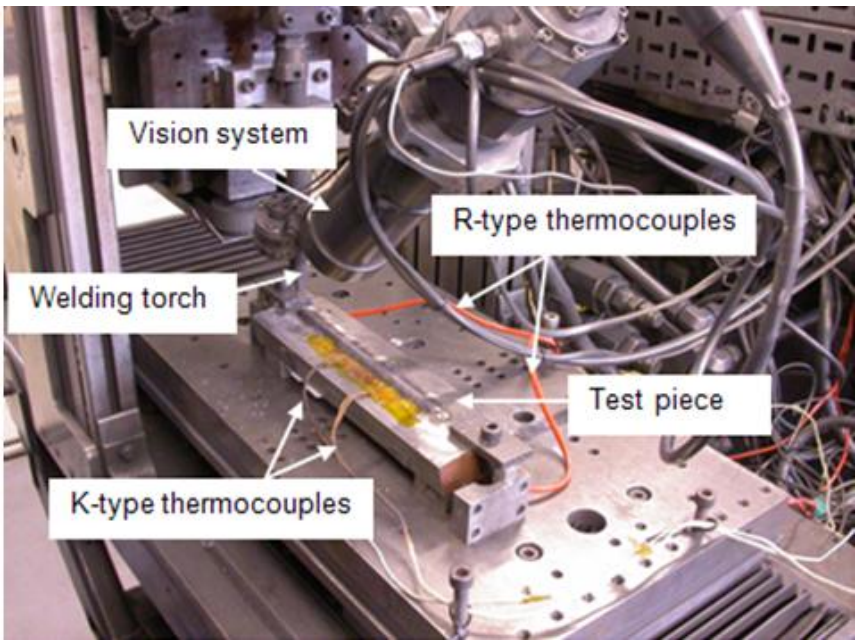

Figure 3-7: Photograph of completed weld on a 25 mm thick X65 pipeline steel

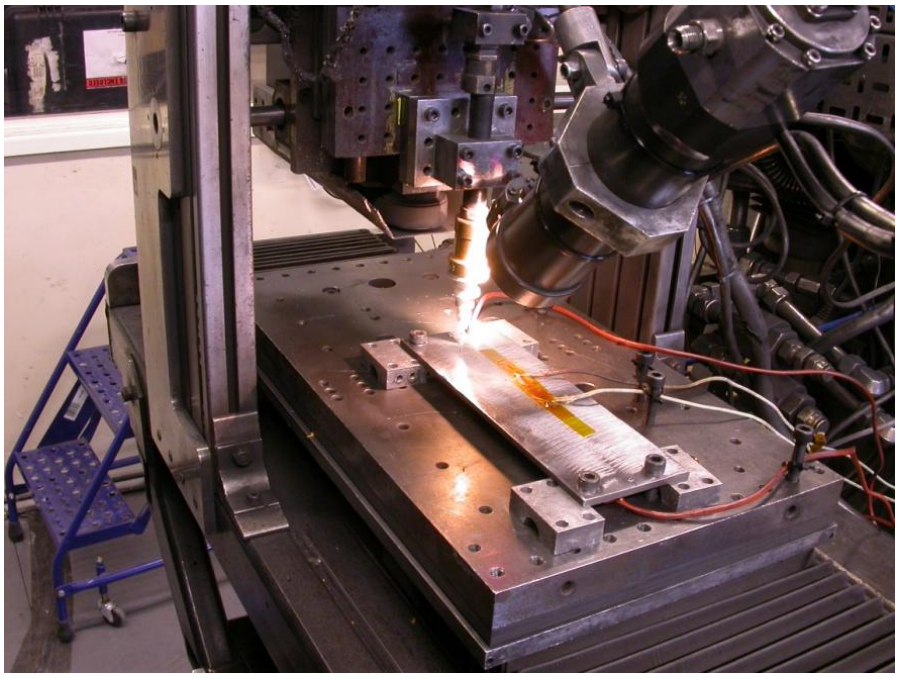

Figure 3-8: Photograph of completed weld on a 5 mm thick mild steel section

3.3.2 Cooling Block Calibration

A (198×81×25) mm X65 steel block was heated up to a temperature of approximately 100 °C using a resistance heating mat as shown in Figure 3-9. The steel block was insulated from the manipulator stage of the hyperbaric chamber and allowed to cool down to ambient chamber temperature at different pressures ranging from 1 bar, 18 bar, 37 bar, 100 bar to 150 bar. The ambient temperature was typically between 19 and 20 °C for all the tests. Three K-type thermocouples were attached to the surface of the steel block and were used to generate cooling curves at each pressure level. The average time for the block to cool from the peak temperature to ambient chamber temperature was measured at each pressure level. This experiment was performed to investigate the influence of pressure on convective heat loss to the chamber gas. It was assumed that the heat loss was mainly by convection in the absence of heat transfer by conduction in the material (i.e. without welding).

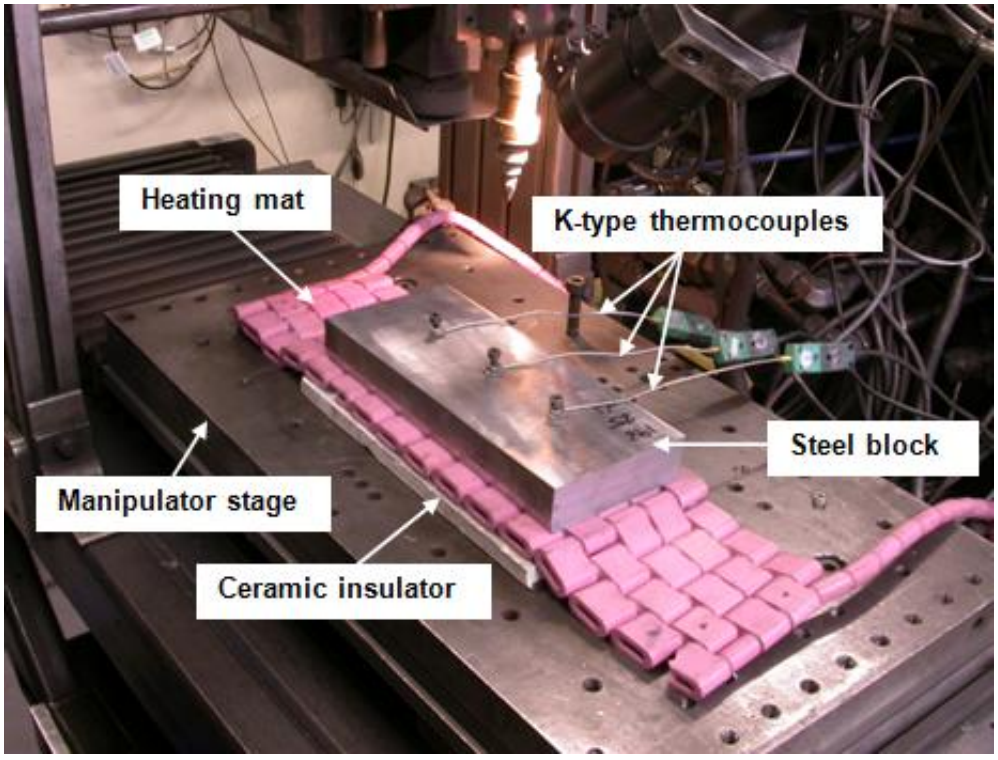

Figure 3-9: Set up for cooling block calibration

3.3.3 Generation of Weld Thermal Cycle

The depths of the embedded thermocouples in section 3.3.1 were 24.5 mm and 4.5 mm for the thick and thin plates respectively. This placed the R-type thermocouples inside the weld pool in order to measure the actual weld pool thermal cycle as shown in Figure 3-10. Also, two K-type thermocouples were attached 5 mm and 10 mm away from the weld centre line as shown in Figure 3-7 and Figure 3-8. The thermocouples were used to measure the weld thermal cycles.

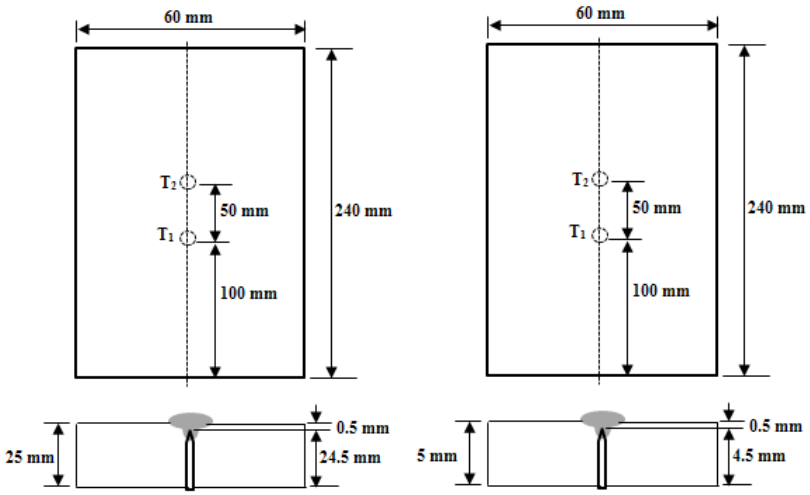

Figure 3-10: Arrangement of the R-type thermocouples inside the test piece (Left) 25 mm and (right) 5 mm plate.

3.3.4 Measurement of Heat Input and Cooling Time

The measurements of instantaneous welding current and arc voltage were used to calculate the weld heat input according to equation (3-1).

$$Q = \eta . \frac{\int_0^t (V.I)\, dt / \Delta t}{v}, \qquad (3\text{-}1)$$

where Q is the heat input based on average instantaneous power input; V and I are instantaneous arc voltage and welding current, while v is the welding speed. The arc efficiency η used was 0.8 [74].

The approximate cooling time from 800 °C to 500 °C $(\Delta t_{8/5})$ was determined from the weld thermal cycle.

3.3.5 Macrostructure and Microstructure Examination

The weld joints were sectioned, ground and polished according to standard metallographic procedures as described in section 3.2.2.5.1 to show the geometry of the weld metal and HAZ. The polished samples were then etched with 2% nital solution before macrographs were taken using an optical microscope to show the weld bead profile. Examination was carried out on the samples to reveal the microstructures of the weld metal and HAZ.

3.3.6 Hardness Test

Vickers micro hardness traverse mapping was performed on the cross section of the etched samples using the set up shown in Figure 3-6 of section 3.2.2.5.2.The test was carried out in compliance with BS EN ISO 6507-1: 2005 [22]. Ten traverses of fifty indentations each were made horizontally across the weld using a 500 g traverse load from the left side of the base metal (BM), across the HAZ and weld metal (WM) to the other side of the base metal (Figure 3-11). To ensure effective mapping of the hardness distribution, the distance between each traverse was 0.4 mm while that between each indentation was 0.3 mm. A hardness contour map was produced with the aid of a Matlab code.

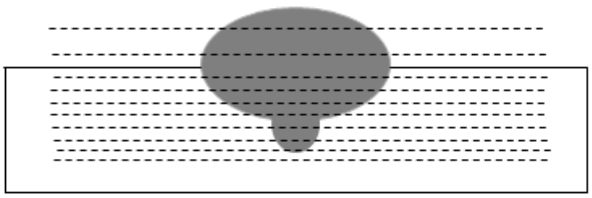

Figure 3-11: Schematic illustration of hardness measurement

3.4 Experimental Error

An experimental result is contentious if nothing is known about the likely size of its error. Therefore, to generate confidence in the experimental data and results presented here, it is vital to identify and describe possible experimental errors. The potential sources of the experimental errors in this research work are presented here.

There is a possibility of operator errors and system errors in this research. To avoid the likelihood of the latter, the welding power source, hyperbaric chamber and measurement instruments were calibrated (the power source calibration is given in Appendix B). However, the most likely source of significant error is the thermocouple position. This is because the thermocouple holes were drilled manually. It is possible that there could have been deviations from the set position, and that the depth of the holes was not fully repeatable. The positions of thermocouples attached to the test piece surface were measured with a metre rule. This could have introduced parallax errors that affect accurate measurement of the positions.

There is also the possibility that the weld cooling times measured from the data obtained with these thermocouples might be affected by the holes drilled to attach the thermocouples inside the melt pool. This is because the holes will create separation within the bulk material, which could affect heat transfer through conduction. However, the chances of such errors are minimised since the holes were only 3 mm in diameter and well separated from each other.

A measure of the uncertainty in computation of the cooling time was determined by welding with thermocouples placed inside holes drilled to 24.5 mm from the material surface as shown in Figure 3-10. Welds were made on four different test pieces with the same welding parameters. Another weld was made on a test piece with five thermocouples attached at different positions on the weld centre line. This was done to ascertain errors due to positional variability. The cooling time between 800 °C to 500 °C is given in Table 3-3.

Table 3-3: Data of Cooling Time

Test No	t_{800} (s)	t_{500} (s)	Cooling time $\Delta t_{8/5}$ (s)
TC_1	55.11	58.88	3.77
TC_2	55.46	58.38	3.37
TC_3	61.12	65.06	3.94
TC_4	60.24	64.40	4.16
TC_5	31.14	34.76	3.62
TC_6	41.69	45.54	3.85
TC_7	48.61	52.64	4.03
TC_8	49.55	53.32	3.77
TC_9	42.38	46.05	3.67

The standard error of the mean SE_X of the cooling time was used to estimate the experimental error, and is given by:

$$SE_{\bar{X}} = {}^{s}/_{\sqrt{n}}\,, \tag{3-2}$$

where s is the sample standard deviation, and n is the number of tests

Therefore, the estimated absolute error of the cooling time is given:

$$\text{Cooling time} = \Delta t_{8/5} \pm 0.08\,(\text{s}) \tag{3-3}$$

Errors during the hardness measurements may have originated from the sample size and the sample holding device. The indenter motion is usually interrupted when the sample holding clamps are close to it. However, steps were taken to avoid this situation.

3.5 Results

Results from the experiments conducted in this research are presented in this section, with their interpretations. The discussion of the results will follow in the next section.

3.5.1 Current and Voltage Waveforms

The current and voltage waveforms of the welding process for all four pressure levels investigated are shown in Figure 3-12. These show that the current peaks increases with pressure. As the short circuit happens voltage drops and current rises to the peak value, and at higher pressure the short circuiting frequency increases. These indicate that at higher pressure the waveforms are oscillating more severely. Despite these fluctuations the average instantaneous power did not change with pressure and as a result the heat input remained relatively constant.

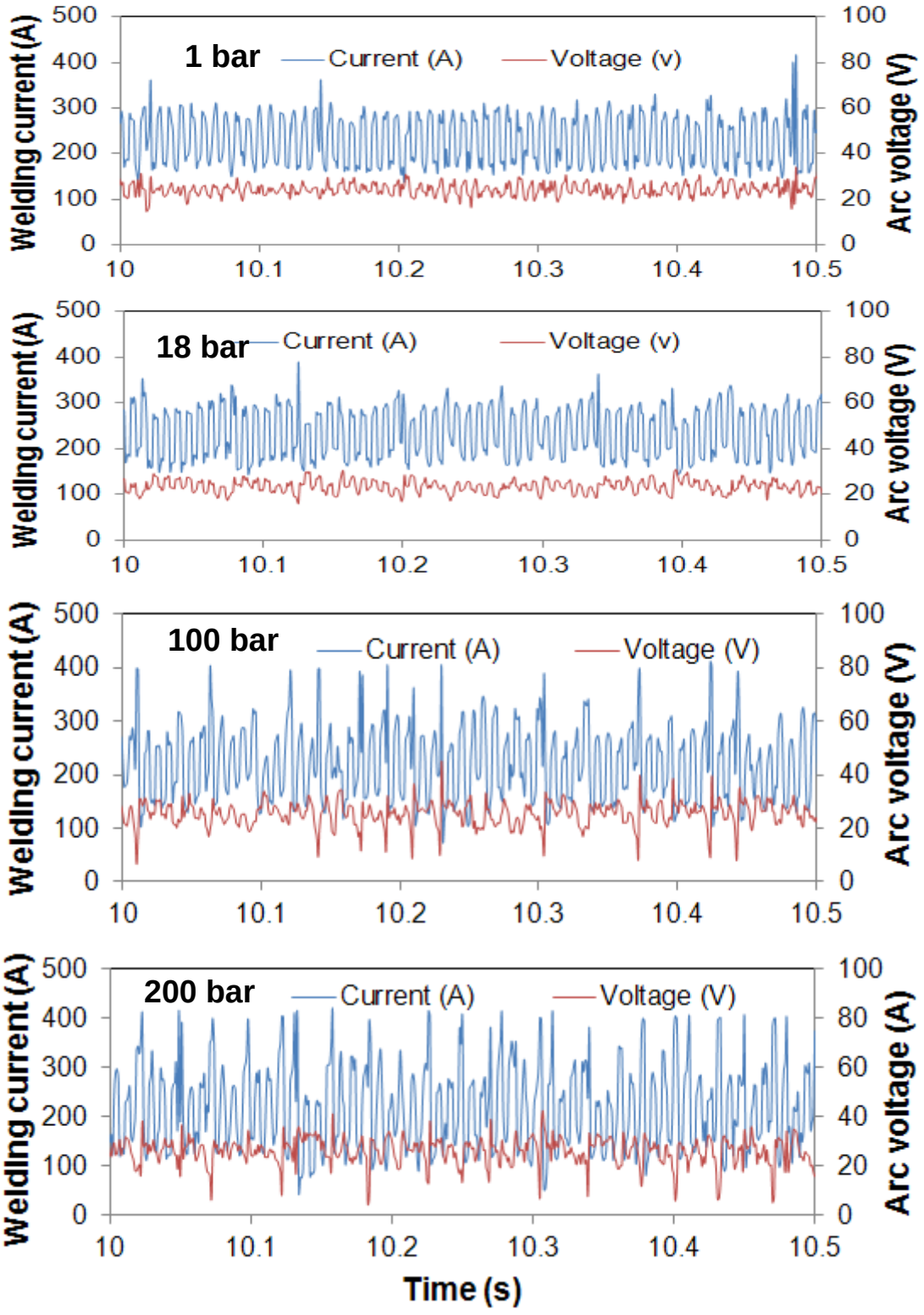

Figure 3-12: Transient behaviour of current and voltage at different pressures for welds made with 8 m/min WFS and 7 mm/s welding speed

3.5.2 Thermal Cycles

3.5.2.1 Weld Thermal Cycles of Different Steel Thickness

Figure 3-13 to 3-15 represent the thermal cycles of welds made at the different pressure levels investigated. A direct comparison of the weld metal cooling behaviour between the 25 mm and 5 mm plate thickness is shown in Figure 3-13. This indicates that the thicker plate cools much faster than the thinner one under identical welding settings. It can also be seen that higher pressure did not have a significant influence upon the weld metal cooling rate for the 25 mm steel thickness. The influence of pressure was significantly more pronounced for the 5 mm plate thickness.

The thermal cycles measured on the surface of the test pieces as represented in Figure 3-14 and Figure 3-15 are further evidence that the influence of pressure on the cooling behaviour depends on the material thickness as described above.

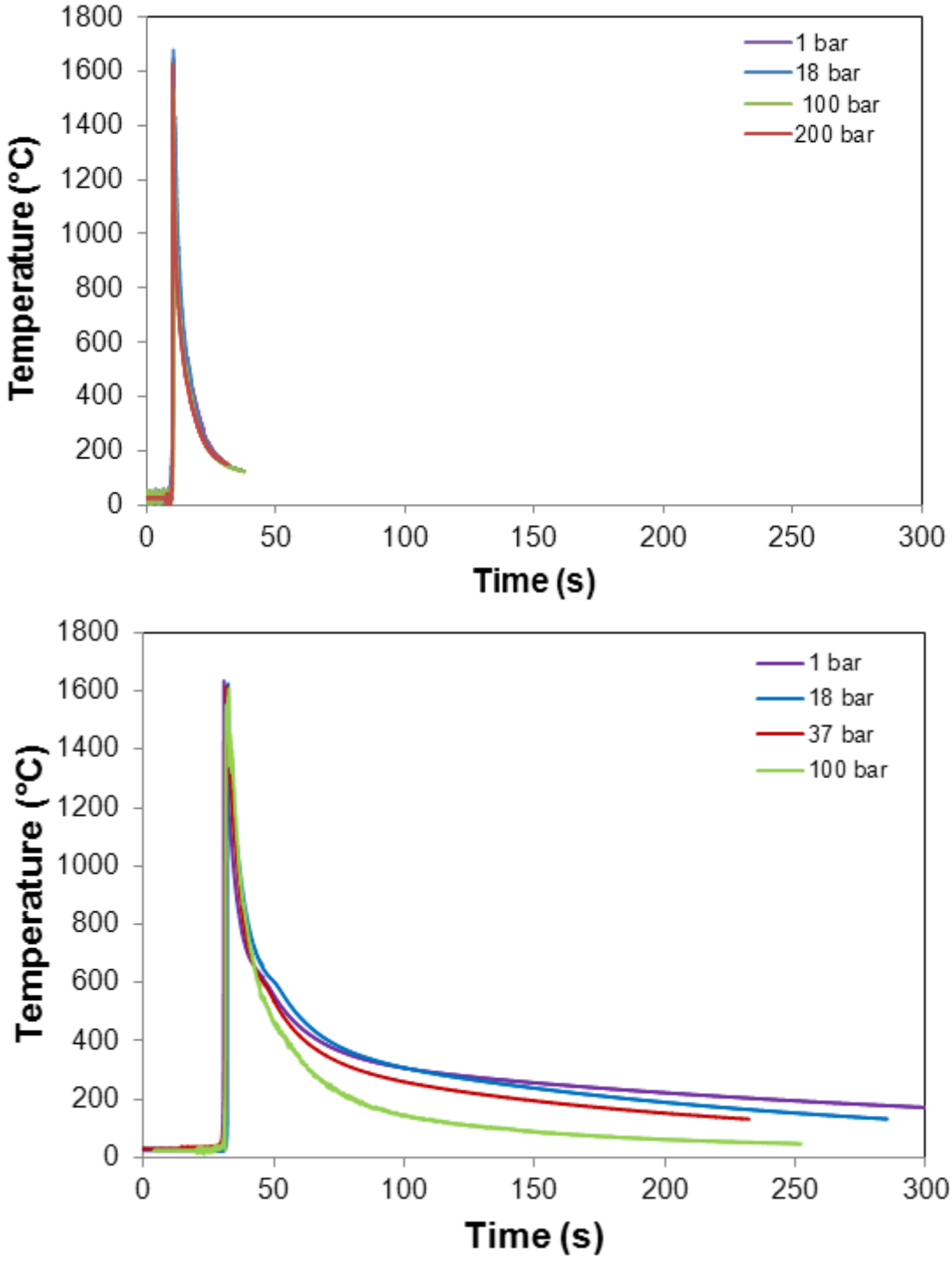

Figure 3-13: Thermal cycles measured with R-type thermocouples for 8 m/min WFS and 7 mm/s welding speed (top) 25 mm thick X65 steel (bottom) 5 mm thick mild steel

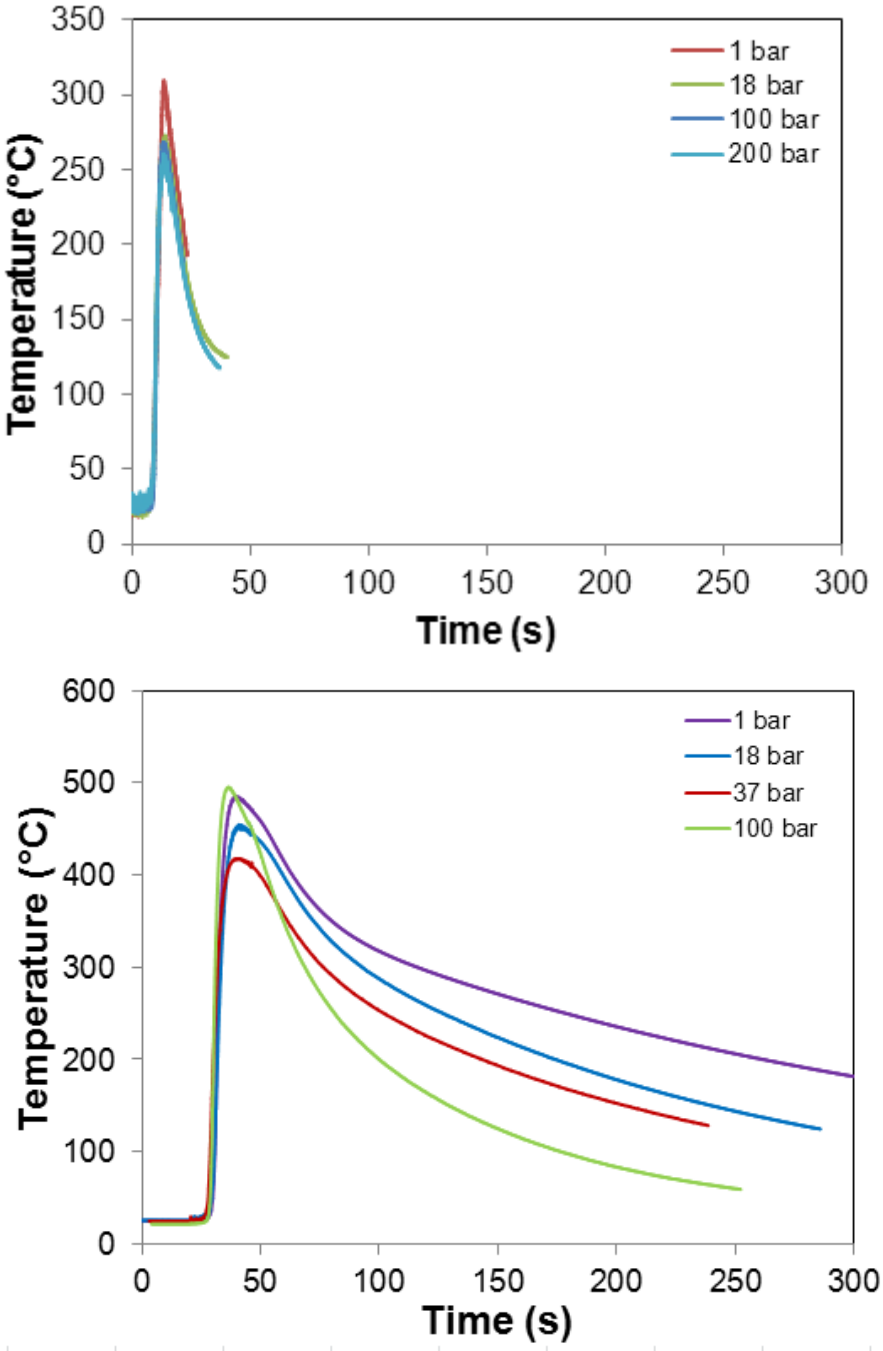

Figure 3-14: Thermal cycles measured with K-type thermocouples for 8 m/min WFS and 7 mm/s welding speed (top) 10 mm from weld centre line on 25 mm thick plate (bottom) 10 mm from weld centre line for 5 mm thick plate

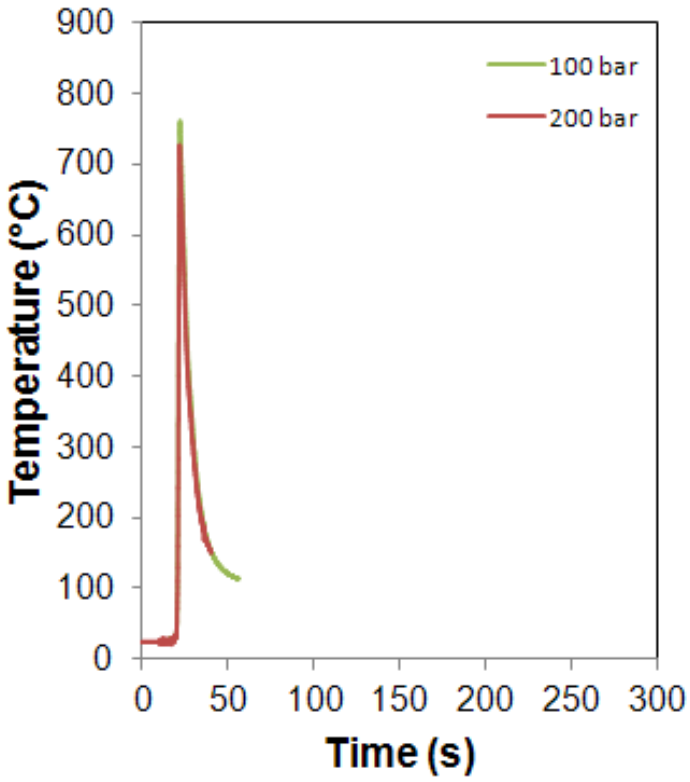

Figure 3-15: Thermal cycles measured with K-type thermocouples for 8 m/min WFS and 7 mm/s welding speed: 5 mm from weld centre line for 25 mm thick plate

3.5.2.2 Cooling Calibration

The cooling curves for the heated steel block which was allowed to cool down to ambient chamber temperature under different chamber gas pressures is shown in Figure 3-16. The plot gives an indication of the correlation between pressure and convective heat transfer since the mode of heat loss by the material to the argon environment was via convection. It is clearly shown that the higher the pressure the faster the material cools at these temperatures (80 to 35 °C)

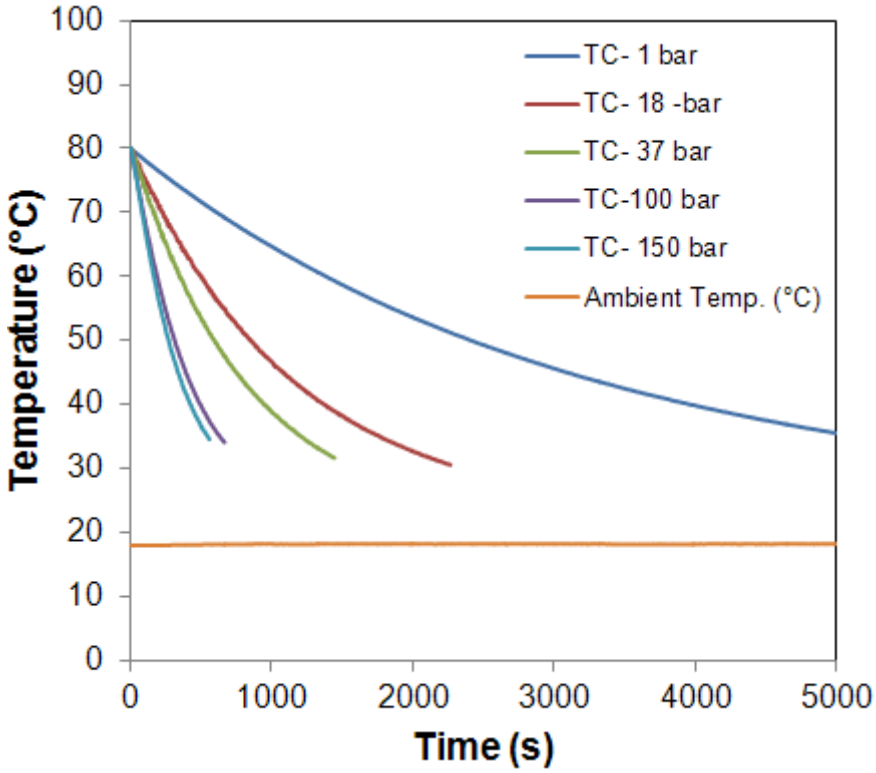

Figure 3-16: Cooling curves of heated steel block under different pressures

This is evident from the cooling times derived from the curves at the investigated pressures. The cooling time was calculated for the temperature range of 80 °C and 35 °C and its relationship with pressure is given in Figure 3-17. The plot shows that as pressure increases the cooling time decreases, indicating that convective heat loss increases with pressure. It can also be seen that the cooling time is significantly longer at 1 bar, and decreases progressively with pressure up to 150 bar.

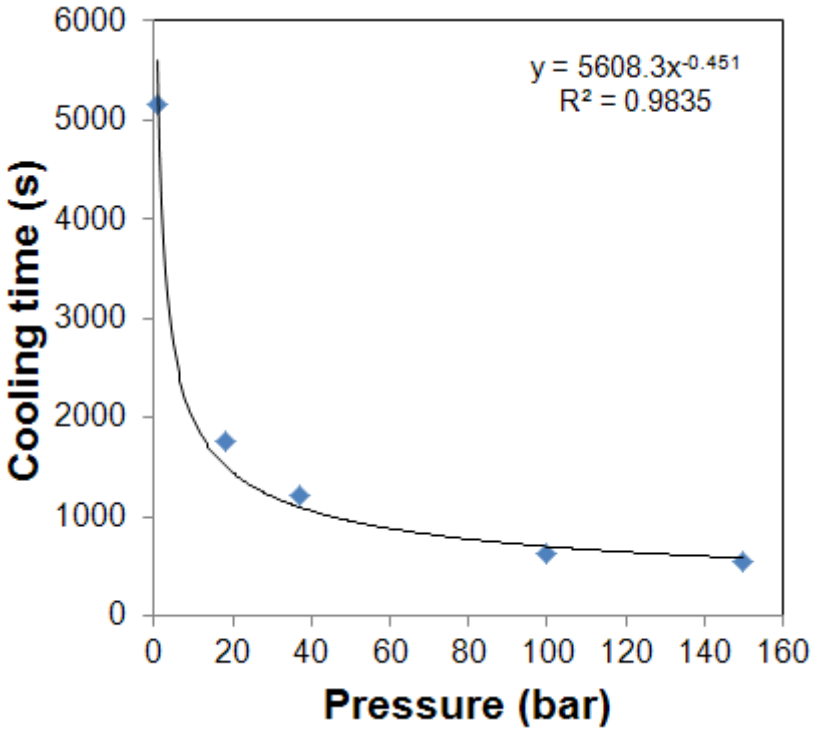

Figure 3-17: Effect of pressure on cooling time

3.5.3 Heat Input and Cooling Time

The computed weld cooling times between the temperature ranges of 800 °C to 500 °C and 800 °C to 200 °C are given in Table 3-4 for both material thicknesses. Plots that show the relationship between pressure and cooling time for both temperature ranges are shown in Figure 3-18. It was described in the previous section that heat input did not change with pressure because the average instantaneous power was comparatively constant irrespective of pressure. The values averaged 0.64 kJ/mm for all of the welds performed with 8 m/min WFS and 7 mm/s welding speed as shown in Table 3-5.

Figure 3-18 shows that pressure has little significant effect on the cooling time for the 25 mm material, while it has an exponential relationship with cooling time for the thin 5 mm steel section. The figure also shows that the cooling time between 800 °C to 200 °C is much longer than 800 °C to 500 °C. For the 5 mm material thickness, the cooling time is shown to significantly decrease as

pressure increases. This shows the dominant influence of material thickness with regards to weld cooling time versus pressure.

Table 3-4: Weld cooling times for 8 m/min WFS and 7 mm/s welding speed

Pressure (bar)	25 mm thick plate		5 mm thick plate	
	Cooling time (s)		Cooling time (s)	
	$t_{8/5}$	$t_{8/2}$	$t_{8/5}$	$t_{8/2}$
1	3.36	12.62	18.21	202
18	3.30	12.48	17.16	147
37	*	*	13.94	106
100	2.95	11.03	8.77	41
200	2.80	11.01	*	*

Table 3-5: Average power consumption of the welds at different pressures

Pressure (bar)	Average current (A)	Average voltage (V)	Average Instantaneous power (W)	Heat Input (kJ/mm)
1	227	25	5569	0.644
18	237	24	5544	0.641
100	223	25	5627	0.643
200	221	26	5595	0.639

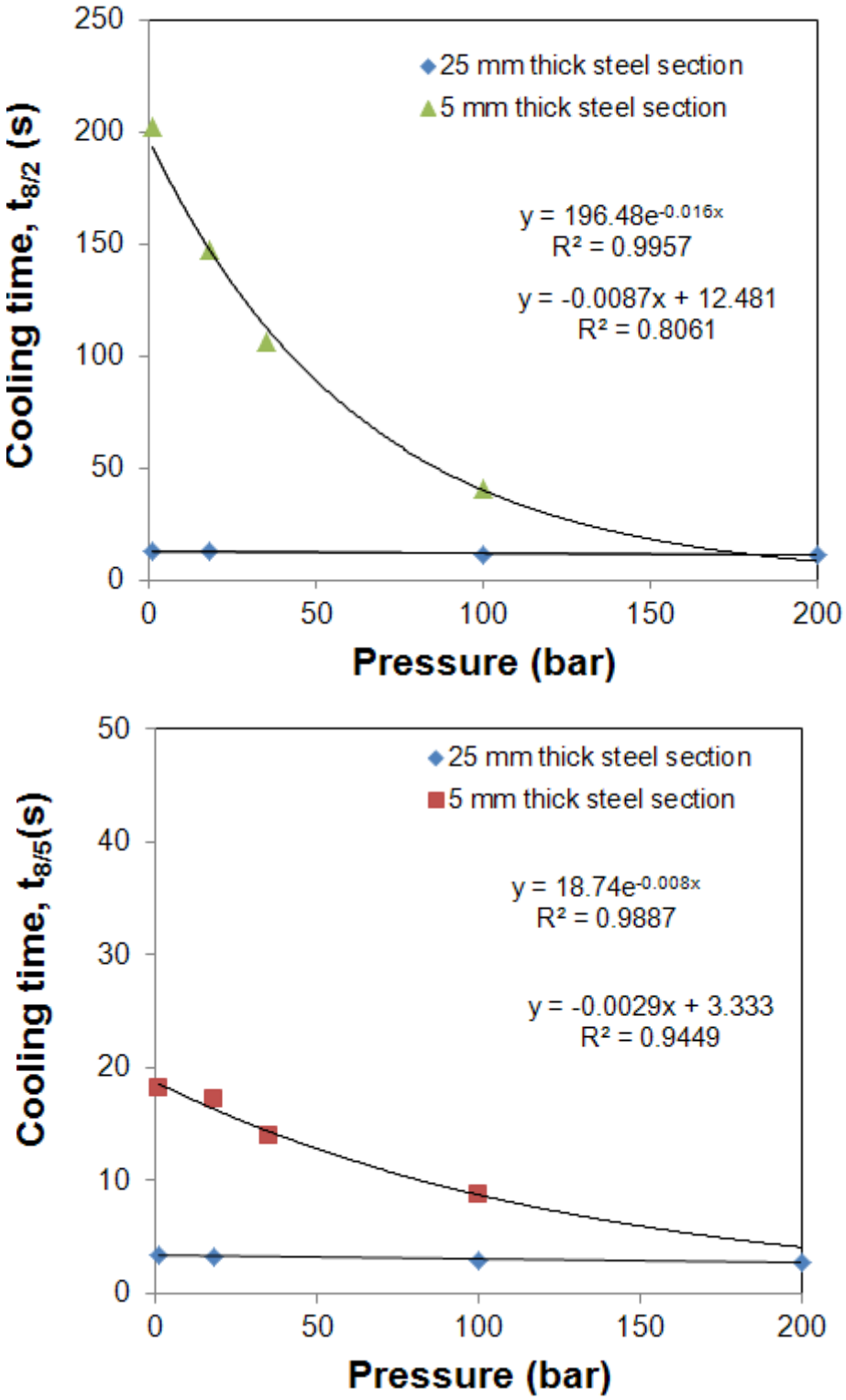

Figure 3-18: Effect of pressure on cooling time for both material thicknesses (top) between 800 °C and 200 °C and (bottom) between 800 °C and 500 °C

3.5.4 Macrostructure and Microstructure Examination

3.5.4.1 Macrostructure

Figure 3-19 shows macrographs of welds at different pressures, while Figure 3-20 represents bead profiles of the same welds for the 25 mm thick material. It can be seen that the weld penetration depth increases as pressure rises while the weld width reduces. Also the area of the re-melted material referred to here as penetration area is shown to increase with pressure due to higher weld penetration, particularly between 1 and 18 bar. However, deposit area or bead reinforcement area remains relatively the same since the same wire feed speed and welding speed was used for all the welds.

This shows that for the same welding settings, ambient pressure plays a significant role in defining the weld bead geometry, particularly in the 1 to 18bar range.

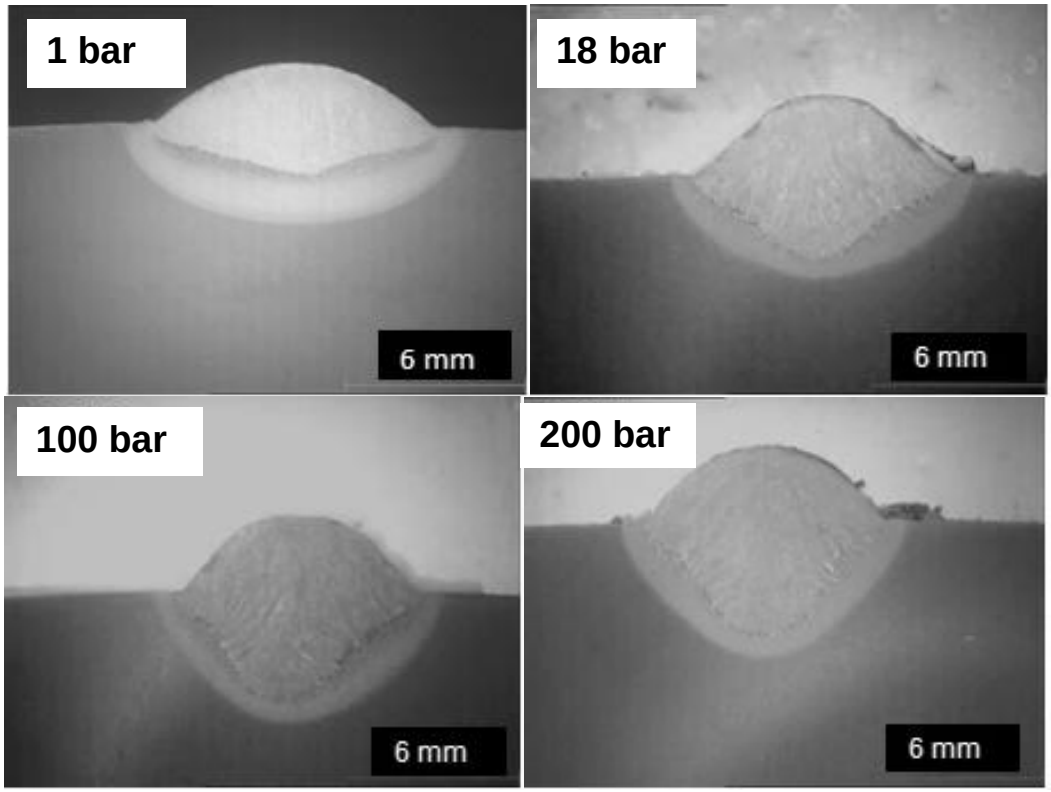

Figure 3-19: Macrographs of welds made with 8 m/min WFS and 7 mm/s welding speed for the 25 mm plate thickness

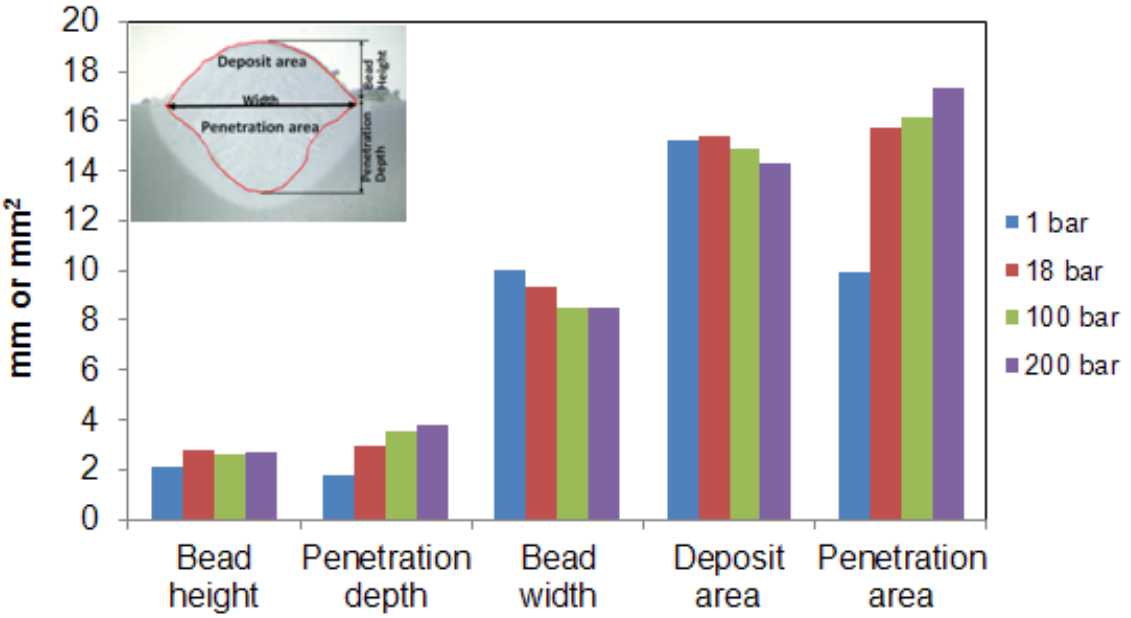

Figure 3-20: Weld bead profile of welds made with 8 m/min WFS and 7 mm/s welding speed for the 25 mm plate thickness

3.5.4.2 Microstructure

Micrographs showing the microstructures of the weld metal in the penetration area and the HAZ close to the fusion boundary for welds made at 8 m/min WFS and 7 mm/s welding speed are given in Figure 3-21 to Figure 3-23. It can be observed that the microstructures of the weld penetration area look highly comparable for the 18 to 200 bar welds with a distribution of fine ferrite structures. The microstructure of the 1 bar weld has more pronounced grain boundary ferrite structures.

The HAZ microstructures were quite similar for the 18 to 200 bar welds. The region closest to the fusion boundary is the coarse-grained supercritical zone. It consists of relatively larger grains compared to the other regions of the HAZ, which are not shown on the microstructures.

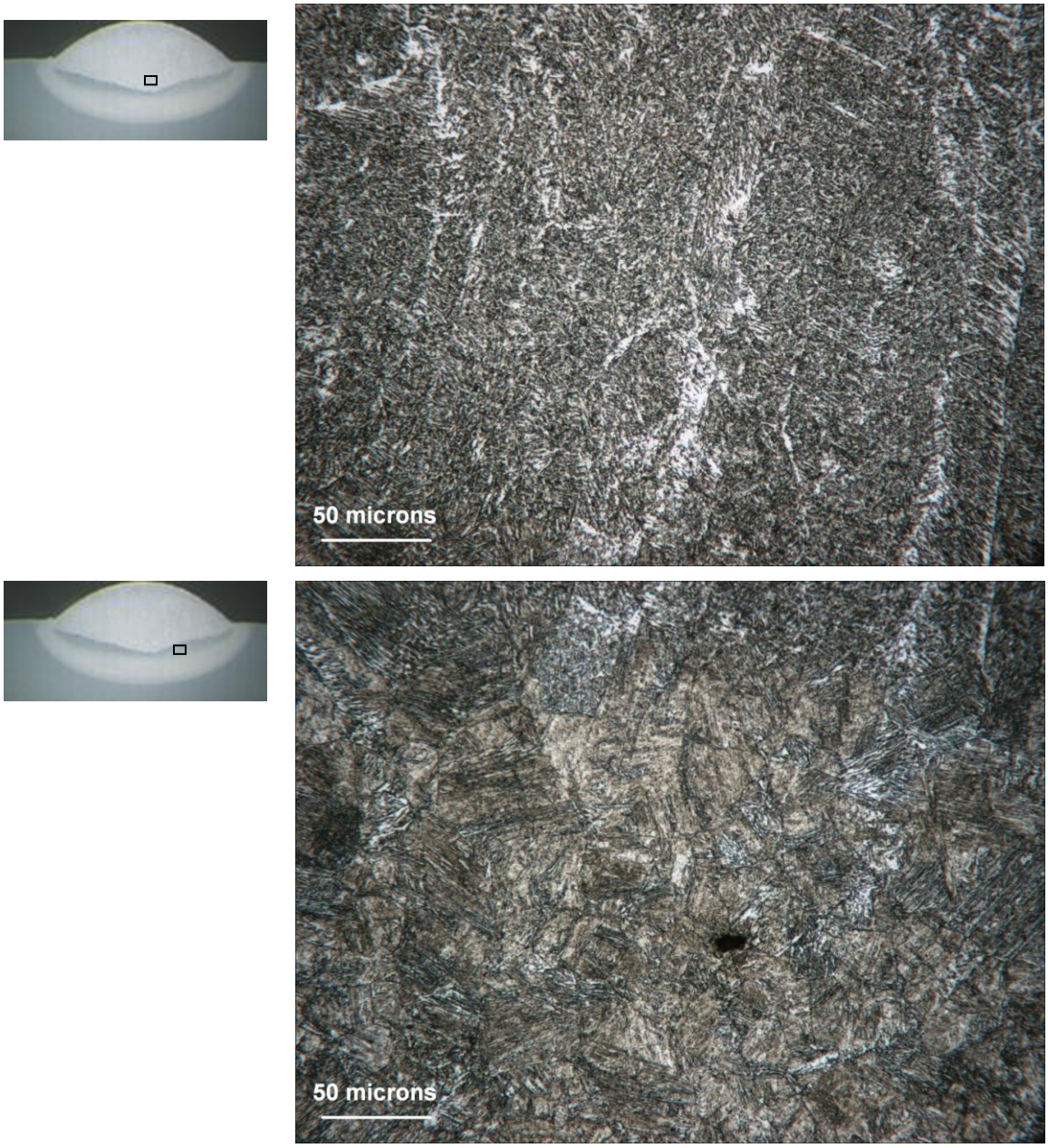

Figure 3-21: Microstructures of (top) penetration area and (bottom) heat affected zone from sections marked on the macrographs (insert) for the weld made at 1 bar with 8 m/min WFS and 7 mm/s welding speed

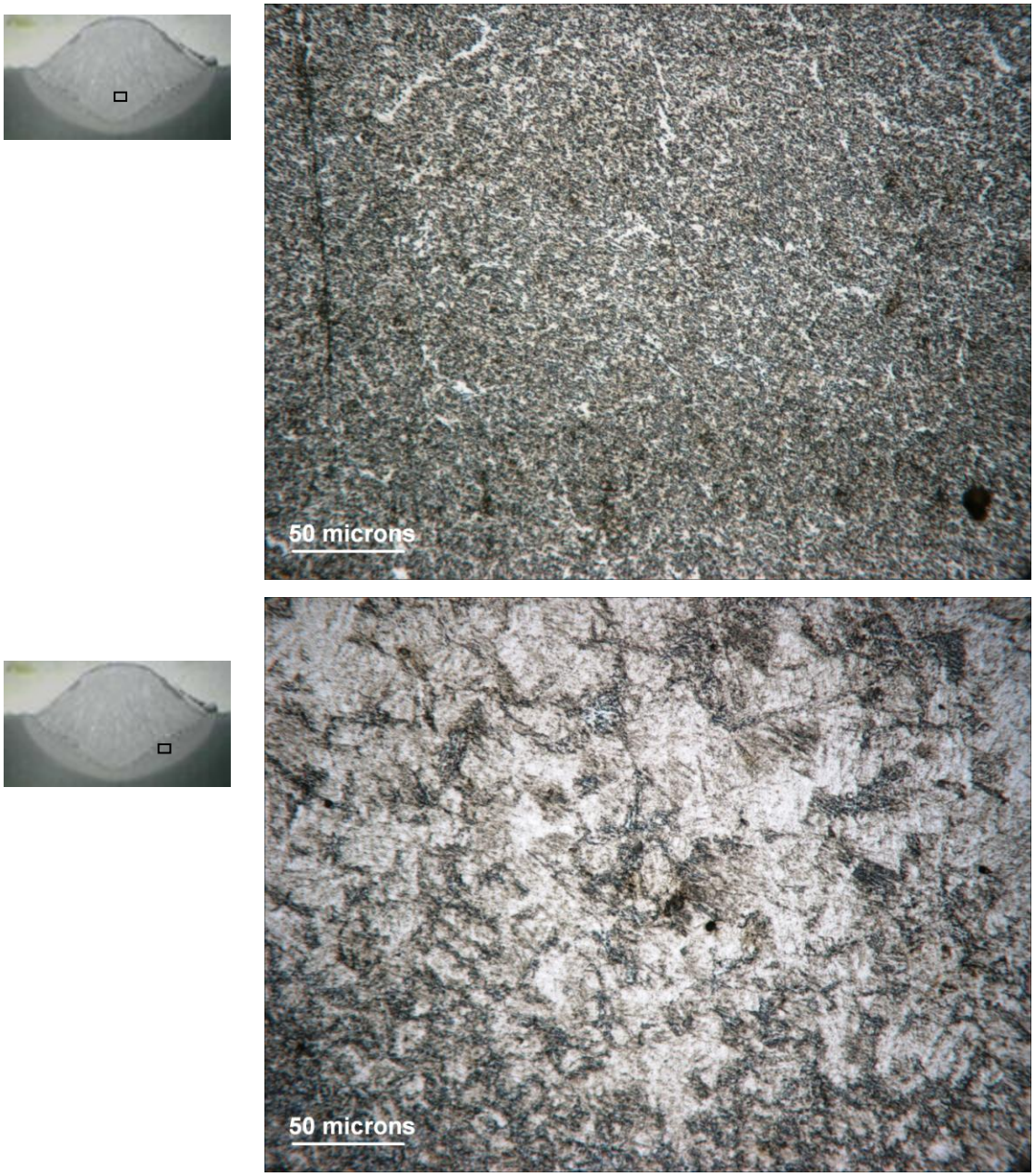

Figure 3-22:Microstructures of (top) penetration area and (bottom) heat affected zone from sections marked on the macrographs (insert) for the weld made at 18 bar with 8 m/min WFS and 7 mm/s welding speed

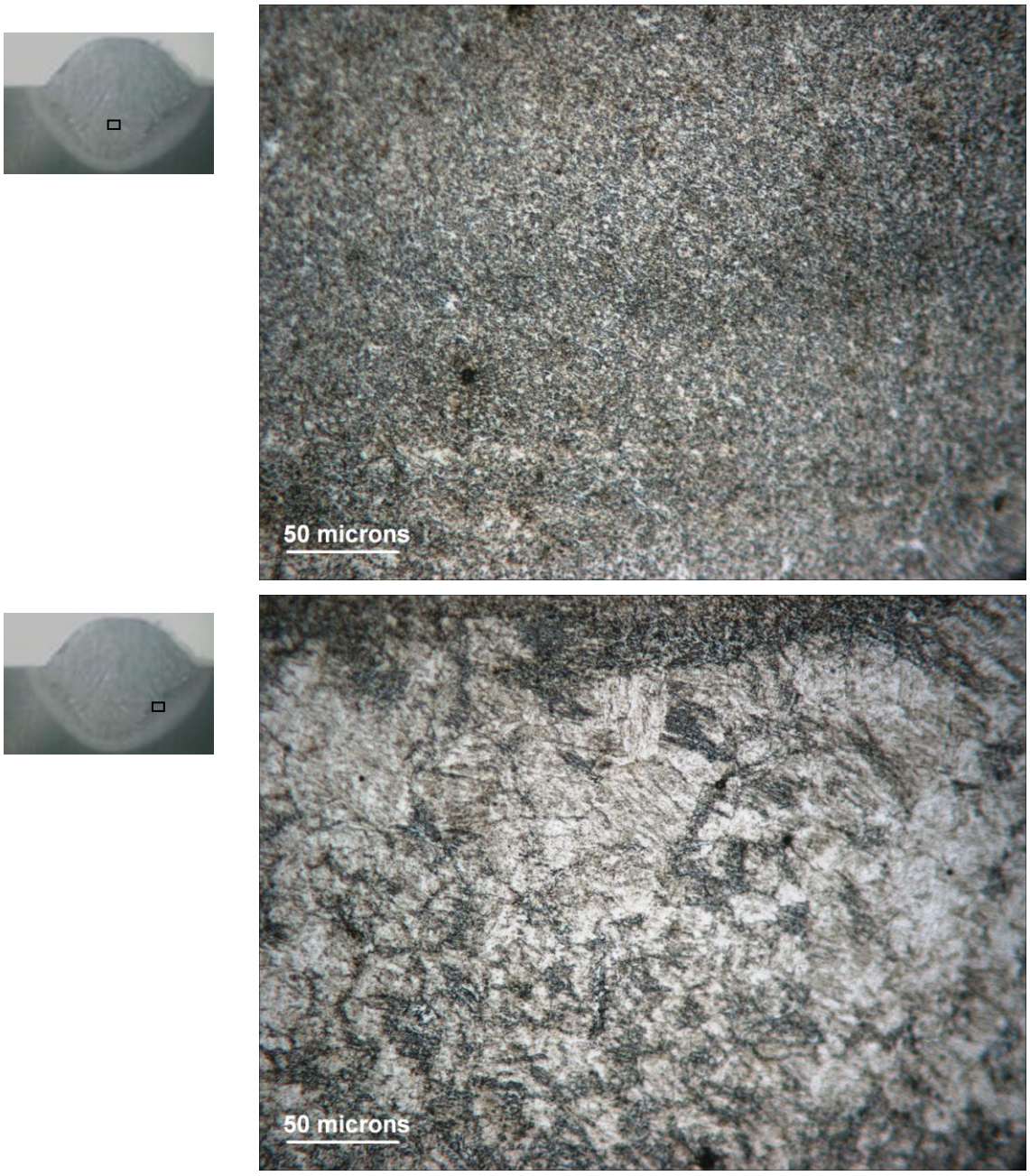

Figure 3-23:Microstructures of (top) penetration area and (bottom) heat affected zone from sections marked on the macrographs (insert) for the weld made at 100 bar with 8 m/min WFS and 7 mm/s welding speed

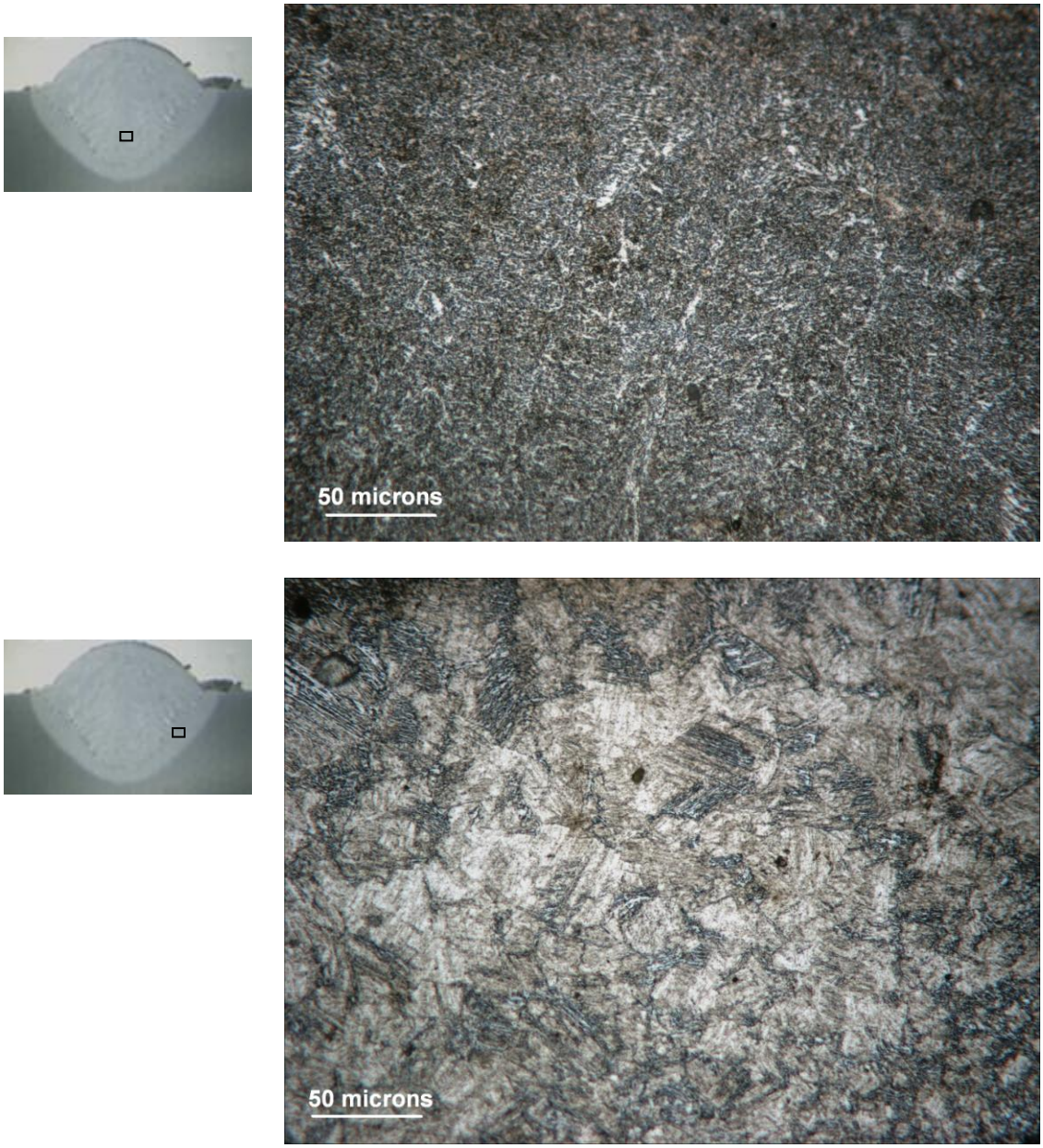

Figure 3-24: :Microstructures of (top) penetration area and (bottom) heat affected zone from sections marked on the macrographs (insert) for the weld made at 200 bar with 8 m/min WFS and 7 mm/s welding speed

3.5.5 Hardness Test

Figure 3-25 and Figure 3-26 show the Vickers micro hardness measurement ($HV_{0.5}$) of the welds from the macrographs shown in Figure 3-19. It can be seen that the hardness distribution follows a similar pattern for all the welds. This shows the hardness of the weld metal (region having a mixture of green and yellow colours), HAZ region (band of red, yellow and light blue), and the parent metal (dark blue). The deep red colour indicates the highest peak hardness values > 370 HV. This is followed by light red colour showing values from about 330 to 370 HV. The mixture of green and yellow colours gives the approximate hardness values from 260 to 330 HV, while lower hardness values are represented by the deep blue and light blue colours.

In all cases, the maximum hardness occurs in the coarse grained HAZ, which is closest to the fusion boundary. However, there is a progression of hardness across the HAZ region with the lowest value in the subcritical HAZ (region just before the dark blue colour). This is followed by the intercritical HAZ (light blue region), and the fine grained HAZ (yellow region). The hardness of the weld metal followed that of the HAZ, while the lowest was the parent metal.

The increase of peak hardness with pressure was not highly significant. Peak values were 401, 397, 386, and 361 HV respectively from 200 bar down to 1 bar. This supports the previous observations that for thick materials such as subsea pipeline steels, the welding process heat input is the dominant effect, rather than the high pressure, controlling the cooling time and consequently weld metal hardness.

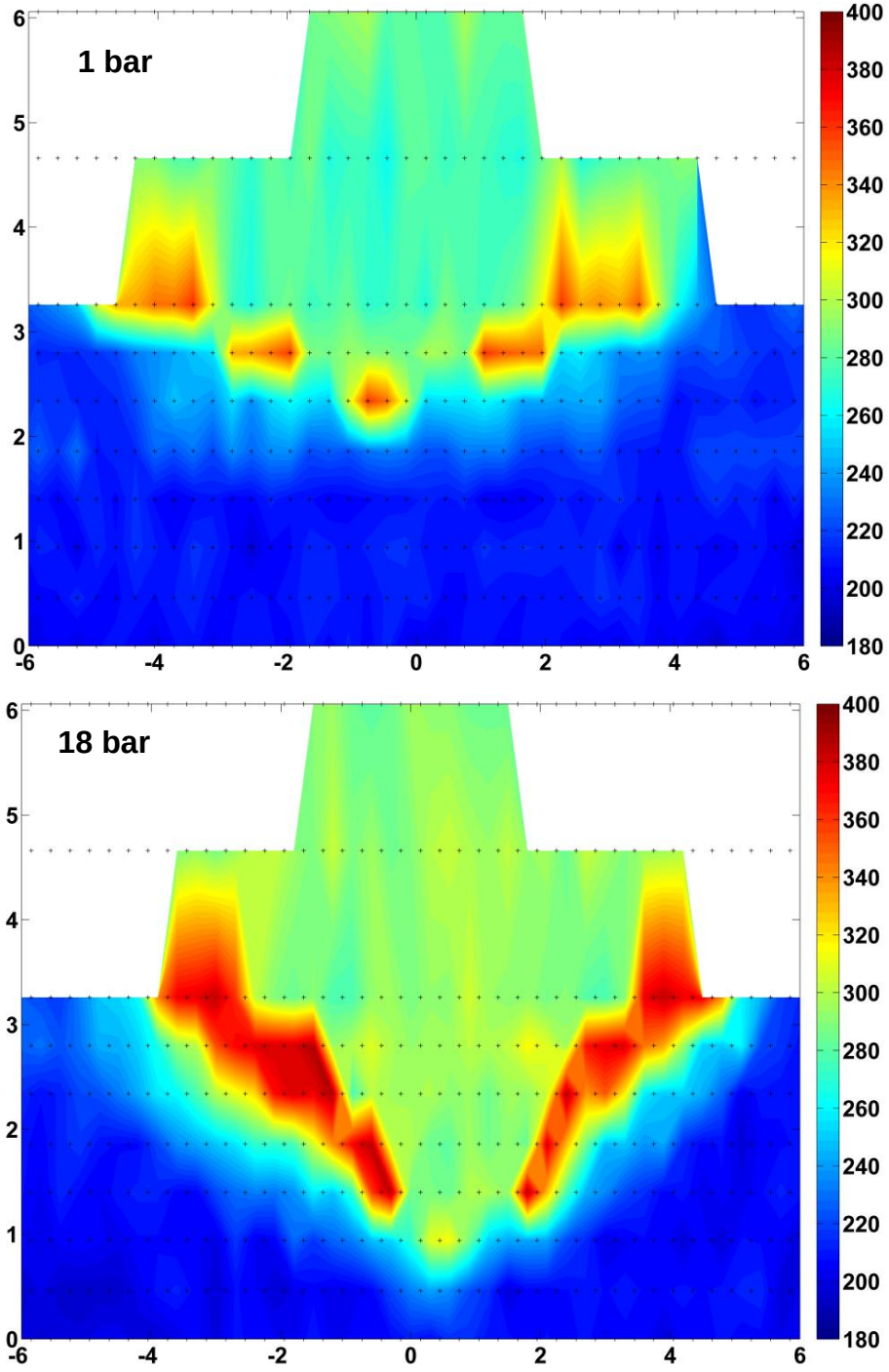

Figure 3-25: Vickers micro hardness map of the 8 m/min WFS and 7 mm/s welding speed welds for the 25 mm thick plate for 1 and 18 bar pressures. Units in mm and hardness measurement in $HV_{0.5}$

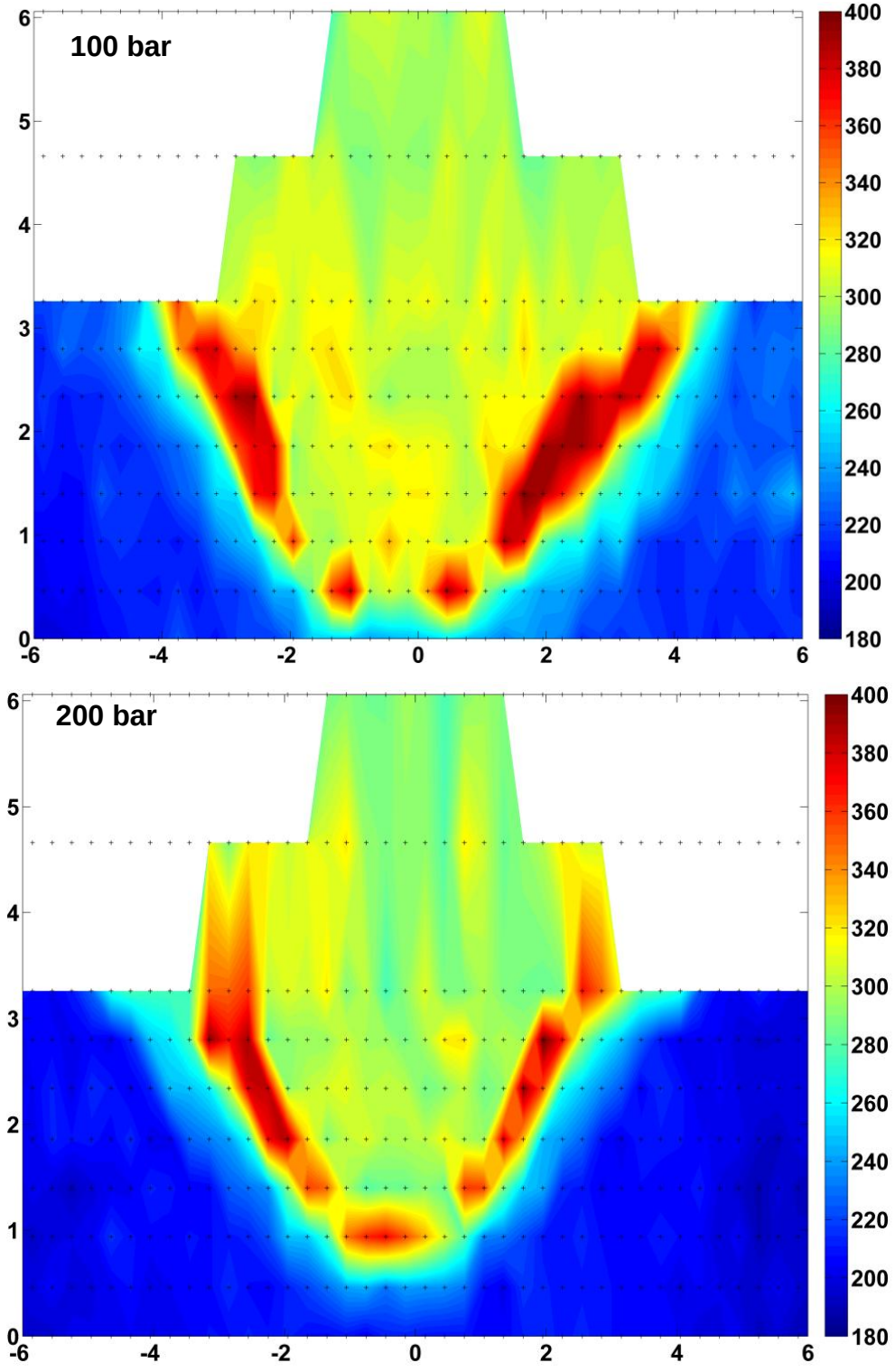

Figure 3-26: Vickers micro hardness map of the 8 m/min WFS and 7 mm/s welding speed welds for the 25 mm thick plate for 100 and 200 bar pressures. Units in mm and hardness measurement in $HV_{0.5}$

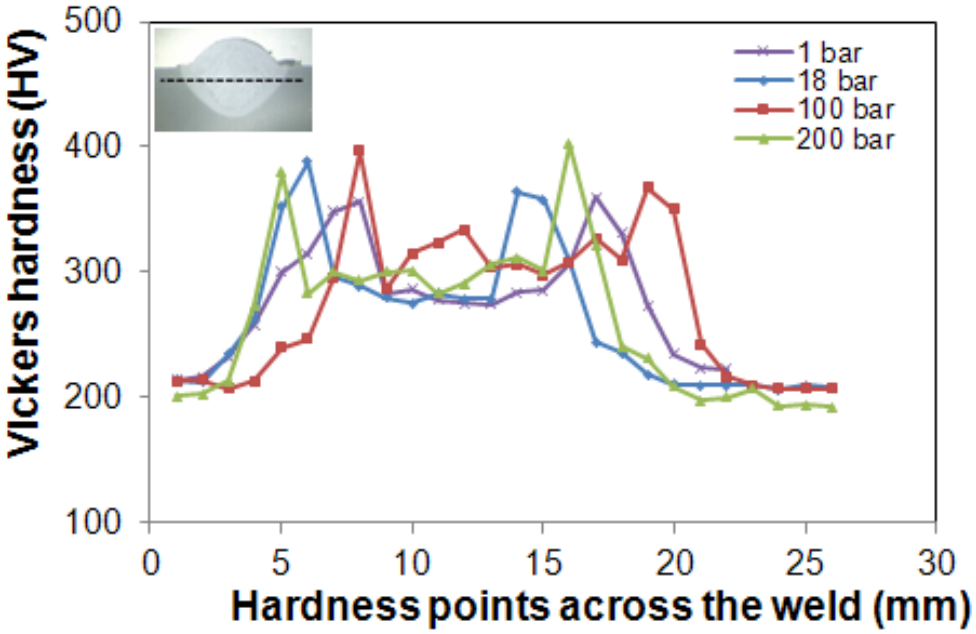

Figure 3-27: Comparing the hardness profiles of the same welds in figure 3-22

3.6 Discussion of Results

This section presents a critical analysis and interpretation of the results. Comparisons with previous work will be made based on the research findings.

3.6.1 Current and Voltage Waveforms

The transient behaviour of the welding current and arc voltage at different pressures as shown in Figure 3-12 was similar to those reported elsewhere [7; 118; 163]. The fluctuation of the waveform was seen to increase with pressure, suggesting a deterioration of the transient power stability. This effect is less marked at lower pressures. A study of the statistical analysis of current and voltage waveforms carried out by Amin et al [7] revealed similar results.

This instability is caused by the influence of the ambient pressure on the physical characteristics of the welding arc. For example, at elevated pressures the gas (argon) concentration in the plasma jet increases due to higher gas density. Amin [5] computed the ionisation energy of argon per mole at 1 bar (g), 10 bar (g) and 250 bar (g) as 17.85 kJ, 178.9 kJ and 4461.1 kJ respectively to verify that the ionisation potential of argon as well as other gases increases with pressure. In order to keep the arc shape constant, greater amount of energy is therefore required at high pressures to ionise the atoms within the arc column.

Amin et al [7] showed in their work that the power required for arc formation increases at higher pressures. They suggested that lower frequencies occur at elevated pressures due to sudden and severe fluctuation of current and very short pulse period. They further suggested that the low frequencies represent the arc instability, which results from the very high pulse amplitude and very short pulse durations.

Although, the behaviour of current and voltage was harmonic in the time domain as shown in Figure 3-12 , Amin et al [7] suggests that lower frequency wave components are prevalent at elevated pressures. At lower pressures, the waveform shows the same behaviour in the frequency domain i.e. at elevated

pressure, voltage waveforms deviate from characteristic frequencies that are produced in the current waveforms.

Finally, it was suggested by Nixon, et al [93] and Richardson et al [117] that process stability should not be determined mainly by electrical stability as there is no direct correlation between them. The regular bead shape observed here across the 1 to 200 bar pressure range supports this.

3.6.2 Thermal Cycles

There is distinct evidence from the weld thermal cycles shown in Figure 3-13 to 3-15 that the effect of pressure on weld cooling behaviour is dependent on the material thickness. This is because for the thicker (25 mm thickness) material, pressure increase had insignificant influence upon the cooling curves for the same welding conditions (Figure 3-13 top). There was however a significant effect of pressure on the cooling curves of the thinner (5 mm thickness) material especially at higher pressures (Figure 3-13 bottom). Related studies conducted by Amin et al [6] on the thermal cycles of hyperbaric GMAW on 30 mm thick steel plates showed similar results. Although they only measured the thermal cycles of the HAZ at relatively lower pressures of 1 bar, 18 bar and 35 bar. Their findings showed that weld cooling time remained relatively unchanged with pressure in this pressure range. Apart from this work, the author could not find any comparative studies in the literature.

Heat transfer through the material medium (conduction) and from the material to the surrounding chamber gas environment (convection) play a key role in understanding this phenomenon. For thicker materials the heat transfer by conduction dominates, while the effect of convective heat loss is significantly more pronounced for thinner materials. During hyperbaric welding of thick section subsea pipelines, the material acts as a heat sink since the welding heat is dissipated into the material by conduction thereby limiting the convective heat loss from the material to the chamber gas environment. Nevertheless, the cooling behaviour is influenced by pressure as evident in Figure 3-13 (bottom).

This is mainly due to greater heat exchange between the material and the environment when the thermal gradient within the material is low.

Process heat input and material thermal conductivity are other factors that can control weld cooling behaviour at different pressures. A high heat input to the material would accelerate convective heat transfer to the chamber environment. However, such heat input cannot be achieved with the hyperbaric GMAW process.

For the thermal cycles at positions 5 mm from the weld centre line of the thicker steel section shown in Figure 3-15, the curves for 1 bar and 18 bar pressures could not be determined since the thermocouple positions were too close to the welding arc. Consequently, they were melted and no data was obtained. This is due to the effect of arc constriction which increases with pressure as already described. As a result, the arc width becomes smaller at higher pressure such that at the same position, the thermocouples were not melted by the welding arc. It may also be seen from the figure that the cooling behaviour of the HAZ represented by the position of the K-type thermocouple is identical to that of the weld metal. Although, the peak temperature is lower, the influence of material thickness on the cooling behaviour can be seen at the pressures shown since the curves for 100 bar and 200 bar were not greatly influenced by pressure.

To isolate the actual influence of convection at different pressures, the cooling curves shown in Figure 3-16 were generated. These show that convective heat loss increases with pressure because as pressure increases, the density of the chamber gas becomes higher. Consequently, there is greater heat extraction from the material due to higher thermal diffusivity of the gas. Some authors attribute this to higher thermal conductivity of the gas [142]. This assumes that due to higher gas density, heat transfer is mainly by intermolecular forces or collisional transfer similar to heat transfer by conduction [130]. In any case, both thermal conductivity and thermal diffusivity are directly proportional.

Pressure and cooling time has a power relationship as given in Figure 3-17, indicating that convective heat loss increases with pressure. The plot denotes

that cooling time changes sensitively with pressure. There is a sharp drop in cooling time from 1 bar to 18 bar, and subsequently the change becomes more gradual. This supports the fact that as pressure increases, gas density becomes higher leading to enhanced heat extraction, but the relationship is not a linear one.

In summary, during hyperbaric GMA thick section pipeline welding in the 1 to 200 bar range the weld cooling behaviour is affected more significantly by the welding process heat input than the ambient pressure. This is based on the premise that subsea pipelines are usually made of thick sections to ensure good collapse strength.

3.6.3 Heat Input and Cooling Time

The calculated heat inputs for all the welds were typically 0.64 kJ/mm irrespective of the ambient pressure (Table 3-5). For the same welding parameters, changes in pressure did not significantly affect the weld process heat input. Although, the transient behaviour of current and voltage was shown to fluctuate very much at higher pressures (Figure 3-12), the average instantaneous power remained relatively constant at all pressures investigated (Table 3-5). The reason for the fairly constant heat input was due to the fact that the time averaged behaviour of the process remains relatively constant over a typical time period for weld pool formation and solidification. The same observations were made by Richardson et al [120; 117]

In the previous section it was shown that the material thickness plays a significant role in the weld cooling behaviour, and that the influence is more significant than the ambient pressure. It was also established that for the thick plate conduction dominates, while convection becomes significant for the thin plate. This is illustrated in the calculated weld cooling time for both temperature ranges as presented in Table 3-4. It can be seen that the cooling time remained fairly unaffected by pressure for the 25 mm thick plate at all pressures investigated. From 800 °C to 500 °C it changed from 3.4 s to 3.0 s between 1 bar and 100 bar, which represents 12% reduction of the cooling time, while it

changed from 12.6 s to 11.0 s representing 13% reduction from 800 °C to 200°C. Considering the large pressure difference, which is similar to comparing conditions at one atmosphere and 1000 m sea depth, this is a relatively small difference.

As already described, the reason for this is due to the influence of the material thickness on the cooling time. Heat is dissipated by conduction through the material thickness (acting as a heat sink), a situation that resulted in the relatively fast weld cooling time. This nullifies the effect of heat transfer by convection to the chamber gas; hence the cooling time remained relatively unaffected by pressure. However, the cooling time over the same temperature ranges for the 5 mm thick plate changed from 18.2 s to 8.7 s between 1 bar and 100 bar, which represents a 52% reduction between 800 and 500 °C, and 202 s to 41 s representing 80% reduction between 800 and 200 °C.

This means that for the thick steel section the influence of pressure on the cooling time is almost insignificant from 800 °C to 200 °C (Figure 3.13 top). However, for a thinner section the influence of pressure on the cooling time is quite significant particularly, between 500 °C to 200 °C (Figure 3.13 bottom). This is because convective heat loss is much greater than conduction in the case of the thinner steel section. Unlike the thicker plate, the material is quickly heated up, resulting in greater heat loss to the environment; hence the significant influence of convection.

The plots given in Figure 3-18 show how the cooling time responds to pressure for both material thicknesses. It is very sensitive to pressure for the thinner plate and remained relatively unaffected by pressure for the thicker plate. This is due to the effect of conduction and convection as already described.

It may be deduced from the previous observations that since for the same welding parameters the process heat input did not change with pressure, and cooling time decreases at elevated pressures, this is due to an increased heat loss by convection as the gas becomes denser. However, material thickness reduces the influence of convection resulting in faster cooling times as

conduction becomes dominant. Therefore, during hyperbaric GMAW for deep water applications, the concern should be focused upon faster weld cooling time due to heat transfer by conduction through the thick pipeline sections, as the contribution of pressure to reduced weld cooling time is minimal.

The fast cooling times recorded over the temperature range of 800 °C to 500 °C is typical of low heat input welding process. Hudson [64] and Eroglu et al[36] reported such fast cooling times over the same temperature range and attributed it to the low welding heat input. According to Arora et al [8] the cooling rates over this temperature range are important in determining the phase transformation behaviour leading to the evolution of final weld microstructure. From the continuous cooling transformation (CCT) diagram of X65 pipeline steel (see Figure 2-32), such fast cooling times will favour the formation of martensite, and the microstructure is known to increase susceptibility to HAC.

Higher process heat input will increase weld cooling time, but as already explained hyperbaric GMAW is limited in providing higher heat input because it is operated at a short arc length in order to minimise process instabilities due to elevated pressures. The main thrust of this research work is therefore to investigate the use of a laser to provide additional heat input in order to extend the cooling time of hyperbaric GMAW and improve the resultant mechanical properties.

3.6.4 Macrostructure and Microstructure Examination

3.6.4.1 Macrostructure

The influence of pressure on hyperbaric GMAW is illustrated by the weld bead profile shown in the macrographs of Figure 3-19. It is observed that the weld penetration depth and area generally increases with pressure, although at high pressure levels (100 and 200 bar), the bead shape did not change significantly. Similar results were reported by Amin [5]; Woodward [157] and Amin et al [7]. The increased weld penetration depth may be due in part to shrinking of the arc column. Richardson et al [120] also reported that the arc shrinks in order to

minimise energy loss due to high heat extraction rate by the chamber environment. In both cases, the resultant reduction in size of the arc column means that the same amount of energy is being carried by a smaller arc column. This results in a higher energy density, which concentrates the heat distribution in the arc centre, causing more material to be melted and consequently deeper weld penetration.

It was reported by Amin [5] that the thermal conductivity of argon increases with temperature and pressure. As a result, a wider gas jet and shallow penetration depth should be expected at higher ambient pressure. However, studies by Woodward [157; 158] have shown that the weld bead profile did not indicate much change beyond 100 bar up to 250 bar. This phenomenon can be attributed to arc constriction at elevated pressures, which counteracts the effect of higher thermal conductivity.

Amin et al [7] reported that the average arc transient power increases with pressure and suggested that the weld bead dimensions should be larger at elevated pressure because of increased heat input and arc energy. This was not observed in this work because as indicated in Table 3-5 the average arc power and heat input remained relatively unchanged. They also suggested that the arc efficiency factor is relatively low at high pressures. Contrary to this the arc should have a higher efficiency factor at elevated pressure. This is because for the same heat input, more material is melted at greater pressures, resulting in higher weld penetration depth and area (Figure 3-20). The increased penetration area from 1 – 18 bar may be due to changes in arc efficiency. It may also be affected by set up of the hyperbaric welding system at 1 bar. The pressure chamber was designed to operate when pressurised. Therefore welding at 1 bar may not give consistent results as 18 – 200 bar.

Since the same power source mode was used by Amin et al [7], the different results they obtained may be because of the method used to compute the their momentary arc power. They obtained the momentary arc power using statistical methods while for this study, the instantaneous arc power was determined directly from the transient current and voltage data.

There is little observable difference in the bead height and deposit area because the same wire feed speed and welding speed were used, which means that the same amount of filler metal was deposited. However, the weld width decreases with pressure but remained relatively the same after 100 bar. Studies conducted by Woodward [158] showed similar results, although his work was mainly at higher pressures. The reason for the reduction of weld width at elevated pressure is due to the effect of arc constriction.

3.6.4.2 Microstructure

Microstructure characterisation of the welds at different pressures as shown in Figure 3-21 to Figure 3-24 shows similar structures for the weld penetration area and HAZ. Apart from the weld at 1 bar, which is dominated by grain boundary ferrite structures others showed a fine distribution of ferrite constituents in the microstructure. This may suggest that the higher energy density at elevated pressures could be responsible for the somewhat fine distribution of constituents of the microstructure.

The distribution of microstructure constituents in the HAZ is comparable at 18 to 200 bar pressures (see Figure 3-22 to Figure 3-24). The coarse grained HAZ being the closest to the fusion boundary has the largest grain size. This is because the heat input and temperature is highest in this region. This temperature typically could be above 1000 °C and is sufficient to permit rapid austenite grain growth. The longer time at high temperature resulted in the formation of large grain sizes. The fine grained HAZ region is farther from the fusion boundary and as a result it is heated to a lower peak temperature, but above Ac_3, However, this is insufficient to produce rapid austenite grain growth. Hence the rather finer grain size distribution. This is followed by the intercritical HAZ, which is heated to a temperature between Ac_1 and Ac_3 resulting in only partial transformation to austenite and substantial grain refinement. The subcritical HAZ not shown in the microstructures is the closest region to the parent metal and farthest from the fusion boundary. The maximum temperature here is less than Ac_1 and the microstructure is similar to that of the parent metal with possible formation of spheroidised pearlite.

3.6.5 Hardness Test

Since there are few observable differences in the microstructure, it is difficult to evaluate the potential effect of pressure on the weld microstructure and consequently the mechanical strength. However, this can be estimated from the hardness distribution, which can give an indication of the type of microstructures present.

The weld hardness distributions as represented by the hardness distribution shown in Figure 3-25 to Figure 3-27 indicate a gradual increase of peak hardness with pressure. It also shows that the peak hardness occurs at the HAZ (coarse grain HAZ) followed by the weld metal and finally the parent metal. However, there is progressive decrease in the hardness distribution of the HAZ from the coarse grained HAZ region towards the parent metal. This is typical of a low heat input process as observed by Eroglu et al [36].

The values of the peak hardness were 361 HV, 387 HV, 393 HV and 402 HV for the 1, 18, 100 and 200 bar welds respectively. The marginal differences in peak hardness from 18 bar to 200 bar may be anticipated since the cooling times indicated similar marginal differences. The weld cooling time is controlled by the material thickness, which in this case determines the weld hardness. The high hardness particularly of the coarse grained HAZ suggests the presence of martensite in this region due to the relatively low process heat input and resultant high cooling rate.

The peak hardness from the single pass welds at all pressure levels was higher than the 350 HV_{10} specified by DNV-OS-F101 [32] as acceptable limits to avoid hydrogen assisted cracking of offshore structures. It is worth mentioning that the 500 g load is more effective in identifying the hard phases, as the 10 kg hardness load specified by the standard may span over a large region because of the larger indentations thereby averaging hardness from different phases.

The high peak hardness measurements for the pressure range investigated are a reflection of the relatively low heat input of hyperbaric GMAW process. This

justifies the investigation of a laser to provide additional process heat input. The additional laser heat input significantly reduced the peak hardness of GMAW. This is reported in Chapter five.

3.7 Conclusion

The main conclusions drawn from the work presented in this chapter are as follows:

- The magnitude of the current peaks and short circuiting frequency increases with pressure giving higher fluctuations of the current and voltage waveform particularly at high pressures. Nevertheless, the average instantaneous power and therefore heat input remained relatively unchanged with pressure.

- Higher ambient pressures resulted in higher weld pool cooling rates due to higher thermal diffusivity caused by the increased gas density. For a relatively thick steel section (≥25 mm), as used for deep water offshore pipelines, the heat input is dissipated through the material thickness by conduction thereby limiting heat loss by convection to the chamber gas. For thinner steel sections (5 mm) it was shown that the weld cooling rate is much more sensitive to increases in ambient pressure.

- For similar welding parameters, the weld bead geometry did not significantly change between 18 and 200 bar, and it is suggested that the narrowing of the weld bead and increased penetration depth was due to the influence of arc constriction with increased pressure.

- The hardness distribution is reflected in the thermal profile of the processes. For the thicker steel section, the maximum was measured on the 200 bar weld while the lowest peak hardness was observed on the 1 bar weld. However, there was not much difference with pressure from 18 to 200 bar.

- The hardness peak values are unacceptable by standards. Therefore to reduce the peak hardness levels in hyperbaric Gas Metal Arc Welding, there is a need to provide additional heat input. This will reduce susceptibility to hydrogen assisted cracking.

4 Process Characteristics of Traditional and Controlled Dip Transfer GMAW at One Atmosphere

Scope

Hyperbaric GMAW is performed at a very short arc length of the order 1 mm to 3 mm to ensure process stability. This involves welding in traditional short circuit or dip molten metal transfer mode that is characterised by low heat input because the arc momentarily extinguishes during short circuiting. Also, arc re-ignition occurs under high power output resulting in spatter generation that may affect weld quality.

GMAW short circuit processes were improved significantly during the past few years. Today a number of "energy reduced" short arc processes are available. These include: Cold Metal Transfer (CMT), ColdArc, ColdMIG, Surface Tension Transfer (STT) etc., and have primarily been developed to reduce the heat input for welding of thin sheets and improved control of the weld pool.

In this chapter, the process characteristics of short circuit GMAW is compared with some advanced GMAW power sources such as CMT and ColdArc. These processes were designed to ensure controlled dip molten metal droplet transfer, and reduce associated process instabilities and weld spatter. The aim is to establish whether the controlled processes can be used as alternatives to short circuit GMAW for hyperbaric welding operation. The heat input, current and voltage waveforms, thermal cycles and weld bead profiles are compared. Finally, the results and discussion are presented.

4.1 Aim and Objectives

The study presented in this chapter is aimed at establishing whether the Cold Metal Transfer (CMT) and ColdArc GMAW conditionscan be used as alternatives to traditional GMAW for hyperbaric welding. To achieve this, the process characteristics of dip transfer GMAW will be compared with that of CMT and ColdArc.

The main objectives are to compare the transient behaviour of welding current and arc voltage, heat inputs and cooling times, and the weld bead profiles of the different welding process variants.

4.2 Materials and Equipment

In this section the materials used for the experimental trials, which include: pipeline steel and welding consumables are presented. The equipment used for the welding trials, weld instrumentation, and macrostructure examination are also presented.

4.2.1 Materials

4.2.1.1 Steels

The same X65 pipeline steel with chemical composition given in Table 3-1 of chapter 3 was used for this experiment.

4.2.1.2 Welding Wire

The welding wire used was G4Si1 with a nominal diameter of 1.0 mm. This wire was used for all the remaining experiments presented in this thesis. Therefore, reference will be made to it in subsequent chapters. The as-deposited chemical composition is given in Table 4-1.

Table 4-1: Chemical composition of G4Si1 welding wire

Material	Chemical analysis in wt. %													
	C	Mn	Cr	Ni	Cu	V	Al	Mo	Si	S	P	B	Nb	Ti
Filler wire G4Si1 (ø 1. 0 mm)	0.06	1.64	0.20	0.02	0.02	-	-	0.02	0.94	-	0.013	0.013	-	-

4.2.1.3 Shielding Gas

Argonshield Heavy (18% carbon dioxide and 2% oxygen in argon) was used as shielding gas for this and the remaining experiments described in this thesis.

4.2.2 Equipment

The equipment used for the experimental trials is presented in this section. This includes three welding power sources, a Fronius TPS 5000 CMT, an EWM Alpha Q 552 RC Puls (ColdArc) and an ESAB LUD 450, as well as an ABB Robot. Additionally, weld instrumentation and metallurgical characterisation equipment was also employed.

4.2.2.1 Fronius TPS CMT Power Source

The Fronius TransPuls Synergic 5000 Cold Metal Transfer (CMT) with an output of 500 A is a MIG/MAG power source for short circuiting, spray and pulsed arcs. It is a completely digitised and microprocessor-controlled machine that is intended for automated and robot-assisted applications. The process is based on a dip-transfer [28]. The most striking features that distinguish it from traditional short circuiting process are that the wire motion is integrated into the process control, with reduced thermal input and spatter free metal transfer. During short circuiting, the digital process control cuts off the power supply and controls the wire retraction. This forward and backward movement occurs at a frequency of 70 Hz, and the wire retraction aids molten metal droplet detachment during short circuiting.

The machine has a robot interface that is suitable for all conventional robots whether digital or analogue. An incorporated full-text display remote control unit called RCU 5000i monitors weld data with the Q- Master function [28]. The RCU has a unique menu structure with an easy to follow user guide. A water-cooled FK 4000 R cooling unit ensures optimum cooling of the welding robot torch. Smooth wire feed is ensured by the digitally controlled VR 7000 CMT and a digitally controlled dynamic AC servo motor guarantees precision wire feed in both directions [28]. The other feature that distinguishes the unit from that of conventional GMAW is that it has two separate wire drives (front and rear) that are separated by a wire buffer. A photograph of the CMT welding machine and its schematic set up with a robot are shown in Figure 4-1 and 4-2.

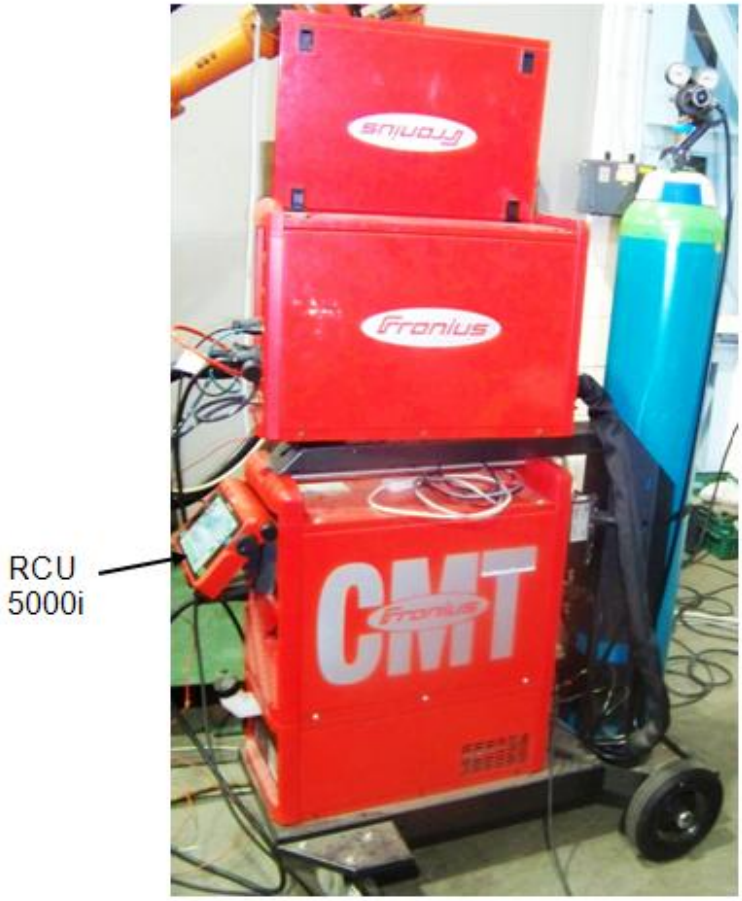

Figure 4-1: The Fronius TPS 5000 CMT power source

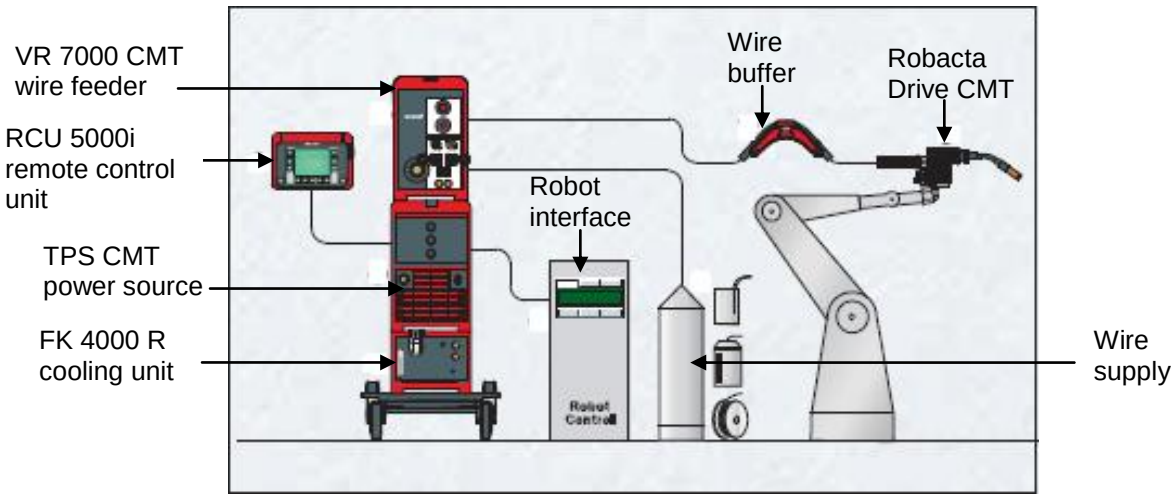

Figure 4-2: Schematic illustration of CMT power source with a robot [28]

4.2.2.2 EWM Alpha Q 552 RC Puls Power Source

The Alpha Q 552 RC Puls shown in Figure 4-3 is a multipurpose welding machine with six processes: ColdArc, ForceArc, MIG/MAG pulse and standard, TIG (Liftarc) and MMA. It is a unique second generation digital system that is easy to integrate into automated systems and has an extended duty cycle (40-100%) with top performance up to 550 A welding current [38]. The machine is optimised for automatic and mechanised applications and is set up with PC300.NET software via PC or RC 300. Welding parameters are adjustable through an interface called “alpha RC2”. The system is gas-cooled with optional water cooling unit [38].

The machine was operated in the ColdArc mode which is a controlled short circuit low heat input process. Unlike the CMT, there is no mechanical intervention in the wire feed as the process flow is controlled electronically (e.g. control of the current surge during short circuiting). As a result, the ColdArc can be operated manually with standard welding torches. A digital signal processor cuts-off power from the arc at the onset of short circuiting, and the arc is re-ignited as soon as droplet transfer happens (the power cut-off takes place in a time period less than 1 μs) [50]. This ensures gradual arc re-ignition and a low energy process. A schematic illustration of the machine set-up with a robot is given in Figure 4-4.

Figure 4-3: The EWM Alpha Q 552 RC Puls power source

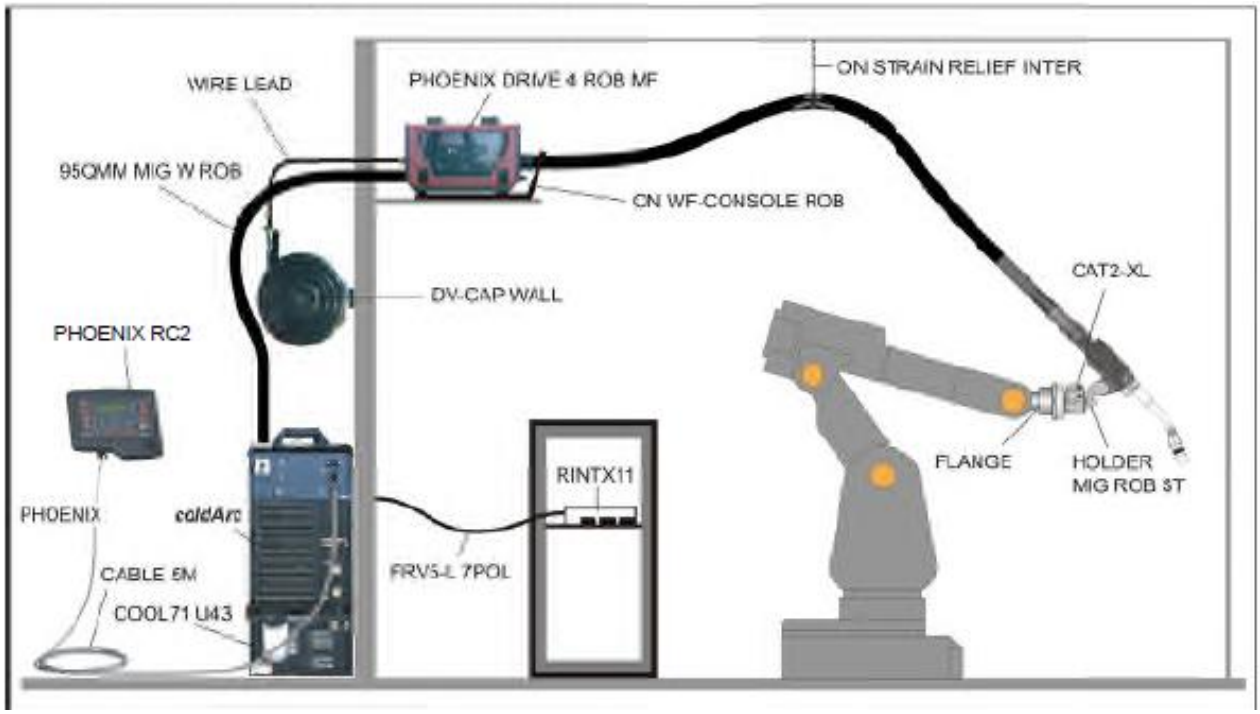

Figure 4-4: Set up of the Alpha Q power source with robot [38]

4.2.2.3 ESAB LUD 450 Power Source

The LUD 450 is a transistorised welding rectifier system designed for MMA, MIG/MAG (semi-automatic), TIG welding and arc gouging that is operated with a controller and wire feed unit (Figure 4-5) [37]. It has a MIG/MAG setting range of 15 A/15 V (8 V) – 320 A/30 V and a 100 % duty cycle at 270 A/30, 8 V and 60 % duty cycle at 320 A/ 32, 8V [37] .

It is fitted with a thermal cut-out to prevent overheating and the welding rectifiers are fan cooled. There is automatic reset of the cut-out once the welding rectifier has cooled down.

Figure 4-5: ESAB LUD 450 power source

4.2.2.4 ABB Welding Robot

The ABB robot is a six axes robot for arc welding. It consists of four main components: robot (IRB 1400) with wire feed system, control system consisting of the control cabinet (upper section) and power source (lower section), manipulator (with fixture for the work piece) and operator's panel. The measurement system in the robot is absolute, which means that the robot does not need to be synchronised if the mains supply has been disconnected for some time. The welding robot system is shown in Figure 4-6.

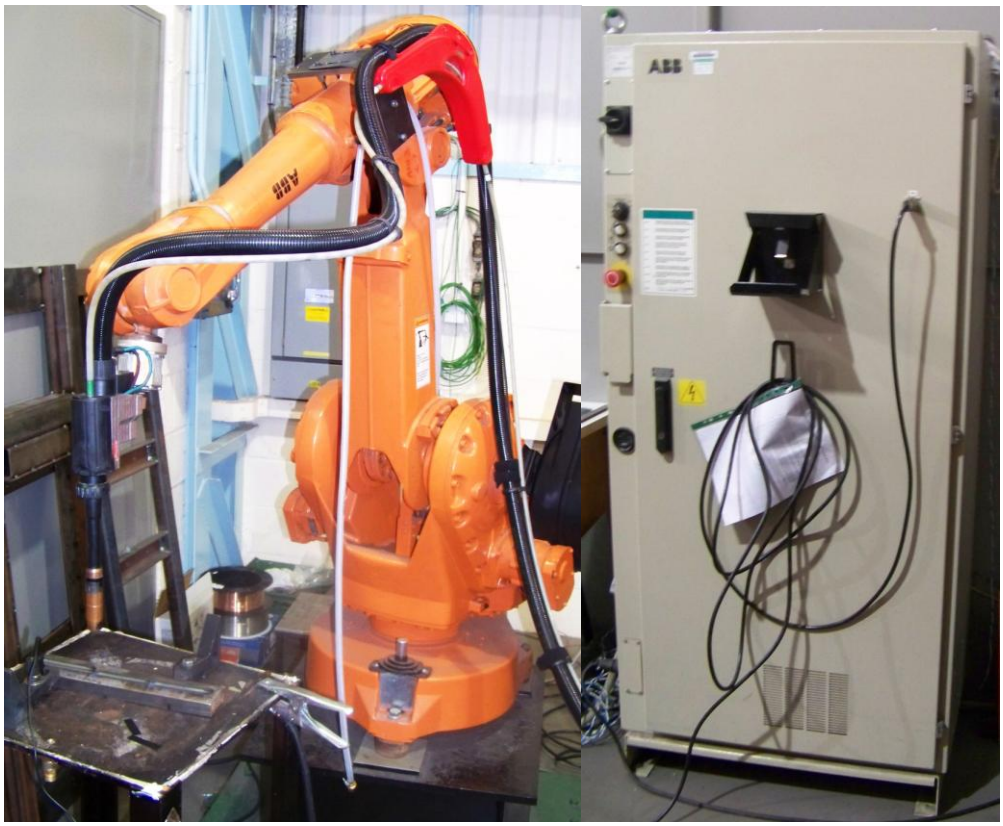

Figure 4-6: The ABB welding robot and controller

4.2.2.5 Weld Instrumentation

Refer to section 3.2.2.4 of chapter 3 for the instruments used for weld instrumentation, monitoring welding current, arc voltage and wire feed speed , and generating weld thermal cycles.

4.2.2.6 Characterisation

The instruments used for the metallurgical and mechanical characterisations are the same as those in section 3.2.2.5 of chapter 3.

4.3 Experimental Method

4.3.1 Welding Trials

A total of eighteen instrumented bead-on-pipe welds were made on the X65 pipeline steel. The ESAB LUD 450 machine was used to perform six welds, which represents the traditional short circuit GMAW. In order to initiate short circuit or dip molten metal transfer, a constant contact tip to work distance (CTWD) of 10 mm was used. The Fronius TPS CMT power source was used to perform another set of six welds on the same material, while the remaining six welds were made with the Alpha Q 552 machine in the ColdArc mode. For all the three processes, the welding torch was mounted on the ABB welding robot before welding. The robot was calibrated before it was used to set the welding speed. The same welding parameters were investigated for each of the process. Wire feed speeds (WFS) used were 3 m/min to 8 m/min at a constant welding speed of 0.42 m/min. In order to ensure consistency, the same CTWD of 10 mm was used for the ColdArc and CMT processes. Weld pool thermal cycles were generated using R-type thermocouples that were dipped inside the weld pool (Harpoon technique) during welding [136].

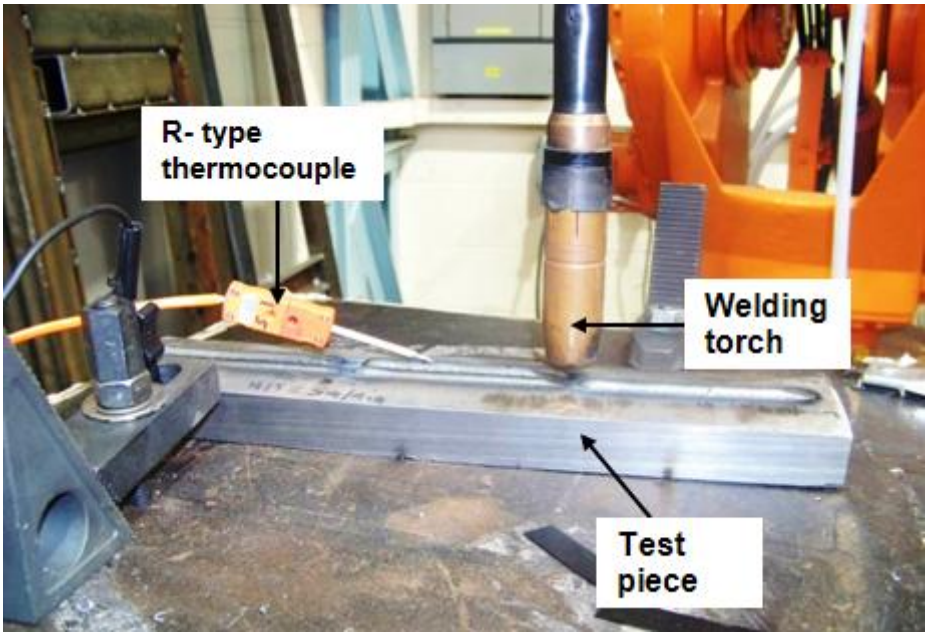

Figure 4-7: A completed weld showing the thermocouple inside the weld metal

4.3.2 Measurement of Heat Input and Cooling Time

A ScopeCorder was used for real time measurement of instantaneous welding current and arc voltage, which were used to calculate the weld heat input according to equation (3-1). The weld cooling time from 800 °C to 500 °C was calculated from the temperature-time data.

4.3.3 Macrostructure Examination

The weld joints were sectioned, ground and polished according to standard metallographic procedures as described in section 3.2.2.5.1 of chapter 3 to show the geometry of the weld metal and HAZ. The polished samples were then etched with 2% nital solution before macrographs were taken using an optical microscope to show the weld bead profile.

4.4 Experimental Error

The main experimental error of this research may have resulted from the determination of the weld thermal cycles. This is because the dipping of the thermocouples inside the weld pool may not have been repeatable since it was not likely that the thermocouples were dipped at the same position for all the welds. The implication is that the peak temperature may not be exactly the same for all the welds and this may introduce some errors in the measurement of the weld pool cooling time. To minimise the likelihood of this error, the thermocouples were placed in the centre of the weld pool as this gave similar peak temperatures.

Another likely source of error may be from the wire feed speed of the welding processes. It was discovered that the set wire feed speed was not always the same as the actual value during welding. This was particularly noticeable for the CMT and ColdArc processes, and it has to do with the processes mechanisms. It is possible that errors could be introduced as a result of variable wire feed speeds from the set values. These errors could not be avoided because the average wire feed speed was always marginally different from the set value. Therefore, for consistency the set wire feed speed was used.

4.5 Results

The interpretation of the experimental results is presented in this section. This is followed by their discussion in the subsequent section.

4.5.1 Current and Voltage Waveforms

Transient relationship of the welding current, arc voltage and power for the traditional short circuit GMAW, CMT and ColdArc over a time interval of 0.05 s are given in Figure 4-8 to 4-13. These were for welds made with 3 m/min and 8 m/min WFS. The complete waveform of all the welds is shown in Figure B-1 to B-6 in Appendix B.

The waveform shapes obtained from the welding processes indicate significant variations for the same welding parameter. The variations can be seen for the peak current, background current, voltage and power. It has also been observed that at low WFS (Figure B-1 to B-6 in the Appendix) the waveform behaviours are regular and reasonably predictive while they become increasingly irregular from 5 m/min to 8 m/min WFS. The difference in the process behaviour is indicative of the control mechanisms.

The transient behaviour of welding current, arc voltage and power for the short circuit transfer GMAW (Figure 4-8 and 4-9) shows that the welding current rises rapidly as the wire touches the melt pool or short circuits to a peak value, which Goecke [50] referred to as short circuit current. At the short circuit current, the voltage drops to zero and rises rapidly after the short circuit is broken to re-ignite the arc. The power is shown to also drop close to zero at the point of short circuit. After the short circuit breaks and the molten metal detachment take place, there is a spike in the power before the cycle is repeated.

The transient behaviour of the ColdArc process as shown in Figure 4-9 suggests that it is a pulsed process that is quite regular at low WFS and becomes increasingly unstable at high WFS. As can be observed there is an arcing phase and a short circuit phase. The former is indicated by a high current pulse during arc ignition while the latter is shown by the voltage drop after the

peak current. There is also a low background current after arc re-ignition to minimise further wire melting [50].

Three phases can be identified in the CMT waveforms shown in Figure 4-10 and 4-11: the peak current phase, background current phase and short circuiting phase. The same observation was made by Zhang et al [166]. However, the waveform pattern changes at high WFS (Figure 4-13), and the process tends to exhibit a combined pulse and short circuit behaviour, but with significantly reduced short circuit frequency.

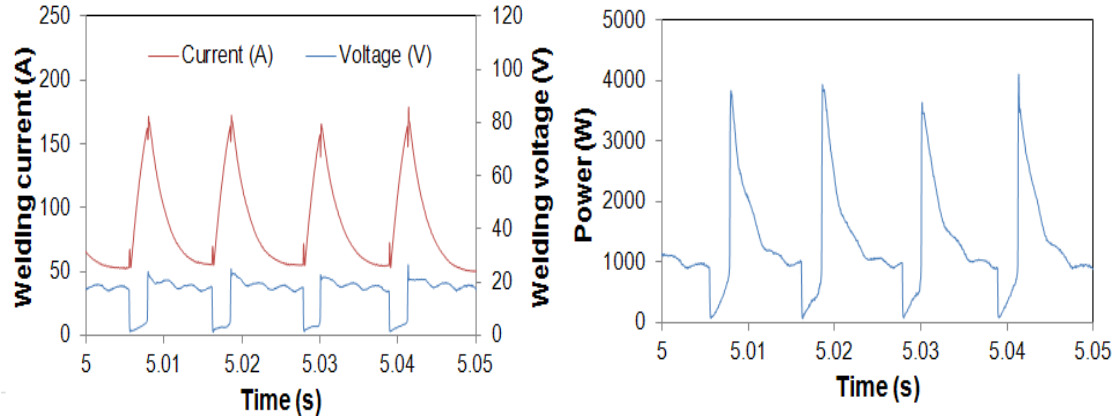

Figure 4-8: Transient relationship of current, voltage and power for short circuit GMAW with 3 m/min WFS

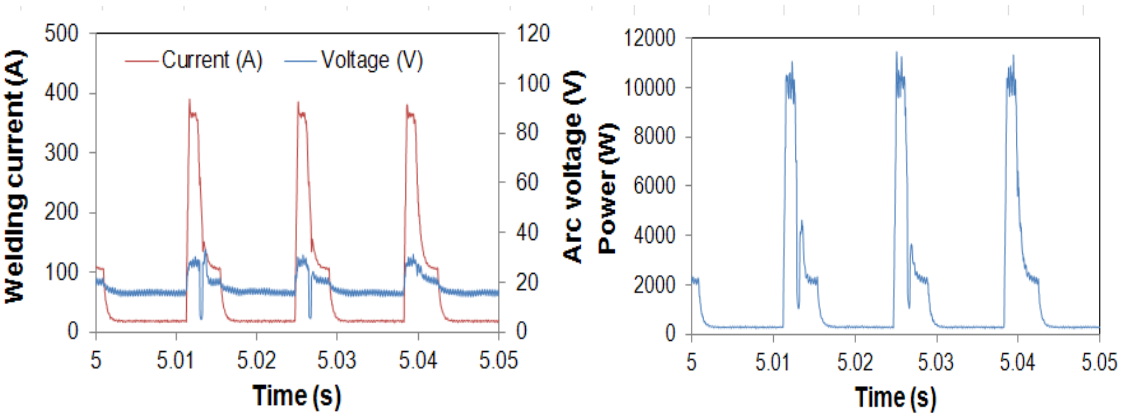

Figure 4-9: Transient relationship of current, voltage and power for ColdArc weld with 3 m/min WFS

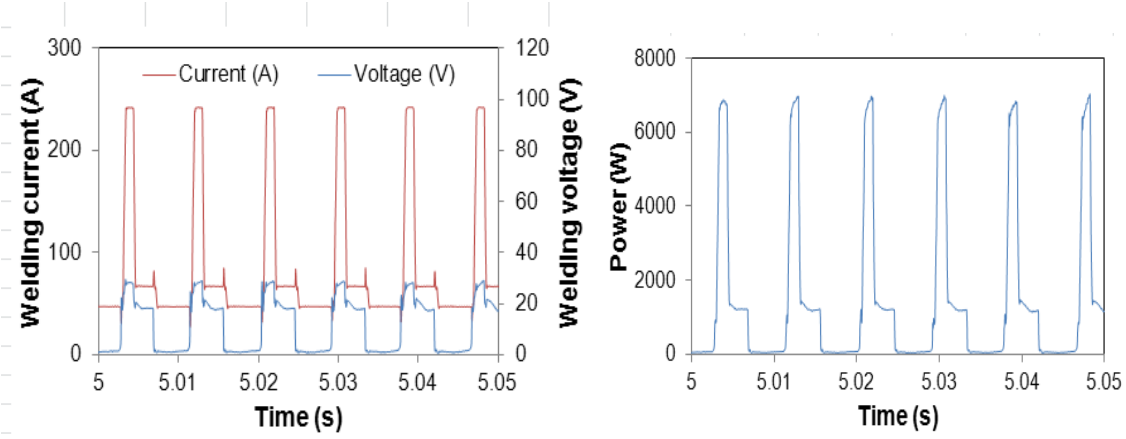

Figure 4-10: Transient relationship of current, voltage and power for CMT weld with 3 m/min WFS

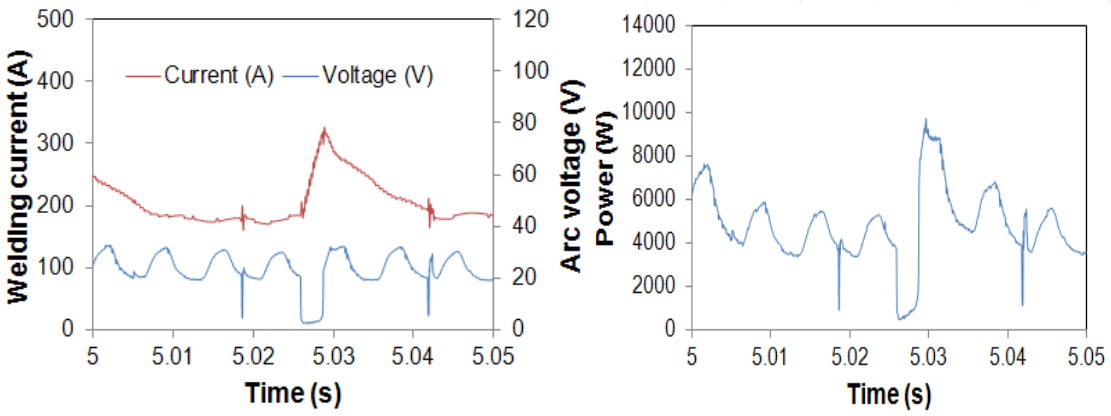

Figure 4-11: Transient relationship of current, voltage and power for short circuit GMAW with 8 m/min WFS

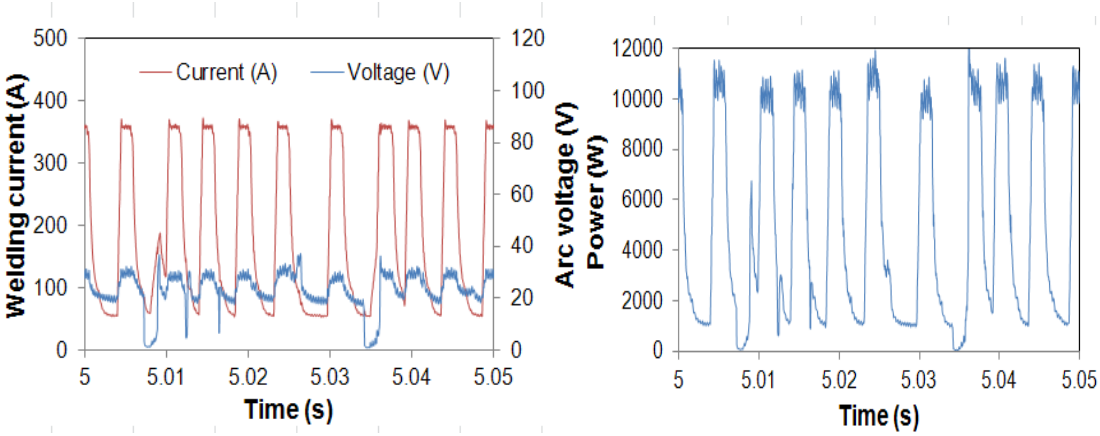

Figure 4-12: Transient relationship of current, voltage and power for ColdArc weld with 8 m/min WFS

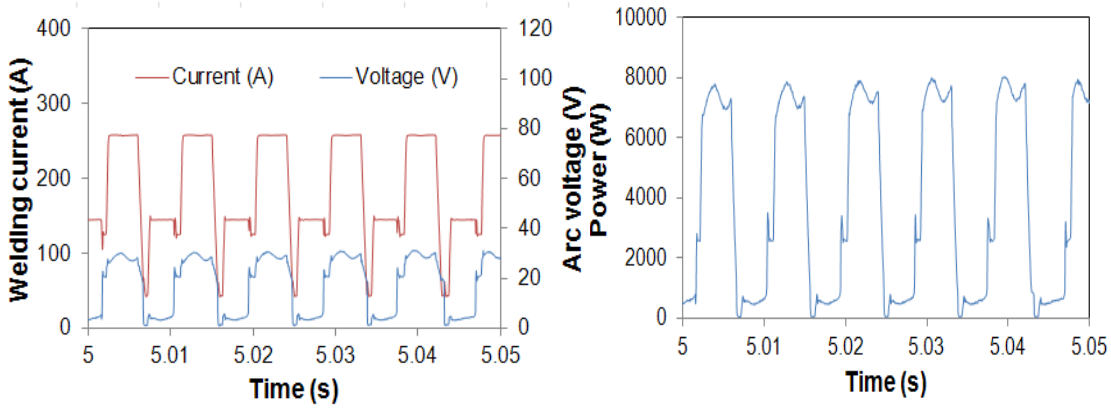

Figure 4-13: Transient relationship of current, voltage and power for CMT weld with 8 m/min WFS

4.5.2 Thermal Cycles, Heat Input and Weld bead profile

Figure 4-14 to 4-16 show the weld pool thermal cycles measured with the "harpooned" R-type thermocouples. The thermal cycles indicate little observable differences in cooling rate between the ColdArc and short circuit GMAW while that of the CMT is shown to cool faster than the two. This means that there is not much difference in the heat input of the ColdArc and short circuit GMAW for the same WFS while that of CMT is relatively lower under the same conditions as shown in Figure 4-17.

The heat inputs of the processes were shown to be the same at low wire feed speed of 3 m/min but from 4 m/min to 8 m/min that of the short circuit GMAW and ColdArc becomes relatively higher than the CMT. There was no significant difference of the heat input values between the ColdArc and short circuit GMAW.

The weld pool cooling times between 800 °C and 500 °C ($t_{8/5}$) are shown in Figure 4-18, and Figure 4-19 to 4-21 are the weld macrographs and weld bead profiles respectively. These are a reflection of the process heat input and cooling times. It can be seen that the CMT welds has shorter cooling times than the other two processes. The weld bead profile represented in Figure 4-21 shows that the CMT weld penetration depth is the lowest while there is little difference between those of the short circuit GMAW and ColdArc for similar

welding conditions. But the reinforcement area and weld width remained essentially unchanged for the three processes under the same welding conditions. It can also be seen from the figure that bead height, penetration depth, penetration area, deposit area and weld width all increase with wire feed speed for each process.

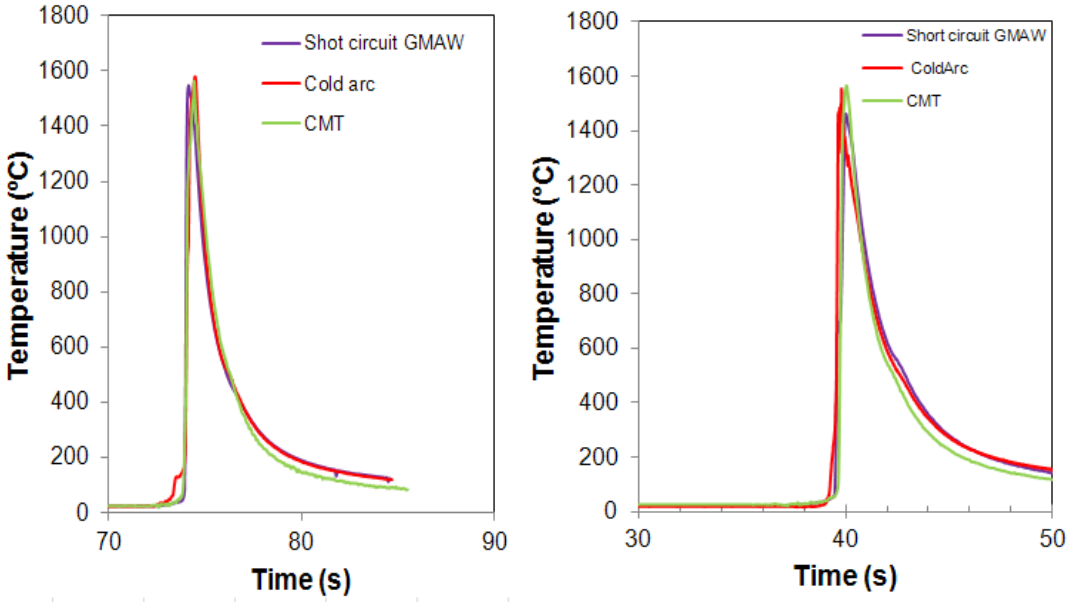

Figure 4-14: Weld thermal cycles for (left) 3 m/min and (right) 4 m/min WFS

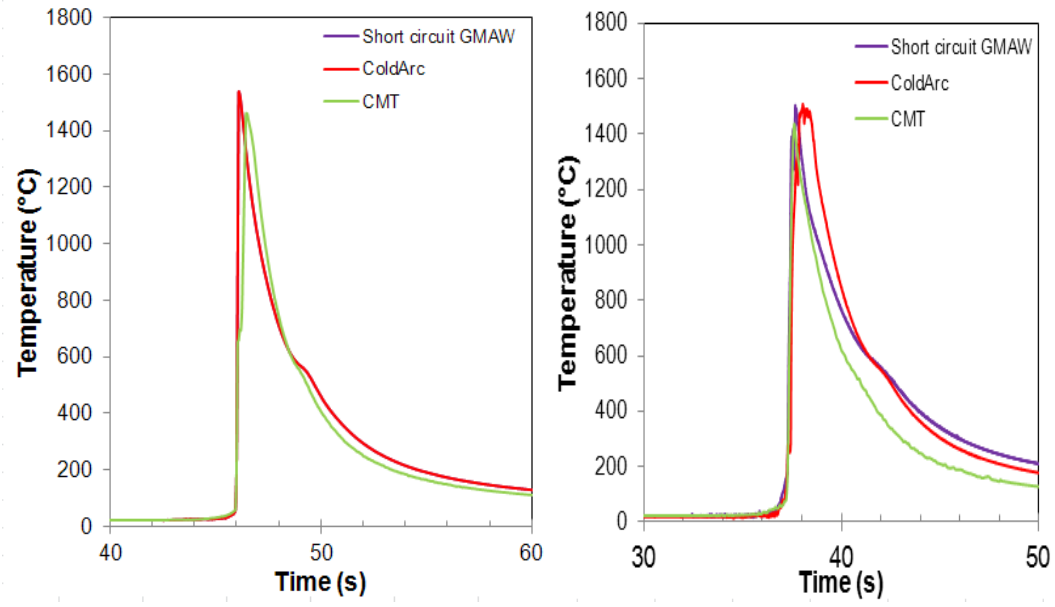

Figure 4-15: Weld thermal cycles for (left) 5 m/min and (right) 6 m/min WFS

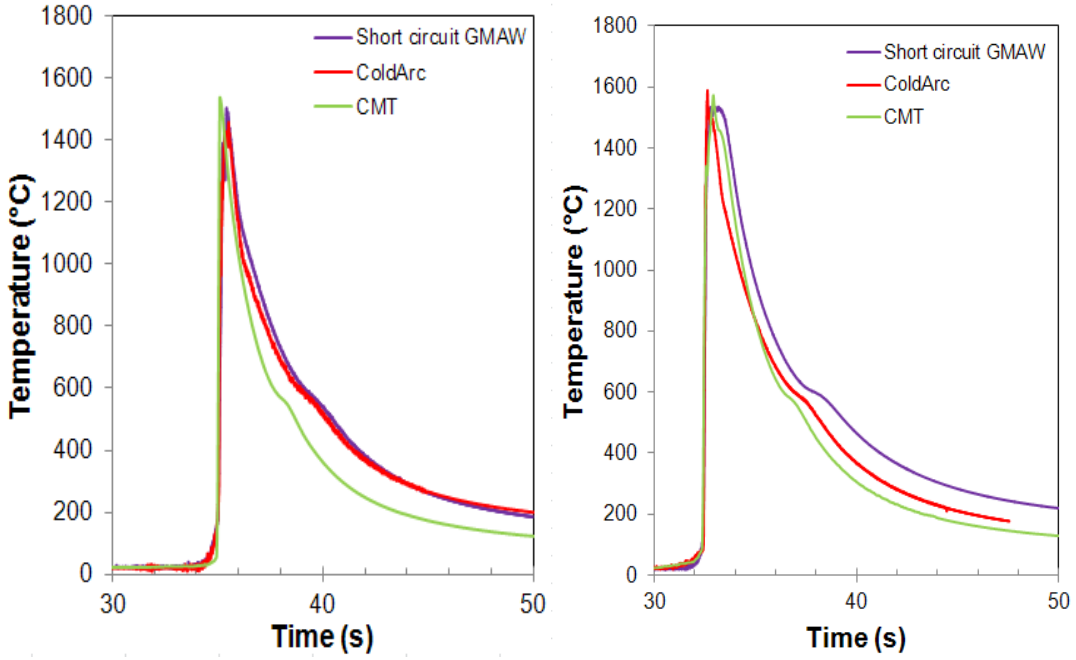

Figure 4-16: Weld thermal cycles for (left) 7 m/min and (right) 8 m/min WFS

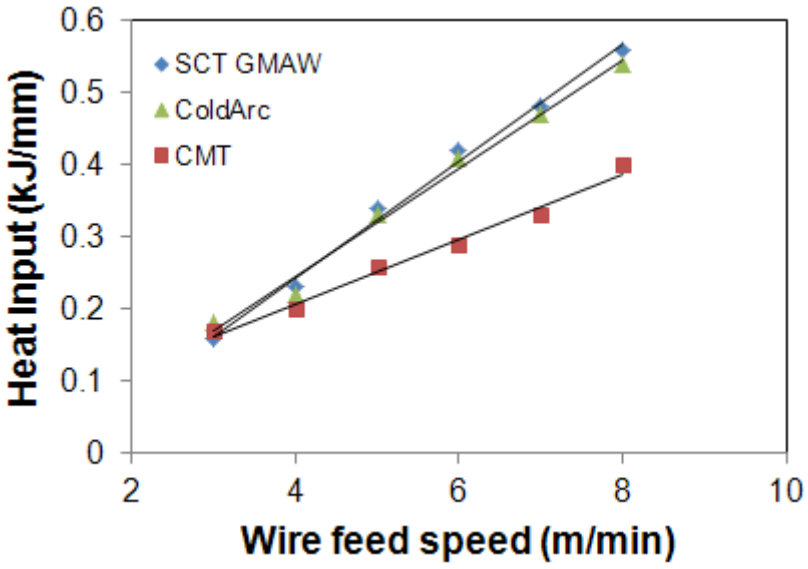

Figure 4-17: Relationship between WFS and heat input for the three processes

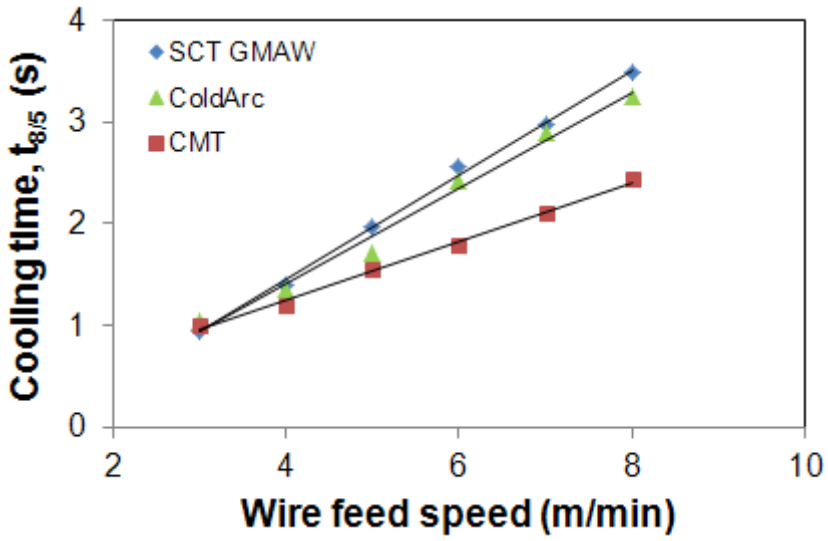

Figure 4-18: Relationship between WFS and cooling time for the three processes

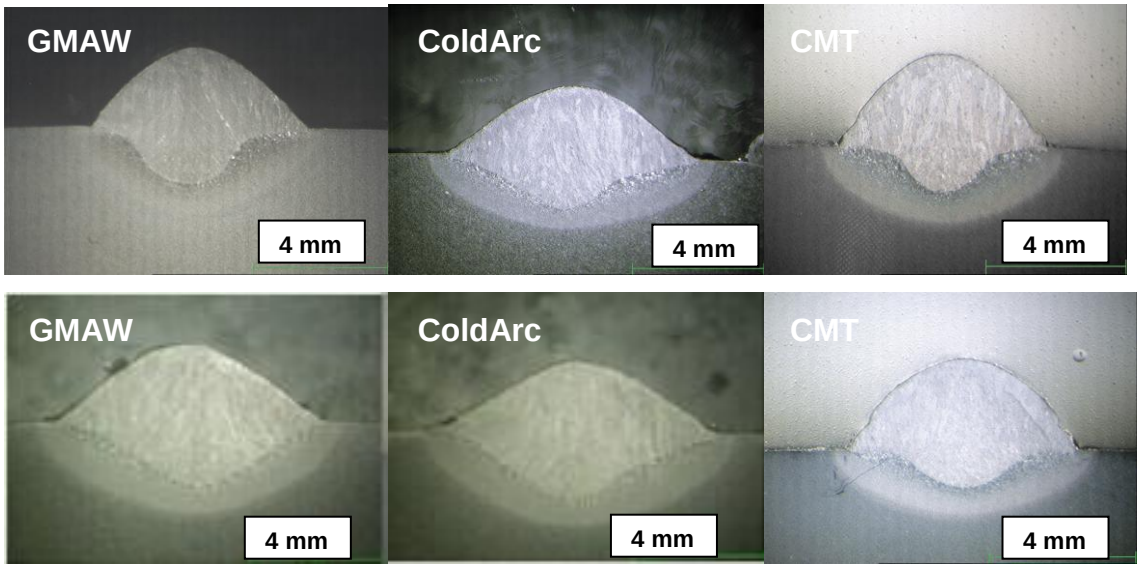

Figure 4-19: Macrographs showing the welds with (top) 5 m/min WFS and (bottom) 6 m/min WFS

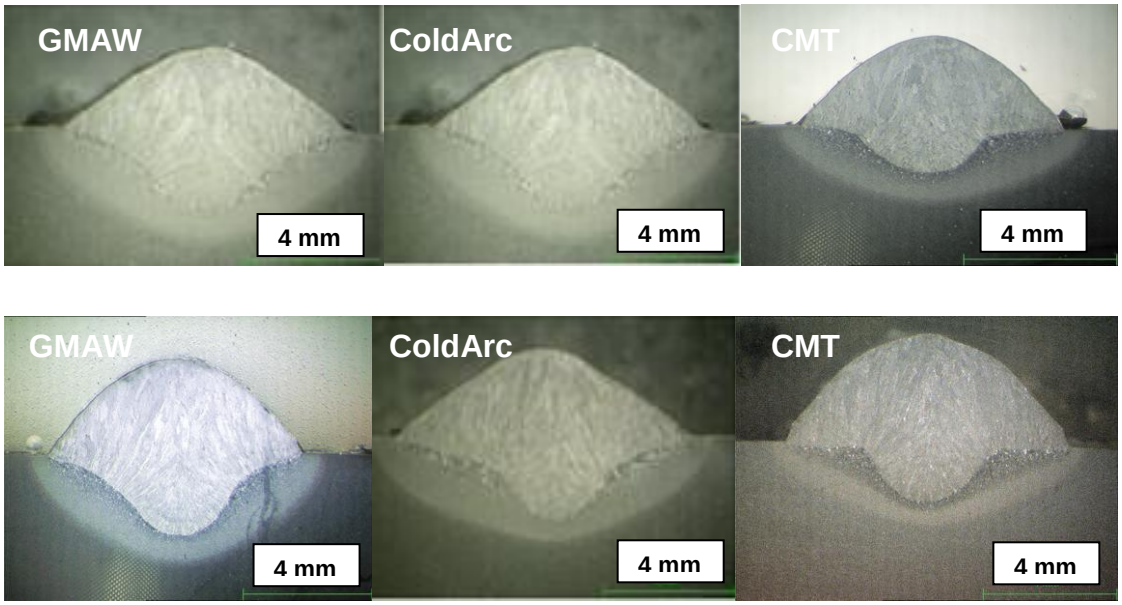

Figure 4-20: Macrographs showing the welds with (top) 7 m/min WFS and (bottom) 8 m/min WFS

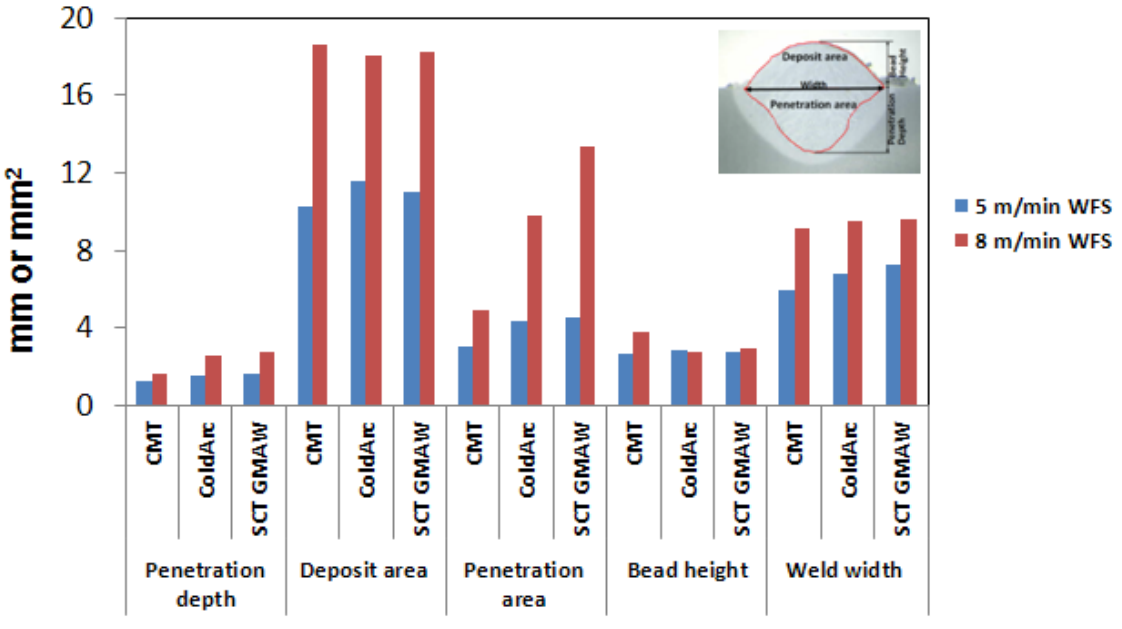

Figure 4-21: Weld bead profile of the three processes

4.6 Discussion of Results

A critical analysis and interpretation of the results is presented in this section. This will compare the research findings with previous studies where available.

4.6.1 Current and Voltage Waveforms

The variation of the current and voltage waveforms of the three processes as shown in Figure 4-8 to 4-13 is because of the different mechanisms by which short circuit or dip molten metal transfer occurs. The traditional short circuit GMAW is not a controlled process. As a result, molten metal droplet transfer and arc re-ignition is associated with process instabilities and spatter generation. The equipment manufacturers of the other two processes claim that they were designed to minimise these instabilities by controlling the detachment of the molten metal droplet through power source manipulation.

Goecke [50] and Pepe [103] observed that during traditional dip transfer GMAW, the welding wire touches the molten weld pool, momentarily extinguishing the arc. At the initiation of short circuit, the arc voltage drops rapidly to zero due to the low electrical resistance of the arc caused by the liquid bridge. Simultaneously, the welding current rises quickly to the short circuit current. The combined effects of electromagnetic pinch force and surface tension helps in molten metal droplet detachment thereby breaking the short circuit [103]. As soon as the liquid bridge breaks, the voltage rises quickly in order to re-establish the arc. According to Goecke [50], the arc re-ignition occurs with a high electrical power output, giving rise to significant spatter level or process instability. Rose [122] and Cramer and Dudziak [27] reported that during conventional short circuit GMAW the power input at the moment of short circuiting break-up is significantly high. This could cause the molten metal droplets to evaporate and be thrown out of the arc as spatter.

The above observations were also made for the short circuit GMAW process as shown in Figure 4-8. Furthermore, the process becomes increasingly unstable as the WFS increases (Figure 4-11 and Appendix B). Hermans and Ouden [59]

suggested that the short circuiting frequency increases with WFS. At lower WFS the frequency of the oscillating surface of the weld pool is greater than the short circuiting frequency and as a result the growing liquid column at the end of the wire is not making frequent contacts with the weld pool surface. But at higher WFS, they reported the reverse to be the case, and therefore more frequent short circuiting. This may be an indication of increasing instability as it was observed that spatter generation increased with WFS and the highest level was observed for the 8 m/min WFS weld.

Goecke [50] reported that the transient behaviour of the voltage of the ColdArc process is similar to that of the traditional short circuit GMAW as it drops to a minimum value corresponding to the peak current during the induced short circuit phase. But unlike the traditional short circuit GMAW, the process is highly dynamically regulated by a digital signal processor, which results in arc re-ignition occurring at a low power [50]. According to Goecke [50], a digital signal processor in the power source cuts-off power from the arc just before arc re-ignition in a time period of $1\mu s$. However, these features are only discernible at low WFS (3 m/min to 4 m/min). The ColdArc process was relatively more stable at low WFS for the given material and welding parameters investigated. At relatively higher WFS (5 m/min to 8 m/min) it becomes very unstable, and was observed to even generate more spatter than the short circuit GMAW. This may be because the process is designed for welding and brazing of very thin metal sheets used in the automobile industry. Goecke [50] reported brazing of 0.8 mm thick zinc-plated steel using the ColdArc with a current of 50 A and a voltage of 13.5 V. This suggests that the ColdArc process is optimised for low WFS and consequently low heat input application. Effectively, the ColdArc becomes a globular or spray transfer process at higher WFS.

The three phases of the CMT waveform as shown in Figure 4-10 are the peak current or arcing, short circuit and background current. The peak current phase or arcing phase shows a pulse of high current that corresponds to a constant arc voltage. The high current helps to ignite the welding arc and melt the welding wire through resistance heating to form a molten droplet [106]. In the

background current phase, the current is dropped to a lower value to prevent the molten droplet from growing thereby inhibiting globular transfer. This is kept constant until short circuit occurs. In the short circuit phase, the wire touches the weld pool and the arc voltage drops to zero, causing the arc to momentarily extinguish. Unlike in traditional short circuiting where electromagnetic pinch force and surface tension breaks the short circuit [103], the wire is mechanically retracted from the weld pool. This drawback force aids the molten droplet detachment and as a result, the welding arc re-igniting occurs at low electrical power to restart the cycle again.

Unlike the ColdArc process, CMT showed more clearly defined and regular short circuiting when the arc voltage drops to zero particularly at relatively low WFS (3 m/min to 5 m/min) as shown in Figure 4-10. The voltage drop corresponds to low background current, which results in significantly reduced short circuit current and spatter generation. But as the WFS increases it also becomes less stable as shown in Figure 4-13 with observed spatter generation. Nevertheless, the spatter levels were minimised even at high WFS when compared with the other two processes. This is because of the mechanical intervention in the wire feed. The wire retraction as short circuit is detected considerably reduces spatter that is usually associated with traditional short circuit GMAW. The increasingly random behaviour of CMT at high WFS could be because the frequency of wire feeding may be higher than 70 Hz, which is the frequency of the forward and backward movement of the wire. This means that the process benefit may be limited to low WFS. It is worth noting that CMT was designed for low heat input application, which may explain why it is more stable at low WFS.

4.6.2 Thermal Cycles, Heat Input and Weld bead profile

The thermal cycles of the weld metal shown in Figure 4-14 to 4-16 indicate that the CMT process cools faster than short circuit transfer GMAW and ColdArc processes as WFS increases. This is because the process heat input is the lowest as shown in Figure 4-17. The reduced heat input may be due to the low

average current of CMT relative to the other processes. On the other hand, the thermal input of the ColdArc is slightly lower than that of the conventional short circuit GMAW, which suggest that there is not much difference between the process behaviours for the range of welding parameters investigated. It is suggested that the similar heat input of the three processes at 3 m/min WFS, could be because at low WFS the process energy inputs are comparable.

Apart from reduction of weld spatter, another notable difference between CMT and short circuit GMAW is reduction in thermal input since there is virtually current-free molten metal droplet detachment. Hasselberg [56] reported that there is brief heat input by the arc during the arcing phase, which is reduced immediately the arc is extinguished during short circuiting, resulting in an alternating hot/cold weld pool. He also showed graphically that the thermal input of the CMT arc is lower than that of conventional short circuit GMAW.

The weld pool cooling times computed over the temperature range of 800 °C and 500 °C as shown in Figure 4-18 is a reflection of the overall low thermal inputs of the processes for the range of parameters investigated. The cooling times are relatively fast (the longest cooling time is about 3.5 s for the short circuit GMAW at 8 m/min WFS) and from the CCT curve of X65 pipeline steel (Figure 2-32), such fast cooling times will likely lead to the formation of martensitic microstructure.

The weld bead profile as shown in the macrograph (Figure 4-19 and 4-20) and Figure 4-21 signifies that the weld penetration profile of CMT is different from the other two processes in terms of shape and penetration depth. Pepe [103] reported similar weld bead shapes for CMT welds. The low penetration depth is a further indication of the low thermal input of CMT. Conversely, the weld bead profile of short circuit GMAW and ColdArc were quite similar for all WFS due to very close heat input values. Although the transient relationship of welding current and arc voltage showed a random behaviour with increasing WFS, it did not affect the weld bead profile. This further supports the suggestions by Nixon et al [93] and Richardson et al [117] that a welding process could be stable even though there is randomness in the electrical characteristics.

It can be established from the foregoing discussion that the overall heat input of short circuit GMAW and that of CMT and ColdArc are relatively low on account of the short circuit mode of metal transfer. Since hyperbaric GMAW is operated in short circuit mode, there is the need for additional heat input to extend the weld cooling time and reduce susceptibility to hydrogen assisted cracking. Based on the findings of this experiment it might be possible to use these processes under hyperbaric conditions with modification to the power source control circuit. Both were shown to produce welds without defects even though the process behaviour was different. However, if the choice is to be based on the level of spatter generated, CMT could be the ideal substitute for short circuit GMAW because it produced the lowest spatter levels even at high WFS. Nevertheless, it is necessary to investigate these processes further under high pressure conditions to make an informed decision.

The subsequent chapter will focus on the investigation of a laser as an additional heat source to CMT welding.

4.7 Conclusion

The following conclusions can be made from this experiment:

- At one atmosphere the short circuit GMAW and ColdArc produced almost the same heat input and identical weld beads, which were different from that of CMT

- The overall heat input of the processes over the range of parameters investigated is relatively low, which is indicative of short circuit transfer GMAW. The weld pool cooling time ($t_{8/5}$) and weld bead profile are a reflection of this.

- The electrical characteristics of the three processes showed that welding current and arc voltage waveform were more stable at low wire feed speed. But as wire feed speed increases the behaviour becomes more random. However, this did not affect the quality of the welds produced.

- Based on the experimental findings, either the CMT or ColdArc can be used as alternatives to short circuit GMAW because both produced defect free welds. But in terms of weld spatter levels, CMT will be the obvious choice since it produced the lowest spatter. However, it is necessary to investigate these processes further under high pressure conditions.

5 Laser Assisted GMAW (CMT) Trials at One Atmosphere

Scope

The low heat input of hyperbaric GMAW, coupled with the potential presence of water vapour inside the chamber environment and restraint imposed on the solidifying weld pool by the thick pipeline sections are conditions that will favour hydrogen assisted cracking. Also, the surrounding cold sea water at a temperature of about 4 °C renders pre-heating almost ineffective as it acts as a heat sink. These exacerbate the problem of low heat input and high cooling rate of hyperbaric GMAW. Also spatter generation is a concern as already mentioned in previous chapters.

This chapter investigates the use of a laser in conduction mode to provide additional heating to the GMAW process. The laser is expected to modify the weld pool thermal cycle thereby extending the cooling and solidification time such that dissolved weld hydrogen will have enough time to diffuse out before the weld solidifies. Also, a controlled dip transfer GMAW power source (CMT) was used to minimise weld spatter generation. Several single bead-on-pipe welds were performed on the test specimen.

The weld pool thermal cycles and resulting cooling times were determined by embedding thermocouples in the pipeline steel section. Microstructure analysis and micro hardness tests were performed to understand the metallurgical phase formation and hardness profiles respectively. An experimental error analysis is discussed, followed by the presentation and discussion of results.

5.1 Aim and Objectives

The experiments presented in this chapter are the main theme of this thesis. The aim is to investigate the laser assisted GMAW (CMT) process that will provide additional heat input to reduce hydrogen assisted cracking tendency and lower weld spatter in hyperbaric welding operations. The presented work was carried out to optimize the laser parameters at one atmosphere. The optimised parameters should be further evaluated under hyperbaric conditions.

The key objective is to evaluate the use of a laser in conduction mode to control weld thermal cycle in GMAW (CMT) process, and to assess the improvements offered.

5.2 Materials and Equipment

The materials used for the experimental trials, which include: pipeline steel and welding consumables are presented. The equipment used for the welding trials, weld instrumentation, metallurgical characterisation and mechanical tests are also presented.

5.2.1 Materials

5.2.1.1 Steels

The same X65 pipeline steel with chemical composition given in Table 3-1 of chapter 3 was used for these experiments.

5.2.1.2 Welding Wire

The G4Si1welding wire with chemical composition given in Table 4-1 of chapter 4 was also used for this experimental trial.

5.2.1.3 Shielding Gas

Refer to section 4.2.1.3 of chapter 4 for the shielding gas used in this study.

5.2.2 Equipment

The equipment used for the experimental trials is presented in this section. These include the Fronius TPS 5000 CMT welding power source described in chapter 4, Fanuc M-710iB 45 Robot and IPG YLR-8000 Fibre Laser. The other equipment was for weld instrumentation, metallurgical characterisation and mechanical testing.

5.2.2.1 Fanuc M710iB 45 Robot

The Fanuc M 710iB 45 is a six axes robot designed for manufacturing and systems processes [121]. This model is electric servo-driven with a 45 kg payload capacity [121]. The robot features includes: H-Reach 1706 mm, repeatability - $\pm$0.07 mm and mass of 600 kg [121]. An additional one axis purpose built

translation stage was incorporated, making it a seven axis welding system. The translation stage moves in the negative and positive x-axis and is used for positioning of the work piece.

The complete robot system has a Fanuc RJ3iB controller and a pendant with touch screen option. Figure 5-1 shows the complete welding robot system.

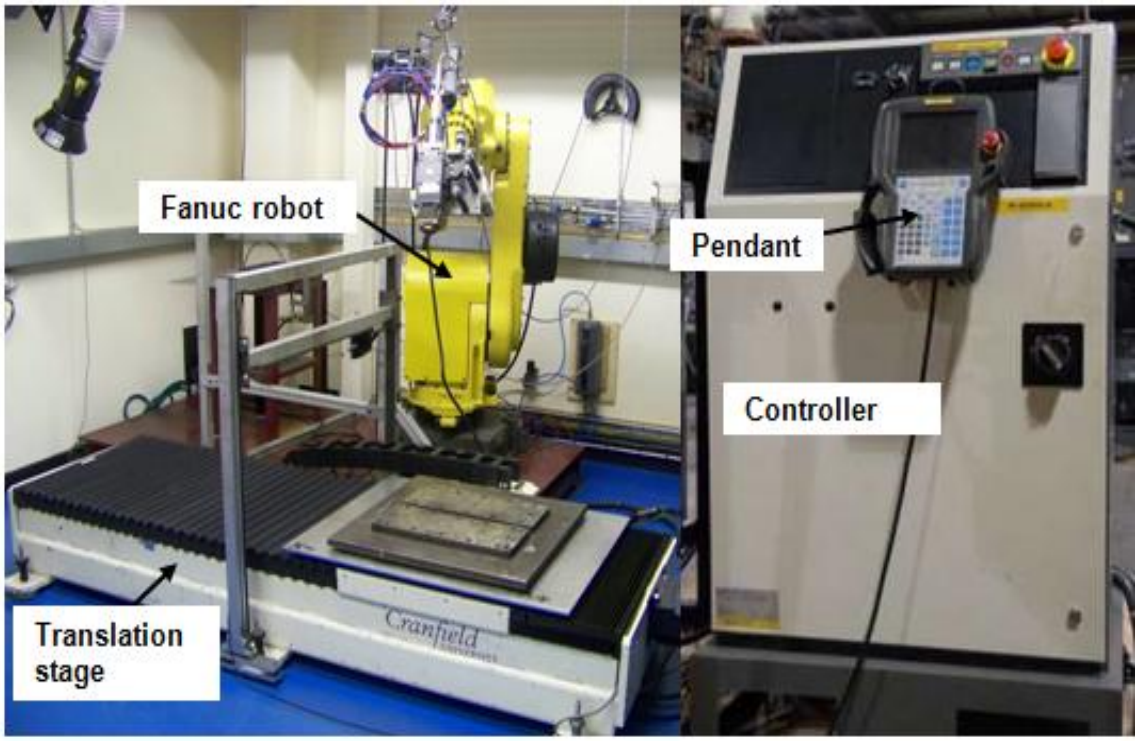

Figure 5-1: Photograph of the complete Fanuc welding robot system showing the robot, controller and pendant

5.2.2.2 IPG YLR-8000 Fibre Laser

The IPG YLR-8000 laser system shown in Figure 5-2 is a diode-pumped continuous wave (CW) ytterbium fibre laser of near infrared spectral range. This is a high power fibre laser with a maximum output of 8 kW and emission wavelength of 1.070 μm [69]. It has a unique combination of high power, beam with quality fibre delivery. The configuration includes a compact water cooling unit.

The laser is produced from an active optical fibre and semiconductor diode, representing a fusion of the two most innovative and advanced laser technology

[69]. The active fibre is pumped using a single emitter semiconductor diode as the light source. The fibre is doped with rare earth ions, allowing for very bright light from a very small core [69].

Figure 5-2: Photograph of the laser system

5.2.2.3 Weld Instrumentation

Refer to section 3.2.2.4 of chapter 3 for the instruments used for weld instrumentation, measurement of welding current, arc voltage and wire feed speed , and generation of weld thermal cycles.

5.2.2.4 Characterisation

The instruments used for the metallurgical and mechanical characterisations are the same as those in section 3.2.2.5 of chapter 3.

5.3 Experimental Method

5.3.1 Welding Trials with Constant CMT Parameters

Fifty instrumented bead-on-pipe welds were made on (165 × 60 × 25) mm sections of X65 pipeline steel using the 8 kW ytterbium fibre laser and the GMAW (Fronius TPS CMT) power source. The laser beam was transmitted from the source to the laser head through a 300 micron diameter optical fibre and used in a defocused condition on the test piece. The laser head was mounted on the Fanuc robot head manipulator, and the focal length of the focusing lens was 500 mm. The CMT torch was fixed at an angle of 78.5° to the horizontal while the laser head was positioned at 66° as shown in Figure 5-3 and 5-4. The work piece was clamped on a jig that was fixed to the translation stage. The separation distance between both heat sources, referred to here as process distance was measured by allowing the tip of the filler wire to just touch the edge of guide laser beam (Figure 5-4). This position was denoted as the zero process distance and subsequent distances were measured by moving the laser beam away from the wire tip at measured incremental values. The laser parameters: beam diameter and power, and the process distance were varied. Wire feed speed and welding speed were kept constant at 5 m/min and 0.42 m/min respectively. Argoshield heavy shielding gas was fed through the CMT torch at a flow rate of 15 l/min and a CTWD of 15 mm was used. The complete experimental matrix is given in Table B-3 of Appendix B.

The experimental programme was designed to establish the laser process parameter range that will bring about optimal reduction of the weld metal cooling rate without compromising weld quality.

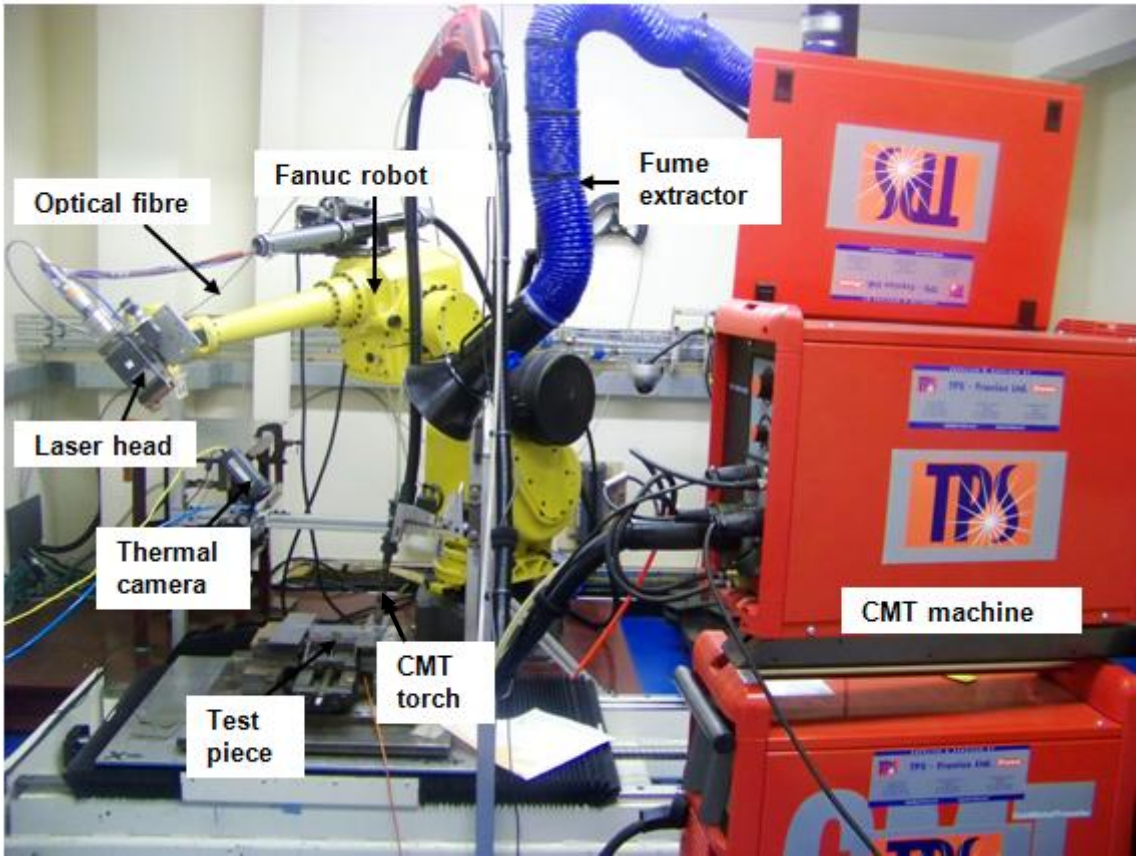

Figure 5-3: Experimental set-up of laser assisted CMT process

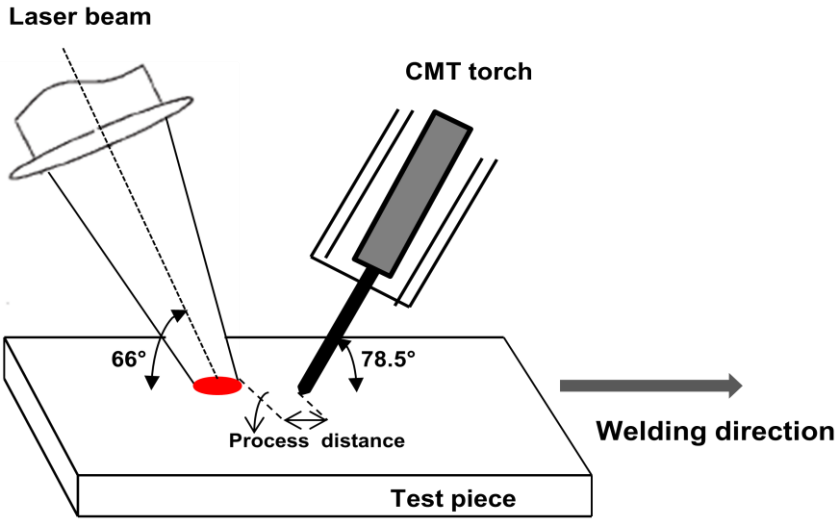

Figure 5-4: Schematic illustration of experimental set up

5.3.2 Welding Trials with Variable CMT Parameters

The same experimental set-up and welding conditions were used for this trial but the laser parameters were kept constant while the CMT wire feed speed was varied from 5 m/min to 8 m/min in order to investigate the effect of increasing wire feed speed on the weld cooling time. Four instrumented bead-on-pipe welds were made and the experimental data is given in Table B-4 of Appendix B. The laser parameters used were 3 kW laser power, 20 mm beam diameter and 20 mm process distance.

5.3.3 Welding Trials with Elliptical Laser Beam

The laser beam produced with the setup shown in Figure 5-4 was fairly circular in shape. For this trial the laser head was inclined at an angle of 30^{o} to give a more elliptical shaped beam. This was used to investigate the effect of beam shape on the weld cooling time.

After establishing the optimised laser parameters with the previous setup, four welds were made using the elliptical beam. Two welds were made with 6 kW laser power and 20 mm laser spot size at 20 mm and 0 mm process distances, while the other two were made with the same parameters, but only changing the laser power to 3 kW. Apart from the beam shape, the setup is essentially the same as the previous one.

5.3.4 Generation of Weld Thermal Cycle

R-type thermocouples were embedded in the test piece similar to Figure 3-10 (left) in chapter 3. The weld thermal cycles were produced from the thermocouple data generated with the Scopecorder 750.

5.3.5 Measurement of Heat Input and Cooling Time

The ScopeCorder was also used for real time measurement of instantaneous welding current and arc voltage, which were used to calculate the weld heat

input according to equations (3-1). The weld cooling time from 800 °C to 500 °C was derived directly from the time-temperature data.

5.3.6 Metallurgical Characterisation

Refer to section 3.2.2.5.1 of chapter 3 for the macrostructure and microstructure examination.

5.3.7 Hardness Test

The hardness test was performed as described in section 3.2.2.5.2 of chapter 3 using the micro hardness equipment shown in Figure 3-6.

5.4 Experimental Error

The experimental errors and analysis described in section 3.4 of chapter 3 were also applicable here. In addition, the method of determining the process distance could be another source of errors in this experiment.

The process distance was measured by bringing the tip of the welding wire to touch the edge of the guide laser. This position was denoted as 0 mm process distance. The laser head was subsequently moved away at incremental values of 5 mm to measure other process distances. There is a possibility of errors being introduced because the edge of the guide laser is a bit blurred and therefore, the wire tip may not repetitively be positioned at the edge of the guide laser.

In order to minimise this error, the light was turned off in the welding bay before the wire tip was positioned at the edge of the guide laser. The measurement was then made with a flash light. The reason for this was because the outline of the guide laser was much clearer in the dark and therefore a more accurate positioning of the wire tip at the edge of the guide laser was possible.

5.5 Results

This section presents the experimental results and their interpretation. The discussion of the results is given in the following section.

5.5.1 Weld Thermal Cycles

A plot comparing the time-temperature relationship of a CMT weld with that of an equivalent laser assisted CMT weld of the same wire feed speed of 5 m/min is shown in Figure 5-5. This clearly depicts how the CMT weld thermal cycle is modified by the addition of a laser, resulting in the extension of weld cooling time. The position of both heat sources relative to each other (process distance) is shown in Figure 5-6 to significantly change the shape of the laser assisted CMT welds thermal cycles.

The weld thermal cycles with different CMT wire feed speed and constant laser parameters of 3 kW laser power, 20 mm beam diameter and 10 mm process distance is given in Figure 5-7. It can be seen that as the wire feed speed increases the weld cooling time also increases due to higher heat inputs.

Figure 5-8 and 5-9 compare the weld thermal cycles of a circular laser beam with that of an elliptical laser beam under the same welding conditions. The plots suggest that there is little difference between the weld cooling behaviour for both beam shapes especially at 0 mm process distance.

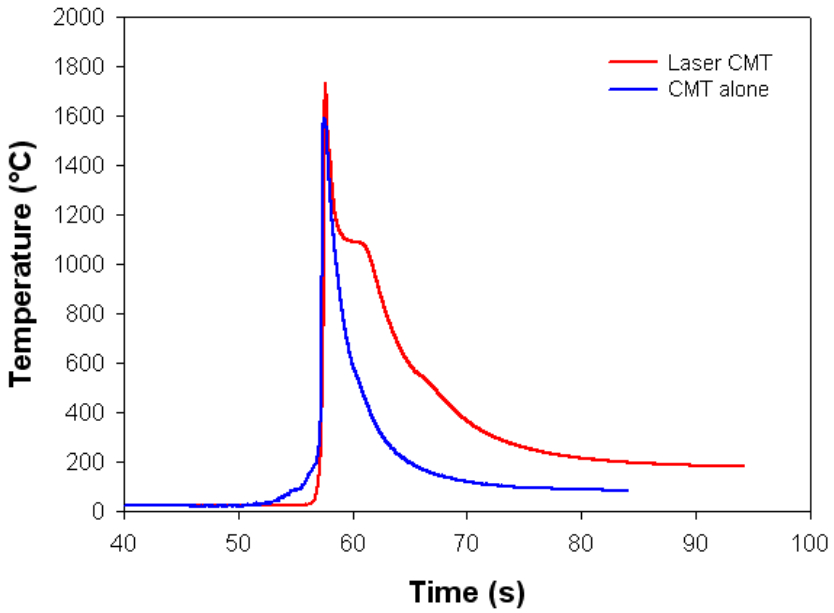

Figure 5-5: The thermal cycle of CMT with an equivalent laser assisted CMT weld of 6 kW laser power, 20 mm beam diameter and 0 mm process distance

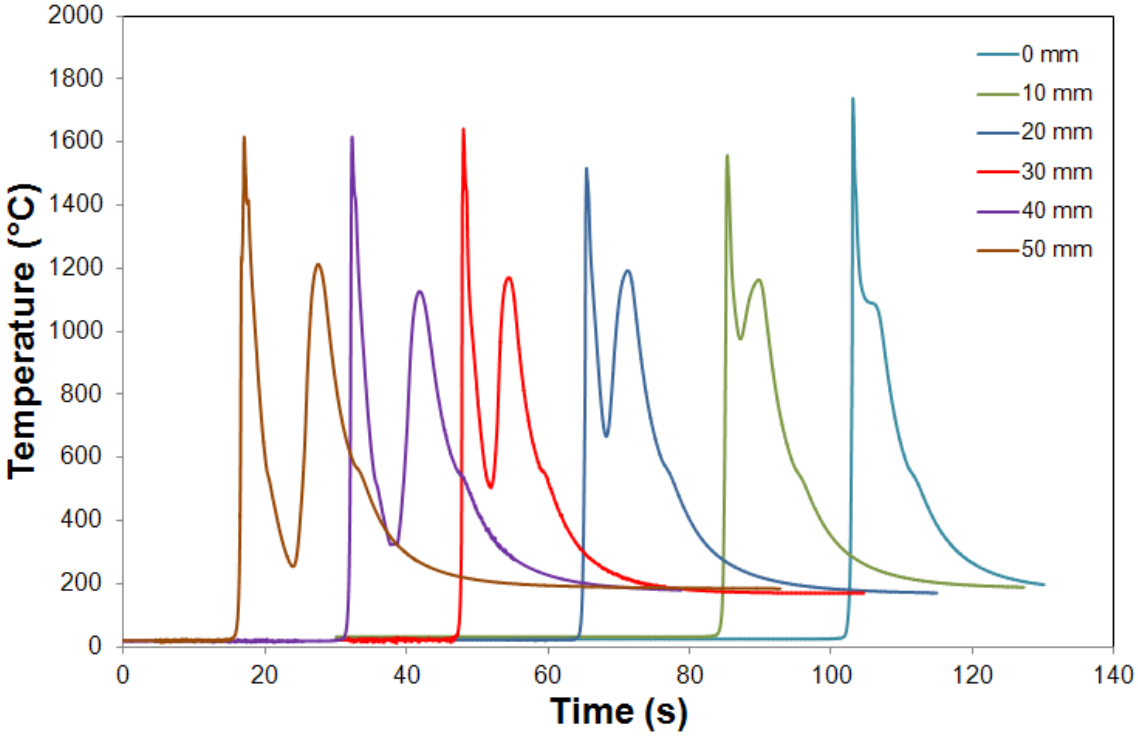

Figure 5-6: Effect of process distance on the thermal cycles of welds made with 20 mm laser beam diameter and 6 kW laser power

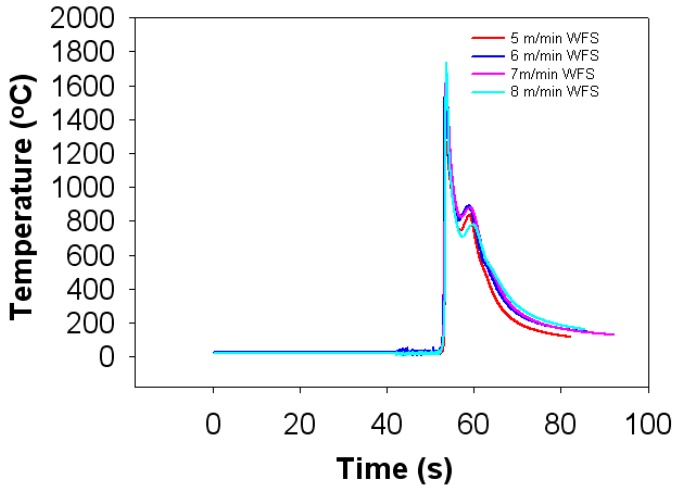

Figure 5-7: Thermal cycles of welds with 3 kW laser power, 20 mm beam diameter, 10 mm process distance and varying wire feed speeds

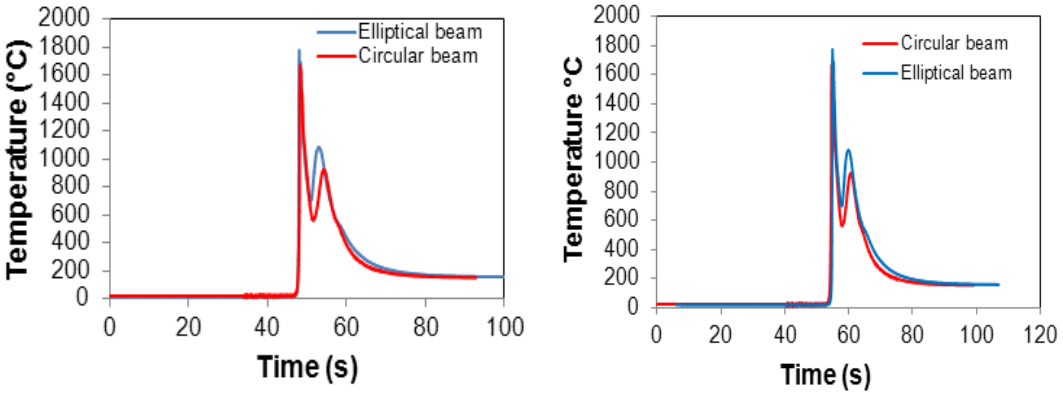

Figure 5-8: Thermal cycles of different beam shapes (left) 6 kW and (right) 3 kW laser power with the same 20 mm beam diameter, and 20 mm process distance

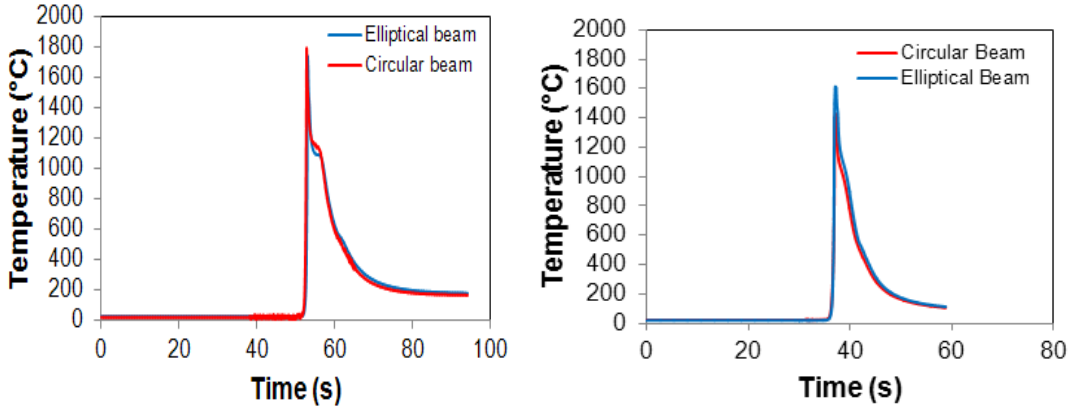

Figure 5-9: Thermal cycles of different beam shapes (left) 6 kW and (right) 3 kW laser power with the same 20 mm beam diameter, and 0 mm process distance

5.5.2 Effect of Laser Parameters on Weld Cooling Time and Time at High Temperature for Constant CMT Parameters

Figure 5-10 gives an indication of the influence of beam diameter and process distance on the weld cooling time between 800°C and 500 °C. It can be seen that the larger beam diameter favours prolonged weld cooling time and consequently slower cooling rate. Suder et al [141] reported that bigger beam size gives longer interaction time and therefore higher specific point energy according to equations (5-1) and (5-2). Therefore, the 20 mm beam diameter produced the longest cooling time for the three beam sizes investigated. It can also be observed from the figure that changes in the process distance showed a gradual increase in cooling time as the heat sources are brought close together.

The Specific point energy, $E_P = \frac{2rP}{v}$ (5-1)

And the interaction time, $t_i = \frac{2r}{v}$, (5-2)

where P, r and v are laser power, beam radius and welding speed respectively.

A relationship between weld cooling time and specific point energy is given in Figure 5-11. This indicates an increase in cooling time with specific point energy because of longer interaction time. However, this effect is more pronounced at 6 kW laser power. Figure 5-12 is a plot of laser power against cooling time, which indicates that increasing the laser power provides more energy that extends the weld cooling time.

The addition of a laser to the arc process extends the weld cooling time as shown in Figure 5-6 and also prolongs the total weld residence time at a high temperature. This is evident in Figure 5-13, which shows that the residence time over 300 °C increases with the process distances.

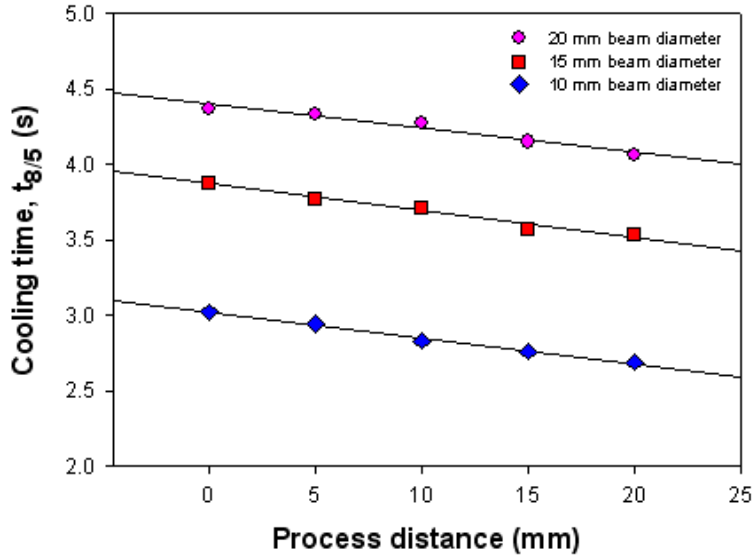

Figure 5-10: Effect of beam diameter and process distance at constant (6 kW) power on cooling time

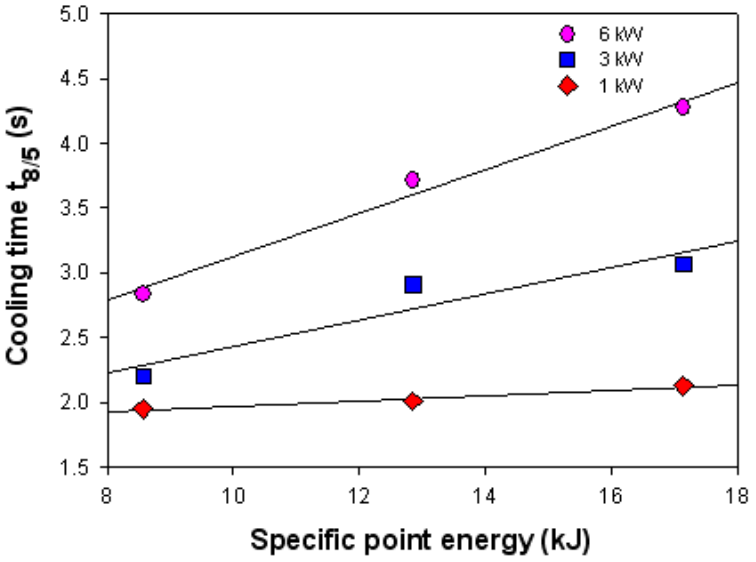

Figure 5-11: Effect of specific point energy on cooling time for 6 kW laser power and 5 mm process distance

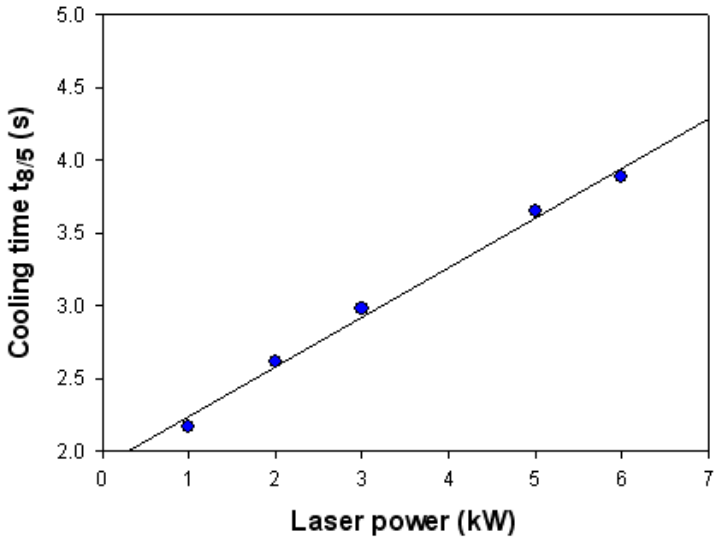

Figure 5-12: Effect of laser power on cooling time

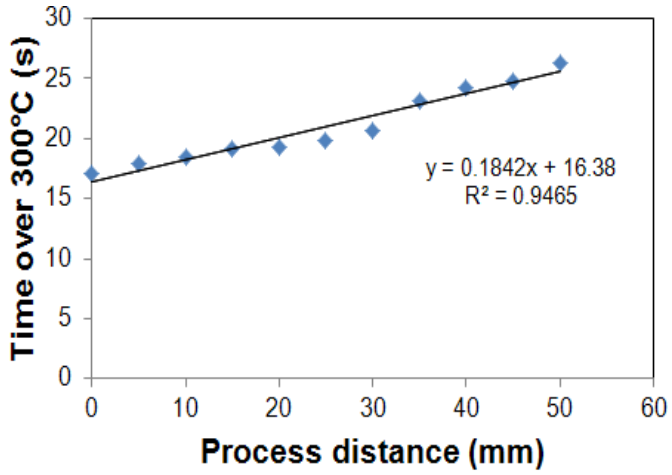

Figure 5-13: Relationship between process distance and total residence time over 300°C for welds with 6 kW power and 20 mm beam diameter

A 3-D response surface and contour plot presented in Figure 5-14 gives the relationship between the laser parameters and weld cooling time. It is shown that increasing laser power and beam diameter favours longer cooling time. However, the effect of laser power is more pronounced than beam diameter. Also, the interaction between the parameters is very clear in establishing the longest cooling time of 4.37 s given by (6 kW laser power and 20 mm beam diameter), and the shortest cooling time of 1.79 s given by (1 kW laser power and 10 mm beam diameter).

However, because of the marginal changes in cooling time with process distance (Figure 5-10), the model considered the effect of process distance as not statistically significant hence its interaction with other parameters was not established.

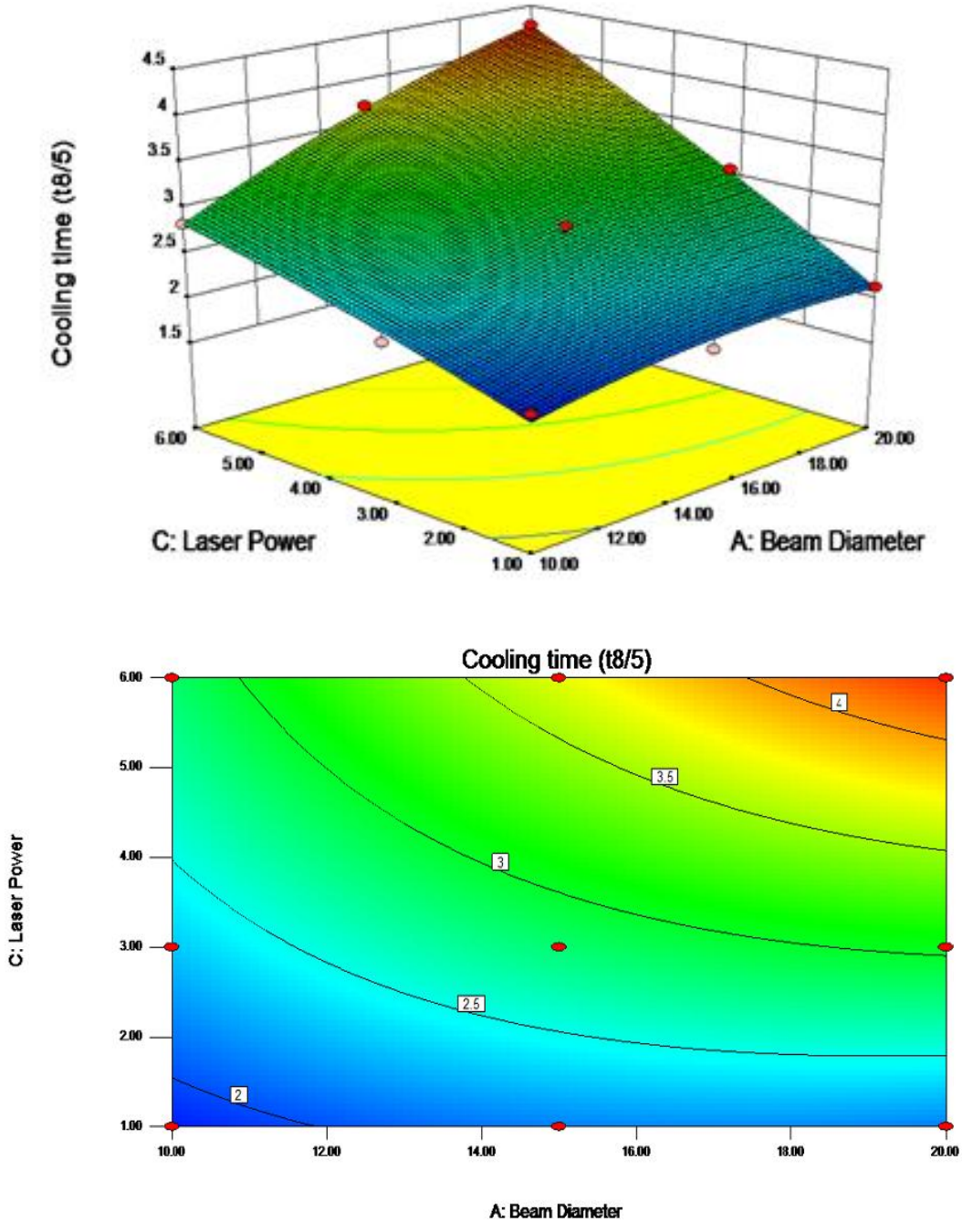

Figure 5-14: A response surface and contour plot showing the effect of laser power and beam diameter interaction on cooling time at 10 mm process distance

5.5.3 Effect of Wire Feed Speed on Weld Cooling Time for Constant Laser Parameters

A relationship between weld cooling time and wire feed speed for constant laser parameters and process distance is given in Figure 5-15. This shows that increasing the wire feed speed to welding speed ratio leads to longer weld cooling time. This is because for the GMAW (CMT) process, wire feed speed is integrated in the process. As a result higher wire feed rate will result in higher heat input to melt the additional wire. Higher wire feed speed to travel speed ratio means more wire deposition per unit length.

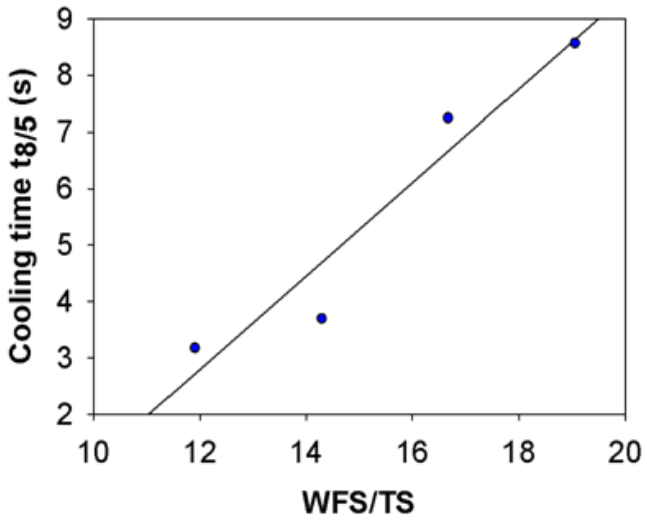

Figure 5-15: Effect of wire feed speed to travel speed ratio on the cooling time for laser assisted CMT welds with constant laser parameters

5.5.4 Metallurgical Characterisation

5.5.4.1 Macrostructure Examination and Weld Quality

The macrostructure of laser assisted CMT welds with 20 mm process distance is compared with that of a CMT weld of the same wire feed speed of 5 m/min as shown in Figure 5-16. There were no observed defects in the laser assisted CMT welds. Similar macrographs comparing CMT welds of variable wire feed speed with the equivalent laser assisted ones are given in Figure 5-18 and Figure 5-18. As can be observed in Figure 5-16 the laser did not influence weld

penetration depth. Nevertheless, the laser assisted weld has a reduced bead height and smooth transition between the weld toe and pipe material. The laser serves as post weld heating, reheating and elongating the weld bead and extending the cooling time.

The laser influence on the CMT weld bead shape depends considerably on the power. As can be seen in Figure 5-18, the effect of laser heating is not as pronounced as that of Figure 5-16. While 6 kW laser power elongated the weld pool, 3 kW did not produce the same effect for the same beam diameter and process distance. Clearly the heat affected zone of the laser assisted weld is wider than that of CMT weld alone because of the additional thermal input by the laser. Table B-5 in Appendix B represents the measured weld bead profiles of CMT and laser assisted CMT welds.

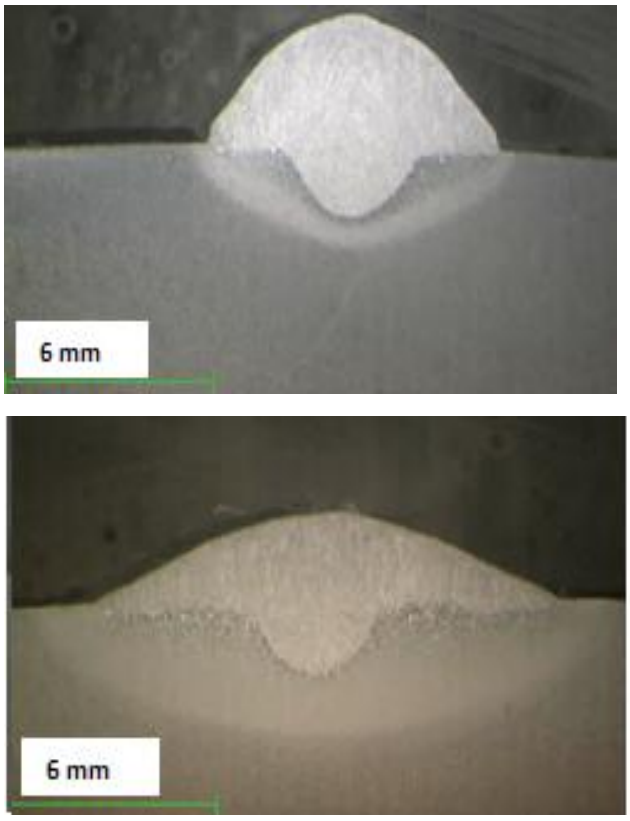

Figure 5-16: Macrographs of CMT weld with 5 m/min WFS (top) and equivalent laser assisted weld of 6 kW laser power, 20 mm spot size and 20 mm process distance (bottom)

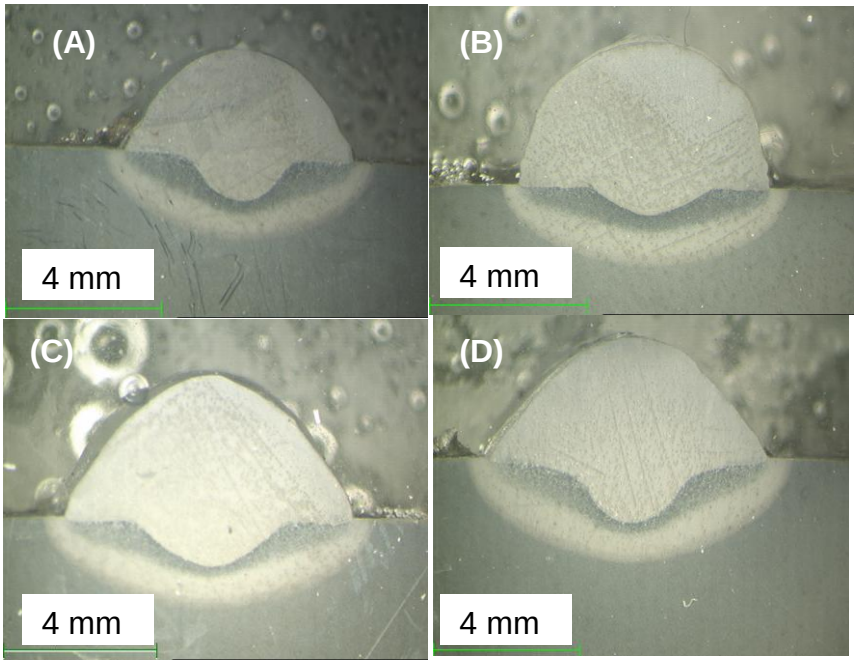

(A) 5 m/min WFS, (B) 6 m/min WFS, (C) 7m/min WFS, (D) 8 m/min WFS

Figure 5-17: CMT welds with different WFS and 7 mm/s welding speed

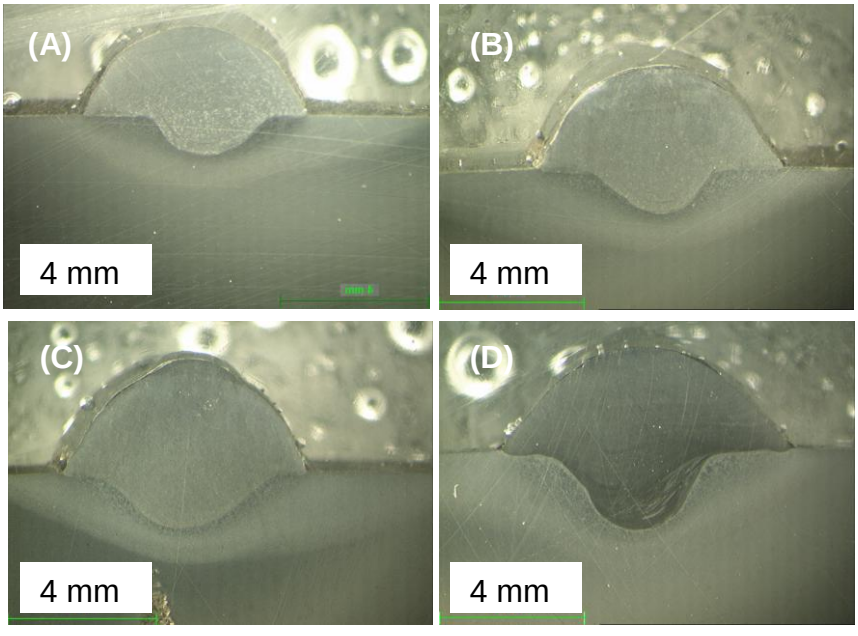

(A) 5 m/min WFS, (B) 6 m/min WFS, (C) 7m/min WFS, (D) 8 m/min WFS

Figure 5-18: Laser assisted CMT welds with 3 kW laser power, 20 mm beam diameter and 20 mm process distance

5.5.4.2 Microstructure Examination

The microstructures of laser assisted CMT welds and those of the equivalent CMT welds are presented in Figure 5-19 and Figure 5-20. These distinctly show the different microstructural constituents of the weld metal and HAZ. The different regions of the HAZ are also clearly highlighted in Figure 5-19. The same microstructural constituents can be observed in both the CMT and laser assisted welds for the different microstructures shown. However, the HAZ of the laser assisted CMT weld is wider than that of CMT. It can be seen that while the CMT micrograph in Figure 5-19 (top) shows the HAZ region and part of the base metal, the laser assisted CMT micrograph in Figure 5-19 (bottom) revealed only the HAZ region even though both micrographs were taken with the same magnification. Apart from this, the micrographs look quite similar for both types of welds. The dark marks in the micrographs may be due to corrosion caused by the etchant and not part of the microstructures.

The different structures of the HAZ as seen in Figure 5-19, depends on the heat input, cooling rate, time at peak temperature, and distance from the fusion boundary between the weld metal and HAZ. These are the coarse grained HAZ (CGHAZ), fine grained HAZ (FGHAZ), intercritical HAZ and subcritical HAZ respectively. This is a typical HAZ microstructure of carbon manganese steels for low heat input processes as reported by Eroglu et al[36].

The coarse grained HAZ (CGHAZ) depicted in Figure 5-20 is the closest region to the fusion boundary and as such the peak temperature is high enough to cause transformation. Depending on the heat input and cooling rate, different microstructures can be formed. However, the degree of coarsening and hardness distribution is shown to vary. The hardness distribution is presented in the next section.

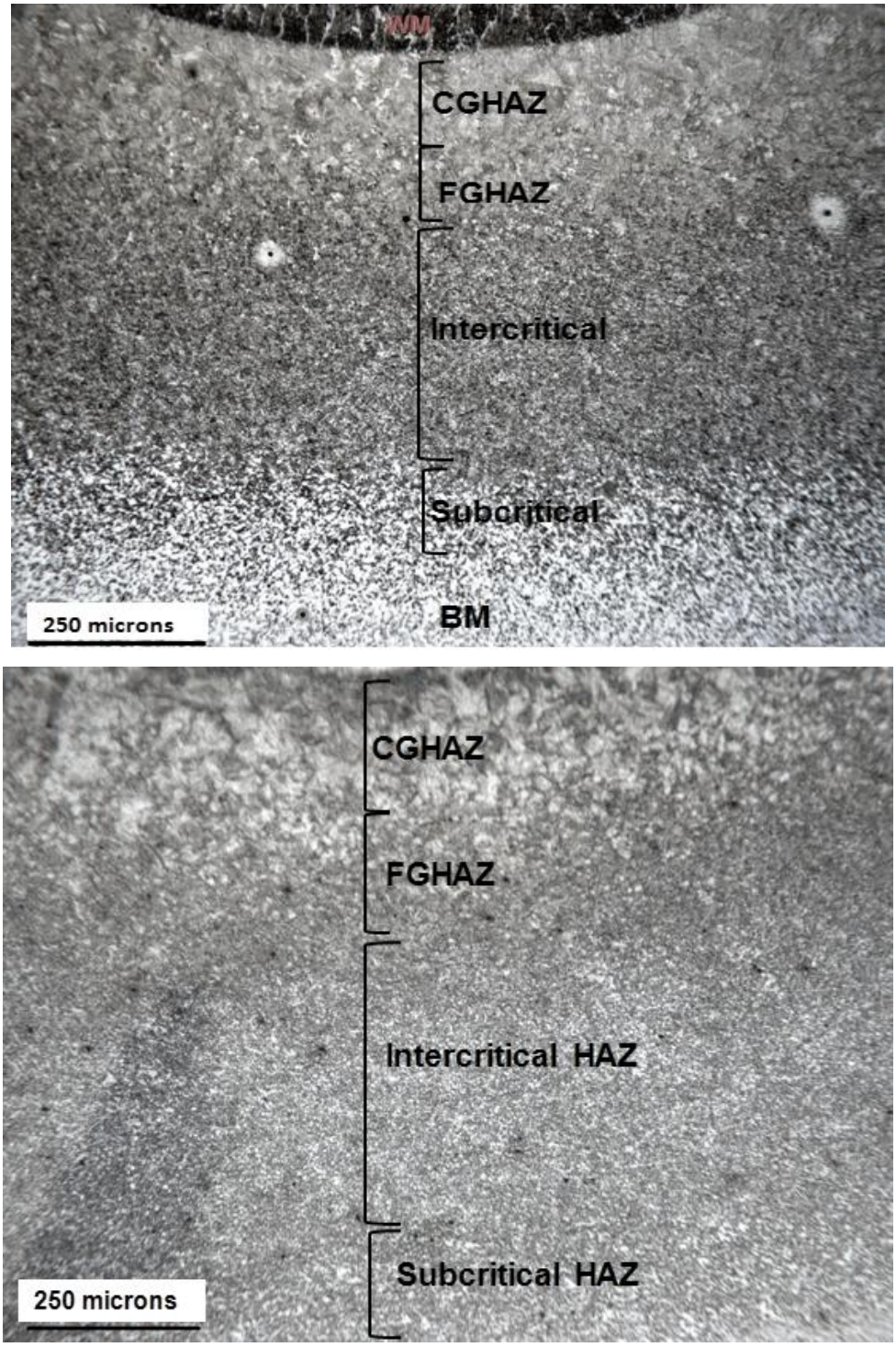

Figure 5-19: Microstructure of (top) CMT and (bottom) laser CMT welds with 5 m/min WFS, 6 kW laser power, 20 mm beam diameter and 20 mm process distance

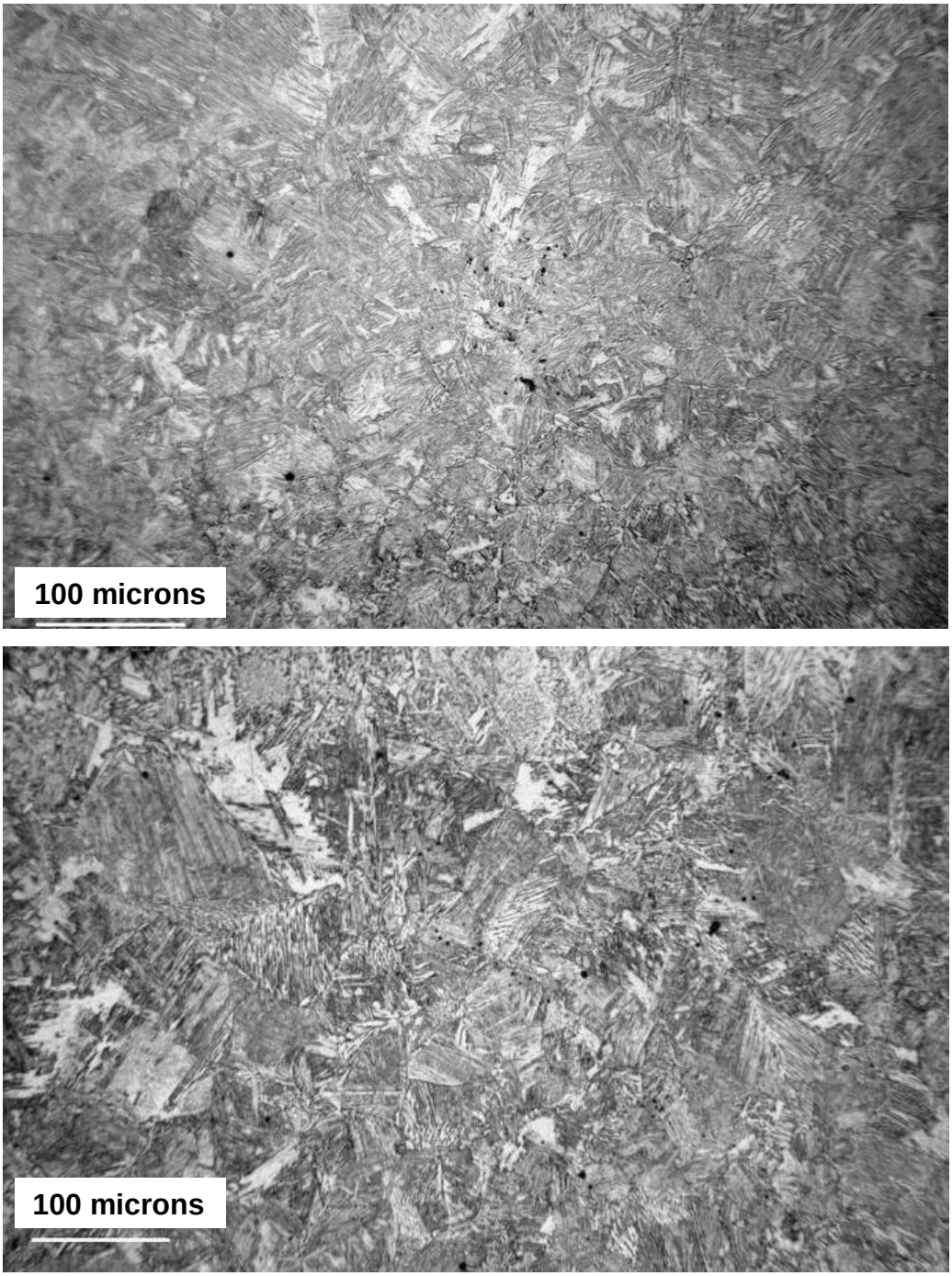

Figure 5-20: Coarse grained HAZ microstructure (left) CMT and (right) laser CMT weld with 5 m/min WFS, 6 kW laser power, 20 mm beam diameter and 20 mm process distance

5.5.5 Hardness Test

Figure 5-21 to Figure 5-24 shows the Vickers micro hardness ($HV_{0.5}$) mapping of the CMT, laser assisted CMT with 3 kW laser power and laser assisted with 6 kW power. A plot comparing the hardness distribution across the welds is also given in Figure 5-24. It can be seen that the hardness distribution follows a similar pattern for all the welds. This shows the hardness of the weld metal (region having a mixture of green and yellow colours), HAZ region (band of red, yellow and light blue), and the parent metal (dark blue).

In all cases, the maximum hardness occurred at the coarse grained HAZ, which is closest to the fusion boundary. However, there is a progression of hardness across the HAZ region with the lowest value at the subcritical HAZ (region just before the dark blue colour). This is followed by the intercritical HAZ (light blue region), and the fine grained HAZ (yellow region). The hardness of the weld metal followed that of the HAZ, while the lowest was the parent metal.

It is clearly shown that the addition of a laser to CMT significantly lowered the weld peak hardness. However, this depends on the laser power for a constant beam diameter and process distance. For example, the addition of 6 kW laser power reduced the peak hardness from about 420 HV to about 320 HV, while 3 kW laser power reduced it to about 340 HV as shown in Figure 5-24. Nevertheless, both laser powers were shown to significantly reduce the peak hardness.

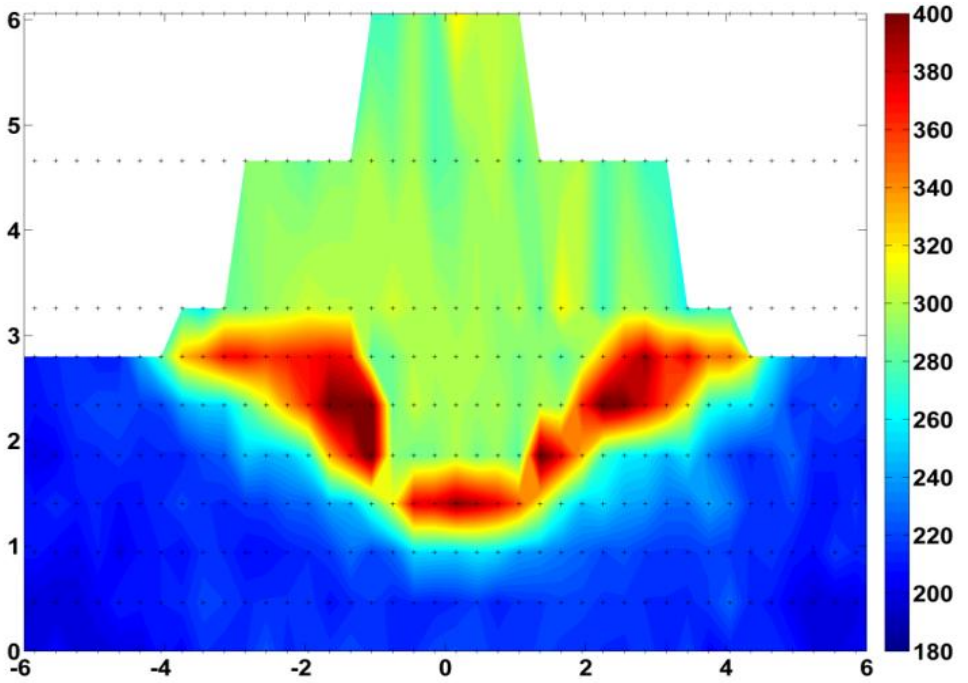

Figure 5-21: Vickers micro hardness map of the 5 m/min WFS CMT weld. Units in mm and hardness measurement in $HV_{0.5}$

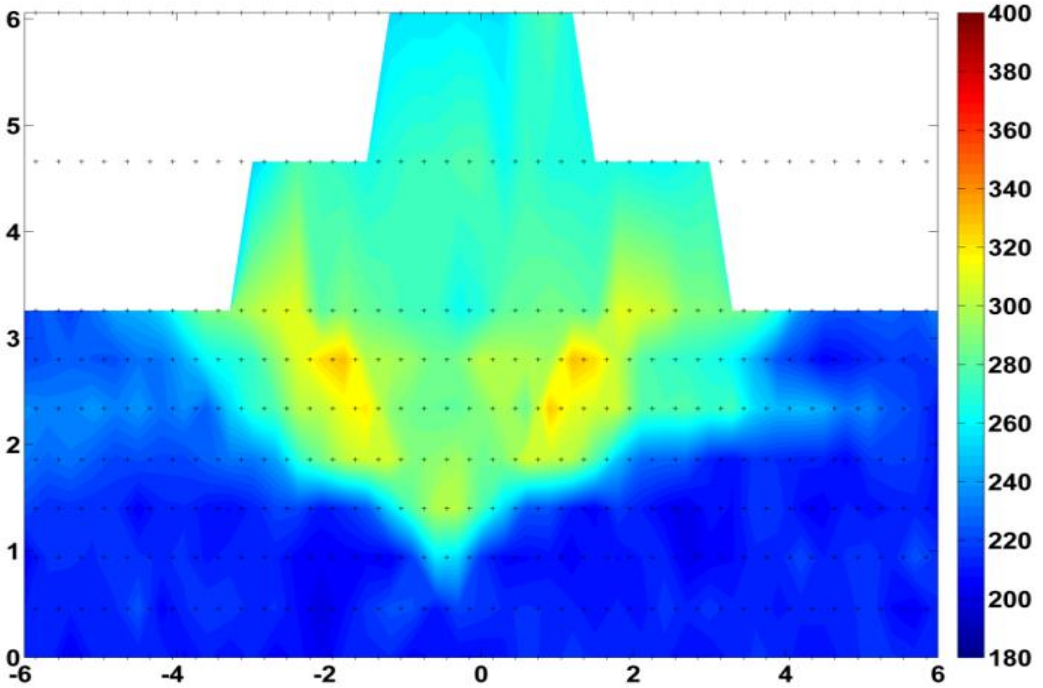

Figure 5-22: Vickers micro hardness map of laser assisted CMT weld with5 m/min WFS, 3 kW power, 20 mm beam diameter and 20 mm process distance. Units in mm and hardness measurement in $HV_{0.5}$

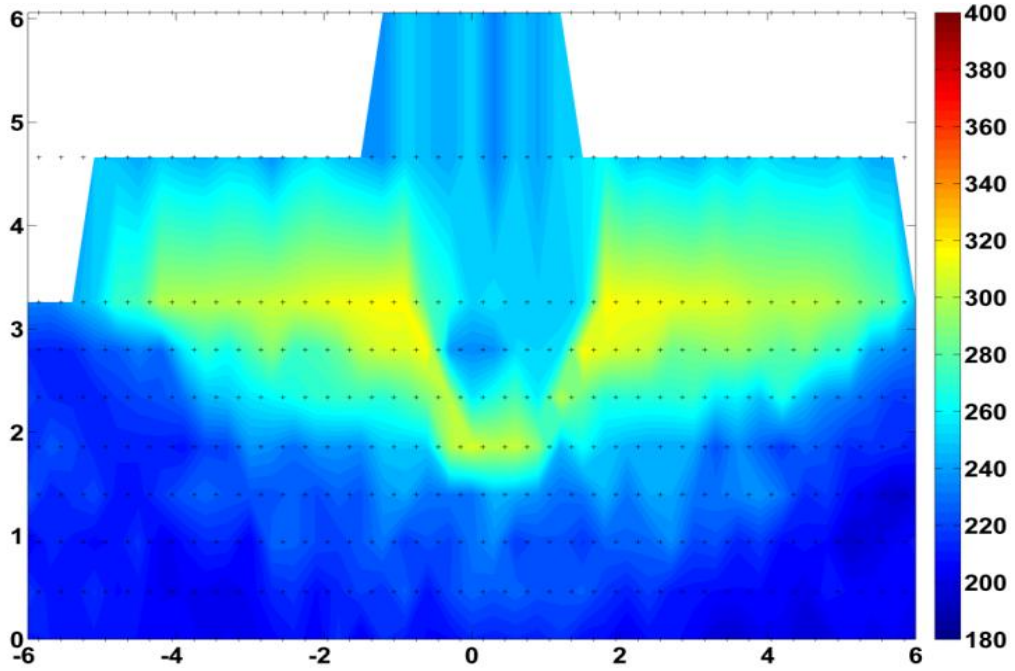

Figure 5-23: Vickers micro hardness map of laser assisted CMT weld with5 m/min WFS, 6 kW power, 20 mm beam diameter and 20 mm process distance. Units in mm and hardness measurement in $HV_{0.5}$

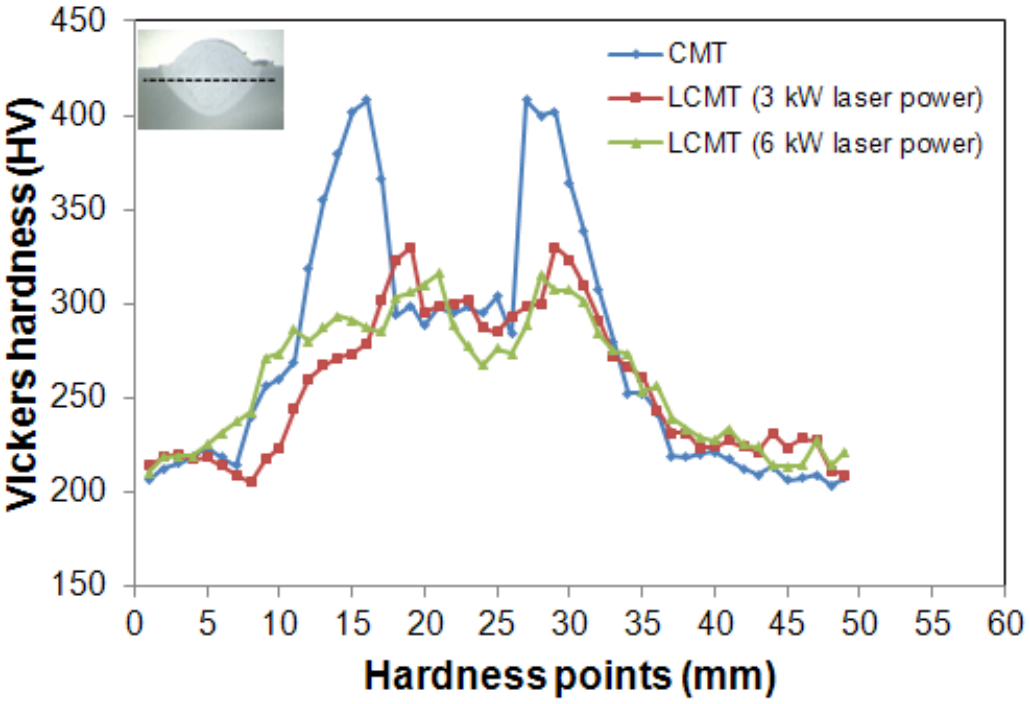

Figure 5-24: Comparing the hardness distribution of CMT weld with that of laser assisted CMT welds of different laser power

5.6 Discussion of Results

A critical analysis and interpretation of the results is presented in this section. The research finding will be compared with previous studies where available.

5.6.1 Weld Thermal Cycles

Weld thermal cycles of the laser assisted CMT process shown in Figure 5-5 are an indication of how the laser can be used to control the thermal cycles of not just the CMT but other arc welding processes. It demonstrates that with additional laser heating, the weld pool cooling and solidification times can be prolonged. This will be beneficial in terms of reduction of weld cooling rate and formation of hard metallurgical phases that may promote hydrogen assisted cracking sensitivity.

The shape of the weld thermal cycles is shown to be influenced by the process distance. At 50 mm, which is the longest process distance in the plot (Figure 5-6), there were two distinct peaks: the one to the left is from the CMT source and the other one from the laser. These show that at the longest process distance the weld pool produced by the CMT heat source had already cooled down to about 250 °C before the laser beam impinged on it, subsequently reheating it to around 1200 °C before finally cooling down to room temperature. But as both heat sources were brought close together (process distance equal to 0 mm) the thermal cycles became more integrated. Consequently, the laser beam impinged on the weld metal at a higher temperature of about 1200 °C and maintained the temperature for some time before the cooling cycle begins.

An important consideration from the thermal cycles shown in Figure 5-6 is that the laser reheats the weld to a temperature above austenite transformation. Therefore, even when the weld pool cools down to temperatures below 400 °C, which is about the martensite start temperature for the test piece (see Figure 2-32) before the laser impinged on it, the resulting phase will be reheated and transformed to austenite. In addition, the extended cooling time and slower

cooling rate will eventually promote the formation of a desirable weld microstructure that would not be susceptible to hydrogen assisted cracking.

The thermal cycles of laser assisted CMT weld with constant laser parameters and different wire feed speeds (Figure 5-7) show that when the wire feed speed of CMT, and indeed of any synergic GMAW process is increased, a higher amount of welding current will be required to melt the additional welding wire. As a result, the weld cooling time will increase as indicated by the thermal cycles.

The thermal cycles of welds made with different beam shapes shown in Figure 5-7 and 5-9 indicates little difference between the cooling time of a circular and an elliptical laser beam under identical welding conditions. For the 3 kW laser power and 20 mm process distance, the cooling time from (800 °C to 500 °C) was 3.13 s compared with 2.93 s for the equivalent circular beam. While the cooling time at 0 mm process distance was the same and approximately 3.43 s. The 6 kW laser power and 20 mm process distance produced a cooling time of 4.26 s compared with 4.06 s for the circular beam, and at 0 mm process distance a cooling time of 4.49 s compared with 4.37 s for the elliptical and circular beams respectively.

The observation did not give a clear indication of the influence of beam shape on weld cooling time. However, the elliptical beam has a longer interaction time, since the beam area is increased when stretched. But the power density correspondingly decreases. So a more reasonable comparison will be to increase the laser power of the elliptical beam in order to achieve the same power density as that of the circular beam. This would have a more pronounced effect on the weld cooling time and cooling rate since the heat input will be considerably higher. A detailed study of beam shape and its effect on weld thermal cycle is recommended for further research in continuation of this work.

5.6.2 Effect of Laser Parameters on Weld Cooling Time and Time at High Temperature for Constant CMT Parameters

The application of a laser in conduction mode in combination with CMT is to provide additional heat to prolong the cooling time of the solidifying weld metal. Previous studies performed at Cranfield University have shown that the system parameters e.g. laser power, beam diameter and welding speed can be expressed as fundamental laser material interaction parameters (equations (5-1) and (5-2)) and can be optimised to control the overall energy input for laser processing [141].

For the three beam sizes investigated, the 20 mm beam diameter gave the longest cooling time (Figure 5-10). This is because interaction time and specific point energy are dominant factors, both increase with beam radius as expressed in equations (5-1) and (5-2). The bigger beam size and consequent longer interaction time and higher specific point energy cause a larger area of the material to be heated up resulting in longer cooling time and consequently slower cooling rate (Figure 5-11). Longer cooling time will reduce the likelihood of formation of hardened metallurgical phase such as martensite, consequently reducing hydrogen assisted cracking sensitivity.

The cooling time as shown in Figure 5-12 increases with laser power because the additional laser thermal input increases the specific point energy, thereby prolonging the weld pool cooling time. Studies conducted by Ribic et al [111] on laser GTAW hybrid welding of AISI 321 stainless steel observed that the additional heat input from the laser source resulted in a larger weld pool being formed, which consequently reduces the cooling rate. It must be pointed out that the study was on keyhole welding with obvious difference in process characteristics, hence the melting of more material.

Changes in the process distance showed a gradual increase in cooling time as the heat sources are brought close together. This effect can be attribute to the fact that laser impinging on a hotter surface would reduce the cooling rate further. Since the cooling time from (800°C to 500°C) was computed from the

second thermal cycle due to the laser alone, the process distance did not have significant effect (Figure 5-10). However, it is suggested that the process distance could play a significant role in diffusion of hydrogen from the weld metal. As shown in Figure 5-6 the weld metal had cooled down to below 800°C for process distances (≥ 15 mm) before it was reheated to the laser peak temperature. It is known that hydrogen diffusion coefficient within steel increases with temperature, and if a longer time is allowed at an elevated temperature it would increase hydrogen diffusion. Lacoviello et al [67] showed that above 200°C the diffusion co-efficient is significantly higher than below 200°C [67].

It could therefore be concluded with reasonable confidence that if the laser beam impinges on the weld metal when it has cooled to just above 200°C, the weld will be heated for an extended time before cooling to ambient temperature, which will favour removal of diffusible hydrogen. Based on this, the 50 mm process distance weld in Figure 5-6 is expected to give the longest residence time (about 27 s) over 300 °C temperature. This is evident in Figure 5-13, which shows the relationship between process distances and the weld residence time over 300°C. The time at the same temperature for CMT weld shown in Figure 5-5 is 4.63 s. Therefore, it can be seen that additional laser heating and indeed longer process distance will extend the time at high temperature to increase hydrogen diffusion rate. This will be beneficial to hyperbaric welding where the potential for moisture pick-up from the welding chamber is high.

In any case it can be seen in Figure 5-5 that additional laser heat input significantly extends the cooling time. So for simplicity we would accept the cooling times computed from the laser curves. The experimental results showed that all the laser parameters investigated produced welds with longer cooling times than the CMT weld alone, even though these depended on the chosen laser parameters. In comparison, the CMT weld alone had a cooling time from 800°C to 500°C of 1.62 s while the laser assisted weld of 6 kW power, 20 mm beam diameter and 0 mm process distance produced a cooling time within the same temperature range of 4.41 s. This represents over 200% increase in

cooling time. Due to the absence of information in the literature on laser assisted GMAW in conduction mode, some of these results could not be corroborated by comparable studies.

The benefit of using additional laser heat input has been shown both in terms of prolonging weld cooling time (slower cooling rate) and longer time at high temperature. Since diffusible hydrogen is the main cause of hydrogen assisted cracking among other factors, reducing it to acceptable limits as specified by the standards (5 ml H_2 per 100 g of weld metal) should be given more emphasis. The reason is that even if a susceptible microstructure is formed due to fast cooling rate, the absence of diffusible hydrogen means that the likelihood of hydrogen assisted cracking is low.

5.6.3 Effect of Wire Feed Speed on Weld Cooling Time for Constant Laser Parameters

The plot of wire feed speed to travel speed ratio against weld cooling time as shown in Figure 5-15 reveals that higher wire feed speed leads to increase in process heat input. This will increase the weld cooling time and consequently reduces the cooling rate. This is because for CMT like most GMAW power sources, the wire feed rate is coupled with heat input. Therefore there is concomitant increase of welding current with wire feed speed in order to melt the additional filler wire. As a result, more material is melted with resultant increase in weld pool volume. Consequently, the weld pool cooling and solidification time is prolonged, which implies slower cooling rate.

The highest WFS/TS were obtained for the weld with 8 m/min wire feed speed and this gave a cooling time from 800 °C to 500 °C of 8.57 s. This is a marked improvement from the corresponding CMT weld alone with a cooling time of 2.36 s for the same temperature range.

5.6.4 Metallurgical Characterisation

The experimental results revealed that for the laser parameters investigated, 6 kW laser power and 20 mm beam diameter gave the longest cooling times and consequently, the slowest cooling rates for all process distances. Therefore, these will be considered as the optimum laser parameters and as a result, the discussion on macrostructure and microstructure examinations will be based on these parameters. However, comparison will be made with other parameters where necessary.

5.6.4.1 Macrostructure Examination and Weld Quality

As observed the laser assisted welds were defect-free and spatter generation was considerably minimised when compared to the traditional short circuit GMAW process. This was because of the controlled short circuiting and droplet detachment offered by the CMT process as reported by Pickin and Young [106]. This is in contrast to short circuit GMAW that generates a lot of spatter due to explosive molten metal detachment that is caused by rapid increase of welding current during short circuiting [50]. The laser had no noticeable effect on spattering as it only acts as a secondary heat source to maintain the heat of the weld pool. In addition, it did not affect the weld penetration depth. The reduced bead height and smooth transition between the weld toe and parent material would give improved fatigue properties by lowering the areas of stress concentration. Also, in case of multi-pass welds this will improve fusion during depositing of successive passes. It is worth mentioning that the process distance also plays a role in the reshaping of the weld bead. As the heat sources are brought closer the weld bead becomes flatter because the laser heats up the weld bead directly unlike at longer process distance where the heating is on the pipe materials.

The laser, positioned in trailing configuration to the CMT arc was employed to provide post weld heating. This was not necessarily to cause material melting or increased weld penetration. Rather, it reheats and elongates the weld bead as shown in Figure 5-16.

The other obvious effect of the laser is that it produced a wider heat affected zone than the CMT. The main explanation for this is that the 20 mm beam diameter laser beam heats up a larger area of the material than the CMT arc, giving a wider heat affected zone. This implies more heat retention and wider microstructural changes in the HAZ. However, the width of the HAZ decreases with beam diameter. Therefore, for the beam sizes investigated, 10 mm produced the smallest HAZ, which was still wider than that of the CMT.

It must be emphasised that the modifying effect of the laser on the weld bead depends principally on the laser power. This becomes obvious when comparing the macrograph of Figure 5-16 (bottom) with that of Figure 5-18 (A). The former was a 6 kW weld while the latter was 3 kW for the same beam diameter, process distance and CMT parameters. The elongation of the weld bead is more pronounced for the 6 kW weld. This is because the 6 kW weld has twice more power and consequently as much more specific point energy than the 3 kW weld.

5.6.4.2 Microstructure Examination

Figure 5-19 and Figure 5-20 indicate that the laser assisted CMT weld has a similar microstructure to those of the equivalent CMT weld. The main differences are that the HAZ is wider for the former as previously mentioned, and also there may be less martensite formed in the CGHAZ. The tempering of martensite by the additional laser heat could be responsible for this.

Since the CGHAZ (Figure 5-20) is the closest HAZ region to the fusion boundary, it is heated to a temperature sufficient to cause rapid austenite grain growth. The FGHAZ indicated being further away from the fusion boundary than the CGHAZ is also heated to a temperature above Ac3, but insufficient to produce rapid austenite grain growth.

The intercritical HAZ is heated to a temperature between Ac1 and Ac3, resulting in only partial transformation to austenite. However, substantial refinement occurs. The subcritical HAZ is the closest region to the base metal and as such the maximum temperature may be less than Ac1. The ferrite (F) grains are finer than those of the base metal). The microstructure of the base metal is predominantly pearlite and ferrite.

The low heat input (0.38 kJ/mm) and cooling time (1.62 s) of the CMT weld may have resulted in the formation hard metallurgical phases in the HAZ microstructure, particularly the CGHAZ. It can be inferred that higher heat input resulted in longer cooling and solidification time, and slower cooling rate, which produced softer phases compared with CMT alone. This is reflected in the hardness profile presented in the next section. The above findings are in agreement with results in the literature [12; 36; 55].

5.6.5 Hardness Test

The measured hardness values as presented in Figure 5-21 to Figure 5-24 show that the maximum hardness occurred in the HAZ, followed by the WM, while the BM has the minimum hardness. The maximum hardness occurred in the CGHAZ and decreases progressively towards the base metal. This hardness profile, which is indicative of HAZ hardening, is consistent with reported works on low heat input and high cooling rate welding of low carbon steels as reported by Eroglu [36]. The high hardness of the CGHAZ could be because of the presence of martensite in the microstructure, which was caused by high cooling rate.

The peak hardness of the CMT weld is considerably higher than those with additional laser heating as shown in Figure 5-24. This is due to the low heat input and high cooling rate. The addition of a laser to CMT can significantly reduce the peak hardness by 25% depending on the laser power while other parameters are kept the same. The decrease in hardness could be attributed to the higher heat retention resulting in tempering of martensite present or may be

austenisation and formation of other softer phases e.g. ferrite (this could be because of lowering of the cooling rate).

Since the maximum hardness is considered an approximate index for susceptibility to hydrogen assisted cracking, it is usually limited to 350 HV_{10} in welding of offshore structures and pipelines [12; 55]. A HAZ hardness of 248 HV_{10} and higher was reported to increase susceptibility to stress corrosion cracking when the pipeline is used for sour service [40]. It has to be pointed out that this test is a Vickers micro hardness test with a load of 500 g, which is different from the one specified by the standard as reported in 3.6.5. The hardness load specified by the standard is 10 kg. The larger indentation produced by the latter will not give an accurate indication of the different phases present. On the other hand, the smaller indentations of the 500 g load could be more representative of the hardness distribution of the different phases present in the weld microstructure.

This high peak hardness justifies the need for additional heat input to the CMT process if it is to be used for hyperbaric welding of X65 pipeline steel. It is important to note that CMT was designed for low heat input applications, and as such the option of increasing the wire feed speed to achieve higher heat input may negate other process benefits as shown in chapter four.

5.7 Conclusion

The conclusions from this research are as follows:

- The laser serves as post weld heating, elongating the weld pool and extending the cooling time. It also gives a smooth transition between the weld toe and pipe material, which would reduce areas of stress concentration and improve the structural integrity and also better fusion in multi-pass welding.;

- Laser power and beam diameter were shown to be the main parameters that influence the cooling time. Large beam diameter and high laser power favours longer weld cooling time because of longer beam interaction time and higher specific point energy;

- The process distance was shown not to significantly affect the cooling time, $t_{8/5}$ because it was computed from the laser thermal cycle which did not take into account the overall weld thermal cycle. However, it was shown to influence hydrogen diffusion rate from the weld metal. It is suggested that separating both heat sources such that the laser just impinges on the weld metal above 200°C will result in prolonged heating time, and favour desorption of diffusible hydrogen;

- It has been shown that with laser assistance an overall increase of cooling time (200%) is achievable as compared to equivalent cold metal transfer weld alone.

- For the parameters investigated, it was shown that the additional laser thermal input to Cold Metal Transfer process could bring about significant reduction of weld peak hardness to acceptable levels recommended for welding of offshore structures for sour service application.

6 Numerical and Experimental Study of Temperature Distribution in Laser Assisted GMAW (CMT)

Scope

The temperature distribution and cooling rate of a welded structure influences formation of the final weld microstructure and the resultant mechanical properties. These determine the strength of the welded joint and susceptibility to failure. Predicting the strength of a welded structure requires accurate analysis of the thermal cycle, which will provide an understanding of the temperature gradient and subsequent cooling rate during welding. The correct prediction of thermal cycles requires understanding of the effects of different welding and heat source parameters on the model. This is vital to the development of effective simulation strategy for weld thermal analysis. In addition, hydrogen diffusivity increases with temperature, thereby making temperature profile crucial to the avoidance of hydrogen assisted cracking, which is a potential problem during hyperbaric GMAW.

In this chapter, a thermal model was developed by Jialuo Ding, a Research Fellow in the Welding Group using Abaqus 6.11 software. The model was applied for accurate prediction of temperature distribution and cooling time of the weld metal and HAZ for laser assisted GMAW (CMT) at atmospheric conditions. The results of the model were validated by welding experiments under similar conditions. The cooling block calibration shown in chapter 3 was used to validate the simulated convection coefficient under different pressures. This was used to simulate the temperature distribution and cooling time of laser assisted GMAW under different pressures. However, laser assisted hyperbaric GMAW could not be performed to validate the model results at high pressures.

6.1 Aim and Objectives

The aim of the work presented in this chapter is to apply an efficient numerical simulation technique for prediction of the temperature distribution and cooling time of the weld metal and heat affected zone of laser assisted GMAW (CMT). Developing predictive capability is important to understand the underlying mechanism of interaction between the two heat sources and generate thermal cycles for different welding parameters after the model is calibrated. This will also minimise the errors associated with using thermocouples to generate weld thermal cycles. To achieve this, the following objectives are addressed:

- To apply a developed thermal model using Abaqus 6.11 finite element model software to simulate the thermal cycle of laser assisted GMAW (CMT) at one atmosphere;
- To validate the thermal model by experimental welding results; and
- To use the model to predict the thermal cycles of laser assisted GMAW (CMT) at different pressures.

6.2 Experimental Procedure

6.2.1 Materials and Equipment

The same materials, equipment and experimental set-up used in chapter five were employed in this work. These were used for the purpose of generating the weld metal and heat affected zone thermal cycles that were used to validate the thermal model.

6.2.2 Experimental Method for Welding Trials

Two instrumented bead-on-pipe welds were performed on a 310 mm × 120 mm × 25 mm section of X65 pipeline steel by attaching K-type thermocouples on the pipe surface in order to determine the transient weld thermal cycle. Five thermocouples were placed 5 mm, 10 mm, 15 mm, 20 mm and 25 mm away from the weld centre line as shown in Figure 6-1. The first thermocouple was positioned 50 mm from the weld start position. In addition, R-type thermocouples were placed inside holes drilled through the pipe thickness to depths of about 24 mm and 24.5 mm (refer to Figure 3-10 of chapter 3). These were used to determine the temperature distribution of the weld pool and heat affected zone. The laser parameters investigated were 6 kW laser power with 20 mm beam diameter. The process distance was 20 mm and the laser head was travelling behind the CMT torch. The laser head and CMT torch were fixed at an angle of 66° and 78.5° to the horizontal respectively as illustrated in Figure 5-4 of chapter five. For the CMT, 5 m/min wire feed speed was used. The specimen was clamped to the translation stage moving with constant welding speed of 7 mm/s.

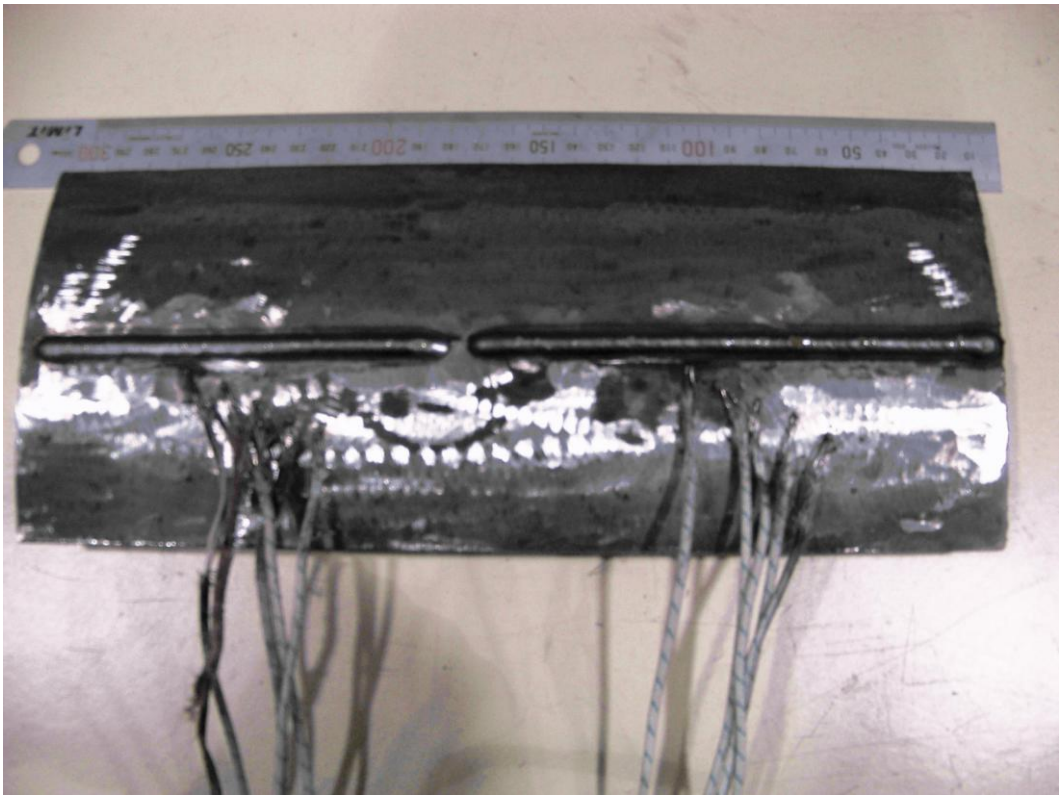

Figure 6-1: K-type thermocouple position on a welded specimen

6.2.3 Determination of the Convective Coefficient under Different Pressures

The data generated from the cooling block calibration experiment described in section 3.3.2 of chapter 3 was used to validate the simulated convection coefficients at different pressures.

6.3 Finite Element Model (FEM)

FEM software Abaqus 6.11 was used to perform the thermal analysis [58; 79]. The heat sources of the process were simulated using a user defined subroutine written in Abaqus. A steady state model was used to compute the temperature distribution during welding.

6.3.1 Computational mesh

As shown in Figure 6-2 (a), the model was built with the same width and thickness as the substrate. The length of the substrate was setup as 0.7 m to make sure the temperature history of the cooling can be captured. Since the pipe geometry is symmetrical along the weld centre line, only half of the welded pipe section was considered in the model. The weld bead was simplified by using two rectangular shapes with the width and height shown in Table 6-2 for the CMT section and laser section respectively. Apart from that, a transition section of 5 mm length was modelled between the two sections (shown in Figure 6-2 (b)).

A three-dimensional hexa mesh was generated on the computational domain. The Welding direction was along the x-axis. Since high temperature and heat flux gradients are predicted within the fusion zone (FZ) and HAZ, a comparatively fine mesh is assigned to these regions. The element size increases with distance away from the heat source regions (shown in Figure 6-2(c)).

Forced convection/ diffusion linear elements were utilised in this model. Instead of modelling the heat source moving along the weld line as in transient models, the steady-state method attaches the reference frame to the welding heat sources and models the material ‘flow’ through the meshes. The welding torch movement is represented by a mass flow rate per area, which equals the welding speed multiplied by the material density [30].

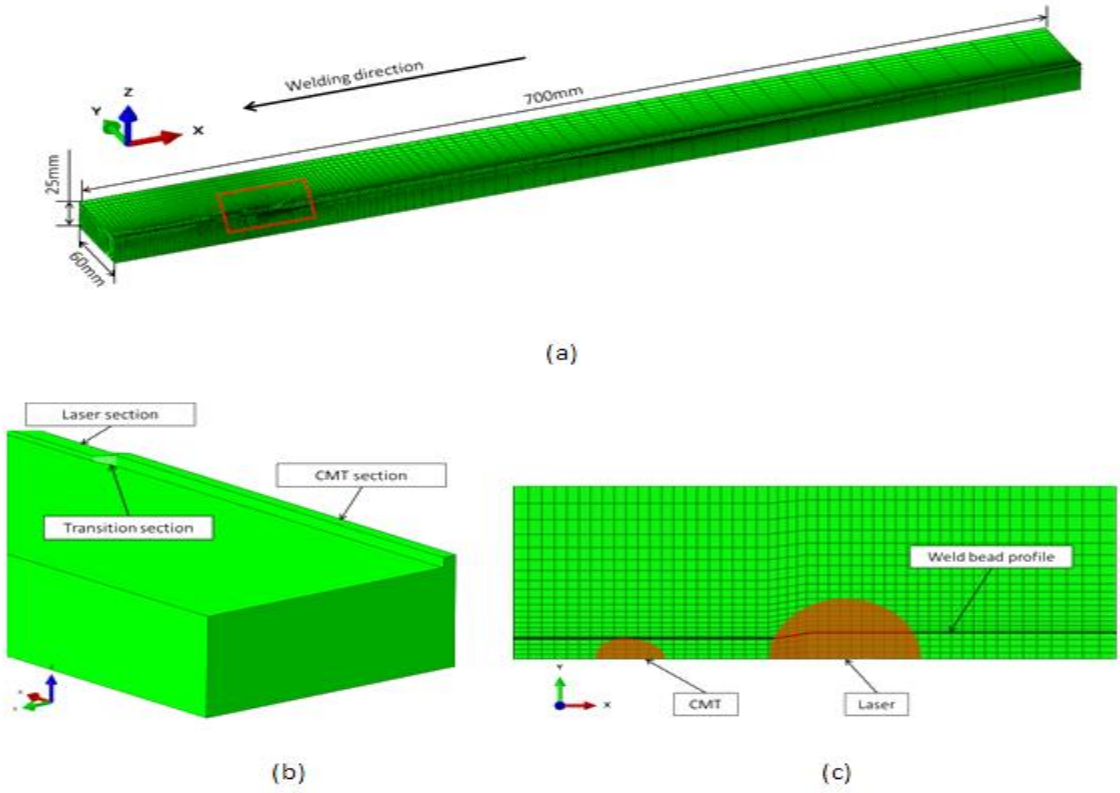

Figure 6-2: FEM mesh and cross section of test piece geometry. (a) Isometric view of the model; (b) geometry of the weld bead; (c) enlarged top view of the focused area indicated by the red square in (a)

6.3.2 Heat flux distribution for the model

Heat input required to melt a metallic material during welding is described by:

$$Q_{weld} = {\eta \cdot I_{weld} \cdot V_{weld}}/{v} \quad (6\text{-}1)$$

Where Q_{weld} is effective heat input during welding η is the heat source efficiency, which depends on the welding process. For GMAW, it is in the range of 0.75 to 0.90, and 0.05 to 0.60 for laser beam welding depending on surface conditions [74]. I_{weld} and V_{weld} are the welding current and arc voltage respectively and v is the welding speed [152].

Since the laser head and CMT torch were fixed relative to the moving slide, a steady state model of heat flux was assumed. In order to simulate the moving slide at the specified welding speed, the computed heat flux densities were

distributed to specific elements around the welding region in the model. Therefore, the origin of the coordinate system is positioned at the centre of the heat flux surfaces. A user defined function was used to compute the Eulerian distance of elements from the heat source centres at any given time. The laser and CMT heat sources were applied to elements as surface and volumetric heat generation respectively.

6.3.3 Laser heat flux

During the experimental trials, the laser beam was defocused and used in conduction mode. As a result, the power density was significantly reduced. This is because the laser beam was intended to provide additional heat input to the CMT process or used for post-weld heating and not necessarily to melt the specimen.

The defocused laser beam distribution was modelled with a spherical approximation [109], which can be described with the following expression:

$$q(x,y) = \eta_l \frac{3Q_{laser}}{2\pi {r_0}^2} \cdot \sqrt{1 - \frac{x^2}{{r_0}^2} - \frac{y^2}{{r_0}^2}}, \quad (6\text{-}2)$$

where $q\ x,y$ is the surface heat flux in W/m^2. Q_{laser} is the laser power (W), r_0 is the laser beam radius (mm) and a laser heat source efficiency η_l of 0.45 was assumed.

6.3.4 GMAW (CMT) heat flux

A volume heat source represented by double-ellipsoidal Gaussian distribution of power density (shown in Figure 6-3) as proposed by Goldak et al [51] was adopted as the CMT heat source. Given that the temperature gradient in front of the heat source is steeper than that at the trailing edge of the molten pool, the power density of the region in front of the arc centre and the region behind the arc centre were defined separately [30].

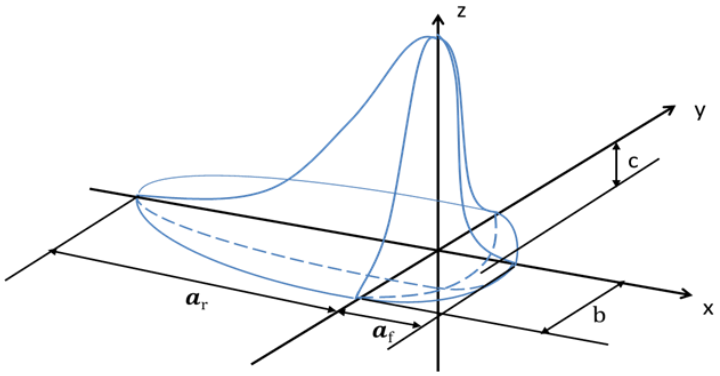

Figure 6-3: Goldak's double ellipsoid heat source model [51]

The power density distribution in the front quadrant can be described as

$$q_f = \eta_c \frac{6\sqrt{3} f_f Q_{CMT}}{a_f bc\pi\sqrt{\pi}} e^{-3x^2/a_f^2} e^{-3y^2/b^2} e^{-3z^2/c^2} \quad (6\text{-}3)$$

and the power distribution for the rear quadrant is:

$$q_r = \eta_c \frac{6\sqrt{3} f_r Q_{CMT}}{a_r bc\pi\sqrt{\pi}} e^{-3x^2/a_r^2} e^{-3y^2/b^2} e^{-3z^2/c^2}, \quad (6\text{-}4)$$

where q_f and q_r are the power density (W/m^3) of the frontal ellipsoid and the rear ellipsoid respectively; a_f and a_r represents the length (mm) of these ellipsoids; b and c are the heat source width (mm) and depth (mm) respectively; Q_{CMT} is the energy input (W) of the CMT. A heat source factor, η_c of 0.90 is assumed; f_f and f_r are the factors for distributing the power to the front and rear of the heat source (f_f=0.5 and f_r=1.5), and they have the relation that $f_f + f_r = 2$ [30].

In the model the two heat sources were described by a user defined subroutine. The subroutine defines the laser and CMT heat fluxes as given in equations 6-2 to 6-4. The detailed parameter settings used in this study are shown in Table 6-1.

Table 6-1: Heat source parameters

Laser		CMT						
Q_{laser}(W)	r_0(mm)	Q_{CMT} (W)	a_f(mm)	a_r(mm)	b(mm)	c(mm)	f_f	f_r
6000	10	2509.7	2.5	7.5	2.9	2.9	0.5	1.5

6.3.5 Boundary conditions

The heat loss due to radiation and convection was modelled on most of the surfaces except for the symmetry plane. Constant convective heat transfer coefficients were used in this study. The value of this coefficient is different under different pressures. In this study the convection coefficient under different pressures was decided by running a series of numerical trials and adjusting the model so that the predicted temperature histories match the experimental results [30]. In additional, a constant radiation coefficient of 0.8 was used. The heat loss through the clamping devices was ignored in this model because the contact area of the clamps and the base was very small. The initial temperature was set at room temperature 25 °C. The Stefan-Boltzmann constant was set to 5.67×10^{-8} J/ (m^2K).

6.3.6 Materials properties

Constant density of 7850 kg/m^3 was used in the simulation. The same thermal properties were set for materials in the weld bead as well as in the base plate. Temperature-dependent thermal conductivity and specific heat were used in this study (as Shown in Figure 6-4). In order to take the effect of liquid flow in the weld pool into consideration, an arbitrarily high thermal conductivity was used for greater temperature than the material melting temperature. The latent heat for the material transformation from solid to liquid was considered in this model by artificially increasing the liquid specific heat capacity around the melting point.

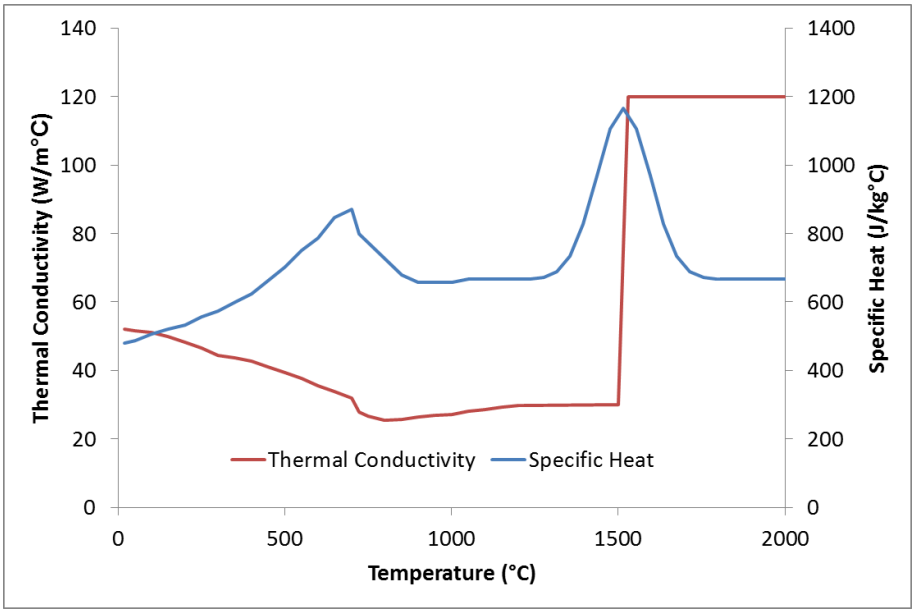

Figure 6-4: Temperature-dependent materials properties [30]

6.4 Results

The results of the temperature field distribution and their analysis is presented in this section. This is followed by a discussion of these results in the next section.

6.4.1 Analysis of temperature field distribution

Figure 6-5 shows the temperature distribution of a 5 m/min WFS weld for 6 kW laser power, 20 mm beam diameter and 20 mm process distance and the predicted weld penetration depth. The temperature distribution made with the same WFS but with 3 kW laser power, 15 mm beam diameter and 20 mm process distance is shown in Figure 6-7.

It can be seen that temperature around the heat sources exceeds 1540°C indicating material melting in the weld fusion zone (FZ). The interaction of temperature fields of both heat sources is also clearly visible in the figures. These reveal a wider thermal field by the laser heat source relative to CMT. The laser provides post-weld heating that elongates the weld bead, which is in agreement with the experimental results (Figure 6-6). The measured penetration depth of the experimental weld is approximately 1.20 mm, while the simulation predicted approximately 0.9 mm (Figure 6-5 bottom) for the same parameters. Table 6-2 gives the measured experimental weld bead profile.

Table 6-2: Weld bead profile of experimental welds

Weld	WFS (m/min)	HAZ width (mm)	Penetration depth (mm)	Cap (mm)	Weld width (mm)
CMT	5	0.58	1.21	3.22	6.42
LCMT	5	2.19	1.23	1.44	8.60

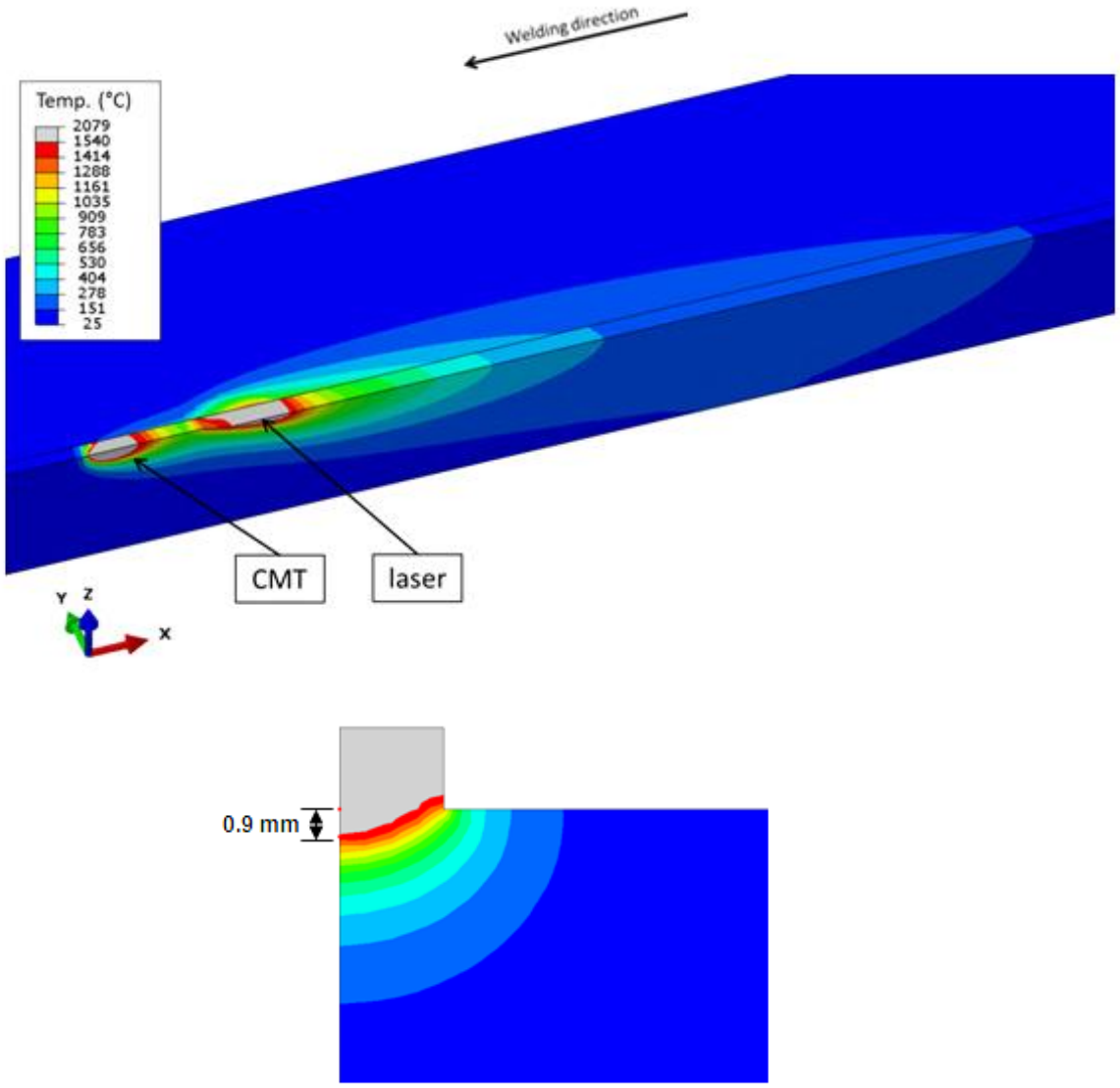

Figure 6-5: (Top)Temperature distribution of weld with 6 kW laser power, 20 mm process distance, 20 mm beam diameter and 5 m/min WFS. (Bottom) measurement of weld penetration depth

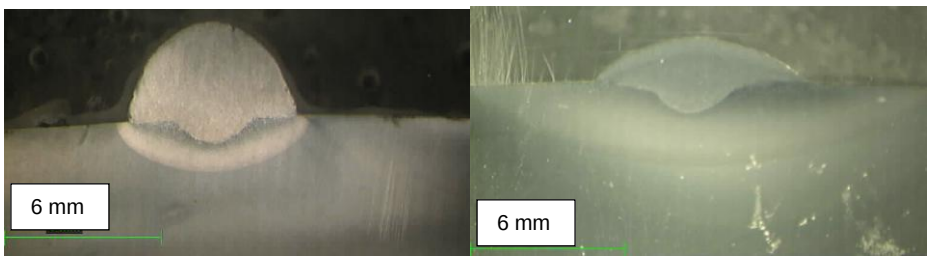

Figure 6-6: Macrographs of CMT weld (left) and laser CMT assisted weld (right) of 6 kW laser power, 20 mm process distance, 20 mm beam diameter and 5 m/min CMT WFS

As can be observed in Figure 6-7 the laser peak temperature is significantly lower when compared to that of the 6 kW laser power shown in Figure 6-5. Consequently, the 3 kW laser power did not cause significant re-melting and reshaping of the weld bead as evident from the macrographs shown in Figure 6-8.

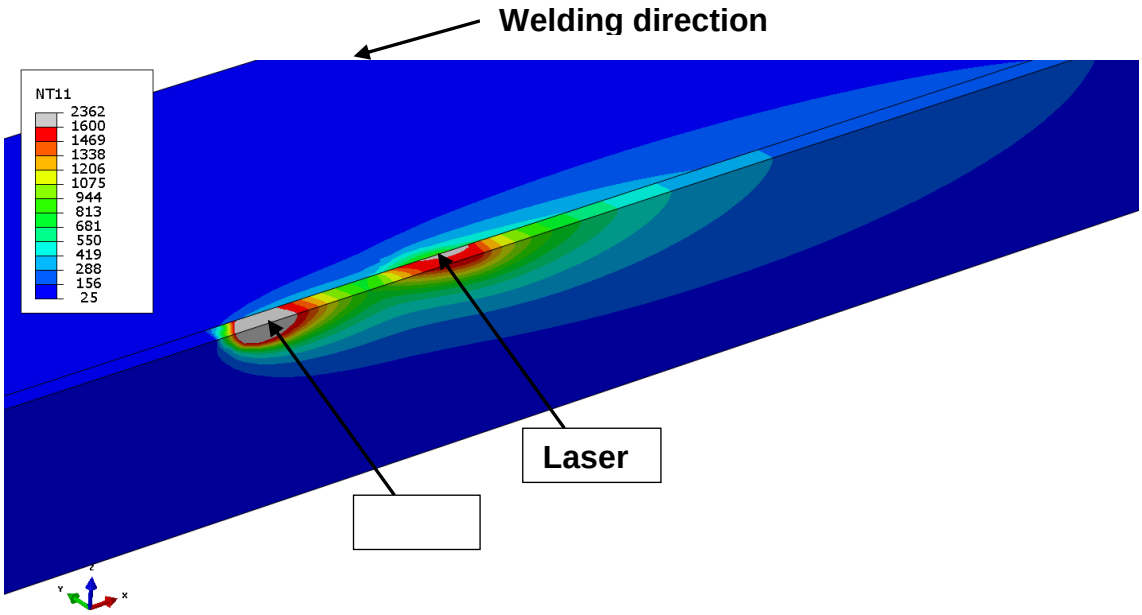

Figure 6-7: Temperature distribution of weld with 3 kW laser power, 20 mm process distance, 15 mm beam diameter and 5 m/min CMT WFS

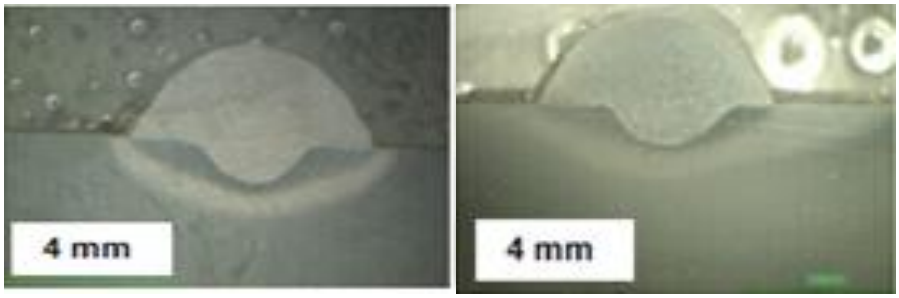

Figure 6-8: Macrographs of CMT weld (left) and laser CMT assisted weld (right) of 3 kW laser power, 20 mm process distance, 15 mm beam diameter and 5 m/min CMT WFS

6.4.2 Analysis of thermal data

Figure 6-9 compares the experimental and simulated thermal cycles at different positions on the pipe surface for 6 kW laser power, 20 mm beam diameter and 20 mm process distance. The weld metal thermal cycles for model and experiment at 0.5 mm and 1.0 mm from the pipe surface is also compared in Figure 6-10. Similarly, comparison of weld metal thermal cycles of model and experiment for a 3 kW laser power is given in Figure 6-11.

As shown in Figure 6-9 the thermocouple placed closest to the weld centre line (Exp_5 mm) recorded the highest peak temperature. The temperature progressively decreases with distance away from the fusion boundary to give the lowest value at 25 mm. The figure shows two distinct peaks of the thermal cycles. The first one is due to the CMT and the second one is caused by the laser. Temperature peaks generated by the laser are significantly higher than those for the CMT. The calculated and predicted cooling times from 800 °C to 500 °C were approximately 2.65 s and 2.12 s respectively for the 5 mm (Exp_5 mm and Simu_5 mm) distance. The measured HAZ and weld widths (Table 6-2) indicate that only the closest thermocouple to the fusion boundary (Exp_5 mm) was in the HAZ of the weld joint.

As shown in Figure 6-10, the weld metal temperature distributions also show two distinct peaks similar to Figure 6-9. But the former indicates a higher value for the CMT curve as against the latter. The predicted peak temperatures of the CMT and laser thermal cycles closely match those of the experiments. The peak temperature of the CMT curves for both positions is above 1540°C, which is about the melting temperature of the test piece. For the laser peaks, the predicted temperature is about 1200 °C, which is similar to experimental results. However, it is slightly higher for the 0.5 mm position. The calculated and predicted cooling times from 800 °C to 500 °C were approximately 4.06 s and 3.19 s respectively for the 0.5 mm (Exp_0.5 mm and Simu_0.5 mm), While those of the 1 mm (Exp_1 mm and Simu_1 mm) position were approximately 3.96 s and 3.07 s respectively.

As shown in Figure 6-11 the simulated weld metal thermal cycle and that of the experiment are also in close conformity. However, the laser peak temperature is shown to be lower when compared to the weld thermal cycle for 6 kW laser power. The calculated and predicted cooling times from 800 °C to 500 °C were approximately 2.80 s and 2.13 s respectively for the 0.5 mm (Exp_0.5 mm and Simu_0.5 mm).

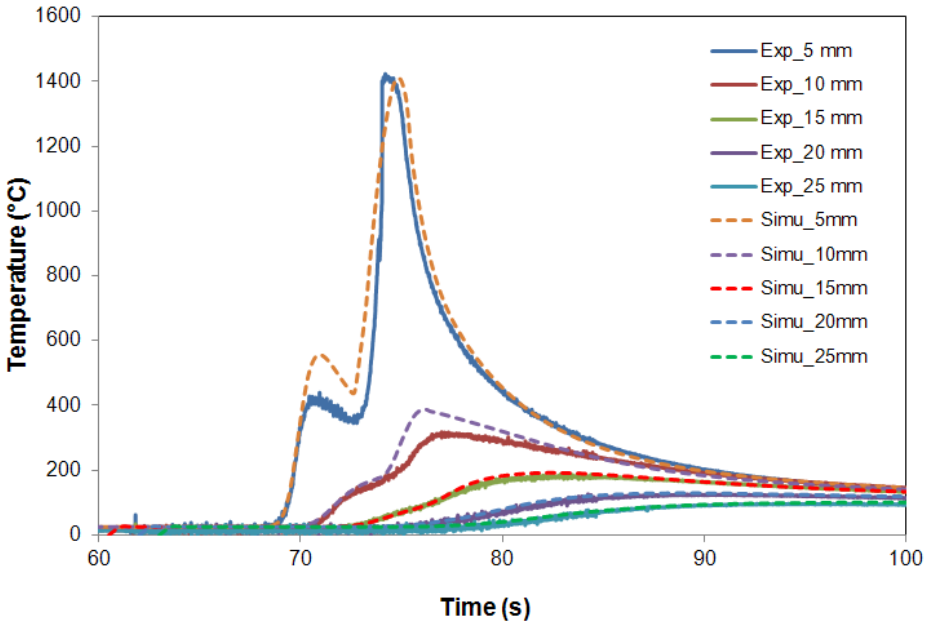

Figure 6-9: Comparing the thermal cycle of model and experiment at different positions on the material surface

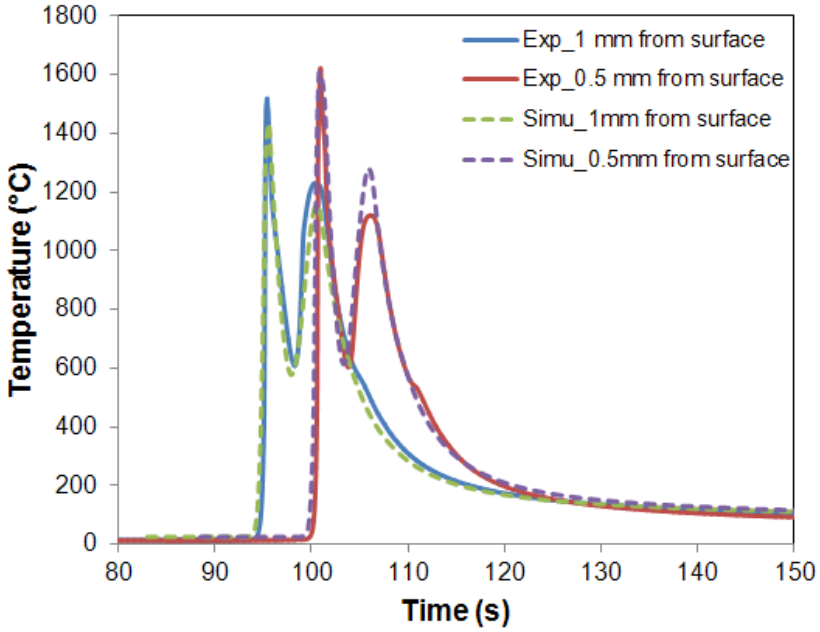

Figure 6-10: Thermal cycles of the weld metal for model and experiment for 6 kW laser power, 20 mm beam diameter and 20 mm process distance

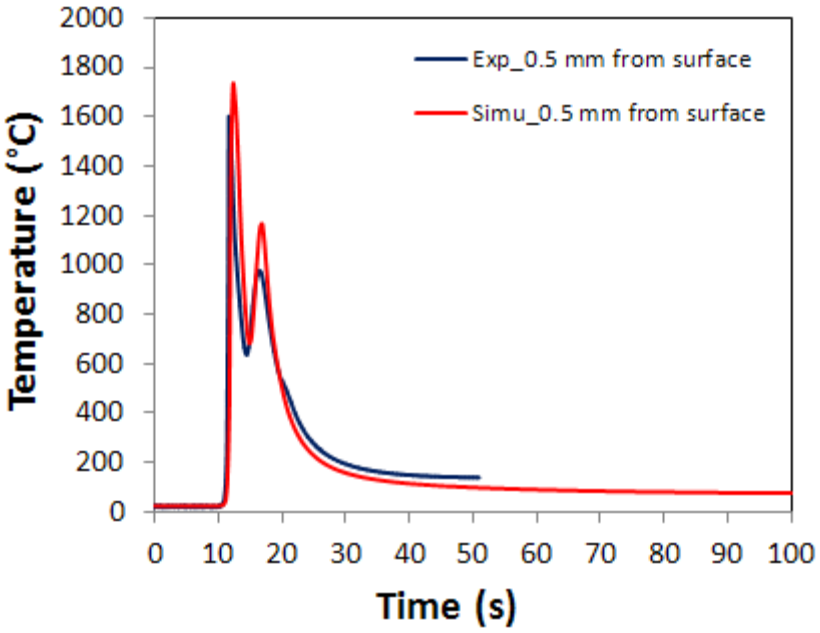

Figure 6-11: Thermal cycles of the weld metal for model and experiment for 3 kW laser power, 15 mm beam diameter and 20 mm process distance

6.4.3 Predictive capability of the model

The predictive capability of the developed model is investigated in this section. The model was used to predict the thermal field and temperature profile of laser assisted GMAW (CMT) for a longer process distance than those investigated. It was also used to predict the weld thermal cycle for laser assisted GMAW (CMT) under different ambient pressures. However, the model will not be validated by experimental data because laser assisted GMA welding has not yet been performed under high pressure conditions as this will require significant modifications to the hyperbaric chamber to incorporate a laser, which has not yet been done.

6.4.3.1 Thermal field and temperature profile for 50 mm process distance

Figure 6-12 and Figure 6-13 show the temperature field distribution and predicted thermal cycles respectively for 3 kW laser power, 20 mm beam diameter and 50 mm process distance with 5 m/min WFS. It can be seen that the temperature field is similar to those described in the previous section. The main difference is the clear separation of both heat sources because of the longer process distance. Also, the laser peak temperature is shown to be significantly lower.

The simulated thermal cycles follow a similar pattern to the previous ones. There is clear distinction between the weld metal thermal cycles of both heat sources with the arc source temperature being much higher than the laser as shown in Figure 6-13 (0.5 mm below welding surface). This indicates that the laser impinges on the weld metal after it has cooled down to about 250 °C while the laser peak temperature is just below 800 °C. For the predicted thermal cycles at positions away from the weld centre line, it can be observed that the laser induced peak temperature is higher than the arc induced peak.

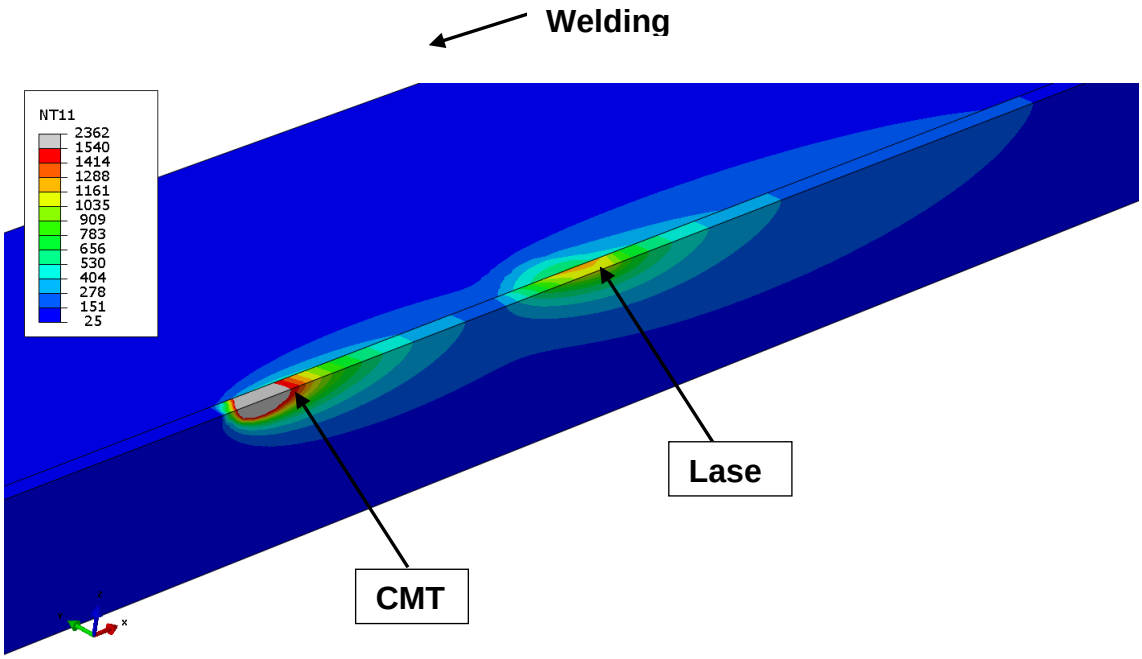

Figure 6-12: Temperature distribution of weld with 3 kW laser power, 50 mm process distance, 20 mm beam diameter and 5 m/min WFS

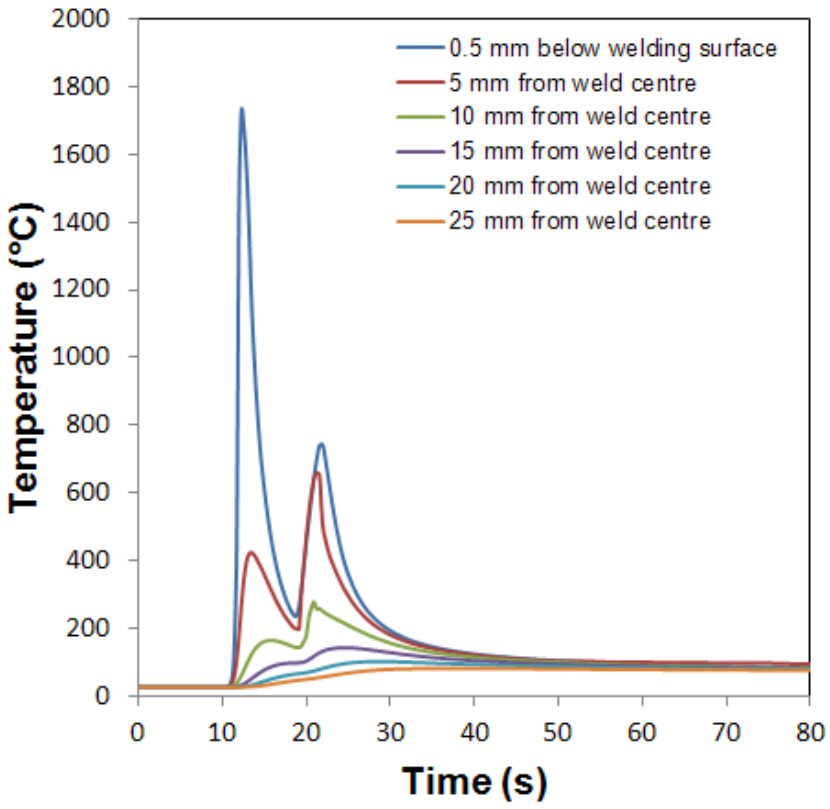

Figure 6-13: Predicted thermal cycles of the weld metal for 3 kW laser power, 20 mm beam diameter and 50 mm process distance

6.4.3.2 Laser assisted GMAW under high pressure

In order to model the weld thermal cycles under high pressures, the convection coefficient for a given ambient pressure has to be established. To achieve this, the result of the cooling block calibration experiment reported in chapter three was used. As reported, a steel block was heated up by resistance heating and allowed to cool under different ambient pressures. The resultant cooling curves were simulated using the finite element model, and the result was validated by the cooling block calibration experiment. Figure 6-14 compares the simulated and experimental calibration of the convection coefficients under different pressures. The derived convection coefficients at different pressures are given in Table 6-3. It can be seen from the figure that the model and experimental results are in good agreement. This indicates that convective heat loss increases with pressure, resulting in faster cooling times as earlier described in chapter three.

The convection coefficients at the given pressures were assigned to the model to predict the thermal cycles of laser assisted GMAW (CMT) welds under different ambient pressures. The welding parameters used for the model were identical to those used at one atmosphere condition. These were 6 kW laser power, 20 mm beam diameter, 20 mm process distance and average instantaneous GMAW arc power of approximately 2.3 kW. Figure 6-15 and Figure 6-16 shows the simulated thermal cycles at 0.5 mm from the material surface for a 25 mm and 5 mm thick plate respectively.

The model indicates little difference in cooling time from 1 to 150 bar pressure for the 25 mm plate thickness. For the 5 mm thick plate, the effect of pressure on the cooling time is more significant. This is similar to the results obtained at one atmosphere, as previously described in chapter three. However, the model did not account for the arc constriction phenomenon at elevated pressure. This is expected to narrow the heat source profile with increasing pressure.

Figure 6-17 and Figure 6-18 compare the effect of pressure on the cooling time with and without laser heating for the different plate thicknesses. The computed

weld cooling times given in chapter 3 are compared with that simulated by the model. The same laser parameters as above were used and average instantaneous GMAW arc power of approximately 5.5 kW. It can be seen from the plots that the laser has the same effect of extending the weld cooling time at elevated pressure as it did at one atmosphere.

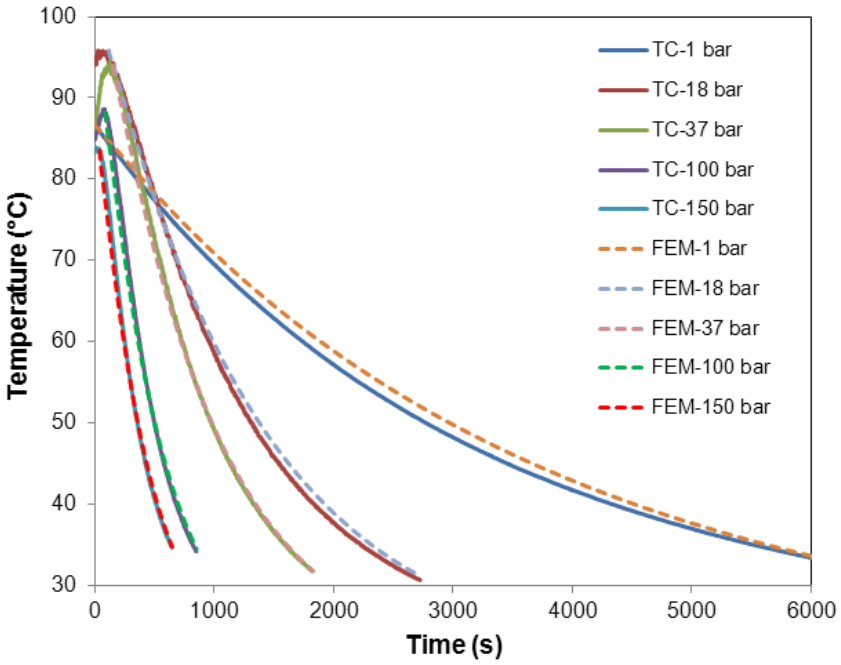

Figure 6-14: Calibration of the convection coefficients under different pressures

Table 6-3: The convection coefficient at different pressures

Pressure (bar)	1	18	37	100	150
Convection ($Wm^{-1}K$)	8.4	33.5	53.0	105.0	127.0

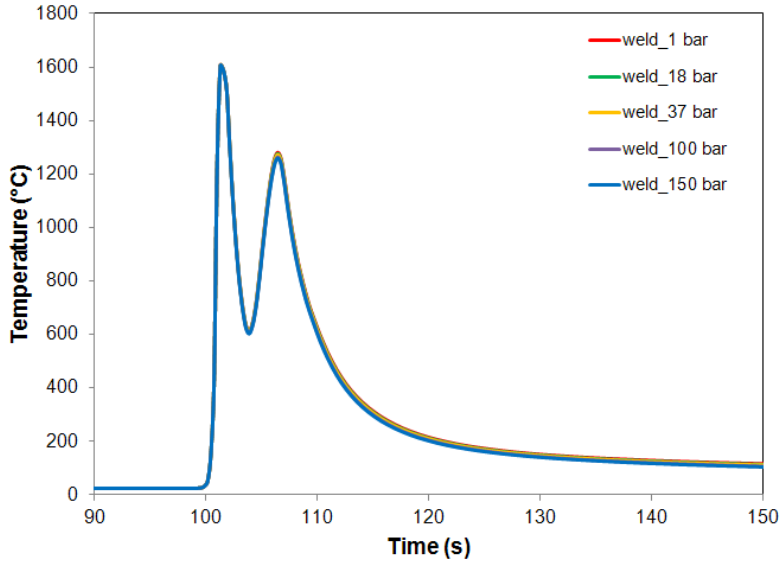

Figure 6-15: Simulated thermal cycles of laser assisted CMT welding with 5 m/min WFS and 7 mm/s welding speed on a 25 mm plate thickness for 6 kw laser power, 20 mm beam diameter and 20 mm process distance

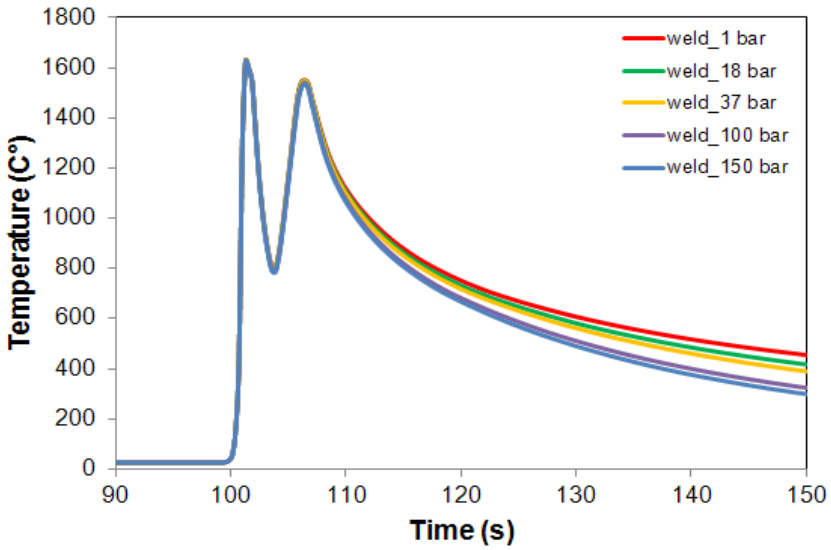

Figure 6-16: Simulated thermal cycles of laser assisted CMT with 5 m/min WFS and 7 mm/s welding speed on a 5 mm plate thickness for 6 kw laser power, 20 mm beam diameter and 20 mm process distance

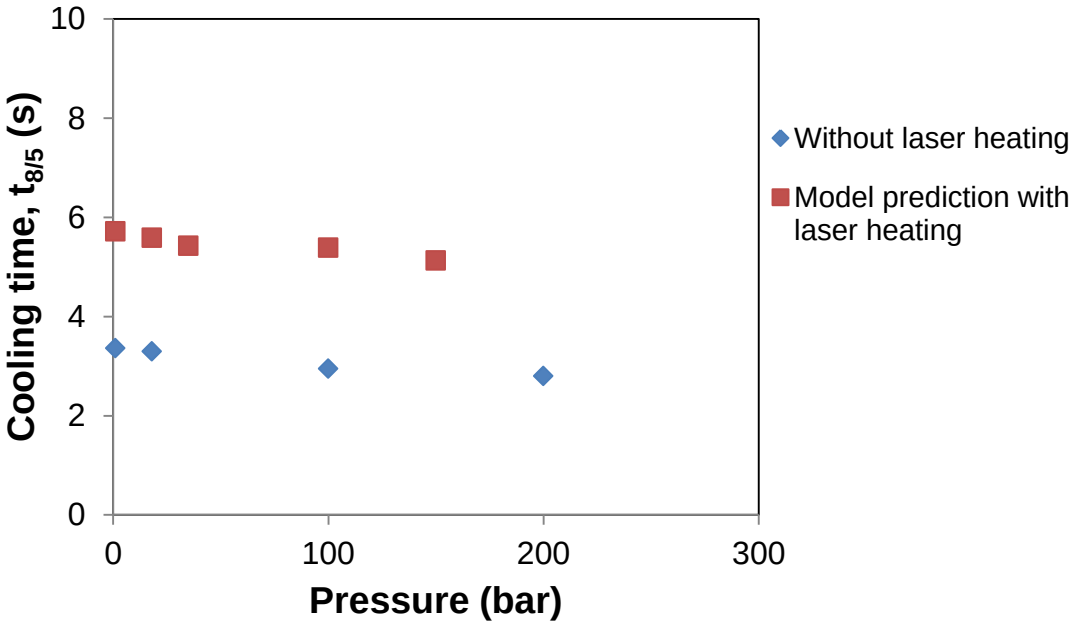

Figure 6-17: Comparing the weld cooling time with and without laser heating for a 25 mm plate thickness with 8 m/min WFS and 7 mm/s welding speed

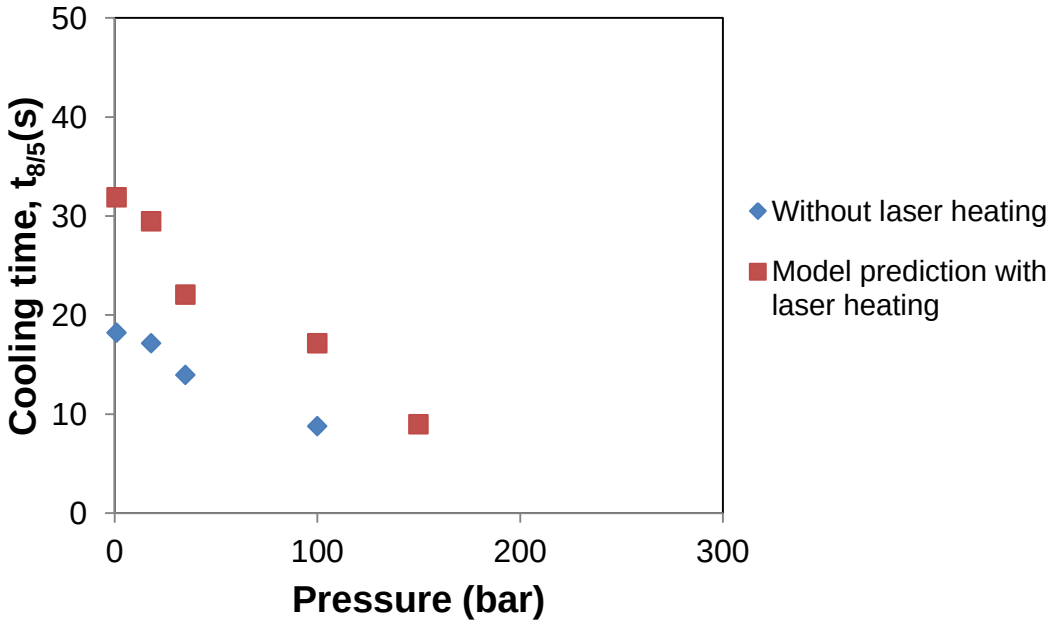

Figure 6-18: Comparing the weld cooling time with and without laser heating for a 5 mm plate thickness with 8 m/min WFS and 7 mm/s welding speed

6.5 Discussion of Results

This section presents the analysis and interpretation of the model results. The results will be compared with previous studies where available.

6.5.1 Analysis of temperature field distribution

The process heat input from the heat sources is quickly transferred in the thickness direction (z-axis) and then in the width direction (y-axis) to attain uniform distribution (Figure 6-5 and 6-7). Similar results were reported by Chaowen et al [24]. Although the laser was not intended to cause material melting, it can be observed that there is some material melting caused by the laser heat source (Figure 6-5). This is because of the high laser power used, even as the melting is localised on the material surface. Similar welds made with 3 kW laser power did not cause significant material melting as evident in Figure 6-7.

The wider temperature distribution produced by the laser heat source in comparison with that of CMT was because of the large beam diameter, which heats up a wider area of the material surface.

As shown in Figure 6-5 (bottom) and Table 6-2, the weld penetration was produced by the CMT heat source. This is because the CMT arc produced the heat input for melting of the material while the laser merely prolongs the weld cooling times. The simulation results suggest the same behaviour. The explanation for this is because of the higher heat flux of the CMT heat source, compared to the defocused laser beam with significantly lower energy density. The model prediction of weld penetration depth was close to that measured from the macrograph in Figure 6-6. However, the slight difference in the values may be due to the difference in geometry of the bead reinforcement between the actual weld profile and the model. The model assumed a rectangular shape for ease of computation while the actual bead reinforcement is convex in shape.

6.5.2 Analysis of thermal data

The thermal cycles shown in Figure 6-9 to 6-11 indicate that the simulation results were in good agreement with the experiments. These show that the material was rapidly heated up to peak temperature as the heat sources moved across it and then slowly cools down after it passes.

Since the width of the CMT heat source (denoted as b in Figure 6-3) used in the model was approximately 3 mm, it was obvious that none of the thermocouples were heated directly, but through conduction (Figure 6-9). This explains why the peak of CMT part of the thermal cycle was much lower than that of the laser for the 5 mm position (Exp_5 mm and Simu_5 mm). On the other hand, the laser beam radius was approximately 10 mm, and as a result, this point lies within the laser heat domain while the 10 mm point (Exp_10 mm and Simu_10 mm) may just be on its periphery (Figure 6-9). Therefore, the laser directly heats up the thermocouple, resulting in the higher laser peak temperature. The lower temperature peaks of points further away from the weld centre line is because of their distance from the direct heating effect of the heat sources, a situation not helped by the low heat input of CMT process and the thick pipeline section, which acts as a heat sink.

The mismatch between the model and experiment on the CMT part of the thermal cycles for the 5 mm distance (Exp_5 mm and Simu_5 mm), as can be observed in Figure 6-9, could be a result of errors due to the thermocouple position. The same is applicable to the thermal cycles representing 10 mm distance from the weld centre line (Exp_10 mm and Simu_10 mm). It may also be attributed to the change in shape of the weld bead as a result of the elongated weld pool caused by laser heating. Apart from these, the model and experimental results are a good match. The possible experimental error due to thermocouple position was described in chapter three. The model also gives a close approximation of the actual weld cooling time between 800°C and 500°C. However, the slightly faster cooling indicated by the model may also be due to modelling errors.

Since the point 5 mm from the weld centre line lies within the HAZ of the weld joint (Table 6-2), thermal cycles represented by (Exp_5 mm and Simu_5 mm) in Figure 6-9 can be used to approximate the cooling time of the HAZ for the set of welding parameters used.

As shown in Figure 6-10 to Figure 6-11 the CMT peak temperature exceeds 1540 °C which is approximately the material melting temperature. This indicates that the measured thermal cycle represents that of the weld pool. Also, the model prediction of the weld metal thermal cycles is in good agreement with experiment. However, the slight differences between the predicted and measured laser peak temperatures may also be due to modelling errors. The model indicates slightly faster cooling times compared with the experiment. This may be due to the material properties used in the model.

6.5.3 Predictive capability of the model

6.5.3.1 Thermal field and temperature profile for 50 mm process distance

The temperature field distribution shown in Figure 6-12 follow a similar pattern to those discussed in section 6.5.1. However, the distinct separation of the heat sources is because of their distance apart which in this case is 50 mm. This shows that as the heat sources are moved apart, it will reach a point where they have distinct temperature fields. This is in contrast to shorter process distances where both heat sources are in close proximity; hence the temperature fields are integrated. When compared to the temperature filed distribution of the same laser power (Figure 6-7), it can be observed that the laser peak temperature is lower than the former. This may also be because of the different beam sizes. The former had a beam diameter of 15 mm which should produce a higher energy density for the same laser power.

The weld metal thermal cycle shown in Figure 6-13 (0.5 mm from the welding surface) is quite similar to that of Figure 5-6 for a 50 mm process distance. Both indicate that the weld metal has cooled down to about 250 °C before the laser impinged on it. Apart from the laser power which is different (6 kW for the latter),

identical beam diameter and process distance where used in both cases. This gives a good indication of the predictive capability of the model. When compared with Figure 6-11 with similar laser power, it can be observed that the laser peak temperature is significantly lower. The former indicates a peak temperature of about 1200 °C against the latter of about 800 °C. This is because the thermal cycle described in Figure 6-11 was produced with 15 mm beam diameter, which will give a higher energy density than the simulated 20 mm beam diameter.

Considering the limitations of the model it is in good agreement with the experiment. It can therefore be used to make reasonably accurate predictions of laser assisted arc welding for different laser parameters.

6.5.3.2 Laser assisted GMAW under high pressure

As shown in Figure 6-14, the predicted cooling curves were in good agreement with the experiment. As a result, the model result was used to derive the convection coefficients for the different pressures investigated (Table 6-3). It can be seen that the convection coefficient increases with pressure, and this is because of the increase in the chamber gas density and resulting thermal diffusivity as earlier mentioned. This suggests that with increasing pressure the heat faster by convection to the chamber gas increases, resulting in faster cooling times.

The developed model was run with the derived convection coefficients to predict the weld thermal cycles of laser assisted hyperbaric GMAW. As shown in Figure 6-15, pressure did not significantly influence the weld thermal cycle for the 25 mm thick steel section. A similar result was shown in chapter three, which was attributed to the dominant influence of conduction over convective heat transfer to the chamber gas environment. For the thinner plate, the effect of pressure on the weld thermal cycle is quite significant (Figure 6-16). As the pressure increases, the weld cools faster indicating that pressure and consequently convective heat loss increases. Also, the effect of the laser is more pronounced

on the thinner plate as indicated by the much higher peak temperature of the laser in Figure 6-16.

Similar results were obtained for hyperbaric GMAW welding up to 200 bar pressure as described in chapter three. Although the welding conditions were different, the influence of material thickness and pressure on the thermal cycle of welds made under different ambient pressures was identical. Nevertheless, the effect of arc constriction which was not accounted for by the model may be seen from the thermal cycles of the hyperbaric GMAW shown in Figure 3-13 to 3-15. It can be observed that the temperature peaks were slightly decreasing with pressure. However, the temperature peaks of the predicted thermal cycles of the laser assisted GMAW were identical (Figure 6-15 and Figure 6-16). The results shown in Figure 6-17 and Figure 6-18 indicate that benefit of using a laser to extend the weld cooling time at one atmosphere can also be achieved at elevated pressures.

The model results seem to give a good indication of the temperature profile of laser assisted GMAW (CMT) under different ambient pressure conditions and the increase in weld cooling time. The arc constriction effects were not included in the model and this should have an effect in real life. Finally, the model needs to be validated by experiment data to fully establish its viability and/or limitations.

6.6 Conclusion

The following conclusions can be drawn from this model:

- Combined Gaussian distributed surface and double ellipsoid heat source models were implemented through user written subroutines in Abaqus 6.11 and experimentally validated for the 3D finite element simulations of laser assisted GMAW (CMT) at one atmosphere.
- The thermal field produced by the laser heat source is wider than that of CMT because of the large laser beam diameter when compared with that of CMT heat source. This is an indication of longer beam interaction time, and higher specific point energy that prolongs weld cooling time.
- The temperature distribution of the model was in good agreement with the experiment. Therefore, the model could predict the cooling time of the weld pool and heat affected zone.
- By assigning appropriate convection coefficients to the model, it is possible to predict the weld thermal cycles of laser assisted GMAW (CMT) under different pressures.

7 Simulation of Moisture Pick-up and Hydrogen Analysis of Weld Metal at one Atmosphere

Scope

The potential for moisture pick-up during hyperbaric welding is high. This is because the welding habitat has to be open for access to Remotely Operated Vehicles (ROVs) or divers, welding equipment and other tools used for underwater pipeline installation and repair applications. Consequently, the moisture dissociates inside the welding arc to oxygen and hydrogen, which are picked up by the weld pool. The presence of these hydrogen atoms in the weld pool is the main cause of hydrogen assisted cracking. The hydrogen atoms could diffuse to highly stressed regions of the weld joint, particularly in the HAZ, where they would recombine to form hydrogen molecules. Consequently, the weld fracture toughness is undermined.

This chapter describes the experimental set up used to simulate moisture pick up and hydrogen analysis of the weld metal. Different levels of moisture were deliberately introduced into the shielding gas before welding by CMT and then by laser assisted CMT. This was followed by hydrogen analysis of the weld metal to establish the influence of the laser in removal of diffusible weld metal hydrogen content. Finally, possible experimental errors; followed by the experimental results and their discussion are presented.

7.1 Aim and Objectives

The aim of this study is to investigate the use of a laser to reduce or minimise the diffusible weld metal hydrogen content. The objectives are as follows:

- To analyse the pick-up of hydrogen by the weld metal during GMAW (CMT) and laser assisted GMAW (CMT) welding by introducing different moisture levels into the shielding gas; and
- Evaluate the influence of a laser on the removal of diffusible hydrogen from the weld metal.

7.2 Materials and Equipment

The materials used for the experimental trials, which include: pipeline steel and welding consumables are presented. The equipment used for the welding trials, metallurgical characterisation and hardness tests are also presented.

7.2.1 Materials

7.2.1.1 Steel

Refer to Table 3-1 of chapter 3 for the chemical composition of the X65 pipeline steel used for this experiment. The test specimen, run-on and run-off pieces were produced to dimensions as specified in BS EN ISO 3690:2001(Figure 7-1).

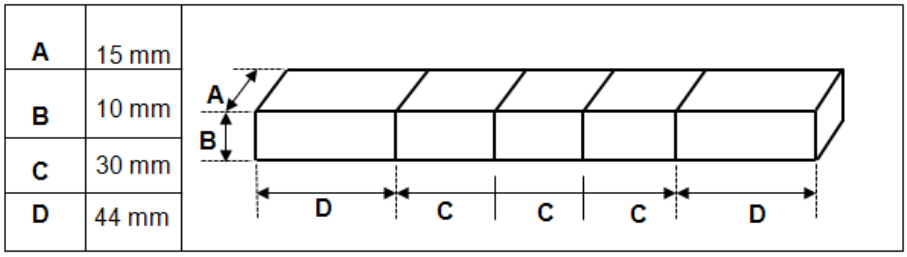

Figure 7-1: Dimension of the test pieces marked as (C) and run-on and run-off plates marked as (D)

7.2.1.2 Welding Wire

The same welding wire given in Table 4-1 of chapter 4 was used for this experimental trial.

7.2.1.3 Shielding Gas

Refer to section 4.2.1.3 of chapter 4 for the shielding gas used in this study.

7.2.2 Equipment

The equipment used for the experimental trials are presented in this section. These include the Fronius TPS 5000 CMT welding power source, Fanuc M-710iB 45 Robot and IPG YLR-8000 Fibre Laser. The other equipment were for:

moisture content measurement and hydrogen analysis. This includes a Cermex II Hygromenter, water containers and a Ströhlein H-Mat 2500 hydrogen analyser. Since the other equipment has been described in the previous chapters, only the moisture content measurement and hydrogen analysis equipment will be described in this section.

7.2.2.1 Moisture Content Measurement

A photograph and schematic illustration of the equipment set-up used for moisture measurement is shown in Figure 7-2. This includes a gas cylinder containing Argoshield heavy gas, rubber hoses, a water container, and two dry containers, a Cermet II Hygrometer manufactured by Michell Instruments, flow regulators and flow meters. Two hoses were connected to the shielding gas via a flow regulator. One supplies gas to the water container where it picks-up moisture. The moist gas is then collected in one of the dry containers. In order to minimise turbulence and possible entrapment of bubbles, the second dry container collects the moist gas and also serves as a humidifier. Dry gas is feed through the second hose and was used to control the moisture levels in the wet gas.

A by-pass connection is made to the hygrometer and a flow meter was used to regulate the high flow rate to the hygrometer because the instrument is sensitive to a high rate (see Figure 7-2 (bottom)). The accuracy of the hygrometer is limited to a maximum flow rate of 5 l/m [87]. With the aid of the dew point sensor; the hygrometer is used to measure the moisture levels in the shielding gas. The moist gas is also connected to another flow meter, which controls the gas flow rate to the CMT welding machine. The gas flow rate setting in the CMT machine was circumvented. Otherwise, it was not possible to weld with moist shielding gas flow.

The Cermet II uses a moisture sensor and a monitor unit, which can be located apart by 1200 mm [87]. It is provided with a 4-20 mA output, and a fully self-contained display system in a 1/8 DIN panel mounting case that indicates the measured humidity [87]. Measurement units can be displayed in °C or °F dew

point, ppm_v, lb/mmscf or g/m^3 across the range -100 to + 20 °C dew point at pressures up to 400 bar [87].

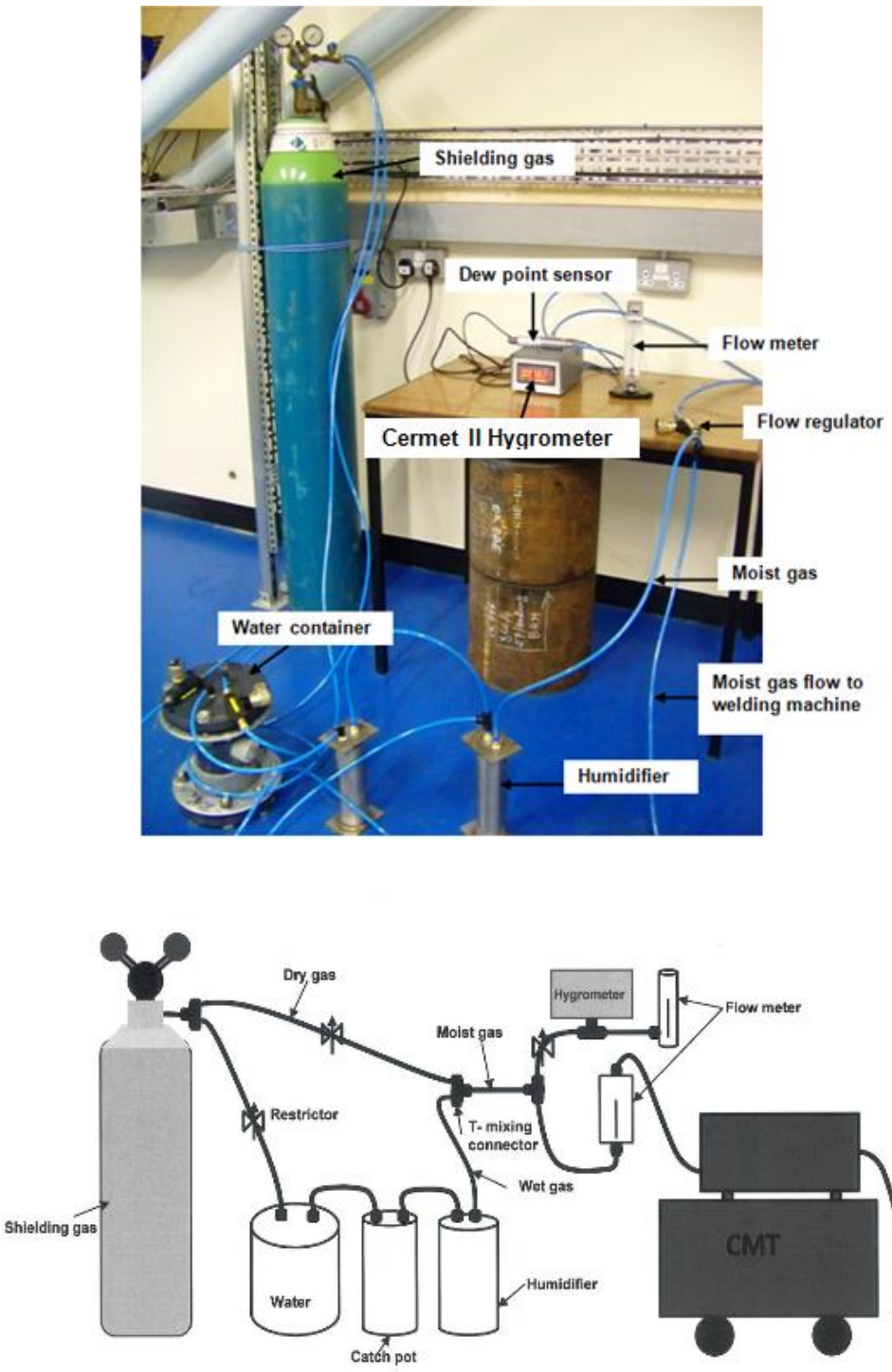

Figure 7-2: Set-up for monitoring of moisture level in the shielding gas (Top) photograph of equipment (bottom) schematic illustration

7.2.2.2 Ströhlein H-Mat 2500 Hydrogen Analyser

The Ströhlein H-Mat 2500 hydrogen analysis system is shown in Figure 7-3. This comprises a computer controlled analysis system, hot extraction furnace, electronic weighing balance and a computer system with printer. The system is capable of performing both hot extraction and melt extraction. The former is used for determination of diffusible hydrogen content in a sample, while the latter measures total hydrogen content in the sample. Hot extraction was used for this analysis.

The sample prepared for analysis is placed in the hot extraction furnace and heated up to a temperature of 400 °C. Hydrogen and carbon monoxide are released from the sample and taken up by a carrier gas (nitrogen) flow. On passing the dust trap, oxidising agents and a molecular sieve, coarse particles are removed from the carrier gas and CO_2 as well as H_2O are retained [140].

The thermal conductivity measuring cell of the analyser system operates as the hydrogen detector. The thermal conductivity of the carrier and reference gas flow is measured by thermistors in a bridge circuit. A measurement signal indicates a change in thermal conductivity of the two gases when hydrogen is released [140]. The magnitude of this signal is proportional to the hydrogen content of the sample. The course in time of the measured signal is displayed on the graphics screen and the time integral of a measured curve corresponds to the hydrogen content of a particular sample [140]. The central processing unit calculates the hydrogen content to an accuracy of 0.01 ppm and displays the result digitally on the screen.

The analyser is first calibrated before use. The calibration is made using the same parameters and environmental conditions as for the subsequent analyses. The calibration factor can be determined either with standard samples or with hydrogen gas [140]. For this analysis, the latter was used. This was done using a computer control system by injection of a specific volume of hydrogen gas into the carrier gas. The important parameters for determining the calibration factor (temperature of the calibrating gas and barometric pressure)

were acquired in the analyser [140]. They can be displayed on the monitor screen during the calibration procedure. Several determinations of the calibration factor were made and the average of the results was taken as a working calibration factor.

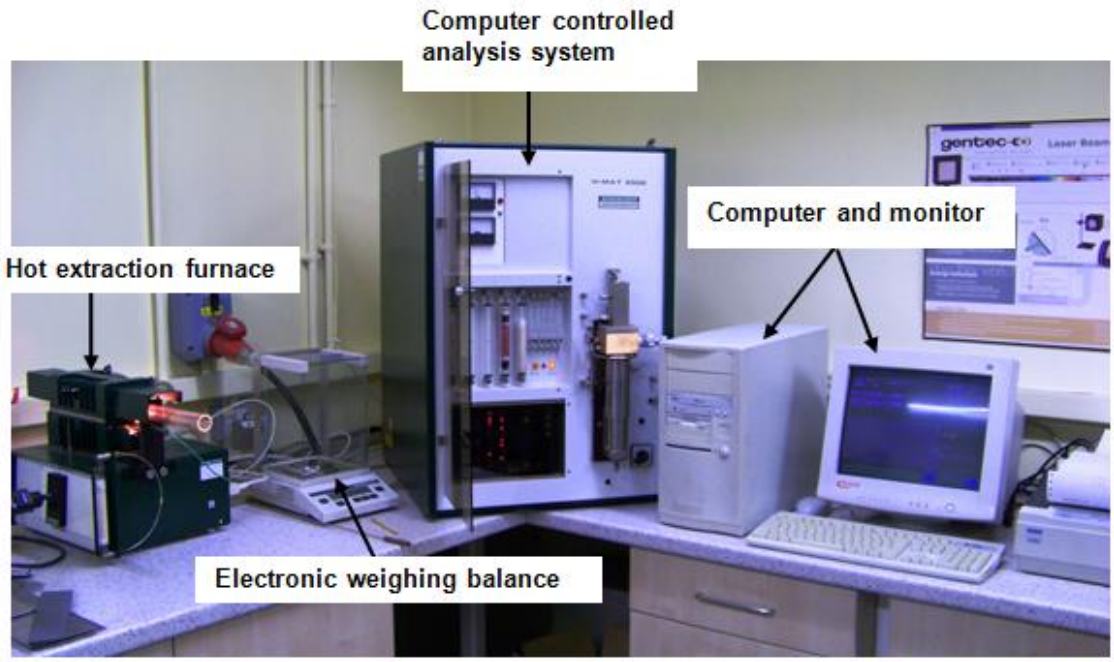

Figure 7-3: The Ströhlein H-Mat 2500 equipment units used for hydrogen analysis

7.3 Experimental Method

7.3.1 Welding Trial

A total of sixteen bead-on-plate welds were performed using the test specimen arrangement shown in Figure 7-1. Four different moisture levels ranging between 300 and 10,000 ppm were introduced into the shielding gas before welding, first with CMT and then laser assisted CMT. The laser parameters investigated were 6 kW and 3 kW laser power with 10 mm beam diameter. The process distances used were 20 mm and 0 mm. The size of the test specimen as stipulated by BS EN ISO 3690-2001did not allow for the investigation of larger beam diameters and longer process distances. For the CMT, a wire feed speed of 7 m/min was used at a fixed welding speed of 7 mm/s. A CTWD of 10 mm, which would ensure short arc length, was used. Prior to welding, the middle test pieces were degassed at 600 ºC for 1h 30 min in a furnace. This was done to remove any diffusible hydrogen that may be present in the sample. The test samples were clamped in the copper jig fixture using copper foils as shown in Figure 7-4. This prevents erosion of the fixture and also serves as a heat sink. The complete experimental data is given in Table B-6 to B-9 of the Appendix B. A photograph of the welding trial set-up is shown in Figure 7-4.

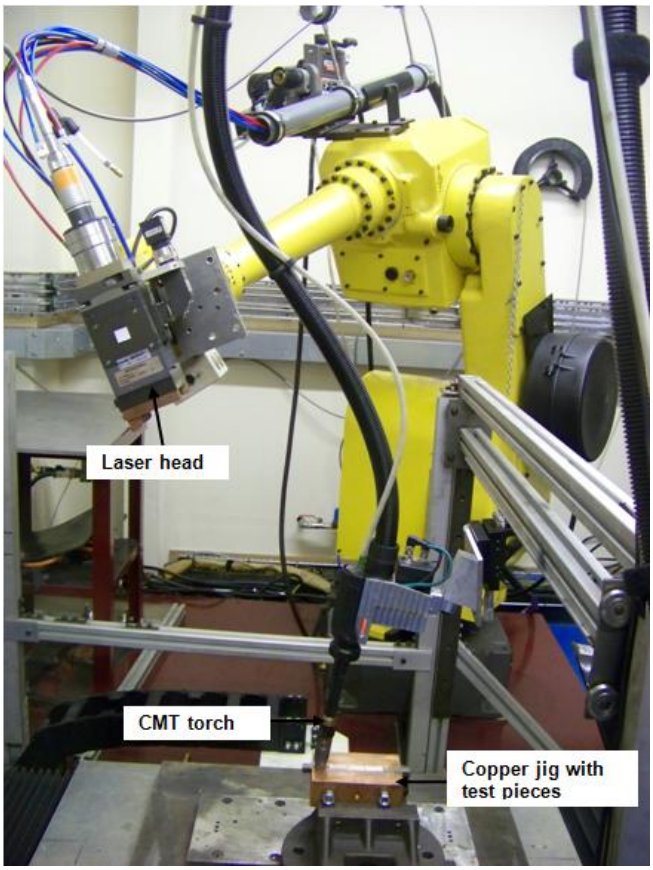

Figure 7-4: Experimental set-up for welding

7.3.2 Hydrogen Testing Procedure

The testing was performed according to BS EN ISO 3690-2001: Determination of hydrogen content in ferritic steel arc weld metal [21]. The three test pieces marked as C in Figure 7-1 were used for the hydrogen analysis. Immediately after welding, the test pieces were cooled in water and thereafter stored inside a flask containing ethanol in solid CO_2 at -78 ºC. This was necessary to minimise hydrogen diffusion after welding. The start and stop pieces were removed and the three test pieces were put back in cold storage until individual hydrogen analyses were carried out. Hot extraction was performed at 400 ºC using the H-Mat H2500 system shown in Figure 7-3. This determines only the amount of diffusible hydrogen in the deposit weld metal. The resulting hydrogen levels reported as H_{DM} (DM = Deposited Metal) in ml hydrogen/100g weld metal are given in Table B-6 to B-9 of the Appendix B.

7.3.3 Microstructure Examination and Hardness Test

Refer to section 3.2.2.5.1 of chapter 3 for the microstructure examination. The hardness test was performed as described in section 3.2.2.5.2 of chapter 3 using the micro hardness equipment shown in Figure 3-6.

7.4 Experimental Error

In addition to the experimental errors described in section 5.4 of chapter five, there is also the likelihood of errors being introduced during the measurement of moisture levels and hydrogen analysis. These errors are presented in details in this section.

There could be both systematic and operator's errors in the determination of moisture levels in the shielding gas when using the hygrometer. This is because the ambient temperature and dew point influences the accuracy of the measurement. The accuracy of the instrument is $\pm$1 °C from -60 °C to +20 °C dew point (dp), and $\pm$2 °C from -100 °C to -60 °C dew dp [87]. To minimise the likelihood of this error, most of the welding trials were performed on the same day, where the ambient temperature and dew point would likely be the same.

Another error could likely come from the value of the measured moisture levels. The moisture levels were rounded up to the nearest whole number because it was difficult to determine the exact set values. However, the measurements were made as close as possible to the set values to reduce the possibility of this error.

For the hydrogen testing, it cannot be guaranteed that the hydrogen introduced during welding would be exactly the same during the test. This is because of the high hydrogen diffusion rate even at low temperature. The time between welding and quenching of the test pieces is not likely to be the same for all the trials. This varied between 2 min to 3 min, which could be crucial to hydrogen diffusion. Therefore, to limit hydrogen diffusion after welding, the unclamping and quenching was carried out as quickly as possible.

To limit the variability in measurement of weld metal hydrogen content by the hydrogen analyser, the equipment was calibrated before performing actual testing, and the calibration factor was used as a benchmark. Also, three tests were performed per trial and the average value of the weld metal hydrogen content was determined.

7.5 Results

The interpretation of the experimental results is presented in this section. This is followed by their discussion in the subsequent section.

7.5.1 Moisture Levels and Hydrogen Concentration for CMT Welding

The effect of shielding gas moisture level on diffusible hydrogen concentration in the weld metal for CMT welding alone is shown in Figure 7-5. This clearly shows that hydrogen concentration in the weld metal is directly proportional to moisture levels in the shielding gas. As the moisture level in the shielding gas increases, more hydrogen is picked up by the weld pool. This would also increase the sensitivity to hydrogen assisted cracking.

From the plot, it can be deduced that for moisture levels ≥ 3000 ppm, there is a high likelihood of hydrogen assisted cracking occurring (other factors taken into consideration) because the hydrogen concentration is more than 5 ml/100 g of deposited weld metal, which is the limit stipulated by the International Institute of Welding (IIW) for avoidance of cracking.

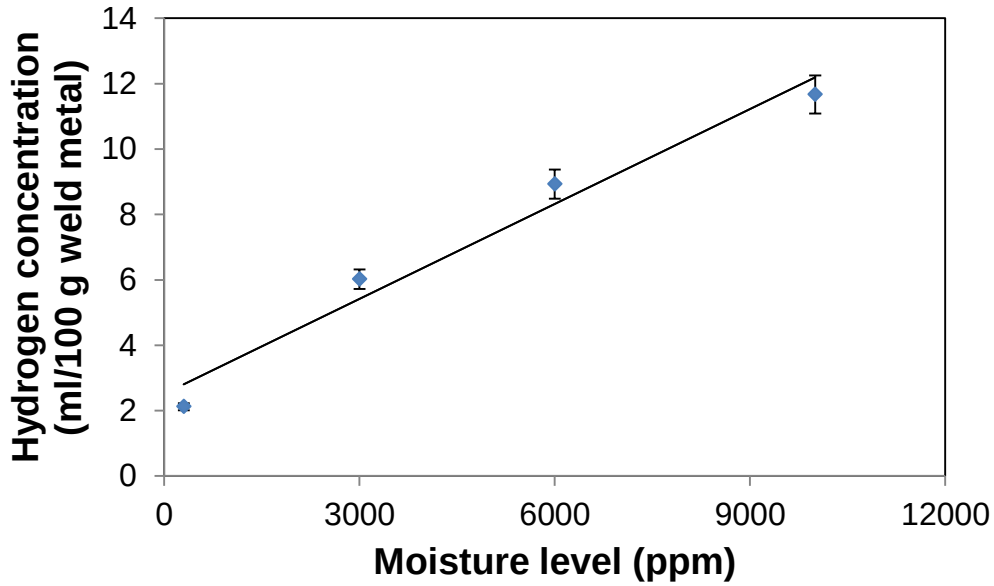

Figure 7-5: Relationship between moisture level and the deposit weld metal hydrogen concentration for CMT

7.5.2 Moisture Levels and Hydrogen Concentration for Laser Assisted CMT Welding

Figure 7-6 and Figure 7-7 show the effect of additional laser heat input to the CMT process (LCMT) on the moisture level and diffusible weld metal hydrogen concentration. The same trend of increasing hydrogen concentration with moisture levels can be observed. It can also be seen from both graphs that the welds hydrogen concentration remains effectively unchanged for 300 ppm moisture level (dry gas). This was for welds made without moisture in the shielding gas.

The influence of a laser on removal of diffusible weld hydrogen content is obvious from the plots. Compared with CMT welding alone, there is significant reduction of hydrogen concentration for all moisture levels investigated. For example, while the hydrogen concentration is about 12 ml/100 g of deposit weld metal for CMT welding with 10,000 ppm (see

Figure **7-6**); it is reduced to about 6.0 ml for the laser assisted CMT welding with 6 kW laser power for the same moisture level. Clearly this depends on the laser power and process distance as evident in Figure 7-7. It can be seen that higher laser power and longer process distance gives lower hydrogen concentration per 100 g of deposited weld metal. Figure 7-7 shows that weld metal hydrogen concentration decreases sharply with laser power. However, beyond 3 kW laser power there is not much change in hydrogen concentration.

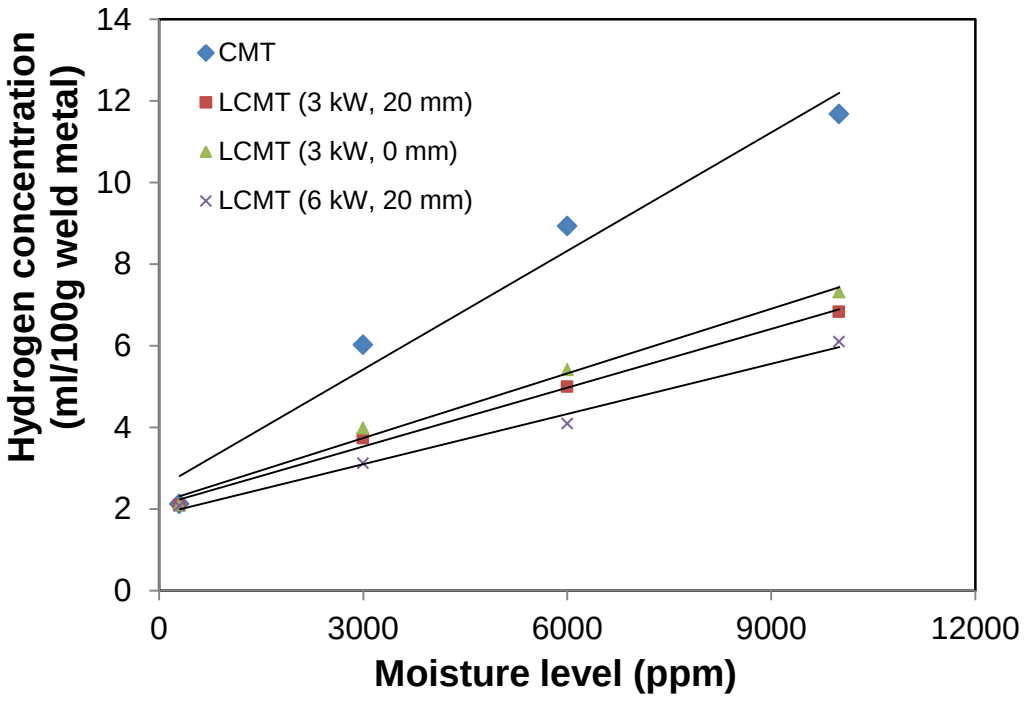

Figure 7-6: Relationship between moisture level and the deposit weld metal hydrogen concentration for laser assisted CMT

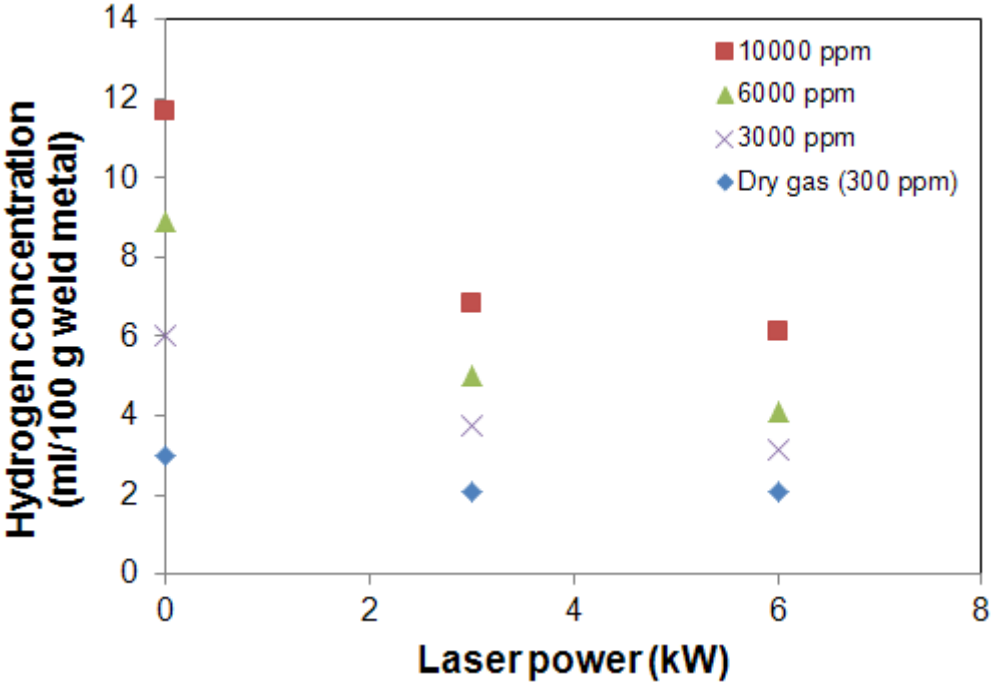

Figure 7-7: Effect of laser power on the deposit weld metal hydrogen concentration for different moisture levels for 20 mm process distance

7.5.3 Microstructure Examination and Hardness Test

The microstructures of specimens welded with 10,000 ppm moisture level in the shielding gas and with dry gas (300 ppm) for CMT and laser assisted CMT are shown in Figure 7-8 to 7-11. The hardness profiles of the CMT and laser assisted CMT welds for both moisture levels is also presented in Figure 7-12.

As can be seen from the figures, the microstructure of the weld metal and HAZ shows significant differences between the CMT and laser assisted CMT welds for both moisture levels. The weld metal and HAZ microstructures of the laser assisted CMT welds were dominated by more soft and ductile ferrite phases than the CMT welds as evident in the hardness distribution (Figure 7-12). This is due to the additional laser thermal input to the CMT process.

The HAZ microstructure looks distinctly different for both welds with 300 ppm and 10,000 ppm moisture levels. That of the laser assisted CMT process consists predominantly of acicular ferrite, and is not easily distinguishable from the weld metal. Conversely, there is a clear demarcation between the weld metal and HAZ for the CMT weld. The microstructure of the HAZ may consist of martensite especially close to the fusion boundary, which can be attributed to the relatively low heat input of the CMT process.

The hardness distribution shows that moisture level has no influence. The hardness profile of the CMT weld is typical of a low heat input weld, with the peak hardness occurring in the coarse grained HAZ close to the fusion boundary and the minimum value in the base metal. The peak hardness occurs in the weld metal and the minimum in the HAZ. The additional laser thermal input to the CMT process accounts for the differences in the hardness distribution.

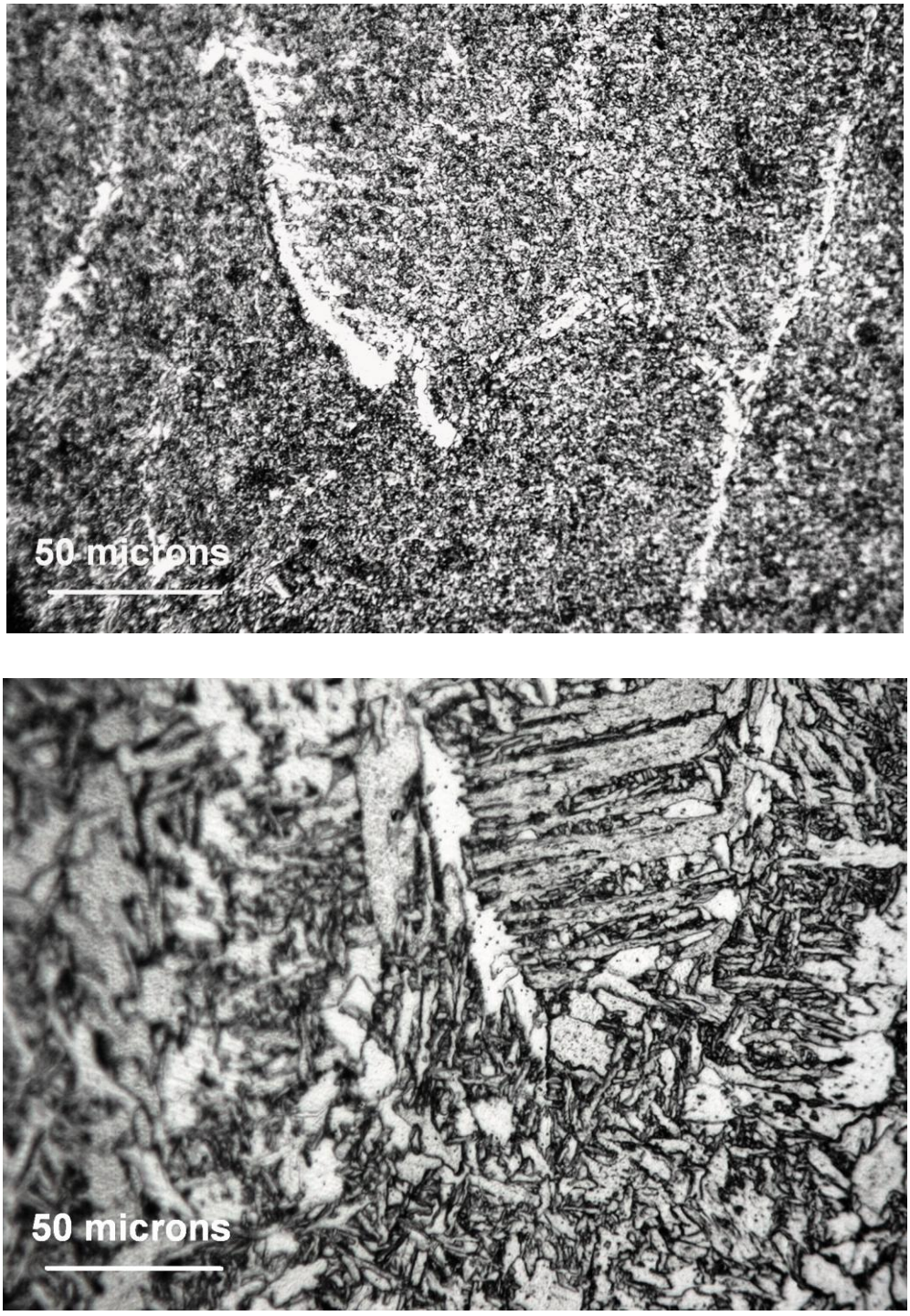

Figure 7-8: Microstructure of the weld metal with 300 ppm moisture level in the shielding gas (top) CMT and (bottom) laser assisted CMT

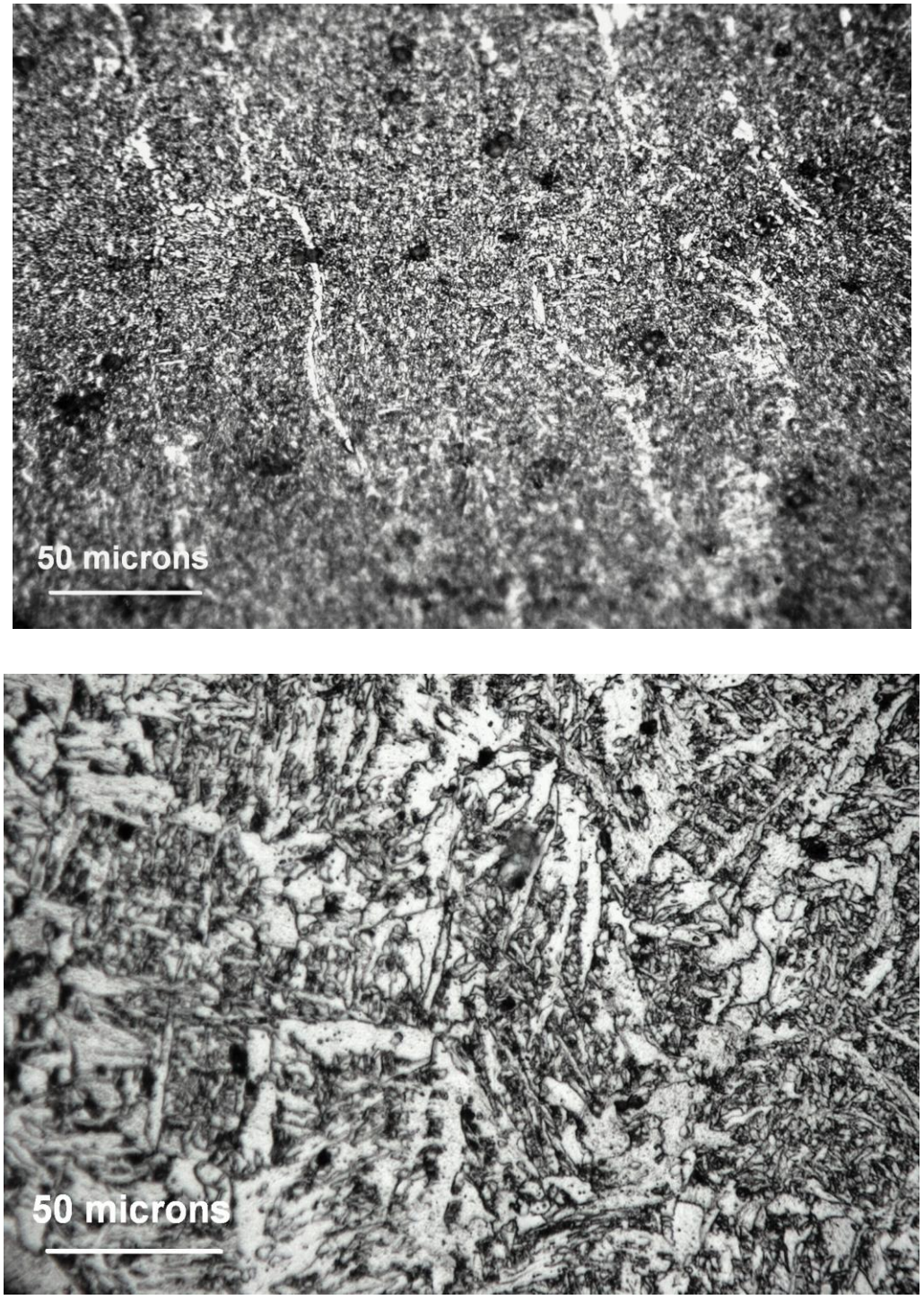

Figure 7-9: Microstructure of the weld metal with 10,000 ppm moisture level in the shielding gas (left) CMT and (right) laser assisted CMT

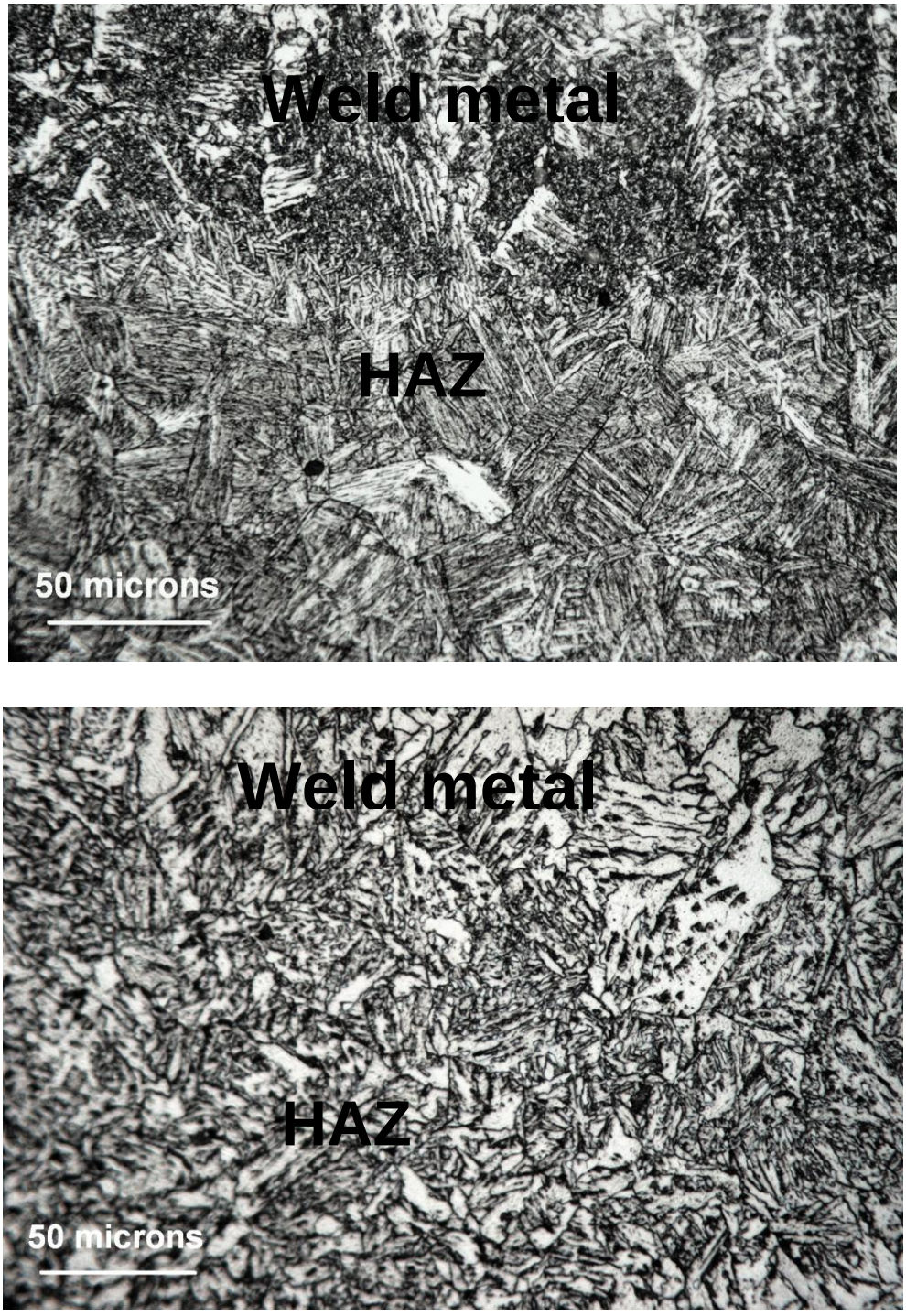

Figure 7-10: Microstructure of the weld metal and HAZ with 300 ppm moisture level in the shielding gas (left) CMT and (right) laser assisted CMT

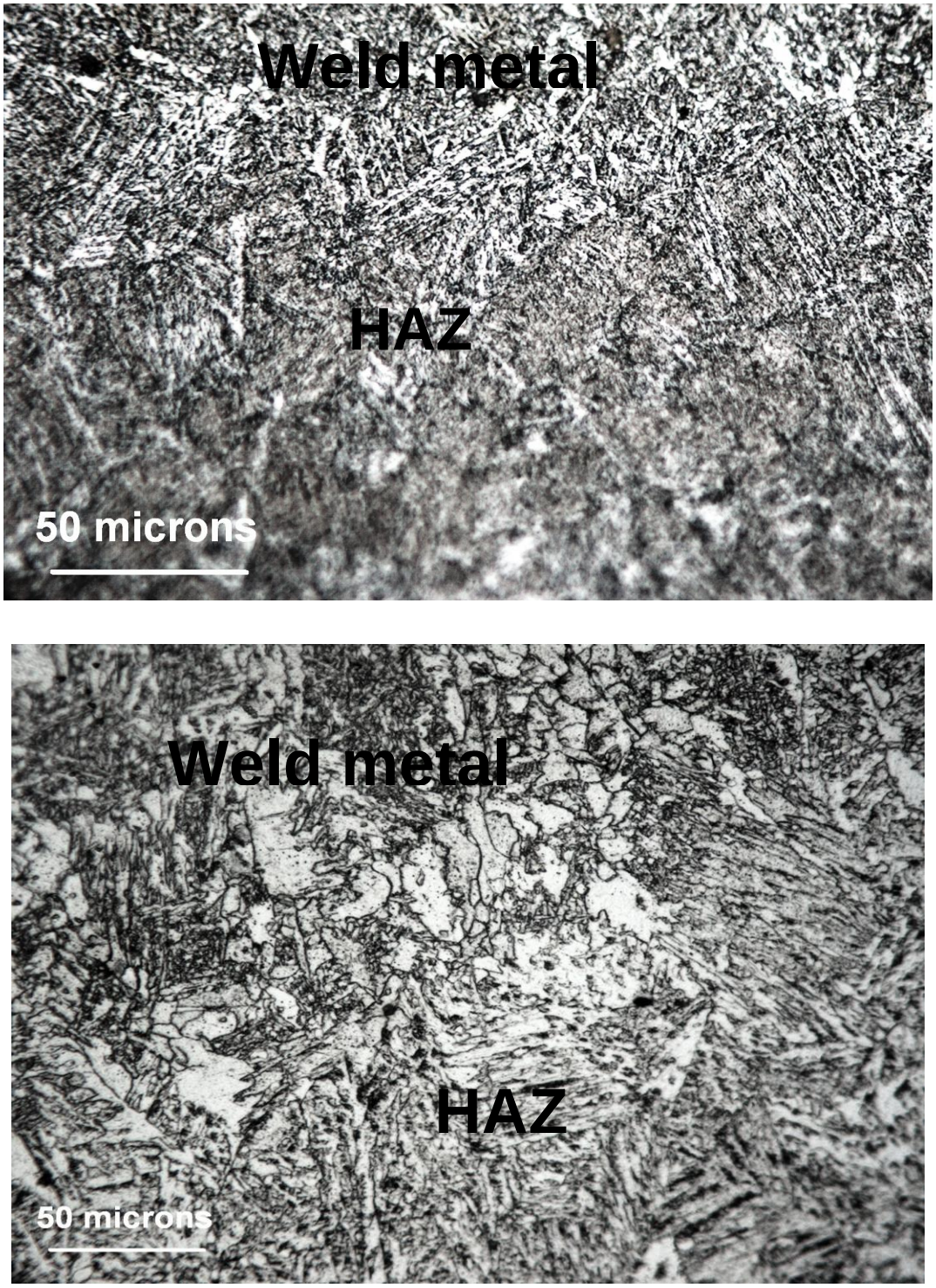

Figure 7-11: Microstructure of the weld metal and HAZ with10,000 ppm moisture level in the shielding gas (left) CMT and (right) laser assisted CMT

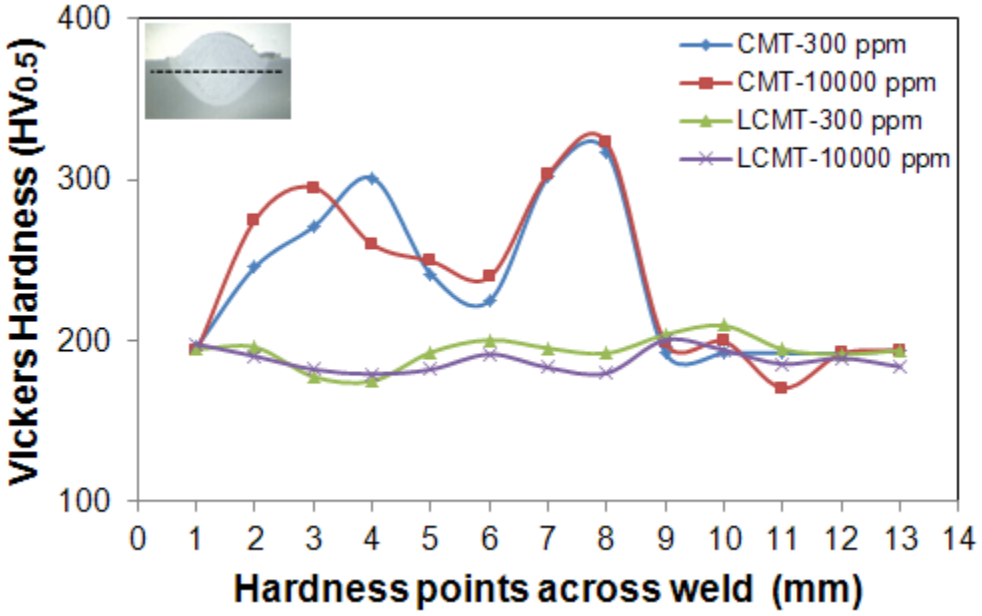

Figure 7-12: Hardness profiles of the CMT and laser assisted CMT welds for different moisture levels in the shielding gas

7.6 Discussion of Results

This section presents the analysis and interpretation of the experimental results. The results will be compared with previous studies where available.

The test piece sizes used for this experiment were prescribed for arc welding processes as outlined in BS EN ISO 3690-2001. There are obvious limitations of adopting this standard to the laser assisted arc welding process. The additional laser heat distribution and weld bead size will be different from that of the arc process and this may affect the measured weld metal hydrogen content. Also, this limited the range of laser power, beam size and process distance investigated.

Another real concern is that hydrogen diffusion phenomenon will be completely different for this small test piece size when compared to real production pipeline welding. Therefore, an ideal way of evaluating the weld hydrogen content would be to carry out this experiment on thick section pipeline steel before determining the weld hydrogen content. However, the hydrogen analysis system used for this work was designed to measure the weld metal hydrogen concentration of the standardised test piece sizes.

7.6.1 Moisture Levels and Hydrogen Concentration

As shown in Figure 7-5 and 7-6, hydrogen concentration in the weld metal is directly proportional to moisture levels in the shielding gas. Aune et al [9] reported that moist shielding gas represents a major source of hydrogen pick-up during hyperbaric welding. Therefore, making acceptable welds require keeping moisture levels low. The increasing hydrogen concentration with moisture level is an indication of increased hydrogen pick-up as water vapour dissociates in the welding arc to hydrogen and oxygen according to equation (7-1)[9]:

$$H_2O = 2\,[H] + [O] \qquad (7\text{-}1)$$

Additional heat input by the laser beam to the CMT process is shown to significantly lower weld metal hydrogen concentration as indicated by Figure 7-

6. An estimated 40% to 50% reduction of hydrogen concentration was achievable depending on the laser parameters used even for 10,000 ppm of moisture in the shielding gas. The lowest influence was obtained with 3 kW laser power and 10 mm beam diameter at a process distance of 0 mm, i.e. when both heat sources are just touching (LCMT 3 kW, 0 mm in Figure 7-6).

Figure 7-6 This is followed by the weld with the same laser power and beam size but 20 mm process distance (LCMT 3 kW, 20 mm). Finally, the weld made with 6 kW laser power, the same spot size and 20 mm process distance (LCMT 6 kW, 20 mm) reduced hydrogen concentration by almost half. Welds could not be performed with 6 kW, 10 mm beam diameter and 0 mm process distance as the intensity of the laser heat persistently destroyed the welding torch because the CMT torch was too close to the laser beam.

The fact that not much hydrogen was removed at powers above 3 kW as shown in Figure 7-7 may be because beam diameter or interaction time and process distance have more dominant effect than laser power in removal of diffusible weld hydrogen. Although larger beam sizes and longer process distances could not be investigated due to the size of the test pieces, results shown in Figure 5-10 and Figure 5-13 of chapter 5 and Figure 7-6 show that these parameters could influence the removal of diffusible weld metal hydrogen.

The influence of the laser on hydrogen removal can be explained by the fact that the additional laser heat input to the CMT extends the weld pool cooling and solidification time. This is because the weld remains at high temperature for a relatively longer time than CMT alone due to laser post weld-heating. Therefore, the hydrogen introduced into the weld pool has the ability to escape via diffusion before the weld cools down to room temperature. This may also be influenced by the Marangoni effect and hydrogen diffusion coefficient of the steel. As shown in Figure 7-13, the average diffusion rate of hydrogen in steel at 100 °C is 1000 times faster than at 20 °C or room temperature [31].

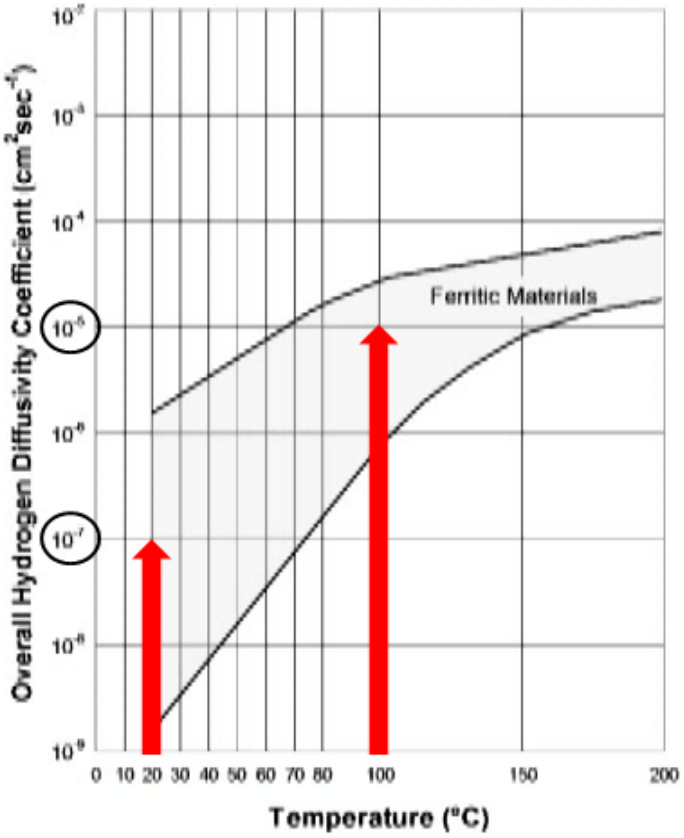

Figure 7-13: Hydrogen diffusion coefficient of ferritic steel [31]

The most hydrogen removal was achieved with the 6 kW laser beam because it has twice the energy density of the 3 kW laser beam for the same beam size, hence, the higher thermal input. The difference in hydrogen removal for LCMT 3 kW, 20 mm and LCMT 3 kW, 0 mm is due to the process distance effect, which was explained in chapter 5. It has been shown from the thermal cycles of laser assisted CMT welds made at different process distances (Figure 5-6) that the further apart both heat sources are, the more influence this could have on hydrogen diffusion rate. This is because the laser beam will heat up the weld metal for a longer period of time as the process distance increases (see Figure 5-13). Since hydrogen diffusivity of steel depends on time and temperature among other variables, it is suggested that longer process distance will favour hydrogen removal because of the longer residence time at high temperature (Figure 5-13).

Since the carbon equivalent of the X65 pipe steel used is CE_{IIW} = 0.40, it is recommended that the hydrogen content is below 5 ml/100 g deposit weld metal to avoid HAC. This experiment has shown that to achieve lower hydrogen concentration, the moisture level in the welding arc environment should be less than 3000 ppm for CMT welding. However, the addition of laser heat input could lower the hydrogen concentration to levels below 5 ml/100 g depending on laser parameters used even for higher moisture levels.

7.6.2 Microstructure Examination and Hardness Test

The differences between the microstructures of the CMT and laser assisted CMT welds for the same moisture levels as indicated in Figure 7-8 to 7-11 is mainly because of the additional thermal input from the laser. The higher heat input of the laser assisted CMT process increase the weld cooling time. Consequently, there is enough time for the formation of softer and more ductile phases in the weld metal and HAZ which favours diffusion. The microstructures are predominantly polygonal ferrite and acicular ferrite phases. These have profound influence on the weld hardness profile shown as shown in Figure 7-12. The high composition of acicular ferrite, which is good for weld toughness, may be due to oxide inclusions. The oxides provide suitable sites for the nucleation of acicular ferrite [89]. Conversely, the HAZ microstructure of the CMT welds consists of some hard phases such as martensite and some ferrite phases formed by the relatively low heat input of the process, and consequent fast cooling time. This is evident in the hardness distribution.

The main effect of moisture content is the formation of oxides in the microstructure as shown in the CMT weld metal and HAZ microstructures (Figure 7-9 and 7-11). The oxides may have been formed by the oxygen atoms picked-up along with hydrogen during the dissociation of water vapour in the welding arc (see equation (7-1)).

The hardness profile of the CMT welds (Figure 7-12), which is indicative of HAZ hardening, is consistent with reported works on low heat input and high cooling rate welding of low carbon steels [36]. The high hardness of the HAZ especially in

the CGHAZ is due to the presence of martensite in the microstructure, which was caused by the fast cooling time and resultant high cooling rate of the weld metal. The addition of laser heat input to the CMT brought about a striking change in the hardness profile as distinctly shown in Figure 7-12. The peak hardness was reduced from about 322 HV to 203 HV In this case; the minimum hardness occurs in the HAZ, which is indicative of HAZ softening. This is because the high heat input favoured the formation of soft ferrite microstructures in both the WM and HAZ.

7.7 Conclusion

The following conclusions can be drawn from this study:

- Hydrogen concentration in the deposited weld metal is directly proportional to the moisture content in the welding atmosphere.
- By applying additional laser heat input to CMT welding, it is possible to reduce the hydrogen concentration in the weld metal by up to 50% depending on the laser parameters used.
- Separation distance between the laser and CMT heat sources (process distance) also influences hydrogen removal from the weld metal. The further the heat sources are apart, the longer the time the laser beam heats up the weld metal resulting in higher hydrogen diffusion rate.
- The weld metal and HAZ microstructures were not affected by moisture levels in the shielding gas for both CMT and laser assisted CMT welds. However, oxide inclusions were observed at high moisture levels for the CMT welds. Although, these were significantly reduced by the addition of laser heat. The oxide inclusions promoted the formation of acicular ferrite that dominated the weld metal and HAZ microstructures of the laser assisted CMT welds.
- The additional laser heat input significantly reduced the peak hardness of the CMT weld from 322 HV to 203 HV.

8 Practical Implications, Main Conclusion and Further Work

Scope

This chapter presents the practical implications and main conclusion of this research work. This is followed by suggestions for further work.

8.1 Practical Implications of Research Findings

The current research focus was aimed at optimizing the laser and arc parameters in atmospheric conditions for the reduction of weld metal cooling rate. Subsequently, these will be employed in welding trials under high pressure conditions.

The current hyperbaric GMAW is operated at a short arc length to ensure process stability at elevated pressures. The concomitant low heat input and spatter generation of this process informed the choice of an advanced GMAW (CMT) process for controlled dip transfer and reduced weld spatter. However, the CMT process needs to be evaluated in high pressure conditions to ascertain its viability for hyperbaric welding. Nevertheless, the traditional GMAW process is already proven for hyperbaric application, and therefore can be used in combination with a laser to achieve the benefit of reduced cooling rate and susceptibility to cold cracking.

Laser hyperbaric welding is not a well-researched area. However, work conducted in Cranfield University shows that conduction welding with a defocused laser beam is feasible since no metal vaporization is expected as this could attenuate the laser energy. Consequently, the laser power is more efficiently used. This would be desirable for this application as the laser would be used as a spatially resolved heat source to control weld cooling rate.

In terms of practical application, the feasibility of the complete laser system must incorporate the beam delivery, focusing optics and containment of the system undersea. Ideally, the laser could be housed on the surface barge, and beam delivery through optical fibre is technically feasible to depths beyond 1000 m. The laser may also be located inside an adjacent subsea container for hyperbaric operations.

Finally, the laser assisted hyperbaric GMAW system must first be assessed in conjunction with procedure qualification performed in a high pressure vessel prior to industrial application.

8.2 Main Conclusion

The following are the main conclusions from this research project:

- Conduction mode of heat transfer dominates the cooling for pipes with higher thickness. It has been observed that for pipes with thickness about 25 mm, the ambient pressure did not play any significant role in determination of the cooling rate. However, for thickness close to 5 mm the convective cooling, determined by the ambient pressure, plays an important role.

- Heat input from standard GMAW processes, results in fast weld cooling times, in the order of 3 s. Such high cooling rates resulted in formation of hard microstructural features with low temperature transformation products which could accelerate hydrogen cracking. The application of a laser can modify the thermal cycle and help in generating microstructures which could prevent hydrogen assisted cracking.

- Laser, used in conduction mode, as an external and flexible heat source was shown to modify the thermal cycle in a controlled manner. Depending upon the parameters, e.g. beam diameter, process distance, it can create different thermal cycles. It has been shown that such modified thermal cycle can extend the weld residence time at high temperature thereby reducing the weld hydrogen content and cracking sensitivity.

- A thermal model of the process showed good agreement with experimental results and indicated that benefits of reduced cooling rate could be obtained at high pressures.

8.3 Recommendations for Further Work

The following further work is recommended:

- Fronius CMT and EWM ColdArc processes should be evaluated under high pressure conditions to ascertain whether they could be used as alternatives to the currently developed pulsed and short circuit mode GMAW for hyperbaric application.

- The laser assisted GMAW (CMT and/or ColdArc) process should be investigated under high pressure conditions in order to evaluate the effect on weld cooling rate and resultant mechanical properties.

- The developed laser assisted GMAW thermal model should be validated by experimental data for high pressure conditions. This will help to give a more accurate prediction of the weld thermal cycles, thereby minimising the errors associated with using thermocouples to determine weld cooling rates.

- Hydrogen testing should be done on real production welds.

- Similar experiments with laser leading configuration should be performed to assess how it compares with laser trailing configuration.

REFERENCES

1. Akselsen, O. M., Aune, R., Fostervoll, H. and Harsvoer, A. S. (2006), "Dry Hyperbaric Welding of Subsea Pipelines", *Welding Journal,* vol. 85, no. 3, pp. 52-55.

2. Akselsen, O. M., Fostervoll, H. and Ahlen, C. H. (2009), "Hyperbaric GMA Welding of Duplex Stainless Steel at 12 and 35 Bar", *Welding Journal,* vol. 88, no. 2, pp. 21S-28S.

3. Akselsen, O. M., Fostervoll, H. and Ahlen, C. H. (2010), "Mechanical Properties of Hyperbaric Gas Metal Arc Welds in X65 Pipeline Steel", *International Journal of Offshore and Polar Engineering,* vol. 20, no. 2, pp. 110-117.

4. Alexander, J. and Steen, W. M. (1979), "Arc Augmented Laser Welding-Process Variables, Structre and Properties", *The Joining of Metals: Practise and Performance,* vol. 7, pp. 155-160.

5. Amin, S. A. (2012), *Dry Hyperbaric Gas Metal Arc Welding of Subsea Piplines* (PhD thesis), Norwegian University of Science and Technology, Trondhein, Norway.

6. Amin, S. A., Fostervoll, H. and Akselsen, O. M. (2012), "Prediction of the Thermal Cycles in Dry Hyperbaric Welding Using Partial Differential Heat Transfer Equations", *Trends in Welding Research,* 4-8 June, Chicago, USA, .

7. Amin, S. A., Woodward, N. J., Fostervoll, H. and Akselsen, O. M. (2012), "Statistical Analysis of the Arc Behaviour in Dry Hyperbaric GMA Welding from 1 to 250 bar", *Journal of Materials Processing Technology,* vol. 212, pp. 211-219.

8. Arora, A., Roy, G. G. and DebRoy, T. (2010), "Cooling Rate in 800 to 500 °C Range from Dimensional Analysis", *Science and Technology of Welding and Joining,* vol. 15, no. 5, pp. 423-427.

9. Aune, R., Knagenhelm, H. O. and Hirsvaer, A. S. (2005), "Hydrogen and Oxygen Pick-up in Hyperbaric TIG Welding of Supermatensitic 13% Cr Stainless Steel with Matching Filler Wire", *Proc. 24th International Conference on Offshore Mechanics and Artic Engineering,* Vol. 3, 2005, Halkidiki, Greece, pp. 289.

10. Bagger, C. and Flemming, O. (2004), "Review of Laser Hybrid Welding", *Journal of Laser Applications,* vol. 17, pp. 2-14.

11. Baierlein, R. (1999), *Thermal Physics,* Cambridge University Press, U.K.

12. Bang, I. W., Son, Y. P., Oh, K. H., Kim, Y. P. and Kim, W. S. (2002), "Numerical Simulation of Sleeve Repair Welding of In-Service Gas Pipelines", *Welding Journal,* , no. S, pp. 273-281.

13. Beacham, C. D. (1972), "Anew Model for Hydrogen Assisted Cracking (Hydrogen Embrittlement)", *Metallurgical Transactions,* vol. 3, pp. 437-451.

14. Berge, J. O., Verley, R. L. P. and Armstrong, M. A. P. (2004), "Deepwater Remote Pipeline Repair using Welded Sleeve Technique", *Proceedings of International Pipeline Conference,* Calgary, Canada, pp. 1919.

15. Birnbaum, H. K. (ed.) (1990), *Environment Induced Crackng of Metals,* NACE, Houston, TX.

16. Birnbaum, H. K. (1995), "Hydrogen Related Second Phase Embrittlement of Solids", *Hydrogen Embrittlement and Stress Corrosion Cracking,* , pp. 153-177.

17. Birnbaum, H. K. and Sofronis, P. (1994), "Hydrogen-Enhanced Localized Plasticity - A Mechanisim for Hydrogen-Related Fracture", *Material Science and Engineering,* vol. A176, pp. 191-202.

18. Boellingghaus, T., Hoffmeister, H. and Dangeleit, A. (1995), "A Scatter band for Hydrogen Diffusion Coefficients in Micro-Alloyed and Low Carbon Structural Steels", *Welding in the World,* vol. 2, no. 35, pp. 2-83.

19. Boellingghaus, T., Viyanit, E. and Hoffmeister, H. (2001), "Numerical Modelling of Hydrogen Assisted Cracking", *NACE International 2001,* Houston, TX, NACE, USA, .

20. Branch, I. (2011), *Hyperbaric Welding Today, An Overview*, available at: www.nui.no/.../NUIPresentation-HyperbaricWeldingTodayAnOverview (accessed 01/20/2012).

21. British Standard BS EN ISO 3690:2001, (2001), *Welding and Allied Processes-Determination of Hydrogen Content in Ferritic Steel Arc Weld Metal*, United Kingdom.

22. British Standard BS EN ISO 6507-1:2005, (2005), *Metallic Materials Vickers Hardness Test*, UK.

23. Bucurel, R. and Hlifika, G. (2010), "Laser Beam Welding Process Automtes Underwater Repairs", *Welding Journal,* , pp. 47-49.

24. Chaowen, L., Yong, W., Liying, L., Tao, H. and Bin, H. (2010), "Numerical and Experimental Study of In-Service Welding on Thin Plate", in Nahadevan, V. (ed.), *2010 2nd International Conference on Computer*

Engineering and Technology, Vol. 3, 16-18 April, 2010, Chengdu, China, Institute of Electrical and Electronics Engineers (IEEE), China, pp. 397.

25. Cotton, H. C. (1983), "Welding Underwater and the Splash Zone - A Review", *Proceedings of the International Conference, "Underwater Welding",* 1983, Trondheim, Norway, .

26. Cottrel, A. H. (1953), *Dislocations of Plastic Flow in Crystals,* Oxford University Press, United Kingdom.

27. Cramer, H. and Dudziak, M. (2012), "Overview of Mordern Arc Processes and their Material Transfer in the case of Gas-Shielded Metal-Arc Welding", *Welding and Cutting,* vol. 11, no. 5, pp. 319-325.

28. Digital Welding Solutions (2007)*, CMT: Cold Metal Transfer*, available at: www.digitalwelding solutions.com/CMT.pdf (accessed 06/02/2013).

29. Dilthey, U. and Wieschemann, A. (2000), "Prospects by Combining and Coupling Laser Beam and Arc Welding Processes", *Welding in the World,* vol. 44, no. 3, pp. 37-46.

30. Ding, J., Colegrove, P., Mehnen, J., Ganguly, S., Almeida, P. M., Wung, F. and Williams, S. (2011), "Thermo-Mechanical Analysis of Wire and Arc Additive Layer Manufacturing Process on Large Multi-Layer Parts", *Computational Material Science,* vol. 50, pp. 3315-3322.

31. DNV & Spectra Energy, (2011), *Hydrogen Cracking Demonstration*, Unite Kingdom.

32. DNV Offshore Standards (DNV-OS-F101), (2012), *Submarine Pipeline Systems*, Norway.

33. Dos Santos, J. F., Dos Santos, V. R. and Jorge, J. C. (1996), "Properties of Ferritic Metal Cored Wire Weld Metal Deposited in the Pessure Range from 51 Bar to 110 Bar", *Proceedings of the Sixth International Offshore and Polar Engineering Conference,* Vol. 4, Los Angeles, The International Society of Offshore and Polar Engineers, USA, pp. 114.

34. Duley, W. W. (1999), *Laser Welding,* 1st ed, John Wiley & Sons, Inc., New York, USA.

35. Enjo, T., Kikuchi, Y., Horinouchi, H. and Ueda, H. (1987), "MIG Welding under High Pressure Ar Arc Atmosphere", *Transaction of JWRI,* vol. 16, no. 2, pp. 39-48.

36. Eroglu, M., Aksoy, M. and Orhan, N. (1999), "Effect of Coarse Initial Grain Size on Microstructure and Mechanical Properties of Weld Metal and HAZ

of Low Carbon Steel", *Materials Science and Engineering A,* vol. 269, pp. 59-66.

37. ESAB (1998), *LUD 320/450,* 980925, ESAB, Sweden.

38. EWM (2009), *The New Dimension of Welding - EWM ColdArc*, available at: www.ewm.sales.co.uk/downloads/wm045501_gb_ewm_coldarc-produktinformation_12-.pdf (accessed 06/12/2013).

39. Faulds, D., Solberg, U. H. and Haabrekke, T. (2008), "Induction Heating of Live Pipeline for Hyperbaric Diver Welding", *Underwater Intervention Conference,* 29-31 January, 2008, New Orleans LA, USA, Marine Technology Society, USA, .

40. Felix, R. D. and Bruce, W. A. (1991), "Development of Procedures for Hot-tap Welding onto Sour Service Pipelines", *Proc International Artic Technology Conference,* pp. 349.

41. Ferreira, P. J., Robertson, I. M. and Birnbaum, H. K. (1998), "Hydrogen Effects on the Interaction between Dislocations", *Acta Materialia,* vol. 46, no. 5, pp. 1749-1757.

42. Fostervoll, H. and Akselsen, O. M. (2004), *Remote PRS: Hydrogen Pick-up at 1 bar MIG Welding,* STF24 F04240, SINTEF, Norway.

43. Fostervoll, H., Aune, R., Berge, J. O. and Woodward, N. J. (2011), "Remotely Controlled Hyperbaric Welding of Subsea Pipelines", *Pipeline Technology Conference,* 4-5 April, Hannover Messe, Germany, Germany, .

44. Fraunhofer IWS (2010), *Focus on Germany's elite institutes: Fraunhofer IWS,* Project No. 096-137, Institut fur Wissenschaftliche Veroffentlichungen and the Alpha Informationsgesellschaft MBH, Dresden, available at: http://www.iws.fraunhofer.de/pub/Elite_Institut_IWS_en.pdf (accessed 21 December 2010).

45. Fraunhofer IWS (2010a), *Induction Assisted Laser Materials Processing*, available at: http://www.designforlasermanufacture.com/.../iws_dopp_03_gesamt.pdf (accessed 12/17/10).

46. Fraunhofer USA (2010), *Laser Welding of Powertrain Components*, available at: http://www.ccl.fraunhofer.org/download/laser_welding_powertrain_components.pdf (accessed 01/07/11).

47. Gangloff, R. P. (2003), "Hydrogen Assisted Cacking of High Strenght Alloys", *Elsevier Science,* vol. 6, pp. 31-101.

48. Gerardin, C., Knispel, D. and Cehaibou, A. (2004), "Induction Preheating and Laser Welding of High Grade Pipelines for Energy Transport: Welding Process Optimization", *Pipeline Technology Confrence,* Vol. 4, May 9-13, Ostend, Belgium, Scientific Surveys Ltd., Belgium, pp. 153.

49. Gerberich, W. W., Marsh, P. G. and Hoehn, J. W. (1996), *Hydrogen Effects in Materials,* The Minerals, Metals and Materials Society, Warrendale, PA.

50. Goecke, S.F., (2005), *Low Energy Arc Joining Process for Materials Sensitive to Heat*, EWM HIGHTECH WELDING GmbH, Mundersbach, Germany.

51. Goldak, J., Chakravarti, A. and Bibby, M. (1984), "A New Finite Element Model for Welding Heat Sources", *Metallurgical Transactions B,* vol. 15B, pp. 299-305.

52. Hart, P. R. (1999), *Study of Non-Consummable Welding Processes for Diverless Deepwater Hyperbaric Welding to 2,500 m Water Depth* (unpublished PhD thesis), Cranfield University, United Kingdom.

53. Hart, P. R., Richardson, I. M., Billingham, J., Nosal, P. E. and Nixon, J. H. (2000), "Underwater Joining to 8,200 ft - An Alternative to Mechanical Connectors", *Proceedings o International Conference on Deep Water Pipelines and Risers Technology,* 6-8 March, 2000, Houston, Texas, USA, .

54. Hart, P. R., Richardson, I. M. and Nixon, J. H. (2001), "The Effects of Pressure on Electrical Performance and Weld Bead Geometry in High Pressure GMA Welding", *Welding in the World,* vol. 45, no. 11/12, pp. 25-33.

55. Hashemi, S. H. (2011), "Strenght-Hardness Statistical Correlation in API X65 Steel", *Materials Science and Engineering A,* vol. 528, pp. 1648-1655.

56. Hasselberg, T. P. (2009), *A Feasibility Study of "Cold Metal Transfer" - Gas Metal Arc Welding (CMT-GMAW) Nickel Base Superalloy Inconel 718* (MSc thesis), Rensselaer Polytechnic Institute, Hartford, Connecticut, USA.

57. Hauge, A. S. (2011), *Hydrogen Embrittlement in Subsea Pipelines made from API X70* (unpublished MSc thesis), Norwegean University of Science and Technology (NTNU), Norway.

58. He, K., Chen, J. and Xiao, S. (2012), "Numerical Simulation for Shaping Features of Molten Pool in Twin-Arc Submerged Arc Welding", *Open Journal of Applied Sciences,* vol. 2, pp. 47-53.

59. Hermans, M. and Ouden, G. (1999), "Process Behavior and Stability in Short Circuit Gas Metal Arc Welding", *Welding Journal,* vol. 78, no. 4, pp. 137-141.

60. Hernandez, S. (2010), *Laser Welding of Hardenable Steel* (unpublished MSc thesis), Lulea University of Technology, Sweden.

61. Hilton, P. A., Ogle, M. H. and Taylor, D. (2003), "An Exploratory Investigation of ND:YAG Laser Welding in High Pressure Gaseous Environments.", *Applications of Laser and Electro-Optics. Proc. 22nd Int. Congress, ICALEO 2003,* Vol. 95, 13-16 October 2003, Jacksonville, Florida, USA, .

62. Hirth, J. P. (1980), "Effects of Hydrogen on the Properties ofIron and Steel", *Metallurgical Transactions,* vol. 11A, pp. 861-890.

63. Hongxin, M., Dongmin, P. and Hu, F. (2010), "Subsea Pipeline Hyperbaric Welding Technology", *Proceedings of the Twenthieth International Offshore and Polar Engineering Conference,* June 20-25, 2010, Beijing, China, The International Society of Offshore and Polar Engineers (ISOPE), pp. 234.

64. Hudson, M. G. (2004), *Welding of X100 Linepipe* (unpublished PhD thesis), Cranfield University, Cranfield Press.

65. Huismann, G., Knagenhelm, H. O., Woodward, N. J. and Hoffmeister, H. (2009), "Testing of Hydrogen Assisted Cracking for Hyperbaric Repair Welds", in David, S. A., Tarasankar, D., DuPont, J. N., et al (eds.), 1-6 June, 2008, Georgia, USA, ASM International, USA, pp. 581.

66. Huismann, G., Woodward, N. J., Armstrong, M. A. P., Hoffmeister, H. and Knagenhelm, H. O. (2010), "Determining and Avoiding Hydrogen Assisted Cracking on Pipeline Repair", *Proceedings 29th International Conference on Ocean, Offshore and Artic Engineering (OMAE),* June 2010, Shanghai, China, China, .

67. Iacoviello, F., Galland, J. and Habashi, M. (1998), "A Thermal Outgassing Method (T.O.M) to Measure the Hydrogen Diffusion Coefficients in Austenitic, Austeno-Ferritic and Ferritic-Perlitic Steels", *Corrosion Science,* vol. 40, no. 8, pp. 1281-1293.

68. Ion, J. C. (2005), *Laser Processing of Engineering Materials,* 1st ed, Elsevier Butterworth- Heinemann, Oxford, United Kingdom.

69. IPG Photonics (2010), *IPG Photonics Fiber Lasers YLR Series*, available at: www.ipgphotonics.com/apps_materials_multi_ylr.htm (accessed 06/14/2013).

70. Jahn, A., Kratzsch, B. and Brenner, B. (2008), "Induction assisted laser beam welding of HSLA steel sheets", *International Scientific Colloquim, Modelling for Electromagnetic Processing,* October 27-29, 2008, Hannover, pp. 195.

71. Kah, P., Salminen, A. and Martikainen, J. (2008), "Assessment of Different Laser Hybrid Welding Processes", *Proceedings of the 27th International Conference on Applications of Laser and Electro-Optics,* 22-23 October 2008, California, USA, Laser Institute of America, USA, pp. 469.

72. Kah, P., Salminen, A. and Martikainen, J. (2010), "The Effect of the Relative Location of Laser Beam and Arc in Different Hybrid Welding Processs", *Mechanika,* vol. 28, pp. 1604-1613.

73. Komizo, Y. (2008), "Overview of Recent Welding Technology Relating to Pipeline Construction", *Transaction of Joining and Welding Research Institute,* vol. 37, no. 1, pp. 1-5.

74. Kou, S. (2003), *Welding Metallurgy,* 2nd ed, John Wiley & Son Inc., New Jersey.

75. Labanowski, D., Fydrych, D. and Rogalski, G. (2008), "Underwater Welding - Review", *Advances in Materials Science,* vol. 8, no. 3, pp. 12-22.

76. Le Bail, A., Danes, F. E. and Bardon, J. P. (1990), "Measurement of the Thermal Conductivity of Argon at High Temperature and High Pressure by Transient Hot-Wire Method", in Cramer, C.J. and Fine, H.A. (ed.), *Proceedings of the Twenty-First International Conference on Thermal Conductivity,* Vol. 21, January 1990, New York, pp. 577-582.

77. Lynch, S. P. (1979), "Mechnisms of Hydrogen Assisted Cracking", *Metals Forum,* vol. 2, no. 3, pp. 189-200.

78. Mach, M., Scuelbe, H. and Nacke, B. (2008), "Investigation and Design of Induction Assisted Welding Process.", *Proceedings of International UIE Conference,* Vol. 84, May 2008, Cracow, Poland, Przeglad Elecktrotechniczny, pp. 159.

79. Malik, M. A., Qureshi, M. E. and Dar, N. U. (2007), "Numerical Simulation of Arc Welding Investigation of Various Process and Heat Source Parameters", *Failure of Engineering Materials & Structures,* vol. 30, pp. 127-142.

80. Marhle, A. and Beyer, E. (2006), "Hybrid Laser Beam Welding - Classification, Characteristics, and Applications", *Journal of Laser Applications,* vol. 18, no. 3, pp. 169-180.

81. Marino, R., Blackman, S. A. and Woodward, N. J. (2004), "Metallurgical Investigation of Hot-Tap and Riser MIG Welds Produced under Deep water Hyperbaric Conditions of 160 Bar", *Pipeline World,* , pp. 11-17.

82. Marino, R., Blackman, S. A. and Woodward, N. J. (2004), "A metallurgical investigation of hot-tap and riser MIG welds produced under deepwater hyperbaric conditions of 160 bar", *Pipeline World,* , pp. 11-17.

83. Matsuba, J., Utsumi, A., Hamasaki, M. and Nagata, S. (1988), "TIG or MIG Augmented Laser Welding of Thick Mild Steel Plate", *Joining and Materials,* , pp. 31-34.

84. Mazzaferro, J. A. E. and Machado, I. G. (2009), "Study of Arc Stability in Underwater Shielded Metal Arc Welding at Shallow Depths", *Proc. IMechE Part C: J. Mechanical Engineering Science,* vol. 223, no. 3, pp. 699-709.

85. McMahon Jr, C. J. (2001), "Hydrogen-Induced Intergranular Fracture of Steels", *Engr. Frac. Mech.,* vol. 68, pp. 773-788.

86. McMahon Jr, C. J., Liu, X., Kameda, J. and Morgan, M. J. (2008), "Recent Observation of Hydrogen-Induced Cracking of High-Strength Steels", *Proceedings of the 2008 International Hydrogen Conference,* Wyoming, USA, ASM International, USA, pp. 46.

87. Michell Instruments (2013)*, Cermet II Hygrometer*, available at: www.michell.com/uk/products/cermet-II.html (accessed 1/07/2013).

88. Mihailescu, D., Mihailescu, A. and Popescu, F. (2004), "The Impact of Pressure on te HAZ sizes in MAG Hyperbaric Gry Welding with Plsated Arc", *Welding Equipment and Technology,* vol. 12, pp. 19-22.

89. Moore, P. L., Howse, D. S. and Wallach, E. R. (2004), "Microstructures and Properties of Laser/Arc Hybrid Welds and Autogenous Laser Welds in Pipeline Steels", *Science and Technology of Welding and Joining,* vol. 9, no. 4, pp. 314-322.

90. Nelson, H. G. (1983), "Embrittlement of Engineering Alloys", in Braint, C. L. and Banerji, S. K. (eds.) *Treatise on Materials Science and Tehnology,* Academic Press, New York, pp. 275-359.

91. Nevasmaa, P. (2004), "Hydrogen Cold Cracking in High Strenght Multipass Weld Metal - A procedure for Predicting the Craking Risk and Necessary precautions for Safe Welding", *Document IX-2088-04 for The 57th Annual Assembly of International Institute of Welding,* 11-16 July, 2004, Osaka, Japan, IIW, Japan, .

92. Nixon, J. H. (2000), *Underwater Repair Technology,* 1st ed, Woodhead Publishing Ltd., United Kingdom.

93. Nixon, J. H., Hart, P. R. and Richardson, I. M. (2000a), "Diverless Underwater Welding: Theory and Operation", *Proceedings of International Conference ICAWT2000: Gas Metal Arc Welding for the 21st Century,* 6-8 December, 2000, Orlando, Florida, USA, .

94. Nosal, P. E. (2001), *Metallurgical Investigation of Hyperbaric Welding at Pressures to 250 Bar for Repairs to Deep Sea Pipelines* (PhD thesis), Cranfield University, United Kingdom.

95. Olden, V. and Akselsen, O. M. (2011), "FE Simulation of Cold Cracking Susceptibility in X70 Structural Steel Welded Joints", *Proceedings of the 30th Internaional Conference on Ocean, Offshore and Artic Engineering,* 19-24June, 2011, Rotterdam, The Netherlands, ASME, The Netherlands, pp. 1.

96. Olden, V., Thaulow, C. and Johnsen, R. (2008), "Modelling of Hydrogen Diffusin and Hydrogen Induced Cracking in Supermartensitic and Duplex Stainless Steels", *Materials for Design,* vol. 29, no. 10, pp. 1934-1948.

97. Oriani, R. A. (1972), "The Mechanistic Theory of Hydrogen Embrttlement of Steels", *Berichte Bunsen Gesellschaft Fur Physik Chem.,* vol. 76, pp. 848-857.

98. Oriani, R. A. (1978), "Hydrogen Embrittlement of Steels", *Annual Reviews in Materials Scence,* vol. 8, pp. 327-357.

99. Oriani, R. A. (1987), "Hydrogen-The Versatile Embrittler", *Corrosion,* vol. 43, pp. 390-397.

100. Oriani, R. A. (1995), "Hydrogen Embrittlement of Steels", *Hydrogen Embrittlement and Stress Corrosion Cracking,* , pp. 43-59.

101. Ozden, H. and Gursel, K. T. (2005), "Service Life of Tungsten Electrodes in Hyperbaric Dry Welding of Subsea Pipelines", *Welding Journal,* vol. 84, no. 6, pp. 94S-99S.

102. Papadopoulos, K. (2009), *Process parameter sensing for remote hyperbaric welding* (MSc thesis), Cranfield University, Cranfield.

103. Pepe, N. V. C. (2010), *Advances in Gas Metal Arc Welding and Application to Corrosion Resistant Alloy Pipes* (PhD thesis), Cranfield University, U.K.

104. Petring, D., Fuhrmann, C., Wolf, N. and Poprawe, R. (2003), "Investigations and Applications of Laser-Arc Hybrid Welding from Thin Sheets up to Heavy Section Components", *22nd International Conference on the Applications of Lasers & Electro-Optics (ICALEO),* Vol. 95, 13-16 October, 2003, Florida, USA, Laser Institute of America, USA, pp. 595.

105. Physorg.com (2011), *Cranfiled University reaches Record Breaking Depths in Deep Sea Welding*, available at: http://www.physorg.com/news/2011-04-cranfield-university-deep-sea.html (accessed 5/07/2011).

106. Pickin, C. G. and Young, K. (2006), "Evaluation of cold metal transfer (CMT) process for welding aluminium alloy", *Science and Technology of Welding and Joining,* vol. 11, no. 4, pp. 1-3.

107. Rao, Z. H., Liao, S. M. and Tsai, H. L. (2011), "Modelling of Hybrid Laser-GMA Welding: Review and Challenges", *Science and Technology of Welding and Joining,* vol. 16, no. 4, pp. 300-305.

108. Rasmussen, D. and Dubourg, L. (2005), *Hybrid Laser-GMAW Welding of Aluminium Alloys: A Review*, available at: http://nparc.cisti-icist.nrc.cnrc.gc.ca/npsi/ctrl?action=rtdoc&an=12919066&lang=en (accessed 04/20/2011).

109. Raykalin, N. N. and Nikolaev, A. V. (1971), "Welding Arc Heat Flow", *Welding in the World,* vol. 9, no. 3, pp. 112-133.

110. Ribic, B. D., Rai, R. and DebRoy, T. (2008), "Numerical Simulation of Heat Transfer and Fluid Flow in GTA/Laser Hybrid Welding", *Science and Technology of Welding and Joining,* vol. 13, no. 8, pp. 683-693.

111. Ribic, B. D., Rai, R., Palmer, T. A. and DebRoy, T. (2009), "Arc-Laser Interactions and Heat Transfer and Fluid Flow in Hybrid Welding", in David, S. A., DebRoy, T., DuPont, J. N., et al (eds.), *Trends in Welding Research, Proceedings f the 8th International Conference,* 1-6 June, 2008, Georgia, USA, ASM International, USA, pp. 313.

112. Richardson, I. M. (1988), *Hyperbaric Open-Arc Pulsed-GMAW at Pressures 20 to 100 Bar,* , Cranfield University, United Kingdom.

113. Richardson, I. M. (2005), *A Flexible Waveform Representation for Gas Metal Arc Welding,* XII-1869-05, IIW Doc.

114. Richardson, I. M. and Nixon, J. H. (1997), "Deepwater Hyperbaric Welding - Initial Process Evaluation", *Proceedings of 7th International Conference on Offshore and Polar Enineering (ISOPE),* Hawaii, USA, .

115. Richardson, I. M., Nixon, J. H., Billingham, J. and Hart, P. R. (2000), "Fusion Welding to 2,500 m Water Depth", *IOCE Subsea 2000,* 3-5 October, 2000, Aberdeen, .

116. Richardson, I. M., Nixon, J. H., Nosal, P. E., Hart, P. R. and Billingham, J. (2000), "Hyperbaric GMA Welding to 2,500 m Water Depth", *Proc. Int. Conf. ETCE/OMAE2000,* 14-17, February, 2000, New Orleans, USA, .

117. Richardson, I. M., Woodward, N. J. and Billingham, J. (2002), "Deepwater Welding for Installation and Repair - A Viable Technology", *Proceedings of 12th International Conference on Offshore and Polar Engineering (ISOPE),* May 2002, Kita-Kyushu, Japan, Japan, .

118. Richardson, M. I. (1993), "The Influence of Ambient Pressure on Arc Welding Processes, in "Physical Aspects of Arc Welding"", in Ouden, G. D. (ed.), *Proceedings of IIW Study Group 212 Seminar,* Sept 1, 1993, Glasgow, Delftse Uitgevers Maatschappij, Glasgow, pp. 43.

119. Richardson, M. I. (2003), *Review of Underwater Welding Processes Part 1,* SCUW-202-03, IIW Doc.

120. Richardson, M. I., Woodward, N. J., Armstrong, M. A. and Berge, J. O. (2010), "Developments in Dry Hyperbaric Welding", *3rd International Workshop on Stat-of-the-Art Science and Reliability of Underwater Welding and Inspection Technology,* November 17-19,2010, Houston, Texas, USA, .

121. Robot Worx (2009), *Fanuc M-710iB*, available at: www.robots.com/fanuc/m-710ib (accessed 06/14/2013).

122. Rose, S. (2012), "Approaches for Better Understanding of the Formation and Reduction of Welding Fumes in GMA Welding under Consideration of Innovative Welding Processes", *Welding and Cutting,* vol. 11, no. 5, pp. 303-309.

123. Rosenfeld, R., Herzog, D., Ostendorf, A. and Haferkam, H. (2008), "Laser Welding of Heat Treatable Steel during Induction Hardening", *International Scientific Colloquium,* October 27-29, Hannover, Germany, Modelling for Electromagnetic Processing, Germany, pp. 209.

124. Ruetzel, E. W., Mikesic, D. A., Tressler, J. F., Crue, R. A., Gwinn, E. A. and Sullivan, M. J. (2005), *Laser Pipe Welding Technology Evaluation and Cost Analysis,* TR 04-014, The Pennsylvania University, USA, USA.

125. Ruetzel, E. W., Sullivan, M. J. and Mikesic, D. A. (2006), "Joining Pipe with the Hybrid Laser-GMAW Process: Weld Test Results and Cost Analysis", *Welding Journal,* , pp. 66-71.

126. Sandrea, I. and Sandrea, R. (2007), "Global Offshore Oil - Growth expected in global offshore crude oil supplies", *Oil & Gas Journal,* vol. 105, no. 9 & 10.

127. Sandrea, I. and Sandrea, R. (2010), "Deepwater Crude Oil Output: How Large will the Uptick Be?", *Oil & Gas Journal,* vol. 108, no. 41.

128. Schweisstechnik, B. (2012), *Welding Consummables for the Oil and Gas Industry*, available at: http://www.t-put.com/pdf/EN_OilGas_0809_Rev1.pdf (accessed 4/20).

129. Seluck, C. and Raghunathan, S. (2010), *High Integrity Underwater Repair Technologies,* PR15283, The Welding Institute, United Ingdom.

130. Sengers, J. V. (1965), "Thermal Conductivity and Viscosity of Simple Fluids", *Int. J. Heat Mass Transfer,* vol. 8, pp. 1103-1116.

131. Sepold, G., Thormy, C., Seefeld, T., Schilf, M., Vollertsen, F. and Hoffmann, R. (2003), "CO2-Laser GMA Hybrid Welding - Aspects of Research and Industrial Application", *Proceedings of the Second International WLT-Conference on Lasers in Manufacturing,* June 2003, Munich, Germany, Germany, .

132. Seyffarth, I. V. and Krivtsun, I. V. (2002), *Laser-Arc Processes and their Applications in Welding and Materials Treatment,* Taylor and Francis, London.

133. Shannon, G. J., McNaught, W., Deans, W. F. and Watson, J. (1997), "High Power Laser Welding in Hyperbaric Gas and Water", *Journal of Laser Applications,* vol. 9, pp. 129-136.

134. Shibata, K., Sakamoto, H. and Iwase, T. (2001), "Laser-MIG Hybrid Welding of Aluminium Alloys", *Proceedings of the 1st International WLT-Conference on Lasers Manufacturing,* June, Munich, pp. 436.

135. Smailowski, M. (1962), *Hydrogen in Steel,* Pergamon Press, Oxford, United Kingdom.

136. Smith, F. J. (1974), "Weld Metal Temperature Measurement - Harpoon Technique with Rhodium-Platinum Thermocouples", *Platimum Metals Rev.,* vol. 18, no. 2, pp. 73.

137. Sofronis, P. (1995), "The Influence of Mobility o Dissolved Hydrogen on the Elastic Response of A Metal", *J. Mech. Phys. Solids,* vol. 43, no. 9, pp. 1385-1407.

138. Statoil (2005), *RPRS Pre-Qualification Report - Welded Sleeve Repair,* OPS-12-01, Statoil and Isotek Oil and Gas Ltd, Norway.

139. Statoil (2012), *Remote-controlled World Record at Asgard*, available at: www.statoil.com/en/NewsAndMedia/News/2012/pages/13sep_hottap.aspx (accessed 10/17).

140. Ströhlein GmbH & Co *H-mat 2500 Operating Instructions,* .

141. Suder, W., Williams, S. and Colegrove, P. (2009), "Absolute Spot Size Effect on Penetration Depth in Laser Welding", *Lasers in Manufacturing (LiM 2009),* 15 - 18 June, 2009, Munich, Germany, Scientific Society for Laser Technology, Germany, .

142. Swetnam, D. (1992), *The Influence of Hyperbaric Environment and Procedures on the Quality of Underwater MMA Welds* (unpublished PhD thesis), Cranfield University, United Kingdom.

143. Szelagowski, P. (1991), *Research and Development Activities in the Federal Republic of Germany in the Field of Underwater Welding and Cutting,* , GKSS.

144. Szelagowski, P. and Pachnuik, I. (1994), "State of the Art and Practice of Underwater Hyperbaric Dry Welding", *International Workshop on Underwater Welding of Marine Structures,* New Orleans, USA, .

145. Szelagowski, P., Schafstall, H. G., Rothe, R. and Sepold, G. (1987), "Wet Underwater Welding with High-Power CO2 Lasers", in Russel, J. D. (ed.), *Proceedings of International Conference on Power Beam Technology,* 10-12 September, 1986, Brighton, United Kingdom, The Welding Institute, Abington, Cambridge, United Kingdom, .

146. Taha, A. and Sofronis, P. (2001), "A Micromechanics Approach to the Study of Hydrogen Transport and Embrittlement", *Engineering Fracture Mechanics,* vol. 68, pp. 803-837.

147. Tien, J. K., Thompson, A. W., Bernstein, I. M. and Richards, R. J. (1976), "Hydrogen Transport by Dislocation", *Metallurgical Transactions A,* vol. 7A, pp. 821-829.

148. Tong, H., Ueyama, T., Nakata, K. and Ushio, M. (2003), "High Speed Welding of Aluminium Alloy Sheets Using Laser Assisted Alternating Current Pulsed Metal Inert Gas Process", *Science and Technology of Welding and Joining,* vol. 8, no. 6, pp. 229-234.

149. Troiano, A. R. (1960), "The Role of Hydrogen and Other Interstitials in the Mechanical Behaviour of Metals", *Trans. ASM,* vol. 52, pp. 54-80.

150. Troiano, A. R. and Hehemann, R. F. (1995), "Stress Corrosion Cracking of Ferritic and Austenitic Stainless Steels", *Hydrogen Embrittlement and Stress Corrosion Cracking,* , pp. 231-248.

151. TWI (2010), *Defects - Hydrogen Cracks in Steels - Identification*, available at: http://www.twi.co.uk/content/jk45.html (accessed 04/05/2011).

152. Viyanit, E. (2005), *Numerical Simulation of Hydrogen Assisted Cracking in Supermartensitic Stainless Steel Welds* (unpublished PhD thesis), Universitat Der Bundeswehr, Hamburg, Germany.

153. Wang, Z., Jiao, X., Zhou, J. C. and Xue, L. (2010), "Research on GTAW Arc Behaviour under High Pressure", *International Conference on Electrical and Control Engineering,* June 25-27, 2010, Wahun, China, IEEE, China, pp. 5889.

154. Wendler-Kalsch, E. (1986), "Grundlage Und Mechanism Der H-Induzierten Korrosion Metallischer Werkstoffe", *Wasserstoff Und Korrosion,* , pp. 8-47.

155. Williams. (Head, Welding Engineering and Laser Processing Centre, Cranfield University, United Kingdom), (2008), *The Ins and Outs of Laser Welding* (unpublished Lecture Note), Cranfield University.

156. Woodward, N. J. (2006), "Developments in Diverless Subsea Welding", *Welding Journal,* vol. 85, no. 10, pp. 35-39.

157. Woodward, N. J. (2009), *Feasibility Study into Deep Water Pipeline Repair,* OPS-19-01, Isotek, England.

158. Woodward, N. J. (2012), *Pre-Qualification Report : Deep Water Welding,* DO46-RW-M-RZ-3001, Isotek Oil and Gas, UK.

159. Woodward, N. J., Apeland, K. E., Berge, J. O., Verley, R. and Armstrong, M. (2013), "Subsea Pipeline: The Remotely Welded Retrofit Tee for Hot Tap Applications", *Proceedings of the ASME 2013 32nd International Conference on Ocean, Offshore and Artic Engineering (OMAE 2013),* June 9-14, Nantes, France, .

160. Woodward, N. J., Fostervoll, H., Akselsen, O. M., Ahlen, C. H., Berge, J. O. and Armstrong, M. (2007), "Inconel 625 Performance as Hyperbaric GMA Welding Consummable for Diverless Retrofit Tee Hot Tap Applications", *International Society of Offshore and Polar Engineers (ISOPE),* 1 -6 July 2007, Portugal, .

161. Woodward, N. J., Fostervoll, H., Akselsen, O. M., Ahlen, C. H., Berge, J. O. and Armstrong, M. A. P. (2008), "Evaluation of Welding Procedures an Consummables for Hyperbaric GMAW for Diverless Retrofit Tee Hot-Tap Applications", *International Journal of Offshore and Polar Engineering,* vol. 18, no. 2, pp. 149-155.

162. Woodward, N. J., Knagenhelm, H. O., Berge, J. O., Verley, R. and Armstrong, M. (2007), "Hyperbaric GMA Welding for Contingency Repair using a Fillet Welded Sleeve at 1,000 m Water Depth", *Proc. 17th International Offshore and Polar Engineering Conference,* Vol. 1-4, July 1-

6, 2007, Lisbon, Portugal, The International Society of Offshore and Polar Engineers (ISOPE), Portugal, pp. 3403.

163. Woodward, N. J., Yapp, D., Blackman, S. A., Richardson, I. M., Widgery, D., Armstrong, M. A. P., Verley, R. L. P. and Berge, J. O. (2004), "Diverless Underwater GMA Welding for Pipeline Repair using Fillet Welding Sleeve", *Proc. Int. Pipeline Conf.* Calgary, Canada, ASME, Canada, pp. 1475.

164. Woodward, N. J., Yapp, D., Richardson, I. M., Widgery, D., Armstrong, M. A. P., Verley, R. L. P. and Berge, J. O. (2005), *Subsea Pipeline Repair - Diverless GMA Welding uing Fillet Welded Sleeve,* XII-1868-05/SCUM 211-05, IIW Doc.

165. Zapffe, C. A. and Sims, C. E. (1941), "Hydrogen Embrittlement, Internal Stress and Defects in Steel", *American Institute of Mining and Metallurgical Engineers,* , no. 1307, pp. 1-37.

166. Zhang, H. T., Feng, J. C., He, P., Zhang, B. B., Chen, J. M. and Wang, L. (2008), "The Arc Charactersitics and Metal Transfer Behaviour of Cold Metal Tranfer and its use in Joining Aluminium to Zinc-Coated Steel", *Materials Science and Engineering A,* vol. 499, no. 2009, pp. 111-113.

167. Zimmer, T., Boellingghaus, T. and Kannengiesser, T. (2004), *Effects of Hydrogen on Weld Microstructure Mechanical Properties of the High Strenght Steels S 690Q and S 1100QL,* II-A-141-04, International Institute of Welding (IIW).

APPENDICES

Appendix A

Table A-1: Tensile properties of an X70 pipeline steel and orbital GMA weld made at 1,630 m (5,350 ft) with a solid wire consumable [117]

	Yield (MPa)	UTS (MPa)	Elongation (%)	Yield/ Ultimate
Weld Upper	589	652	23.9	0.9
Weld Lower	626	696	21.6	0.9
Weld Mean	**601**	**667**	**23.1**	**0.9**
Parent	669	715	20.1	0.94

Table A-2: Tensile properties of an X65 pipeline steel and linear welds made at 1,630 m (5,350 ft) with a solid wire consumable [117]

	Yield (MPa)	UTS (MPa)	Elongation (%)	Yield/ Ultimate
Down hand	585	663	23.0	0.88
Vertical	551	637	23.5	0.86
Overhead	578	647	22.4	0.89
Mean	**571**	**649**	**23.0**	**0.88**
Parent	541	592	20.0	0.91

Appendix B

Table B-1: Power Source Control Parameters

15 V < V_{arc} < 90 V - Pulsed Welding Settings	
$I_{p,}$ Peak settings	173 A
$I_{b,}$ Base settings	125 A
V_{TGT}, Target arc voltage	24 V
I_{TGT}, Target welding current	205 A
T_p, Peak duration	4 ms
Tb, Base duration	4 ms
Peak & base slopes	12 V/100 A
Transition dynamics	500 A/ms
Pulse to end peak/Base	None
V_{arc} < 15 V - Short Circuit Settings	
I_{sc}, Short circuit current	375 A
Short circuit detection	14 V
Short circuit dynamics	400A/ms
Short circuit pulse duration	1 ms
Short circuit characteristics	Constant current
Pulse to end short circuit	Yes
Power Source and Torch Details	
Power source & controller	ISOTEK Equipment ID: WPC1PA10
Setting relationship	0.23I
Polarity	Electrode negative
Arc voltage feedback	Torch & earth for ground reference
Torch design	Straight neck without gas shroud
Stand-off	11 mm nominal
Motion Parameters	
Travel speed	5 mm/s, 6 mm/s, 7 mm/s
Wire feed speed	8 m/min
Weld length	180 mm

Calibration Record Isotek Power Source Control and Fronius Power Sources

Equipment: Isotek Power Source Controller 3 off Fronius TP450 Power Sources in Series (Original Cranfield Power Sources)
70mm^2 Welding Leads

PSC Calibration Values:

VoltInScale = 0.067691 CurrOutScale = 0.114094
VoltinOffset = -0.54 CurrOutOffset = 0.2

Powerslope = 0.2206 CurrDmdScale= 0.109863
Poweroffset = -1.1794 CurrDmdOffset = 0.0

Date: 11th March 2013

Method: Voltage Input Calibration: 0-60V DC Voltage fed into Welding Torch & Monitored with Calibrated Fluke 16 Multimeter

Welding Current Output Calibration: Welding Power Leads short circuited at Welding Table with 10 to 400A DC welding current demands from Welding Power Source Controller & Monitored with Calibrated Current Clamp Isotech ICM-136R

Results:

Table B-2: Isotek Power Source Control and 3 off Fronius TP450 Power Source Calibration

Calibrated Fluke Volt. INPUT (V)	Calibrated Curr. Clamp OUTPUT (A)	Calibrated Fluke Volt. INPUT (V)	Calibrated Curr. Clamp OUTPUT (A)	Calibrated Fluke Volt. INPUT (V)	Calibrated Curr. Clamp OUTPUT (A)
Set-Point = 50A Slope = 0.12V/A		Set Point = 100A Slope = 0.12V/A		Set Point = 150A Slope = 0.12V/A	
15.0	14.0	30.0	35.0	45.0	55.8
12.5	38.2	25.0	81.5	35.0	143.6
10.0	62.0	20.0	124.5	25.0	230.5
7.5	84.0	15.0	168.7	15.0	318.2
5.0	106.2	10.0	212.0	6.0	396.2
Intersection		*Intersection*		*Intersection*	
11.3	*50.0*	*22.77*	*100.0*	*34.25*	*150.0*
Set-Point = 200A Slope = 0.12V/A					
60.0	75				
50.0	162.6				
40.0	249.5				
30.0	336.6				
Intersection	*Intersection*				
45.7	*200.0*				

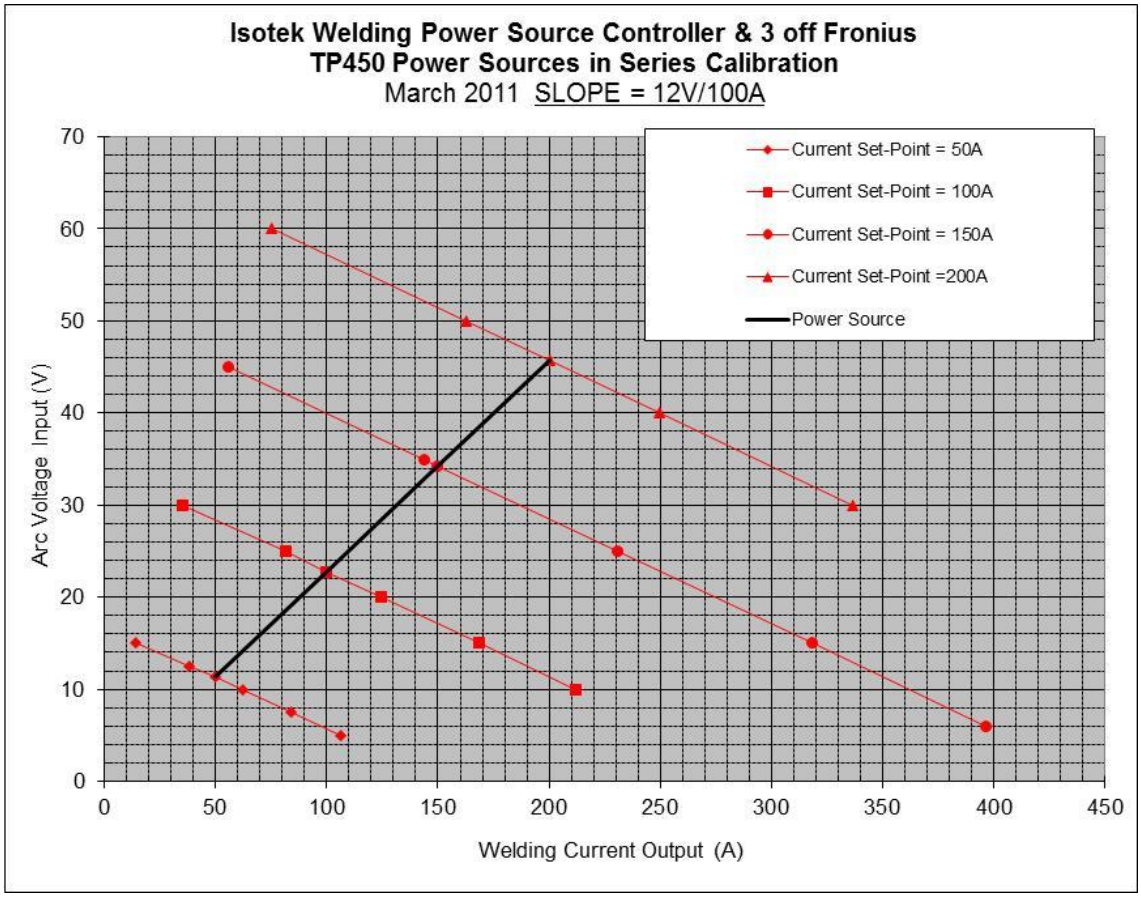
Isotek Welding Power Source Controller & 3 off Fronius
TP450 Power Sources in Series Calibration
March 2011 SLOPE = 12V/100A
Current Set-Point = 50A
Current Set-Point = 100A
Current Set-Point = 150A
Current Set-Point =200A
Power Source
Arc Voltage Input (V)
Welding Current Output (A)
0
10
20
30
40
50
60
70
0
50
100
150
200
250
300
350
400
450

Current, Voltage and Power Waveforms of all the Welds in Chapter 4

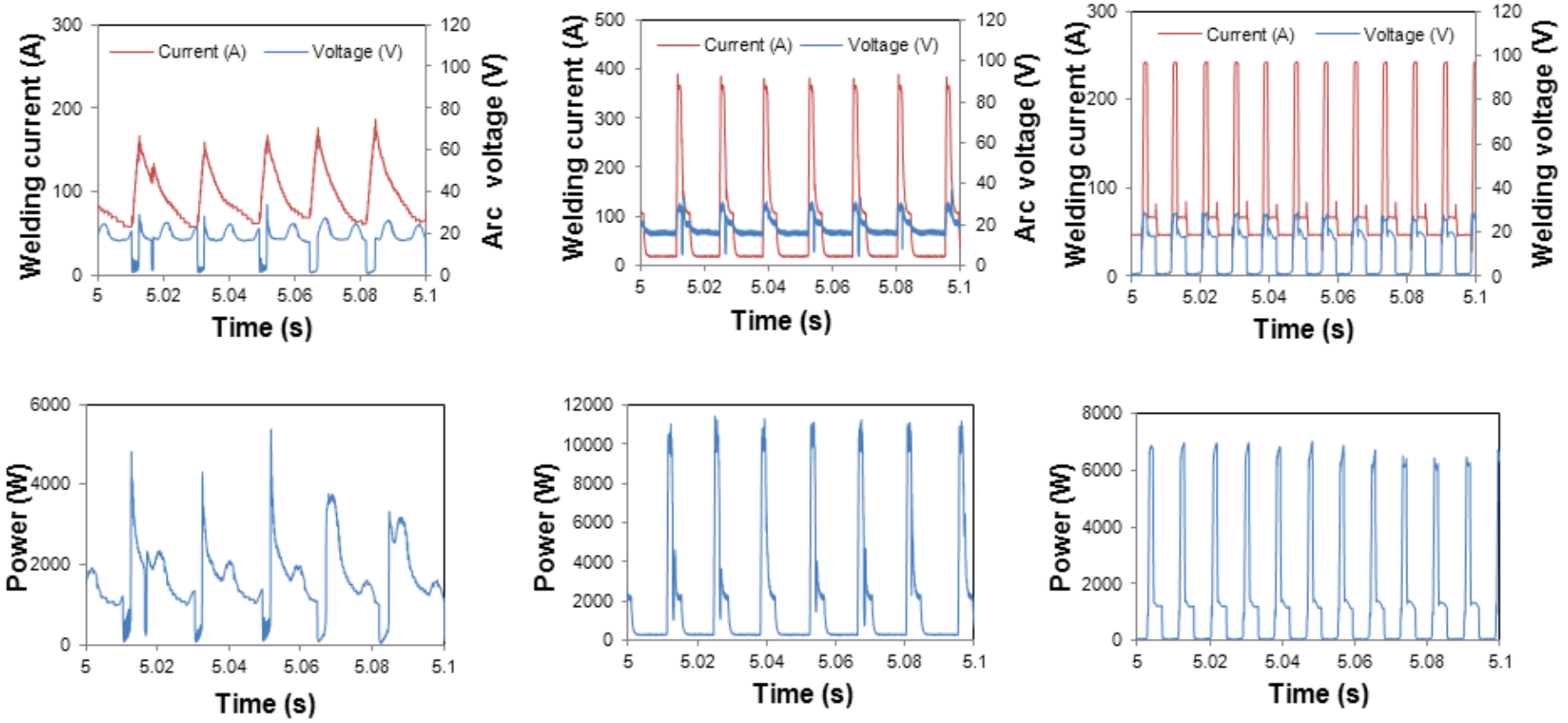

Figure B-1: Transient relationship of current, voltage and power with 3 m/min WFS weld. From left to right, CMT, ColdArc and Short circuit GMAW

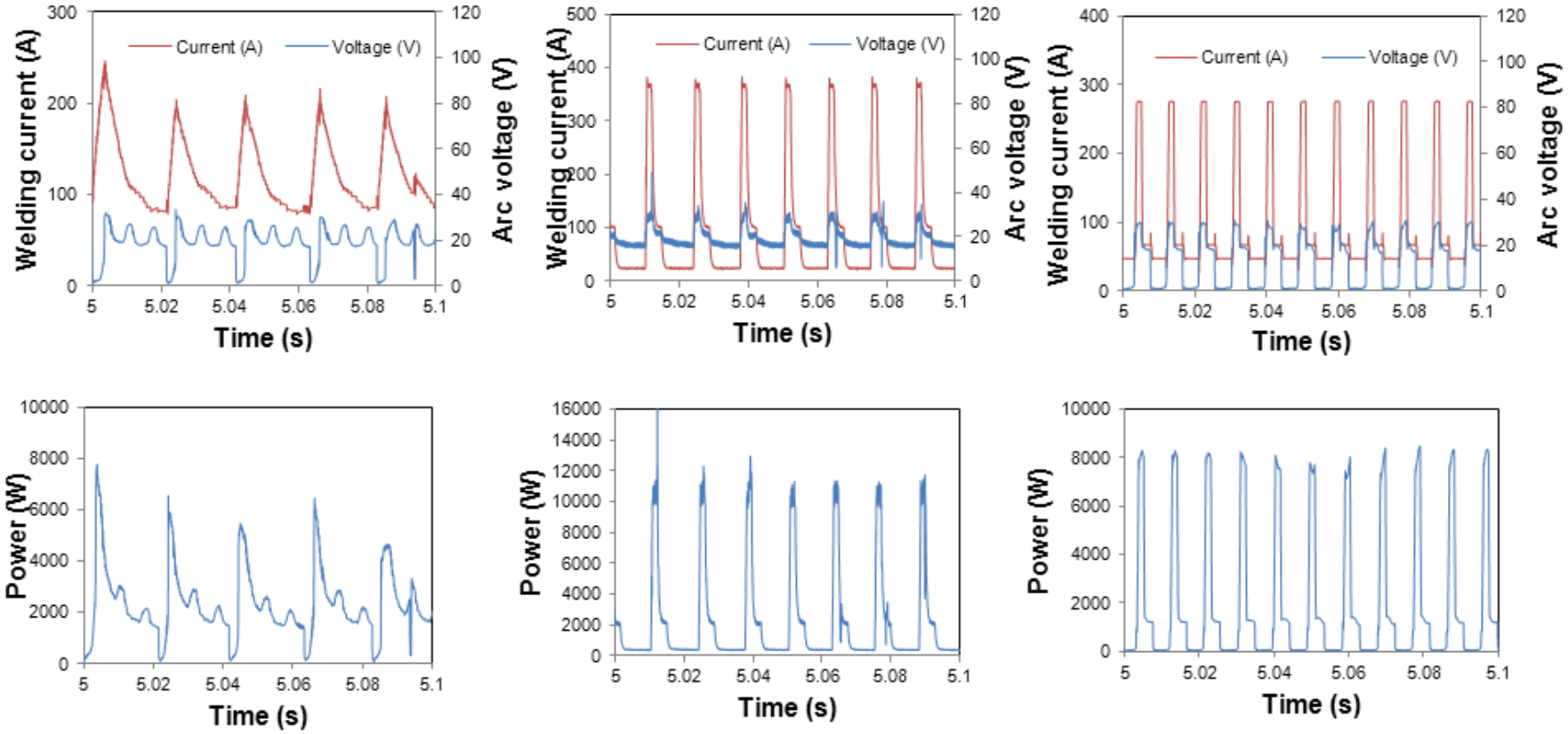

Figure B-2: Transient relationship of current, voltage and power with 4 m/min WFS weld. From left to right, CMT, ColdArc and Short circuit GMAW

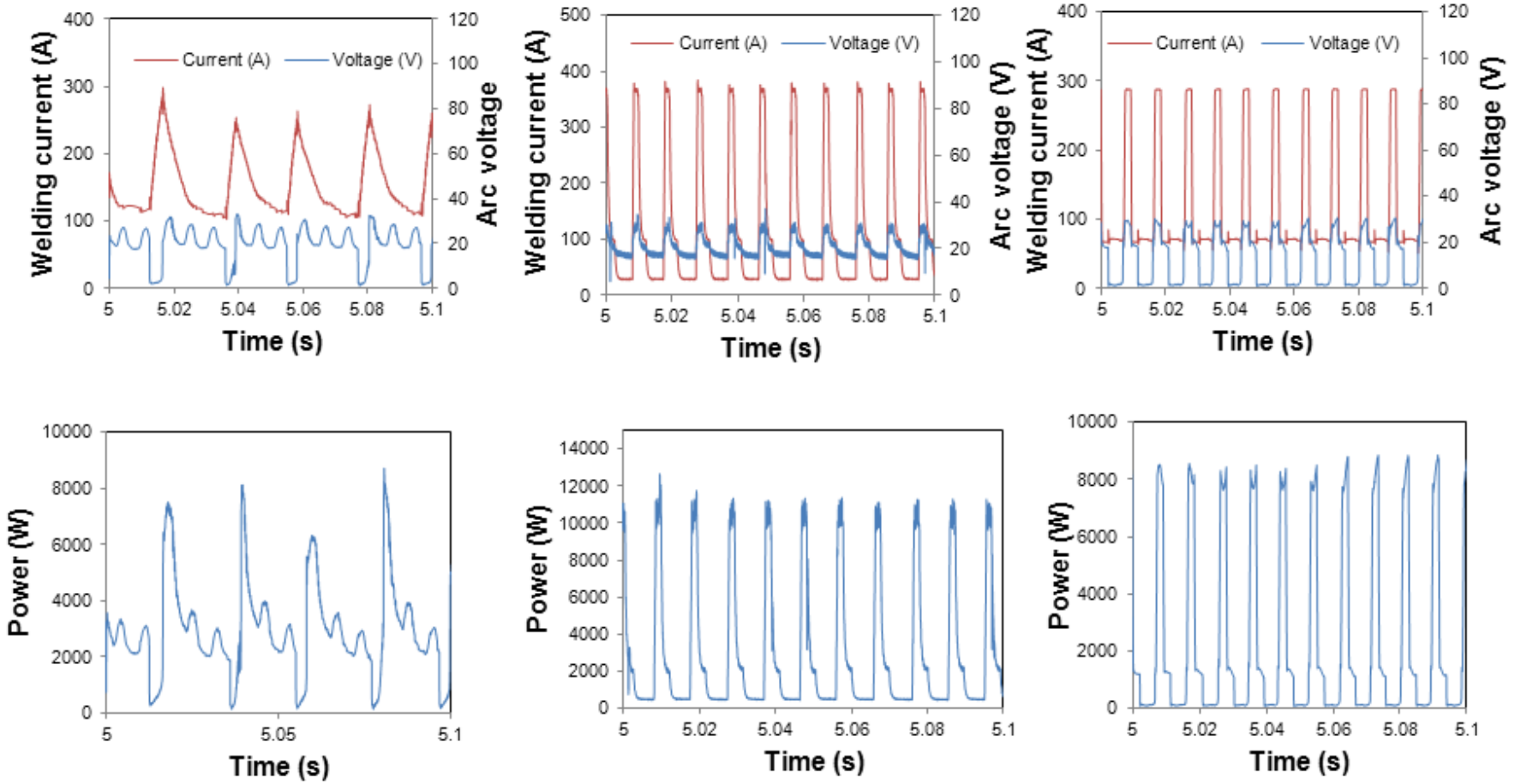

Figure B-3: Transient relationship of current, voltage and power for 5 m/min WFS weld. From left to right, CMT, ColdArc and Short circuit GMAW

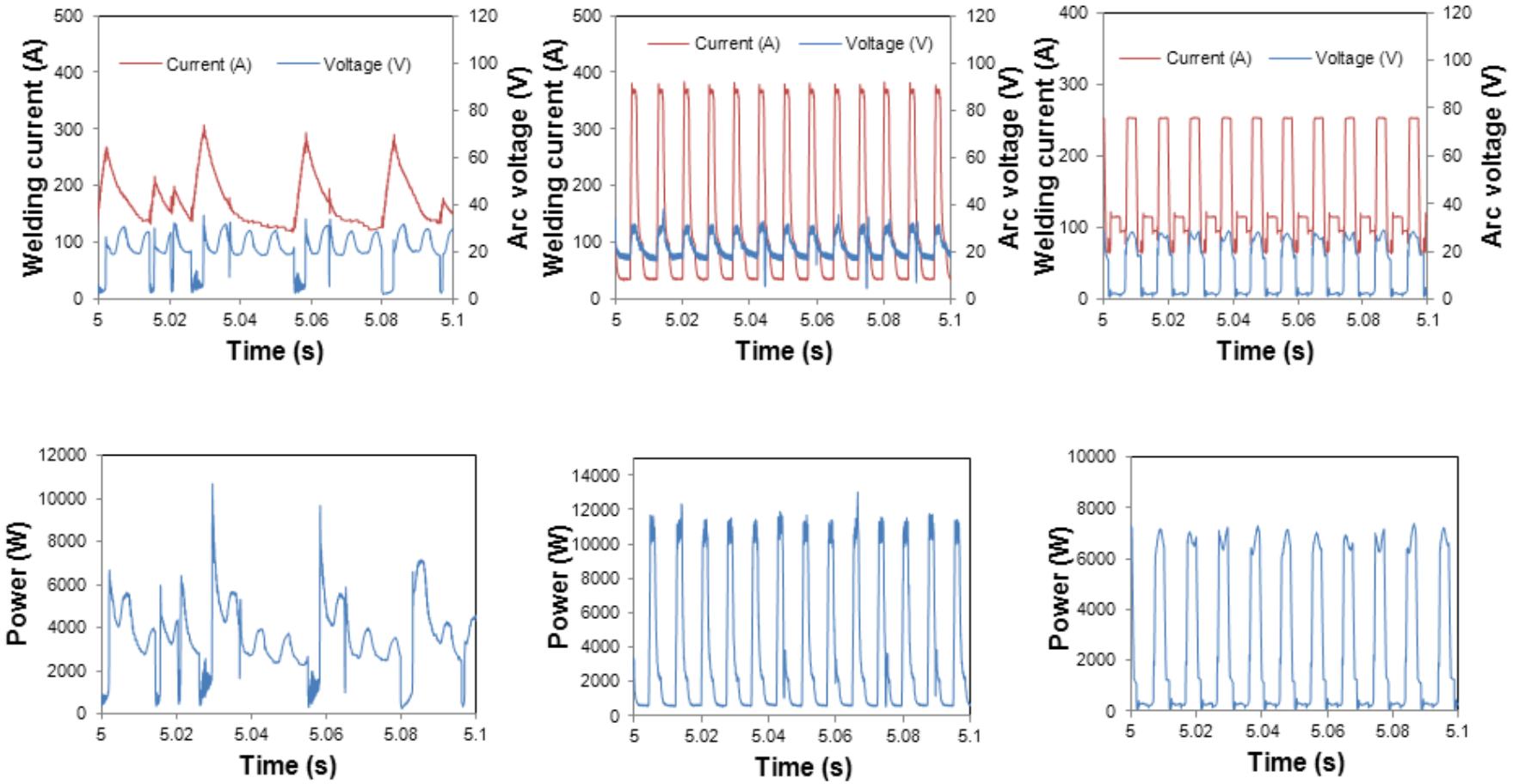

Figure B-4: Transient relationship of current, voltage and power for 6 m/min WFS weld. From left to right, CMT, ColdArc and Short circuit GMAW

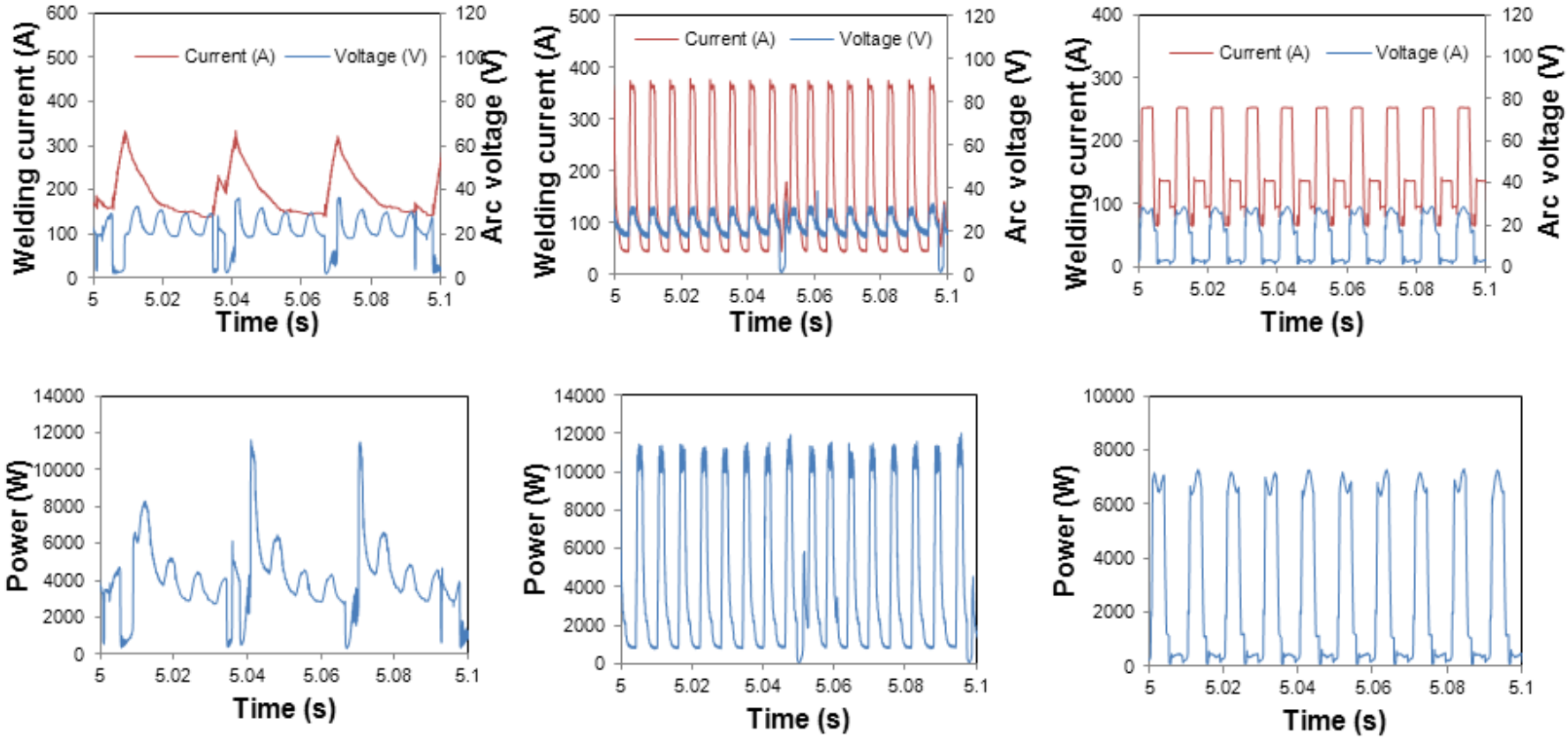

Figure B-5: Transient relationship of current, voltage and power for 7 m/min WFS weld. From left to right, CMT, ColdArc and Short circuit GMAW

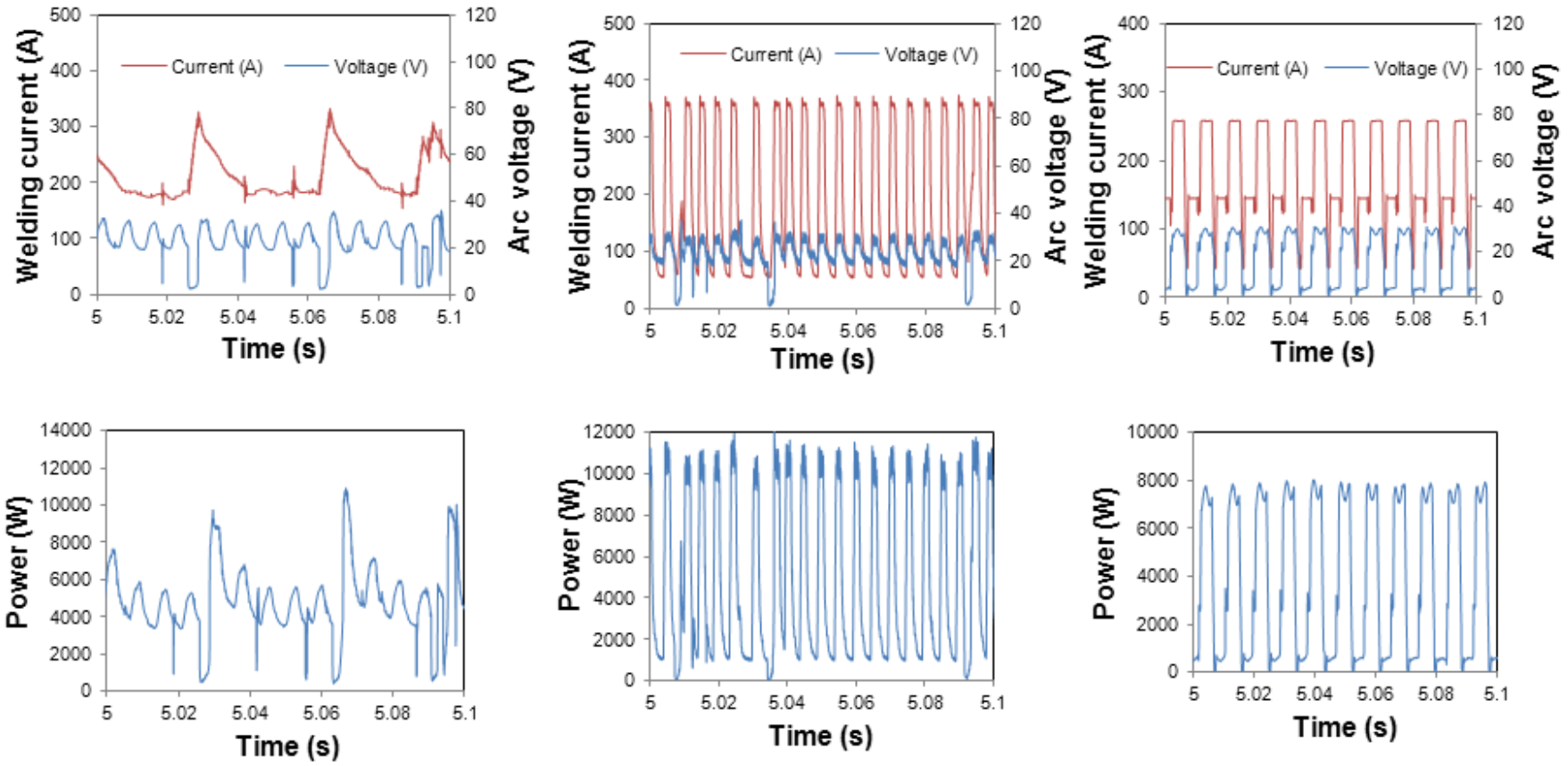

Figure B-6: Transient relationship of current, voltage and power for 8 m/min WFS weld. From left to right, CMT, ColdArc and Short circuit GMAW

Table B-3 : Data of Laser Assisted CMT Welding

Test No.	Laser				CMT						Cooling Time (S)		Cooling Rate ($^{\circ}CS^{-1}$)	
	Beam Dia. (mm)	Laser Power (kW)	Process Distance (mm)	Heat Input (KJ/mm) 50% Eff.	WFS (m/min)	TS (m/min)	Average Voltage (V)	Average Current (A)	Average Inst. Power (kW)	Heat Input (KJ/mm) 80% Eff	$t_{8/5}$	$t_{8/3}$	$t_{8/5}$	$t_{8/3}$
1	20	6	20	0.42	5	0.42	12.20	119.82	2.03	0.23	4.06	9.57	73.89	52.24
2	20	6	15	0.42	5	0.42	12.27	125.25	2.14	0.24	4.16	9.68	72.10	51.64
3	20	6	10	0.42	5	0.42	12.25	129.85	2.22	0.25	4.27	9.84	70.31	50.81
4	20	6	5	0.42	5	0.42	14.63	114.01	2.10	0.24	4.33	10.06	69.27	49.69
5	20	6	0	0.42	5	0.42	12.08	119.25	2.03	0.23	4.37	10.14	68.64	49.30
6	20	3	20	0.21	5	0.42	12.01	132.16	2.26	0.26	2.93	6.58	102.35	76.01
7	20	3	15	0.21	5	0.42	12.14	121.39	2.10	0.24	3.00	6.81	99.87	73.40
8	20	3	10	0.21	5	0.42	12.02	113.80	1.95	0.22	3.07	6.88	97.72	72.71
9	20	3	5	0.21	5	0.42	12.02	123.27	2.08	0.24	3.11	6.97	96.46	71.74
10	20	3	0	0.21	5	0.42	12.08	140.53	2.38	0.27	3.15	7.11	95.04	70.32
11	20	1	20	0.07	5	0.42	14.05	107.37	2.20	0.27	1.99	4.61	150.75	108.46
12	20	1	15	0.07	5	0.42	14.88	108.02	2.12	0.25	2.07	4.75	144.92	105.25
13	20	1	10	0.07	5	0.42	13.88	109.72	2.22	0.25	2.13	4.83	140.84	103.51
14	20	1	5	0.07	5	0.42	13.90	108.28	2.20	0.25	2.21	4.91	135.70	101.83
15	20	1	0	0.07	5	0.42	13.73	110.41	2.20	0.25	2.33	4.96	128.76	100.81
16	15	6	20	0.42	5	0.42	12.44	132.36	2.28	0.26	3.54	8.59	84.72	58.19
17	15	6	15	0.42	5	0.42	12.41	124.93	2.16	0.25	3.57	8.63	84.04	57.94
18	15	6	10	0.42	5	0.42	12.23	114.02	1.95	0.22	3.71	8.69	80.88	57.54
19	15	6	5	0.42	5	0.42	13.00	123.78	2.19	0.25	3.77	8.83	79.60	56.64
20	15	6	0	0.42	5	0.42	15.15	98.35	1.87	0.21	3.88	8.91	78.33	56.12
21	15	5	20	0.36	5	0.42	11.85	124.29	2.10	0.24	3.26	7.97	91.94	62.74
22	15	5	15	0.36	5	0.42	12.69	125.82	2.33	0.27	3.30	7.98	90.80	62.67
23	15	5	10	0.36	5	0.42	12.21	112.50	1.92	0.22	3.41	8.00	88.08	62.50
24	15	5	8	0.36	5	0.42	13.28	108.35	1.95	0.22	3.51	8.38	85.40	59.64

	Laser				CMT									
Test No.	Beam Dia. (mm)	Laser Power (kW)	Process Distance (mm)	Heat Input (KJ/mm) 50% Eff.	WFS (m/min)	TS (m/min)	Average Voltage (V)	Average Current (A)	Average Inst. Power (kW)	Heat Input (KJ/mm) 80% Eff	Cooling Time (S)		Cooling Rate (°CS^{-1})	
											$t_{8/5}$	$t_{8/3}$	$t_{8/5}$	$t_{8/3}$
25	15	5	5	0.36	5	0.42	14.89	114.30	2.14	0.25	3.61	8.41	83.01	59.45
26	15	5	0	0.36	5	0.42	14.21	97.35	1.80	0.21	3.65	8.47	82.19	59.03
27	15	3	20	0.21	5	0.42	12.06	120.66	2.04	0.23	2.80	6.43	106.99	77.00
28	15	3	15	0.21	5	0.42	12.72	115.68	2.02	0.23	2.84	6.52	105.63	76.69
29	15	3	10	0.21	5	0.42	12.40	120.45	2.07	0.24	2.91	6.88	103.09	73.00
30	15	3	8	0.21	5	0.42	11.84	127.26	2.14	0.24	2.93	6.91	102.39	72.36
31	15	3	5	0.21	5	0.42	14.34	102.88	1.79	0.21	2.95	6.94	101.69	72.05
32	15	3	0	0.21	5	0.42	12.01	107.13	1.82	0.21	2.98	7.01	100.67	71.33
33	15	2	10	0.14	5	0.42	12.40	120.57	2.08	0.24	2.51	5.80	119.38	86.28
34	15	2	5	0.14	5	0.42	12.42	116.44	2.00	0.23	2.53	5.84	118.81	85.62
35	15	2	0	0.14	5	0.42	12.27	116.01	1.98	0.23	2.61	5.99	114.94	83.47
36	15	1	20	0.07	5	0.42	14.12	107.21	2.20	0.25	1.93	4.11	155.44	121.65
37	15	1	15	0.07	5	0.42	14.13	104.91	2.16	0.25	1.96	4.30	153.06	116.27
38	15	1	10	0.07	5	0.42	14.26	105.22	2.18	0.25	2.01	4.37	149.25	114.42
39	15	1	5	0.07	5	0.42	13.88	105.94	2.15	0.25	2.09	4.60	143.54	108.70
40	15	1	0	0.07	5	0.42	14.07	108.35	2.22	0.25	2.17	4.63	138.24	107.99
41	10	6	20	0.42	5	0.42	17.38	100.89	2.15	0.25	2.69	6.97	111.52	71.74
42	10	6	15	0.42	5	0.42	15.69	105.39	2.03	0.23	2.76	7.34	108.69	68.12
43	10	6	10	0.42	5	0.42	17.10	105.70	2.12	0.24	2.83	7.76	106.00	64.43
44	10	6	5	0.42	5	0.42	17.71	102.57	2.09	0.24	2.94	8.03	102.04	62.27
45	10	6	0	0.42	5	0.42	17.35	108.05	2.19	0.25	3.02	8.37	99.34	59.67
46	10	3	20	0.21	5	0.42	18.21	100.64	2.21	0.25	1.96	5.99	153.06	83.47
47	10	3	15	0.21	5	0.42	17.36	98.38	2.10	0.24	2.06	6.13	145.63	81.57
48	10	3	10	0.21	5	0.42	16.91	100.32	2.12	0.24	2.20	6.37	136.36	78.49
49	10	3	5	0.21	5	0.42	19.98	115.76	2.30	0.26	2.43	6.78	123.46	73.74
50	10	3	0	0.21	5	0.42	19.82	90.47	2.20	0.25	2.51	6.92	119.52	72.25

Table B-4: Experimental matrix of laser assisted CMT trials with variable CMT WFS

Test No.	Laser				CMT						Cooling Time (S)		Cooling Rate (°CS^{-1})	
	Beam Dia. (mm)	Laser Power (kW)	Process Distance (mm)	Heat Input (KJ/mm) 50% Eff.	WFS (m/min)	TS (m/min)	Average Voltage (V)	Average Current (A)	Average Inst. Power (kW)	Heat Input (KJ/mm) 80% Eff	$t_{8/5}$	$t_{8/3}$	$t_{8/5}$	$t_{8/3}$
1	20	3	20	0.21	5	0.42	19.97	85.50	2.07	0.24	3.18	6.81	94.34	73.42
2	20	3	20	0.21	6	0.42	21.51	107.00	2.60	0.30	3.70	7.96	81.57	62.81
3	20	3	20	0.21	7	0.42	22.56	119.91	2.98	0.34	7.25	11.66	41.35	42.88
4	20	3	20	0.21	8	0.42	23.56	126.06	3.27	0.37	8.57	14.00	35.00	35.71

Table B-5: Measurement of weld bead profile

Weld type	Laser Power (kW)	Beam dia. (mm)	Process distance (mm)	WFS (m/min `	Weld Width (mm)	Weld Penetration (mm)	HAZ Width (mm)
CMT alone	-	-	-	5	5.92	1.16	0.9
CMT alone	-	-	-	6	6.44	0.96	1.01
CMT alone	-	-	-	7	7.83	1.19	1.03
CMT alone	-	-	-	8	7.64	1.56	1.07
Laser assisted CMT	6	20	20	5	8.73	1.32	2.09
Laser assisted CMT	6	20	0	5	6.63	1.55	2.06
Laser assisted CMT	3	20	20	5	6.37	0.98	1.69
Laser assisted CMT	3	20	0	5	6.11	1.25	2.13
Laser assisted CMT	1	20	20	5	6.30	1.04	1.04
Laser assisted CMT	1	20	0	5	6.09	1.07	0.95
Laser assisted CMT	3	20	20	5	6.15	1.19	0.98
Laser assisted CMT	3	20	20	6	6.68	1.28	1.14
Laser assisted CMT	3	20	20	7	6.68	1.55	1.04
Laser assisted CMT	3	20	20	8	8.14	2.27	1.23

Table B-6: Hydrogen content in weld metal for CMT welding with different levels of moisture in the shielding gas

Moist level	Weld mode	Test no.	H_2O content Shielding gas (PPM_V)	Mass of test piece before welding m (g)	Mass of test piece after welding m_1 (g)	Hydrogen content H_{DM} (ml/100g)		
						Single values m = 1 (g)	Single values m_1 - m (g)	Mean value m_1 - m (g)
Level 1 (Dry gas)	CMT	T1(A)	300	35.28	37.36	1.80	3.74	2.98
	CMT	T1(B)	300	35.27	37.37	1.06	2.23	
	CMT	T1(C)	300	35.21	37.28	1.44	2.98	
Level 2	CMT	T2(A)	3000	35.30	37.48	3.11	6.78	6.02
	CMT	T2(B)	3000	35.26	37.38	2.53	5.36	
	CMT	T2 (C)	3000	35.27	37.47	2.70	5.94	
Level 3	CMT	T3(A)	6000	35.30	37.48	-	-	8.93
	CMT	T3(B)	6000	35.35	37.59	4.21	9.43	
	CMT	T3(C)	6000	35.24	37.39	3.92	8.43	
Level 4	CMT	T4(A)	10000	35.28	37.53	5.78	13.00	12
	CMT	T4(B)	10000	35.30	37.37	5.80	12.00	
	CMT	T4(C)	10000	35.20	37.36	6.03	13.02	

Table B-7: Hydrogen content in weld metal for laser assisted CMT welding with different levels of moisture in the shielding gas

Moist level	Weld mode	Test no.	H_2O content Shielding gas (PPM_V)	Mass of test piece before welding m (g)	Mass of test piece after welding m_1 (g)	Hydrogen content H_{DM} (ml/100g)		
						Single values m = 1 (g)	Single values m_1 - m (g)	Mean value m_1 - m (g)
Level 1 (Dry gas)	LCMT	C1(A)	300	35.28	37.50	1.06	2.35	2.09
	LCMT	C1(B)	300	35.30	37.37	0.87	1.80	
	LCMT	C1(C)	300	35.20	37.36	0.98	2.12	
Level 2	LCMT	C2(A)	3000	35.24	37.36	1.84	3.90	3.73
	LCMT	C2(B)	3000	35.12	37.22	2.18	4.58	
	LCMT	C2(C)	3000	35.24	37.26	1.34	2.71	
Level 3	LCMT	C3(A)	6000	35.30	37.37	1.98	4.10	4.99
	LCMT	C3(B)	6000	35.29	37.38	2.36	4.93	
	LCMT	C3(C)	6000	35.23	37.29	2.89	5.95	
Level 4	LCMT	C4(A)	10000	35.34	37.36	3.03	6.12	6.83
	LCMT	C4(B)	10000	35.25	37.49	3.49	7.82	
	LCMT	C4(C)	10000	35.31	37.40	3.13	6.54	

*Laser parameters: 3 kW laser power, 10 mm spot size and 20 mm process distance

Table B-8: Hydrogen content in weld metal for laser assisted CMT welding with different levels of moisture in the shielding gas

Moist level	Weld mode	Test no.	H_2O content Shielding gas (PPM_V)	Mass of test piece before welding m (g)	Mass of test piece after welding m_1 (g)	Hydrogen content H_{DM} (ml/100g)		
						Single values m = 1 (g)	Single values m_1 - m (g)	Mean value m_1 - m (g)
Level 1 (Dry gas)	LCMT	W1(A)	291	35.34	37.74	0.88	2.11	2.10
	LCMT	W1(B)	291	35.38	37.68	0.91	2.09	
	LCMT	W1(C)	291	35.15	37.57	0.87	2.10	
Level 2	LCMT	W2(A)	3000	35.28	37.36	1.94	4.04	3.98
	LCMT	W2(B)	3000	35.25	37.40	1.89	4.01	
	LCMT	W2(C)	3000	35.31	37.63	1.68	3.89	
Level	LCMT	W3(A)	6000	35.28	37.59	2.33	5.38	5.42
	LCMT	W3(B)	6000	35.26	37.46	2.44	5.36	
	LCMT	W3(C)	6000	35.31	37.63	2.39	5.54	
Level	LCMT	W4(A)	10000	35.32	37.60	3.22	7.32	7.31
	LCMT	W4(B)	10000	35.26	37.46	3.32	7.30	
	LCMT	W4(C)	10000	35.31	37.63	3.16	7.33	

*Laser parameters: 3 kW laser power, 10 mm spot size and 0 mm process distance

Table B-9: Hydrogen content in weld metal for laser assisted CMT welding with different levels of moisture in the shielding gas

Moist level	Weld mode	Test no.	H_2O content Shielding gas (PPM_V)	Mass of test piece before welding m (g)	Mass of test piece after welding m_1 (g)	Hydrogen content H_{DM} (ml/100g)		
						Single values m = 1 (g)	Single values m_1 - m (g)	Mean value m_1 - m (g)
Level 1 (Dry gas)	LCMT	S1(A)	291	35.21	37.81	0.84	2.18	2.09
	LCMT	S1(B)	291	35.22	37.29	0.97	2.01	
	LCMT	S1(C)	291	35.13	37.31	0.96	2.09	
Level 2	LCMT	S2(A)	3000	35.21	37.83	1.19	3.12	3.12
	LCMT	S2(B)	3000	35.24	37.78	1.23	3.13	
	LCMT	S2(C)	3000	35.13	37.98	1.09	3.11	
Level 3	LCMT	S3(A)	6000	35.28	37.89	1.61	4.20	4.09
	LCMT	S3(B)	6000	35.06	37.18	1.92	4.07	
	LCMT	S3(C)	6000	35.57	37.67	1.91	4.02	
Level 4	LCMT	S4(A)	10000	35.27	37.35	2.94	6.11	6.10
	LCMT	S4(B)	10000	35.19	37.24	2.94	6.03	
	LCMT	S4(C)	10000	35.08	37.13	3.03	6.21	

*Laser parameters: 6 Kw laser power, 10 mm spot size and 20 mm process distance